

MARCH 2023

AJNR

VOLUME 44 • PP 235-356

AJNR

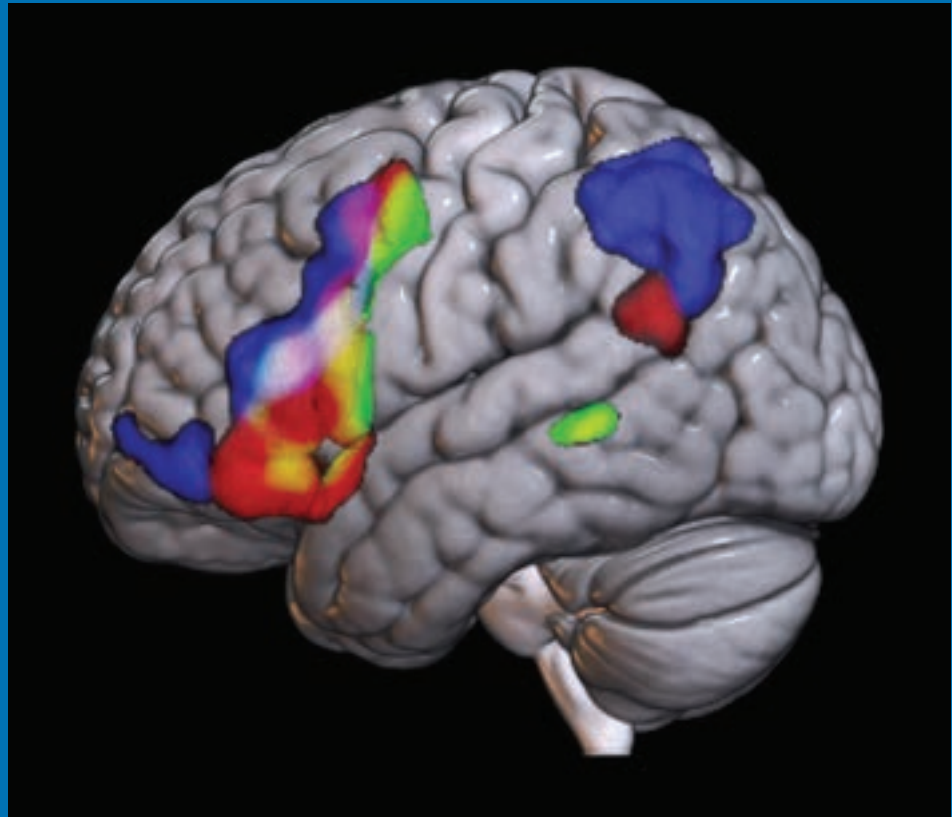
AMERICAN JOURNAL OF NEURORADIOLOGY

MARCH 2023
VOLUME 44
NUMBER 3
WWW.AJNR.ORG

THE JOURNAL OF DIAGNOSTIC AND
INTERVENTIONAL NEURORADIOLOGY

Accuracy of rs-fMRI language network
Multilevel fiber tractography in high-grade gliomas
Persistent opacification of Woven EndoBridge Device
Medullary tegmental cap dysplasia

Official Journal ASNR • ASFNR • ASHNR • ASPNR • ASSR



FRED™ X™

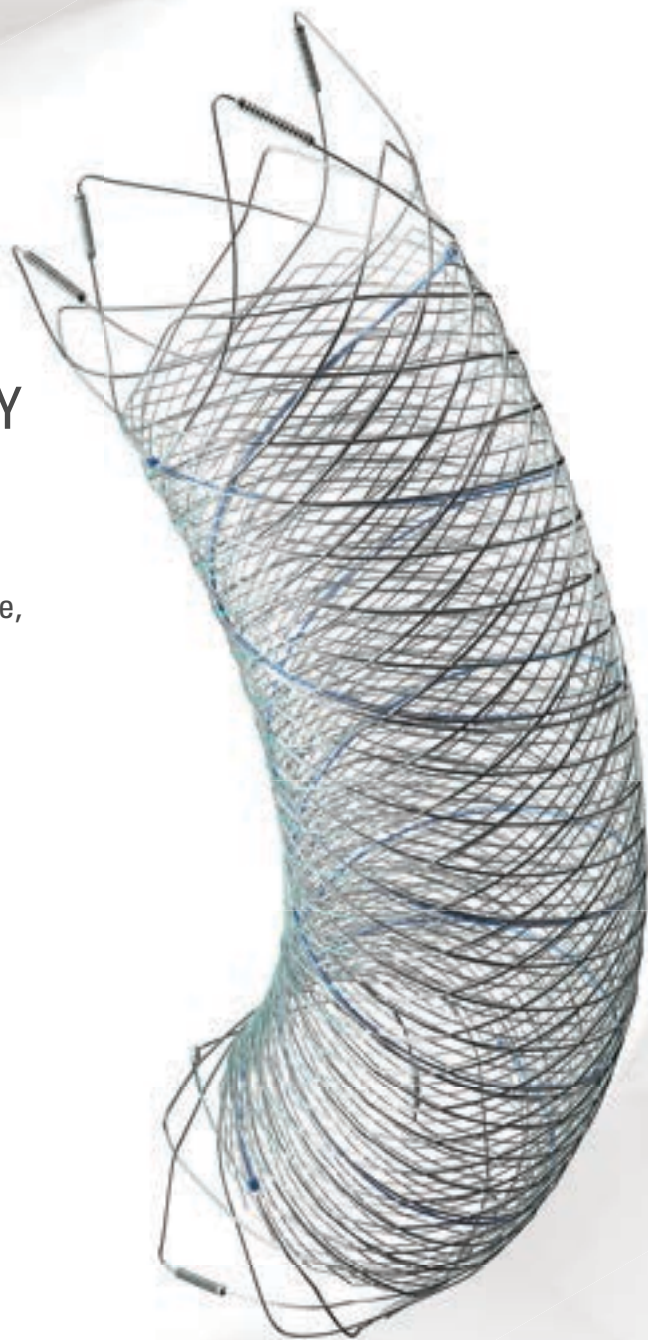
Flow Diverter Stent

THE NEXT ADVANCEMENT IN FLOW DIVERSION TECHNOLOGY

The FRED™ X Flow Diverter features the same precise placement and immediate opening of the FRED™ Device, now with X Technology. X Technology is a covalently bonded, nanoscale surface treatment, designed to:

- **REDUCE MATERIAL THROMBOGENICITY¹**
- **MAINTAIN NATURAL VESSEL HEALING RESPONSE^{2,3,4}**
- **IMPROVE DEVICE DELIVERABILITY AND RESHEATHING¹**

The only FDA PMA approved portfolio with a 0.021" delivery system for smaller device sizes, and no distal lead wire.



For more information, contact your local MicroVention sales representative or visit our website. www.microvention.com



^{*} Data is derived from in vivo and ex vitro testing and may not be representative of clinical performance.

¹ Data on file

² Tanaka M et al. Design of biocompatible and biodegradable polymers based on intermediate water concept. Polymer Journal. 2015;47:114-121.

³ Tanaka M et al. Blood compatible aspects of poly(2-methoxyethylacrylate) (PMEA) – relationship between protein adsorption and platelet adhesion on PMEAs surface. Biomaterials. 2000;21:1471-1481.

⁴ Schiel L et al. X Coating™: A new biopassive polymer coating. Canadian Perfusion Canadienne. June 2001;11(2):9.

Indications for Use: The FRED X System is indicated for use in the internal carotid artery from the petrous segment to the terminus for the endovascular treatment of adult patients (22 years of age or older) with wide-necked (neck width 4 mm or dome-to-neck ratio < 2) saccular or fusiform intracranial aneurysms arising from a parent vessel with a diameter 2.0 mm and 5.0 mm.

Rx Only: Federal (United States) law restricts this device to sale by or on the order of a physician. For Healthcare professionals intended use only.

MICROVENTION, FRED and HEADWAY are registered trademarks of MicroVention, Inc. in the United States and other jurisdictions. Stylized X is a trademark of MicroVention, Inc. © 2022 MicroVention, Inc. MM1222 US 03/22

WEB™ 17

Aneurysm Embolization System

LOWER PROFILE



NEW SIZES



MORE ACCESS OPTIONS



INDICATIONS FOR USE:

The WEB Aneurysm Embolization System is intended for the endovascular embolization of ruptured and unruptured intracranial aneurysms and other neurovascular abnormalities such as arteriovenous fistulae (AVF). The WEB Aneurysm Embolization System is also intended for vascular occlusion of blood vessels within the neurovascular system to permanently obstruct blood flow to an aneurysm or other vascular malformation.

POTENTIAL COMPLICATIONS:

Potential complications include but are not limited to the following: hematoma at the site of entry, aneurysm rupture, emboli, vessel perforation, parent artery occlusion, hemorrhage, ischemia, vasospasm, clot formation, device migration or misplacement, premature or difficult device detachment, non-detachment, incomplete aneurysm filling, revascularization, post-embolization syndrome, and neurological deficits including stroke and death. For complete indications, potential complications, warnings, precautions, and instructions, see instructions for use (IFU provided with the device).

VIA 21, 27, 33 - The VIA Microcatheter is intended for the introduction of interventional devices (such as the WEB device/stents/flow diverters) and infusion of diagnostic agents (such as contrast media) into the neuro, peripheral, and coronary vasculature.

VIA 17,17 Preshaped - The VIA Microcatheter is intended for the introduction of interventional devices (such as the WEB device/stents/flow diverters) and infusion of diagnostic agents (such as contrast media) into the neuro, peripheral, and coronary vasculature.

The VIA Microcatheter is contraindicated for use with liquid embolic materials, such as n-butyl 2-cyanoacrylate or ethylene vinyl alcohol & DMSO (dimethyl sulfoxide).

The device should only be used by physicians who have undergone training in all aspects of the WEB Aneurysm Embolization System procedure as prescribed by the manufacturer.

RX Only: Federal law restricts this device to sale by or on the order of a physician.

For healthcare professional intended use only.



MicroVention Worldwide
Innovation Center PH +1.714.247.8000

35 Enterprise
Aliso Viejo, CA 92656 USA
MicroVention UK Limited PH +44 (0) 191 258 6777
MicroVention Europe, S.A.R.L. PH +33 (1) 39 21 77 46
MicroVention Deutschland GmbH PH +49 211 210 798-0
Website microvention.com



WEB™ and VIA™ are registered trademarks
of Sequent Medical, Inc. in the United States.

©2021 MicroVention, Inc. MM1184 WW 11/2021

LIFE IS FULL OF COMPROMISES.
IT'S TIME TO TAKE A STAND.

NO COMPROMISE

HIGH RELAXIVITY, HIGH STABILITY:^{1,2}
I CHOOSE BOTH.

The individual who appears is for illustrative purposes. The person depicted is a model and not a real healthcare professional. Please see Brief Summary of Prescribing Information including Boxed Warning on adjacent page.

VUEWAY™ (gadopiclenol) solution for injection

Indications

VUEWAY injection is indicated in adults and children aged 2 years and older for use with magnetic resonance imaging (MRI) to detect and visualize lesions with abnormal vascularity in:

- the central nervous system (brain, spine and surrounding tissues),
- the body (head and neck, thorax, abdomen, pelvis, and musculoskeletal system).

IMPORTANT SAFETY INFORMATION

WARNING: NEPHROGENIC SYSTEMIC FIBROSIS (NSF)

Gadolinium-based contrast agents (GBCAs) increase the risk for NSF among patients with impaired elimination of the drugs. Avoid use of GBCAs in these patients unless the diagnostic information is essential and not available with non-contrast MRI or other modalities. NSF may result in fatal or debilitating fibrosis affecting the skin, muscle and internal organs.

- **The risk for NSF appears highest among patients with:**
 - **Chronic, severe kidney disease (GFR < 30 mL/min/1.73 m²), or**
 - **Acute kidney injury.**
- **Screen patients for acute kidney injury and other conditions that may reduce renal function. For patients at risk for chronically reduced renal function (e.g. age > 60 years,**

hypertension, diabetes), estimate the glomerular filtration rate (GFR) through laboratory testing.

- **For patients at highest risk for NSF, do not exceed the recommended VUEWAY dose and allow a sufficient period of time for elimination of the drug from the body prior to any re-administration.**

Contraindications

VUEWAY injection is contraindicated in patients with history of hypersensitivity reactions to VUEWAY.

Warnings

Risk of **nephrogenic systemic fibrosis** is increased in patients using GBCA agents that have impaired elimination of the drugs, with the highest risk in patients chronic, severe kidney disease as well as patients with acute kidney injury. Avoid use of GBCAs among these patients unless the diagnostic information is essential and not available with non-contrast MRI or other modalities.


Hypersensitivity reactions, including serious hypersensitivity reactions, could occur during use or shortly following VUEWAY administration. Assess all patients for any history of a reaction to contrast media, bronchial asthma and/or allergic disorders, administer VUEWAY only in situations where trained personnel and therapies are promptly available for the treatment of hypersensitivity reactions, and observe patients for signs and symptoms of hypersensitivity reactions after administration.



MR Suite

IN MRI

INTRODUCING


Vueway™
(gadopiclenol) injection
485.1 mg/mL

HALF THE GADOLINIUM DOSE COMPARED TO OTHER
MACROCYCLIC GBCAs IN APPROVED INDICATIONS.^{1,3-6}
FROM BRACCO, YOUR TRUSTED PARTNER IN MRI.



LIFE FROM INSIDE

Gadolinium retention can be for months or years in several organs after administration. The highest concentrations (nanomoles per gram of tissue) have been identified in the bone, followed by other organs (brain, skin, kidney, liver and spleen). Minimize repetitive GBCA imaging studies, particularly closely spaced studies, when possible.

Acute kidney injury requiring dialysis has occurred with the use of GBCAs in patients with chronically reduced renal function. The risk of acute kidney injury may increase with increasing dose of the contrast agent.

Ensure catheter and venous patency before injecting as **extravasation** may occur, and cause tissue irritation.

VUEWAY may **impair the visualization of lesions** seen on non-contrast MRI. Therefore, caution should be exercised when Vueway MRI scans are interpreted without a companion non-contrast MRI scan.

The most common adverse reactions (incidence \geq 0.5%) are injection site pain (0.7%), and headache (0.7%).

You are encouraged to report negative side effects of prescription drugs to the FDA. Visit www.fda.gov/medwatch or call 1-800-FDA-1088.

Please see BRIEF SUMMARY of Prescribing Information for VUEWAY, including BOXED WARNING on Nephrogenic Systemic Fibrosis.

Manufactured for Bracco Diagnostics Inc. by Liebel-Flarsheim Company LLC - Raleigh, NC, USA 27616.

VUEWAY is a trademark of Bracco Imaging S.p.A.

References: **1.** Vueway™ (gadopiclenol) Injection Full Prescribing Information. Monroe Twp., NJ: Bracco Diagnostics Inc.; September 2022. **2.** Robic C, Port M, Rousseaux O, et al. Physicochemical and Pharmacokinetic Profiles of Gadopiclenol: A New Macrocytic Gadolinium Chelate With High T1 Relaxivity. *Invest Radiol.* 2019 Aug;54: 475–484. **3.** GADAVIST® (gadobutrol) Injection. Full Prescribing Information. Bayer HealthCare Pharmaceuticals Inc. Whippany, NJ; April 2022. **4.** DOTAREM® (gadoterate meglumine) Injection. Full Prescribing Information. Guerbet LLC. Princeton, NJ; April 2022. **5.** CLARISCAN™ (gadoterate meglumine) injection for intravenous use. Full Prescribing Information. GE Healthcare. Marlborough, MA; February 2020. **6.** ProHance® (Gadoteridol) Injection. Full Prescribing Information and Patient Medication Guide. Monroe Twp., NJ: Bracco Diagnostics Inc.; December 2020.

Bracco Diagnostics Inc.
259 Prospect Plains Road, Building H
Monroe Township, NJ 08831 USA
Phone: 609-514-2200
Toll Free: 1-877-272-2269 (U.S. only)
Fax: 609-514-2446
© 2022 Bracco Diagnostics Inc.
All Rights Reserved. US-VW-2200012 10/22

VISIT
VUEWAY.COM
FOR MORE
INFORMATION



Vueway™

(gadopiclenol) injection, for intravenous use

BRIEF SUMMARY: Please see package insert of full prescribing information.

WARNING: NEPHROGENIC SYSTEMIC FIBROSIS (NSF)
Gadolinium-based contrast agents (GBCAs) increase the risk for NSF among patients with impaired elimination of the drugs. Avoid use of GBCAs in these patients unless the diagnostic information is essential and not available with non-contrast MRI or other modalities. NSF may result in fatal or debilitating fibrosis affecting the skin, muscle and internal organs.

- The risk for NSF appears highest among patients with:
 - Chronic, severe kidney disease (GFR <30 mL/min/1.73 m²), or
 - Acute kidney injury.
- Screen patients for acute kidney injury and other conditions that may reduce renal function. For patients at risk for chronically reduced renal function (e.g. age >60 years, hypertension, diabetes), estimate the glomerular filtration rate (GFR) through laboratory testing.
- For patients at highest risk for NSF, do not exceed the recommended Vueway dose and allow a sufficient period of time for elimination of the drug from the body prior to any re-administration [see Warnings and Precautions (5.1) in the full Prescribing Information].

INDICATIONS AND USAGE

Vueway™ (gadopiclenol) is a gadolinium-based contrast agent indicated in adult and pediatric patients aged 2 years and older for use with magnetic resonance imaging (MRI) to detect and visualize lesions with abnormal vascularity in:

- the central nervous system (brain, spine, and associated tissues),
- the body (head and neck, thorax, abdomen, pelvis, and musculoskeletal system).

CONTRAINDICATIONS

Vueway is contraindicated in patients with history of hypersensitivity reactions to gadopiclenol.

WARNINGS AND PRECAUTIONS

Nephrogenic Systemic Fibrosis Gadolinium-based contrast agents (GBCAs) increase the risk for nephrogenic systemic fibrosis (NSF) among patients with impaired elimination of the drugs. Avoid use of GBCAs among these patients unless the diagnostic information is essential and not available with non-contrast MRI or other modalities. The GBCA-associated NSF risk appears highest for patients with chronic, severe kidney disease (GFR <30 mL/min/1.73 m²) as well as patients with acute kidney injury. The risk appears lower for patients with chronic, moderate kidney disease (GFR 30-59 mL/min/1.73 m²) and little, if any, for patients with chronic, mild kidney disease (GFR 60-89 mL/min/1.73 m²). NSF may result in fatal or debilitating fibrosis affecting the skin, muscle, and internal organs. Report any diagnosis of NSF following Vueway administration to Bracco Diagnostics Inc. (1-800-257-5181) or FDA (1-800-FDA-1088 or www.fda.gov/medwatch).

Screen patients for acute kidney injury and other conditions that may reduce renal function. Features of acute kidney injury consist of rapid (over hours to days) and usually reversible decrease in kidney function, commonly in the setting of surgery, severe infection, injury or drug-induced kidney toxicity. Serum creatinine levels and estimated GFR may not reliably assess renal function in the setting of acute kidney injury. For patients at risk for chronically reduced renal function (e.g., age >60 years, diabetes mellitus or chronic hypertension), estimate the GFR through laboratory testing.

Among the factors that may increase the risk for NSF are repeated or higher than recommended doses of a GBCA and the degree of renal impairment at the time of exposure. Record the specific GBCA and the dose administered to a patient. For patients at highest risk for NSF, do not exceed the recommended Vueway dose and allow a sufficient period of time for elimination of the drug prior to re-administration. For patients receiving hemodialysis, physicians may consider the prompt initiation of hemodialysis following the administration of a GBCA in order to enhance the contrast agent's elimination [see Use in Specific Populations (8.6) and Clinical Pharmacology (12.3) in the full Prescribing Information]. The usefulness of hemodialysis in the prevention of NSF is unknown.

Hypersensitivity Reactions With GBCAs, serious hypersensitivity reactions have occurred. In most cases, initial symptoms occurred within minutes of GBCA administration and resolved with prompt emergency treatment.

- Before Vueway administration, assess all patients for any history of a reaction to contrast media, bronchial asthma and/or allergic disorders. These patients may have an increased risk for a hypersensitivity reaction to Vueway.
- Vueway is contraindicated in patients with history of hypersensitivity reactions to Vueway [see Contraindications (4) in the full Prescribing Information].
- Administer Vueway only in situations where trained personnel and therapies are promptly available for the treatment of hypersensitivity reactions, including personnel trained in resuscitation.
- During and following Vueway administration, observe patients for signs and symptoms of hypersensitivity reactions.

Gadolinium Retention Gadolinium is retained for months or years in several organs. The highest concentrations (nanomoles per gram of tissue) have been identified in the bone, followed by other organs (e.g. brain, skin, kidney, liver, and spleen). The duration of retention also varies by tissue and is longest in bone. Linear GBCAs cause more retention than macrocyclic GBCAs. At equivalent doses, gadolinium retention varies among the linear agents with gadodiamide causing greater retention than other linear agents such as gadoxetate disodium, and gadobenate dimeglumine. Retention is lowest and similar

among the macrocyclic GBCAs such as gadoterate meglumine, gadobutrol, gadoteridol, and gadopiclenol.

Consequences of gadolinium retention in the brain have not been established. Pathologic and clinical consequences of GBCA administration and retention in skin and other organs have been established in patients with impaired renal function [see Warnings and Precautions (5.1) in the full Prescribing Information]. There are rare reports of pathologic skin changes in patients with normal renal function. Adverse events involving multiple organ systems have been reported in patients with normal renal function without an established causal link to gadolinium.

While clinical consequences of gadolinium retention have not been established in patients with normal renal function, certain patients might be at higher risk. These include patients requiring multiple lifetime doses, pregnant and pediatric patients, and patients with inflammatory conditions. Consider the retention characteristics of the agent when choosing a GBCA for these patients. Minimize repetitive GBCA imaging studies, particularly closely spaced studies, when possible.

Acute Kidney Injury in patients with chronically reduced renal function, acute kidney injury requiring dialysis has occurred with the use of GBCAs. The risk of acute kidney injury may increase with increasing dose of the contrast agent. Do not exceed the recommended dose.

Extravasation and Injection Site Reactions Injection site reactions such as injection site pain have been reported in the clinical studies with Vueway [see Adverse Reactions (6.1) in the full Prescribing Information]. Extravasation during Vueway administration may result in tissue irritation [see Nonclinical Toxicology (13.2) in the full Prescribing Information]. Ensure catheter and venous patency before the injection of Vueway.

Interference with Visualization of Lesions Visible with Non-Contrast MRI As with any GBCA, Vueway may impair the visualization of lesions seen on non-contrast MRI. Therefore, caution should be exercised when Vueway MRI scans are interpreted without a companion non-contrast MRI scan.

ADVERSE REACTIONS

The following serious adverse reactions are discussed elsewhere in labeling:

- Nephrogenic Systemic Fibrosis [see Warnings and Precautions (5.1) in the full Prescribing Information]
- Hypersensitivity Reactions [see Contraindications (4) and Warnings and Precautions (5.2) in the full Prescribing Information]

Clinical Trials Experience Because clinical trials are conducted under widely varying conditions, adverse reaction rates observed in the clinical trials of a drug cannot be directly compared to rates in the clinical trials of another drug and may not reflect the rates observed in clinical practice.

The safety of Vueway was evaluated in 1,047 patients who received Vueway at doses ranging from 0.025 mmol/kg (one half the recommended dose) to 0.3 mmol/kg (six times the recommended dose). A total of 708 patients received the recommended dose of 0.05 mmol/kg. Among patients who received the recommended dose, the average age was 51 years (range 2 years to 88 years) and 56% were female. The ethnic distribution was 79% White, 10% Asian, 7% American Indian or Alaska native, 2% Black, and 2% patients of other or unspecified ethnic groups.

Overall, approximately 4.7% of subjects receiving the labeled dose reported one or more adverse reactions.

Table 1 lists adverse reactions that occurred in >0.2% of patients who received 0.05 mmol/kg Vueway.

TABLE 1. ADVERSE REACTIONS REPORTED IN >0.2% OF PATIENTS RECEIVING VUEWAY IN CLINICAL TRIALS	
Adverse Reaction	Vueway 0.05 mmol/kg (n=708) (%)
Injection site pain	0.7
Headache	0.7
Nausea	0.4
Injection site warmth	0.4
Injection site coldness	0.3
Dizziness	0.3
Local swelling	0.3

Adverse reactions that occurred with a frequency ≤ 0.2% in patients who received 0.05 mmol/kg Vueway included: maculopapular rash, vomiting, worsened renal impairment, feeling hot, pyrexia, oral paresthesia, dysgeusia, diarrhea, pruritus, allergic dermatitis, erythema, injection site paresthesia, Cystatin C increase, and blood creatinine increase.

Adverse Reactions in Pediatric Patients

One study with a single dose of Vueway (0.05 mmol/kg) was conducted in 80 pediatric patients aged 2 years to 17 years, including 60 patients who underwent a central nervous system (CNS) MRI and 20 patients who underwent a body MRI. One adverse reaction (maculopapular rash of moderate severity) in one patient (1.3%) was reported in the CNS cohort.

USE IN SPECIFIC POPULATIONS

Pregnancy Risk Summary There are no available data on Vueway use in pregnant women to evaluate for a drug-associated risk of major birth defects, miscarriage or other adverse maternal or fetal outcomes. GBCAs cross the human placenta and result in fetal exposure and gadolinium retention. The available human data on GBCA exposure during pregnancy and adverse fetal outcomes are limited and inconclusive (see Data). In animal reproduction studies, there were no adverse developmental effects observed in rats or rabbits with intravenous administration of Vueway during organogenesis (see Data). Because of the potential risks of gadolinium to the fetus, use Vueway only if imaging is essential during pregnancy and cannot be delayed. The estimated background risk of major birth defects and miscarriage for the indicated population(s) are unknown. All pregnancies have a background risk of birth defect, loss, or other adverse outcomes. In the U.S. general population, the estimated background risk of major birth defects and miscarriage in clinically recognized pregnancies is 2% to 4% and 15% to 20% respectively. Data Human Data Contrast enhancement is visualized in the placenta and fetal tissues after maternal GBCA administration. Cohort studies and case reports on exposure to GBCAs during pregnancy have not reported a clear association between GBCAs and adverse effects in the exposed neonates. However, a retrospective cohort study comparing pregnant women who had a GBCA MRI to pregnant women who did not have an MRI reported a higher occurrence of stillbirths and neonatal deaths in the group receiving GBCA MRI. Limitations of this study include a lack of comparison with non-contrast MRI and lack of information about the maternal indication for MRI. Overall, these data preclude

a reliable evaluation of the potential risk of adverse fetal outcomes with the use of GBCAs in pregnancy.

Animal Data Gadolinium Retention: GBCAs administered to pregnant non-human primates (0.1 mmol/kg on gestational days 85 and 135) result in measurable gadolinium concentration in the offspring in bone, brain, skin, liver, kidney, and spleen for at least 7 months. GBCAs administered to pregnant mice (2 mmol/kg daily on gestational days 16 through 19) result in measurable gadolinium concentrations in the pups in bone, brain, kidney, liver, blood, muscle, and spleen at one-month postnatal age.

Reproductive Toxicology: Animal reproduction studies conducted with gadopiclenol showed some signs of maternal toxicity in rats at 10 mmol/kg and rabbits at 5 mmol/kg (corresponding to 52 times and 57 times the recommended human dose, respectively). This maternal toxicity was characterized in both species by swelling, decreased activity, and lower gestation weight gain and food consumption.

No effect on embryo-fetal development was observed in rats at 10 mmol/kg (corresponding to 52 times the recommended human dose). In rabbits, a lower mean fetal body weight was observed at 5 mmol/kg (corresponding to 57 times the recommended human dose) and this was attributed as a consequence of the lower gestation weight gain.

Lactation Risk Summary There are no data on the presence of gadopiclenol in human milk, the effects on the breastfed infant, or the effects on milk production. However, published lactation data on other GBCAs indicate that 0.01% to 0.04% of the maternal gadolinium dose is excreted in breast milk. Additionally, there is limited GBCA gastrointestinal absorption in the breast-fed infant. Gadopiclenol is present in rat milk. When a drug is present in animal milk, it is likely that the drug will be present in human milk (see Data). The developmental and health benefits of breastfeeding should be considered along with the mother's clinical need for Vueway and any potential adverse effects on the breastfed infant from Vueway or from the underlying maternal condition. Data In lactating rats receiving single intravenous injection of [¹⁵²Gd]-gadopiclenol, 0.3% and 0.2% of the total administered radioactivity was transferred to the pups via maternal milk at 6 hours and 24 hours after administration, respectively. Furthermore, in nursing rat pups, oral absorption of gadopiclenol was 3.6%.

Pediatric Use The safety and effectiveness of Vueway for use with MRI to detect and visualize lesions with abnormal vascularity in the CNS (brain, spine, and associated tissues), and the body (head and neck, thorax, abdomen, pelvis, and musculoskeletal system) have been established in pediatric patients aged 2 years and older.

Use of Vueway in this age group is supported by evidence from adequate and well-controlled studies in adults with additional pharmacokinetic and safety data from an open-label, uncontrolled, multicenter, single dose study of Vueway (0.05 mmol/kg) in 80 pediatric patients aged 2 to 17 years. The 80 patients consisted of 60 patients who underwent a CNS MRI and 20 patients who underwent a body MRI [see Adverse Reactions (6.1) and Clinical Pharmacology (12.3) in the full Prescribing Information].

The safety and effectiveness of Vueway have not been established in pediatric patients younger than 2 years of age.

Geriatric Use Of the total number of Vueway-treated patients in clinical studies, 270 (26%) patients were 65 years of age and over, while 62 (6%) patients were 75 years of age and over. No overall differences in safety or efficacy were observed between these subjects and younger subjects.

This drug is known to be substantially excreted by the kidney, and the risk of adverse reactions to this drug may be greater in patients with impaired renal function. Because elderly patients are more likely to have decreased renal function, it may be useful to monitor renal function.

Renal Impairment in patients with renal impairment, the exposure of gadopiclenol is increased compared to patients with normal renal function. This may increase the risk of adverse reactions such as nephrogenic systemic fibrosis (NSF). Avoid use of GBCAs among these patients unless the diagnostic information is essential and not available with non-contrast MRI or other modalities. No dose adjustment of Vueway is recommended for patients with renal impairment. Vueway can be removed from the body by hemodialysis [see Warnings and Precautions (5.1, 5.3, 5.4) and Clinical Pharmacology (12.3) in the full Prescribing Information].

OVERDOSAGE

Among subjects who received a single 0.3 mmol/kg intravenous dose of gadopiclenol (6 times the recommended dose of Vueway), headache and nausea were the most frequently reported adverse reactions. Gadopiclenol can be removed from the body by hemodialysis [see Clinical Pharmacology (12.3) in the full Prescribing Information].

PATIENT COUNSELING INFORMATION Advise the patient to read the FDA-approved patient labeling (Medication Guide).

Nephrogenic Systemic Fibrosis Inform the patient that Vueway may increase the risk for NSF among patients with impaired elimination of the drugs and that NSF may result in fatal or debilitating fibrosis affecting the skin, muscle and internal organs.

Instruct the patients to contact their physician if they develop signs or symptoms of NSF following Vueway administration, such as burning, itching, swelling, scaling, hardening and tightening of the skin; red or dark patches on the skin; stiffness in joints with trouble moving, bending or straightening the arms, hands, legs or feet; pain in the hip bones or ribs; or muscle weakness [see Warnings and Precautions (5.1) in the full Prescribing Information].

Gadolinium Retention Advise patients that gadolinium is retained for months or years in brain, bone, skin, and other organs following Vueway administration even in patients with normal renal function. The clinical consequences of retention are unknown. Retention depends on multiple factors and is greater following administration of linear GBCAs than following administration of macrocyclic GBCAs [see Warnings and Precautions (5.3) in the full Prescribing Information].

Injection Site Reactions Inform the patient that Vueway may cause reactions along the venous injection site, such as mild and transient burning or pain or feeling of warmth or coldness at the injection site [see Warnings and Precautions (5.5) in the full Prescribing Information].

Pregnancy Advise pregnant women of the potential risk of fetal exposure to Vueway [see Use in Specific Populations (8.1) in the full Prescribing Information].

Rx only

US Patent No. 10,973,934
Manufactured for Bracco Diagnostics Inc. by Liebel-Flarsheim Company LLC - Raleigh, NC, USA 27616.
Toll Free: 1-877-272-2269 (U.S. only)
Revised November 2022

LUCIEN LEVY BEST RESEARCH ARTICLE AWARD WINNER AND NOMINEES NAMED

This award is named for the late *American Journal of Neuroradiology* Senior Editor who championed its establishment and recognizes the best original research paper accepted in 2022. The winning paper was published electronically on December 15, 2022. It was selected by a vote of the journal's Editor-in-Chief and Senior Editors.



The Editors of *AJNR* are pleased to announce the annual Lucien Levy Best Research Article Award has been presented to

“An Artificial Intelligence Tool for Clinical Decision Support and Protocol Selection for Brain MRI ”

by K.A. Wong, A. Hatef, J.L. Ryu, X.V. Nguyen, M.S. Makary and, L.M. Prevedello

Other nominated papers were:

“Normalized Parameters of Dynamic Contrast-Enhanced Perfusion MRI and DWI-ADC for Differentiation between Posttreatment Changes and Recurrence in Head and Neck Cancer” by A. Baba, R. Kurokawa, E. Rawie, M. Kurokawa, Y. Ota, and A. Srinivasan

“Surgical or Endovascular Treatment of MCA Aneurysms: An Agreement Study” by W. Boisseau, T.E. Darsaut, R. Fahed, J.M. Findlay, R. Bourcier, G. Charbonnier, S. Smajda, J. Ognard, D. Roy, F. Gariel, A.P. Carlson, E. Shotar, G. Ciccio, G. Marnat, P.B. Sporns, T. Gaberel, V. Jecko, A. Weill, A. Biondi, G. Boulouis, A.L. Bras, S. Aldea, T. Passeri, S. Boissonneau, N. Bougaci, J.C. Gentric, J.D.B. Diestro, A.T. Omar, H.M. Al-Jehani, G. El Hage, D. Volders, Z. Kaderali, I. Tsogkas, E. Magro, Q. Holay, J. Zehr, D. Iancu, and J. Raymond

“Investigating Brain White Matter in Football Players with and without Concussion Using a Biophysical Model from Multishell Diffusion MRI” by S. Chung, J. Chen, T. Li, Y. Wang, and Y.W. Lui

“Effect of Normal Breathing on the Movement of CSF in the Spinal Subarachnoid Space” by C. Gutiérrez-Montes, W. Coenen, M. Vidorreta, S. Sincomb, C. Martínez-Bazán, A.L. Sánchez, and V. Haughton

“Clinical Evaluation of Scout Accelerated Motion Estimation and Reduction Technique for 3D MR Imaging in the Inpatient and Emergency Department Settings” by M. Lang, A. Tabari, D. Polak, J. Ford, B. Clifford, W.-C. Lo, K. Manzoor, D.N. Splitthoff, L.L. Wald, O. Rapalino, P. Schaefer, J. Conklin, S. Cauley, and S.Y. Huang

“Refining the Neuroimaging Definition of the Dandy-Walker Phenotype” by M.T. Whitehead, M.J. Barkovich, J. Sidpra, C.A. Alves, D.M. Mirsky, Ö. Öztekin, D. Bhattacharya, L.T. Lucato, S. Sudhakar, A. Taranath, S. Andronikou, S.P. Prabhu, K.A. Aldinger, P. Haldipur, K.J. Millen, A.J. Barkovich, E. Boltshauser, W.B. Dobyns, and K. Mankad



The ASNR Career Center

The Go-To Job Site for Neuroradiology Employers and Job Seekers

For Job Seekers

- Access to an expanded network of jobs via the National Healthcare Career Network
- Confidential resume posting
- Professional online profile

For Employers

- Employer resources to help you recruit top talent
- Multiple pricing options, including free Fellowship listings
- Resume search

Start here: careers.asnr.org

AJNR *go green*

***AJNR* urges American Society of Neuroradiology members to reduce their environmental footprint by voluntarily suspending their print subscription.**

The savings in paper, printing, transportation, and postage directly fund new electronic enhancements and expanded content.

The digital edition of *AJNR* presents the print version in its entirety, along with extra features including:

- Publication Preview
- Case Collection
- Podcasts
- The *AJNR* News Digest
- The *AJNR* Blog

It also reaches subscribers much faster than print. An electronic table of contents will be sent directly to your mailbox to notify you as soon as it publishes.

Readers can search, reference, and bookmark current and archived content 24 hours a day on www.ajnr.org.

ASNR members who wish to opt out of print can do so by using the *AJNR* Go Green link on the *AJNR* Website (<http://www.ajnr.org/content/subscriber-help-and-services>). Just type your name in the email form to stop print and spare our ecosystem.

In Planning for Brain Metastases Treatment, Imaging may be the Missing Link in Cost Containment¹

When faced with a patient presenting with metastatic brain cancer, determining whether to use up-front stereotactic radiosurgery (SRS) vs. first treating with whole brain radiotherapy (WBRT) is a significant clinical decision.

WBRT: The whole story on cognitive impairment

While whole brain radiotherapy (WBRT) has been the main treatment option for many years, experts agree that it often results in cognitive deterioration and a negative impact on quality of life. This mental decline has a devastating impact on patients and their families and adds ongoing costs for the healthcare systems managing these symptoms.

Using WBRT instead of SRS in some patients is estimated to decrease the total costs of brain metastasis management, though with increased toxicity.

SRS: Fewer side effects but greater risk of missed tumors

The cost of upfront SRS is the greatest contributor to cost of brain metastasis management.¹ SRS is often more expensive than WBRT. What's more, multiple applications of SRS can increase the cost of treatment greatly.

Stereotactic radiosurgery (SRS) has far fewer side effects, but upfront use of SRS is expensive and can carry the risk of missed tumors, requiring repeat procedures such as salvage SRS.¹

Number of lesions and lesion size are key factors to be considered when determining the treatment plan for these patients. It follows that increased diagnostic information and accuracy could be beneficial in directing the proper therapy and improving overall long-term patient outcomes and containing costs. Getting the diagnosis right the first time is crucial to ensure proper treatment begins quickly, and high cost/high stakes procedures such as SRS need precise surgical planning.

What does optimal visualization mean for outcomes and cost?

For surgical planning with SRS, radiologists need the best visualization achievable to accurately count the number and size of the lesions. These metrics are the key predictors of the need for SRS,¹ WBRT, or a combination of both.

By selecting the ideal contrast agent and equipment protocols, neuroradiologists can identify the proximate numbers of metastases for upfront treatment and reduced salvage treatment occurrences.

The role of radiology

As medical care for oncology patients continues to evolve, it will be increasingly important to assess the cost of various interventions given the often-limited life expectancy of cancer patients, the rising costs of cancer therapy, and the increasing prevalence of cancer in an aging population.

Through seeing all the tumors and tumor borders as clearly as technology allows, radiology can play a part in ensuring that proper treatment can begin quickly,

while containing costs through optimized patient care. Efforts to carefully manage treatment approaches require improvements in protocol design, contrast administration in imaging, and utilizing multimodal imaging approaches.

In this era of precision medicine, radiology departments' contribution to this improved standard of care will have significant short and long-term implications by reducing cost of care, providing a more proximate diagnosis, and ensuring optimal patient outcomes. ■



Getting the diagnosis right the first time is crucial to ensure proper treatment begins quickly.

Reference: 1. Shenker, R. F., McTyre, E. R., Taksler, D et al. Analysis of the drivers of cost of management when patients with brain metastases are treated with upfront radiosurgery. *Clin Neurol Neurosurg.* 2019 Jan;176:10-14.

Join us at **ASNR23** APRIL 29 – MAY 3 • CHICAGO



www.asnr.org/annualmeeting | #ASNR23
Transforming the Future of Neuroradiology

Take Advantage of Early Bird Registration Rates When You Register by March 27!

ASNR 2023 Annual Meeting -- May 1-3

For three days at ASNR23, meet and mingle with friends and colleagues and together explore how the latest educational advances and research are Transforming the Future of Neuroradiology -- all priced at under \$1,000 for members and under \$500 for junior members and members-in-training!

ASNR 2023 Preconference Symposium -- April 29-30

Add on an additional 1.5 days of programming at our Preconference Symposium for only an extra \$150. The Symposium offers additional education on the latest innovations in Artificial Intelligence, neuroimaging virtual and augmented reality, image-guided therapies, and more.

Virtual registration is also available!

Go to www.asnr.org/annualmeeting to get complete details and to register. You'll also find information on booking your hotel room, schedule information, answers to frequently asked questions and more.

AJNR

AMERICAN JOURNAL OF NEURORADIOLOGY

MARCH 2023
VOLUME 44
NUMBER 3
WWW.AJNR.ORG

Publication Preview at www.ajnr.org features articles released in advance of print. Visit www.ajnrblog.org to comment on AJNR content and chat with colleagues and AJNR's News Digest at <http://ajnrdigest.org> to read the stories behind the latest research in neuroimaging.

235 **PERSPECTIVES** *J.S. Ross*

REVIEW ARTICLE






-   236 **Amino Acid Tracer PET MRI in Glioma Management: What a Neuroradiologist Needs to Know** *N. Soni, et al.*

ADULT BRAIN

GENERAL CONTENTS

-   247 **Usefulness of a Rim-Enhancing Pattern on the Contrast-Enhanced 3D-FLAIR Sequence and MRI Characteristics for Distinguishing Meningioma and Malignant Dural-Based Tumor** *T. Panyaping, et al.*
-   254 **Parieto-Occipital Injury on Diffusion MRI Correlates with Poor Neurologic Outcome following Cardiac Arrest** *E. Calabrese, et al.*
-  261 **Validity Assessment of an Automated Brain Morphometry Tool for Patients with De Novo Memory Symptoms** *F. Rahmani, et al.*
-  268 **Edge-Enhancing Gradient-Echo MP2RAGE for Clinical Epilepsy Imaging at 7T** *S. Tao, et al.*
-  271 **Leptomeningeal Interfoliar Enhancement on Vessel Wall MR Imaging as a Unique Radiologic Finding of Susac Syndrome** *P. Cardozo, et al.*
-   274 **Identification of the Language Network from Resting-State fMRI in Patients with Brain Tumors: How Accurate Are Experts?** *S.K. Gujar, et al.*
-    283 **Reconstruction of the Corticospinal Tract in Patients with Motor-Eloquent High-Grade Gliomas Using Multilevel Fiber Tractography Combined with Functional Motor Cortex Mapping** *A. Zhyhka, et al.*
-  291 **Persistent Opacification of the Woven EndoBridge Device: A Conebeam CT Analysis of the Bicêtre Occlusion Scale Score 1 Phenomenon** *J. Caroff, et al.*
-  297 **Embolc Agent Choice in Middle Meningeal Artery Embolization as Primary or Adjunct Treatment for Chronic Subdural Hematoma: A Systematic Review and Meta-analysis** *J.C. Ku, et al.*
- 303 **Endovascular Recanalization of Symptomatic Chronic ICA Occlusion: Procedural Outcomes and Radiologic Predictors** *C. Zhou, et al.*
-  311 **MRI for Cushing Disease: A Systematic Review** *M. Castle-Kirszbaum, et al.*

AJNR (Am J Neuroradiol ISSN 0195–6108) is a journal published monthly, owned and published by the American Society of Neuroradiology (ASNR), 820 Jorie Boulevard, Oak Brook, IL 60523. Annual dues for the ASNR include approximately 19% for a journal subscription. The journal is printed by Intellicor Communications, 330 Eden Road, Lancaster, PA 17601; Periodicals postage paid at Oak Brook, IL and additional mailing offices. Printed in the U.S.A. POSTMASTER: Please send address changes to American Journal of Neuroradiology, P.O. Box 3000, Denville, NJ 07834, U.S.A. Subscription rates: nonmember \$452 (\$530 foreign) print and online, \$320 online only; institutions \$520 (\$594 foreign) print and basic online, \$1029 (\$1103 foreign) print and extended online, \$380 online only (basic), \$825 online only (extended); single copies are \$35 each (\$40 foreign). Indexed by PubMed/MEDLINE, BIOSIS Previews, Current Contents (Clinical Medicine and Life Sciences), EMBASE, Google Scholar, HighWire Press, Q-Sensei, RefSeek, Science Citation Index, SCI Expanded, ReadCube, and Semantic Scholar. Copyright © American Society of Neuroradiology.

- 317 **Increased Labyrinthine T1 Postgadolinium Signal Intensity Is Associated with the Degree of Ipsilateral Sensorineural Hearing Loss in Patients with Sporadic Vestibular Schwannoma** *J.P. Welby, et al.* **HEAD & NECK**
- 323 **Diagnostic Utility of 3D Gradient-Echo MR Imaging Sequences through the Filum Compared with Spin-Echo T1 in Children with Concern for Tethered Cord** *F. Rafiee, et al.* **PEDIATRICS**
-  328 **Neuroimaging Features of Biotinidase Deficiency** *A. Biswas, et al.* **PEDIATRICS**
-   334 **Medullary Tegmental Cap Dysplasia: Fetal and Postnatal Presentations of a Unique Brainstem Malformation** *M. Gafner, et al.* **PEDIATRICS**
-  341 **Modified Dynamic CT Myelography for Type 1 and 2 CSF Leaks: A Procedural Approach** *M.D. Mamlouk, et al.* **SPINE**
-   347 **Conebeam CT as an Adjunct to Digital Subtraction Myelography for Detection of CSF-Venous Fistulas** *A.A. Madhavan, et al.* **SPINE**
-  351 **Postoperative Lumbar Fusion Bone Morphogenic Protein-Related Epidural Cyst Formation** *F. Abel, et al.* **SPINE**
- 356 **35 YEARS AGO IN AJNR**

ONLINE FEATURES

E15 **ERRATUM**

LETTERS

- E16 **Myelographic Timing Matters** *M.D. Mamlouk, et al.*
- E17 **Reply** *S.J. Huls, et al.*
- E18 **Correlation between Sagittal Angle of the Trigeminal Nerve and the Grade of Neurovascular Conflict** *P.P. Suthar, et al.*
- E20 **Reply** *B.F. Branstetter, et al.*

BOOK REVIEWS

R.M. Quencer, Section Editor

Please visit www.ajnrblog.org to read and comment on Book Reviews.



Comparison of task-versus rs-fMRI averaged across subjects, from SK Gujar, et al, in this issue.



Indicates Editor's Choices selection



Indicates Fellows' Journal Club selection



Indicates open access to non-subscribers at www.ajnr.org



Indicates article with supplemental online data



Indicates article with supplemental online video



Evidence-Based Medicine Level 1



Evidence-Based Medicine Level 2

EDITOR-IN-CHIEF

Jeffrey S. Ross, MD

Professor of Radiology, Department of Radiology,
Mayo Clinic College of Medicine, Phoenix, AZ

SENIOR EDITORS

Harry J. Cloft, MD, PhD

Professor of Radiology and Neurosurgery,
Department of Radiology, Mayo Clinic College of
Medicine, Rochester, MN

Christopher G. Filippi, MD

Professor and Alice Ettinger-Jack R. Dreyfuss
Chair of Radiology,
Tufts University School of Medicine,
Radiologist-in-Chief
Tufts University Medical Center, Boston, MA

Thierry A.G.M. Huisman, MD, PD, FICIS, FACR

Radiologist-in-Chief and Chair of Radiology, Texas
Children's Hospital,
Professor of Radiology, Pediatrics, Neurosurgery,
and OBGYN, Baylor College of Medicine,
Houston, TX

Yvonne W. Lui, MD

Associate Professor of Radiology,
Chief of Neuroradiology,
New York University School of Medicine,
New York, NY

C.D. Phillips, MD, FACR

Professor of Radiology, Weill Cornell Medical
College, Director of Head and Neck Imaging,
New York-Presbyterian Hospital, New York, NY

Lubdha M. Shah, MD, MS

Professor of Radiology and Director of Spine
Imaging, University of Utah Department of
Radiology and Imaging Sciences, Salt Lake City, UT

STATISTICAL SENIOR EDITOR

Bryan A. Comstock, MS

Senior Biostatistician,
Department of Biostatistics,
University of Washington, Seattle, WA

ARTIFICIAL INTELLIGENCE DEPUTY EDITOR

Peter D. Chang, MD

Assistant Professor-in-Residence,
Departments of Radiological Sciences,
Computer Sciences, and Pathology,
Director, Center for Artificial Intelligence in
Diagnostic Medicine (CAIDM),
University of California, Irvine, Irvine, CA

EDITORIAL BOARD

Ashley H. Aiken, Atlanta, GA

Matthew D. Alexander, Salt Lake City, UT

Lea M. Alhilali, Phoenix, AZ

Jason W. Allen, Atlanta, GA

Mohammed A. Almekhlafi, Calgary, Alberta,
Canada

Niranjan Balu, Seattle, WA

Matthew J. Barkovich, San Francisco, CA

Joachim Berkefeld, Frankfurt, Germany

Karen Buch, Boston, MA

Judah Burns, New York, NY

Danielle Byrne, Dublin, Ireland

Federico Cagnazzo, Montpellier, France

Gloria C. Chiang, New York, NY

Daniel Chow, Irvine, CA

Kars C.J. Compagne, Rotterdam, The Netherlands

Yonghong Ding, Rochester, MN

Birgit Ertl-Wagner, Toronto, Ontario, Canada

Aaron Field, Madison, WI

Nils D. Forkert, Calgary, Alberta, Canada

Frank Gaillard, Melbourne, Australia

Joseph J. Gemmete, Ann Arbor, Michigan

Brent Griffith, Detroit, MI

Michael J. Hoch, Philadelphia, PA

Joseph M. Hoxworth, Phoenix, AZ

Raymond Y. Huang, Boston, MA

Susie Y. Huang, Boston, MA

Ferdinand K. Hui, Honolulu, HI

Christof Karmonik, Houston, TX

Gregor Kasprian, Vienna, Austria

Timothy J. Kaufmann, Rochester, MN

Hillary R. Kelly, Boston, MA

Toshibumi Kinoshita, Akita, Japan

Ioannis Koktzoglou, Evanston, IL

Stephen F. Kralik, Houston, TX

Luke Ledbetter, Los Angeles, CA

Franklin A. Marden, Chicago, IL

Markus A. Möhlenbruch, Heidelberg, Germany

Mahmud Mossa-Basha, Morrisville, NC

Renato Hoffmann Nunes, Sao Paulo, Brazil

Sam Payabvash, New Haven, CT

Johannes A.R. Pfaff, Salzburg, Austria

Eike I. Piechowiak, Bern, Switzerland

Laurent Pierot, Reims, France

Alexander R. Podgorsak, Chicago, IL

Eytan Raz, New York, NY

Jeff Rudie, San Diego, CA

Paul M. Ruggieri, Cleveland, OH

Fatih Seker, Heidelberg, Germany

Maksim Shapiro, New York, NY

Timothy Shepherd, New York, NY

Mark S. Shiroishi, Los Angeles, CA

Neetu Soni, Rochester, NY

Ashok Srinivasan, Ann Arbor, MI

Jason F. Talbott, San Francisco, CA

Anderanik Tomasian, Los Angeles, CA

Fabio Triulzi, Milan, Italy

Arastoo Vossough, Philadelphia, PA

Richard Watts, New Haven, CT

Elysa Widjaja, Toronto, Ontario, Canada

Ronald Wolf, Philadelphia, Pennsylvania

Shuang Xia, Tianjin, China

Leonard Yeo, Singapore

Woong Yoon, Gwangju, South Korea

David M. Yousem, Evergreen, CO

Carlos Zamora, Chapel Hill, NC

Chengcheng Zhu, Seattle, WA

EDITORIAL FELLOW

Alexandre Boutet, Toronto, Ontario, Canada

SPECIAL CONSULTANTS TO THE EDITOR

AJNR Blog Editor

Neil Lall, Denver, CO

Case of the Month Editor

Nicholas Stence, Aurora, CO

Case of the Week Editors

Matylda Machnowska, Toronto, Ontario, Canada

Anvita Pauranik, Calgary, Alberta, Canada

Classic Case Editor

Sandy Cheng-Yu Chen, Taipei, Taiwan

Health Care and Socioeconomics Editor

Pina C. Sanelli, New York, NY

Physics Editor

Greg Zaharchuk, Stanford, CA

Podcast Editor

Kevin Hiatt, Winston-Salem, NC

Twitter Editor

Jacob Ormsby, Albuquerque, NM

Official Journal:

American Society of Neuroradiology

American Society of Functional Neuroradiology

American Society of Head and Neck Radiology

American Society of Pediatric Neuroradiology

American Society of Spine Radiology

Founding Editor

Juan M. Taveras

Editors Emeriti

Mauricio Castillo, Robert I. Grossman,

Michael S. Huckman, Robert M. Quencer

Managing Editor

Karen Halm

Assistant Managing Editor

Laura Wilhelm

Executive Director, ASNR

Mary Beth Hepp



Title: The Great Barred Spiral Galaxy (NGC 1365) is a double-barred spiral galaxy in the constellation of Fornax. The galaxy has an active galactic nucleus (AGN) due to a super-massive black hole that is thought to be about 2 million solar masses. This image was acquired as a series of 125 5-minute exposures (10 hours) using red, green, and blue filters. The telescope was a Planewave 20" corrected Dall-Kirkham Astrograph, f/4.4 on a Planewave Ascension 200HR mount situated in Australia. The camera was a FLI ProLine PL09000 CCD, with Astrodon filters. The images were processed using PixInsight, Photoshop, and Topaz Labs Adjust AI and DeNoise AI.

Jeffrey S. Ross, Mayo Clinic, Phoenix, Arizona

Amino Acid Tracer PET MRI in Glioma Management: What a Neuroradiologist Needs to Know

N. Soni, M. Ora, A. Jena, P. Rana, R. Mangla, S. Ellika, J. Almast, S. Puri, and S.P. Meyers



ABSTRACT

SUMMARY: PET with amino acid tracers provides additional insight beyond MR imaging into the biology of gliomas that can be used for initial diagnosis, delineation of tumor margins, planning of surgical and radiation therapy, assessment of residual tumor, and evaluation of posttreatment response. Hybrid PET MR imaging allows the simultaneous acquisition of various PET and MR imaging parameters in a single investigation with reduced scanning time and improved anatomic localization. This review aimed to provide neuroradiologists with a concise overview of the various amino acid tracers and a practical understanding of the clinical applications of amino acid PET MR imaging in glioma management. Future perspectives in newer advances, novel radiotracers, radiomics, and cost-effectiveness are also outlined.

ABBREVIATIONS: AAT = amino acid tracer; AA = amino acid; ASCT = alanine-serine-cysteine transporter; BTV = biologic tumor volume; GBM = glioblastoma multiforme; FDOPA = 3,4-dihydroxy-6-¹⁸F-fluoro-L-phenylalanine; FET = O-(2-¹⁸F-fluoroethyl)-L-tyrosine; LAT = large amino acid transporter; HGG = high-grade glioma; LGG = low-grade glioma; MET = ¹¹C-methionine; rCBV = relative CBV; TAC = time-activity curve; TBR = tumor-to-background ratio; TRC = treatment-related changes; TSPO = translocator protein; WHO = World Health Organization

Gliomas represent approximately 80% of malignant brain tumors, with an annual incidence rate of 5.6 cases per 100,000 individuals worldwide. Glioblastoma multiforme (GBM) is the most common primary malignant brain tumor, representing approximately 50% of all gliomas and 16% of all brain tumors.¹ Depending on the size and extent of these tumors, the standard of care for newly diagnosed GBMs usually includes maximal surgical resection followed by radiation and chemotherapy. Despite substantial development in managing high-grade gliomas (HGGs), the median survival is <15 months, with 1- and 5-year survival rates of 40% and 5.5%, respectively.²

Imaging is crucial for diagnosing, guiding biopsy, surgical planning, and distinguishing treatment-related changes (TRC) from recurrence in glioma management. MR imaging is the primary imaging technique; however, it lacks specificity to distinguish between viable neoplastic tissue and tumor-free areas.

Advanced MR imaging techniques such as PWI, DWI, DTI, MRS, and molecular imaging (PET) facilitate visualization and quantification of different metabolic processes and improve overall diagnostic performance in brain tumors. Hybrid PET MR imaging with novel radiotracers provides a noninvasive, simultaneous assessment of brain tumor morphologic, functional, metabolic, and molecular parameters.^{3,4}

This review aimed to provide neuroradiologists with a concise overview of the various amino acid tracers (AATs) and a practical understanding of the clinical applications of amino acid (AA) PET MR imaging in glioma management. We will review the current literature regarding AA-PET MR imaging in glioma treatment and discuss its role in the initial diagnosis, delineation of tumor margin, planning of radiation therapy, assessment of residual tumor, and evaluation of treatment response. We will sum up with future perspectives on newer advances, novel radiotracers, radiomics, and cost-effectiveness.

Received October 13, 2022; accepted after revision November 21.

From the University of Rochester Medical Center (N.S., S.E., J.A., S.P., S.P.M.), Rochester, New York; Sanjay Gandhi Postgraduate Institute of Medical Sciences (M.O.), Lucknow, Uttar Pradesh, India; Indraprastha Apollo Hospital (A.J., P.R.), New Delhi, India; and Upstate University Hospital (R.M.), Syracuse, New York.

Neetu Soni and Manish Ora are first authors.

Please address correspondence to Neetu Soni, MD, DNB, FRCR, 601 Elmwood Ave, Rochester, NY 14612; e-mail: drneetusoni98@gmail.com; @NeetuSo27437480

Indicates open access to non-subscribers at www.ajnr.org

Indicates article with online supplemental data.

<http://dx.doi.org/10.3174/ajnr.A7762>

Radiopharmaceuticals

The Joint European Association of Nuclear Medicine (EANM)/European Association of Neuro-Oncology (EANO)/Response Assessment in Neuro-Oncology (RANO)/Society of Nuclear Medicine and Molecular Imaging (SNMMI) guidelines provide the performance, interpretation of molecular imaging, and clinical application of several PET radiotracers (Online Supplemental Data), including imaging of glucose metabolism FDG and the L-amino acid transport system ¹¹C-methionine (MET), O-(2-

Simultaneous AAT-PET/MRI acquisition protocol

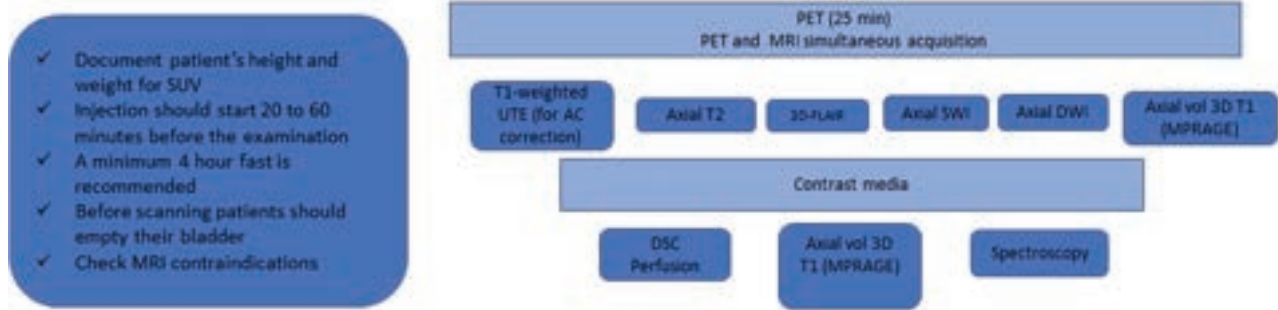


FIG 1. Simultaneous AAT-PET MR imaging acquisition protocol. Min indicates minute; UTE, ultrashort echo time; vol, volume; SUV, standardized uptake value.

[¹⁸F]fluoroethyl)-L-tyrosine (FET), and 3,4-dihydroxy-6-[¹⁸F]fluoro-L-phenylalanine (FDOPA).³

Why Are AATs Supplanting FDG? The radiotracer most comprehensively explored and evaluated for oncology is FDG. Tumors overexpress *GLUT1* with enhanced hexokinase phosphorylation, resulting in increased FDG uptake. FDG has physiologic uptake in the brain parenchyma, resulting in a poor tumor-to-background ratio (TBR). A recent review showed higher sensitivity of AATs than FDG in differentiating tumor progression and TRC in HGGs. FDG (12 studies, 171 lesions), FET (7 studies, 172 lesions), and MET (8 studies, 151 lesions) showed a pooled sensitivity of 84%, 90%, 93% and specificity of 84%, 85%, 82%, respectively.⁵ In a meta-analysis (33 studies, 1734 patients), FET-PET has shown a higher sensitivity (0.88) and lower specificity (0.78) than FDG PET (sensitivity, 0.78; specificity, 0.87) for glioma recurrence. MET and FDOPA-PET also offer good sensitivity (0.92 and 0.85) with moderate specificity (0.78 and 0.70).⁶ Despite the drawbacks, FDG is commonly used due to the limited availability of AATs.³ FDG is a ubiquitous PET tracer and the most widely used tracer in oncology. It has a long half-life (110 minutes) and is easily transportable to a distant lab if the center does not have an onsite cyclotron. At the same time, the ¹¹C-labeled tracer has a short half-life (20 minutes 4 seconds), which limits the remote transport and scheduling of multiple patients.³

What Are Amino Acids, and What Are Their Functions?

AAs are the building blocks of proteins, including enzymes, hormones, membrane channels, and transporters. They are essential for growth regulation, signaling pathways, and energy production. There are 2 main groups of AA transporters: the large amino acid transporter (LAT) and Na⁺-independent transporters (alanine-serine-cysteine transporter [ASCT]). The active intracellular absorption of radiolabeled AATs by the LAT and ASCT is the basis for AAT-PET. L-DOPA, L-tyrosine, and methionine are specific substrates for the LAT1. FET and [¹⁸F] fluciclovine resemble their corresponding AAs, tyrosine and L-leucine.⁷

Why AATs Are an Excellent Choice for Glioma Metabolism Imaging. HGGs show a strong correlation between the uptake of MET and FDOPA with elevated LAT1 expression.^{8,9} LAT1 and

ASCT2 transporters are overexpressed in gliomas more than in normal brain cells, resulting in high TBR. FDOPA exhibits physiologic uptake in the basal ganglia, which underestimates basal ganglia region malignancies.¹⁰

Hybrid PET MR Imaging Acquisition Protocol

Two types of hybrid PET MR imaging scanners are sequential and integrated. A sequential system uses a single bed for both MR imaging and PET scans, which lessens misregistration. An integrated system simultaneously acquires PET and MR imaging data. Brain AAT-PET MR imaging is performed immediately after tracer injection for 20–25 minutes, during which the advanced MR imaging sequences are performed with continuous PET acquisition (Fig 1).³ Dynamic [¹⁸F] FET-PET imaging studies the temporal distribution of tracers within the tumor and healthy brain. It generates the time-activity curves (TACs) to characterize the pattern of FET kinetics in gliomas. Among the various AATs, FET has an established added clinical value for dynamic acquisition.³ HGGs may be distinguished from low-grade gliomas (LGGs) on the basis of their early time-to-peak (0–20 minutes) and the late-phase analysis (20–40 minutes) of plateaued or declining uptake.^{11–13} A steady increase in uptake up to 40 minutes after the injection suggests grade I and II gliomas and TRC.³

Clinical Indications for PET MR Imaging in Glioma Management

Recommendations from the Joint EANM/EANO/RANO/SNMMI guidelines for using AATs in clinical imaging fall into 4 categories: 1) diagnosis and grading, 2) noninvasive tumor genotyping, 3) tumor margin delineation for radiation therapy planning, and 4) disease and treatment monitoring.³ These are discussed in more detail in the following sections.

Initial Diagnosis, Sampling, and Grading. It is crucial to distinguish benign from malignant brain lesions to avoid invasive biopsy (Fig 2). The high specificity and negative predictive value of FET-PET MR imaging help to rule out malignancy with an accuracy of 85% and a change in management in 33% of the untreated equivocal lesions.¹⁴ FET-PET offers supplemental information on tumor extent and biopsy target selection compared

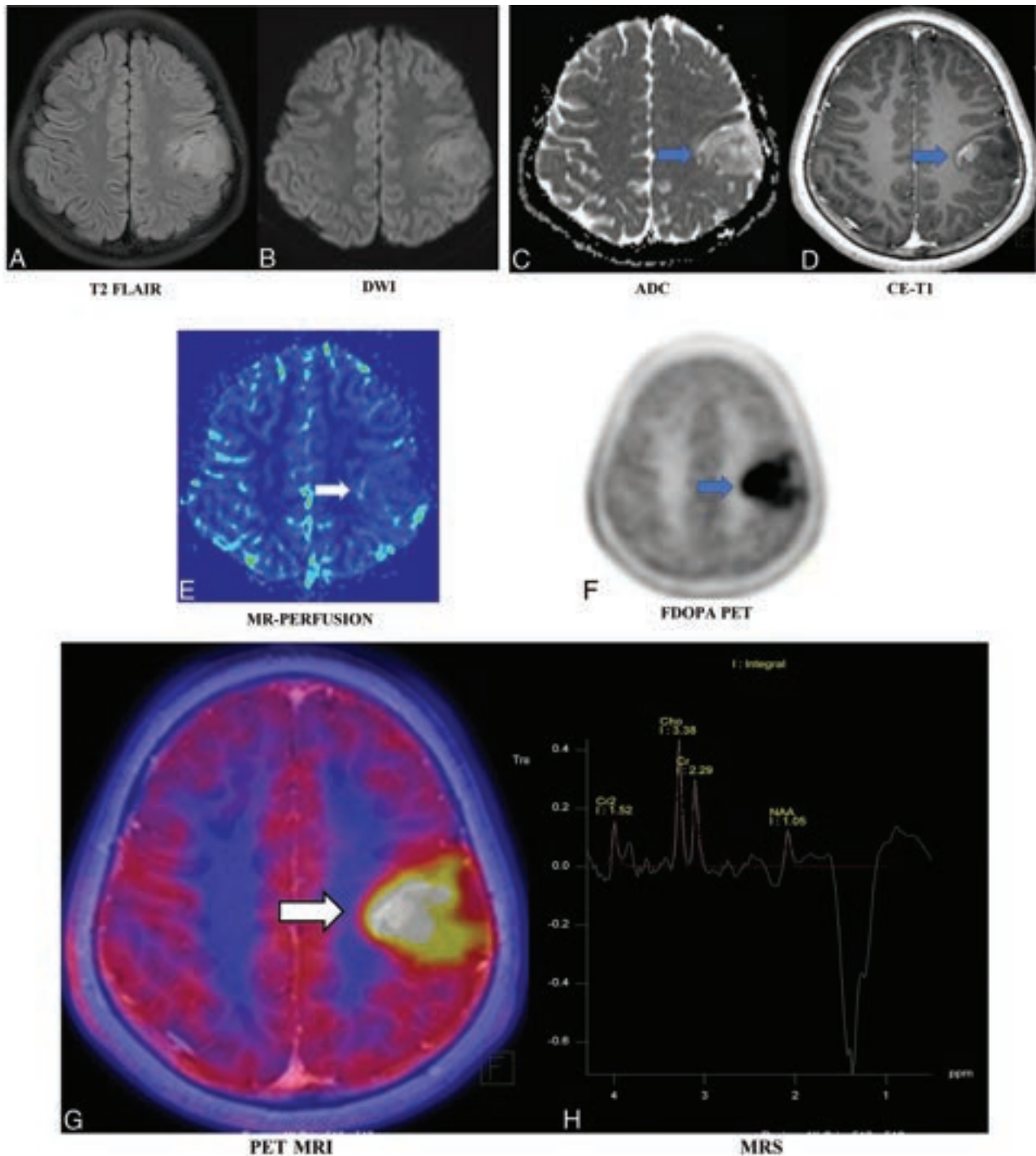


FIG 2. A 12-year-old boy presented with right focal seizures for a month. Electroencephalography was noncontributory. Imaging-based diagnosis of a tuberculoma was made on the initial contrast-enhanced MR imaging in November 2019. Antitubercular treatment was started empirically. Follow-up MR imaging in February 2022 showed an interval increase of the mass from approximately 1.5×1.3 cm to 3.8×3.6 cm (images not shown), which led to further work-up, and the patient underwent AA-PET MR imaging and FDOPA-PET MR imaging. T2 FLAIR (A) demonstrates a hyperintense left posterior frontal mass with equivocal diffusion restriction on the diffusion-weighted image (B and C, blue arrow). A predominantly nonenhancing mass with small peripheral nodular enhancement is seen on postcontrast T1-weighted image (D, blue arrow). No apparent increased regional CBV is seen on DSC PWI (E, white arrow). On FDOPA-PET (F, blue arrow) and fused FDOPA-PET MR imaging (G, white arrow), the lesion showed uniformly increased DOPA uptake throughout with a high maximum standard uptake value of 3.62 (lesion/striatum ratio of 1.81 versus <1.0 as normal) and TBR. Multivoxel MRS (H) showed Cho/NAA and Cho/Cr ratios of 2.78 and 1.4, respectively, with a prominent lactate peak. In this patient, FDOPA-PET MR imaging confirmed the precise diagnosis of neoplastic etiology, which, on biopsy, was revealed to be an anaplastic astrocytoma. CE indicates contrast-enhanced.

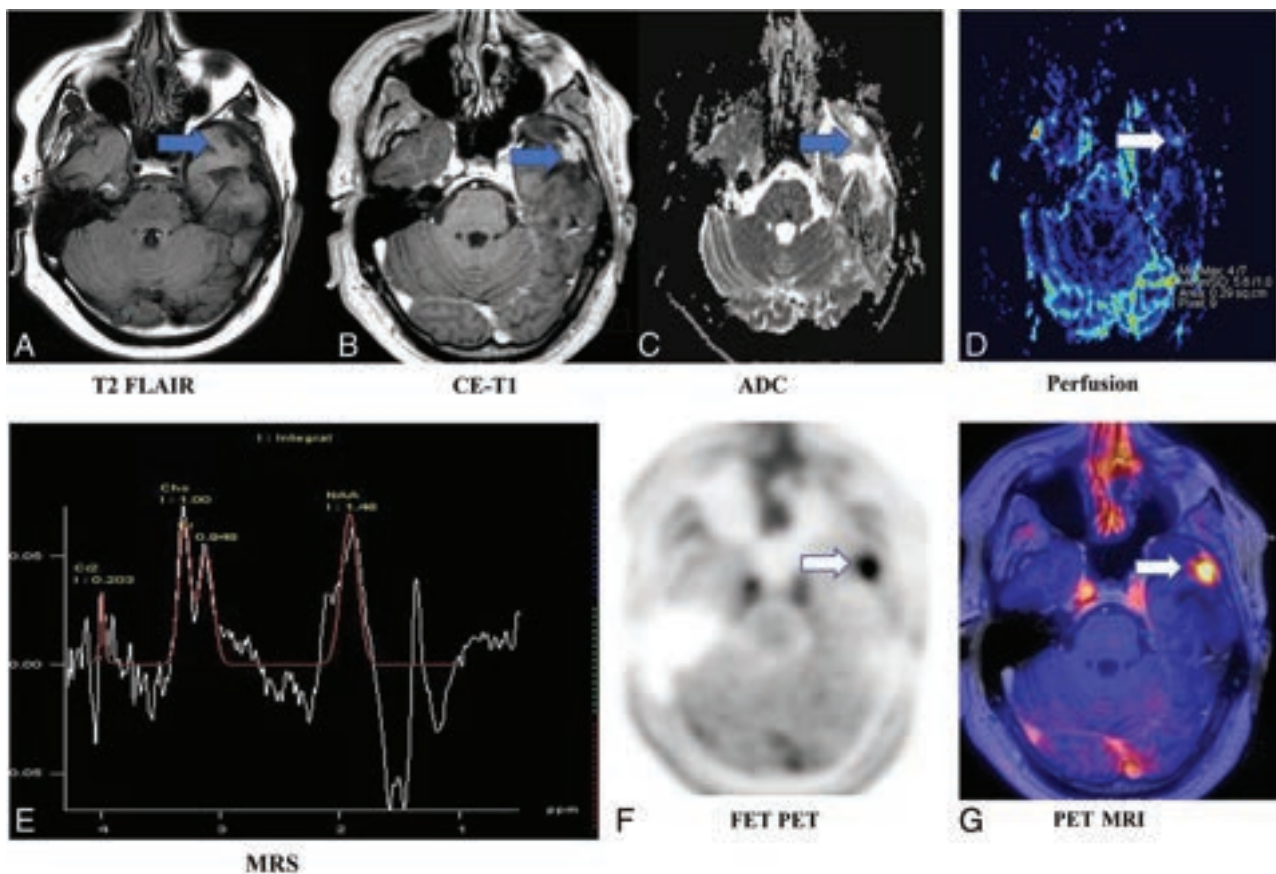


FIG 3. A 43-year-old man treated for a left anterior temporal lobe glioblastoma (*IDH* wild-type) status post resection (positive for generalized paroxysmal fast activity, negative for p53 and *IDH1*, *MIB1* labeling index = 10%–12%, fluorescence in situ hybridization epidermal growth factor receptor amplification, and no loss of 1p19q) and chemoradiation. He underwent follow-up FET-PET MR imaging after 3 years. T2 FLAIR (A, blue arrow) image shows postsurgical changes in the left anterior temporal lobe with peripheral nodular enhancement on the postcontrast T1-weighted image (B), mild increased diffusion restriction (C), and increased perfusion (rCBV of 6.7). Multivoxel MRS (E) shows noisy spectra with mildly raised choline and an inverted lactate peak. Corresponding increased FET uptake (TBR = 2.8; maximum standard uptake value = 3.7) on FET-PET (F) and fused FET-PET MR imaging (G, white arrow). The patient underwent resection, and pathology showed a recurrent tumor. This case highlights the congruent findings on contrast-enhanced MR imaging and FET-PET with a larger TBR leading to less interobserver variability and improving diagnostic performance for differentiating recurrence from TRC. CE indicates contrast-enhanced.

with MR imaging, which further improves with dynamic PET. Dual time-point FET-PET-based targeted biopsies from non-contrast-enhanced areas have shown that FET uptake corresponded to HGGs as far as 3 cm from contrast enhancement.¹⁵ FET-PET-based TBR and PWI-determined relative CBV (rCBV) provide congruent and complementary information on glioma biology, with a moderate overlap of the tumor volumes.¹⁶ FET-PET may improve the outcome of surgical planning in both newly diagnosed and recurrent tumors (Fig 3). AAT-PET biologic tumor volume (BTV) often differs from contrast-enhanced MR imaging BTM (Fig 4). Patients with residual FET uptake have worse outcomes than those with complete FET-PET BTV resection (median overall survival, 13.7 versus 19.3 months, $P = .007$). The results were consistent regardless of age, *MGMT*, *IDH* mutation, promoter, or adjuvant therapy regimens.¹⁷

High- and low-grade subregions may coexist in gliomas. HGGs demonstrate higher uptake of AATs than LGGs. In a recent meta-analysis (7 studies, 219 patients), FDOPA-PET sensitivity and specificity for glioma grading were 0.88 and 0.73, respectively.¹⁸ The diagnostic accuracy of FET-PET and contrast PWI to

discriminate LGGs from HGGs were similar, with an area under the curve TBR maximum of FET-PET uptake and rCBV being 0.83 and 0.81, respectively.¹⁹ Similar trends were observed with combined FDOPA-PET and multiparametric MR imaging.²⁰

Noninvasive Tumor Genetic Profile and Molecular Markers. Gliomas with *IDH1* mutations have better chemoradiation responses and longer survival.²¹ AAT-PET MR imaging has the potential to serve as an alternative to invasive tissue characterization. In 52 patients with gliomas, FET-PET with PWI differentiated 1p/19q codeletion oligodendrogliomas with *IDH* mutations from *IDH* wild-type glioblastomas.²² FDOPA-PET and MR imaging metrics predicted the *IDH* mutation and 1p/19q codeletion with sensitivities of 73% and 76% and specificities of 100% and 94%, respectively.²³ Oligodendrogliomas with the 1p/19q codeletion had MET uptake as high as that of *IDH* wild-type gliomas regardless of *IDH1* mutation status. Therefore, MET-PET seems more useful for glioma grading in *IDH* wild-type gliomas.²⁴ The FET-PET and the DWI-derived TBR/ADC ratio showed higher diagnostic accuracy than the individual technique for HGGs and *IDH1*, human telomerase reverse transcriptase,

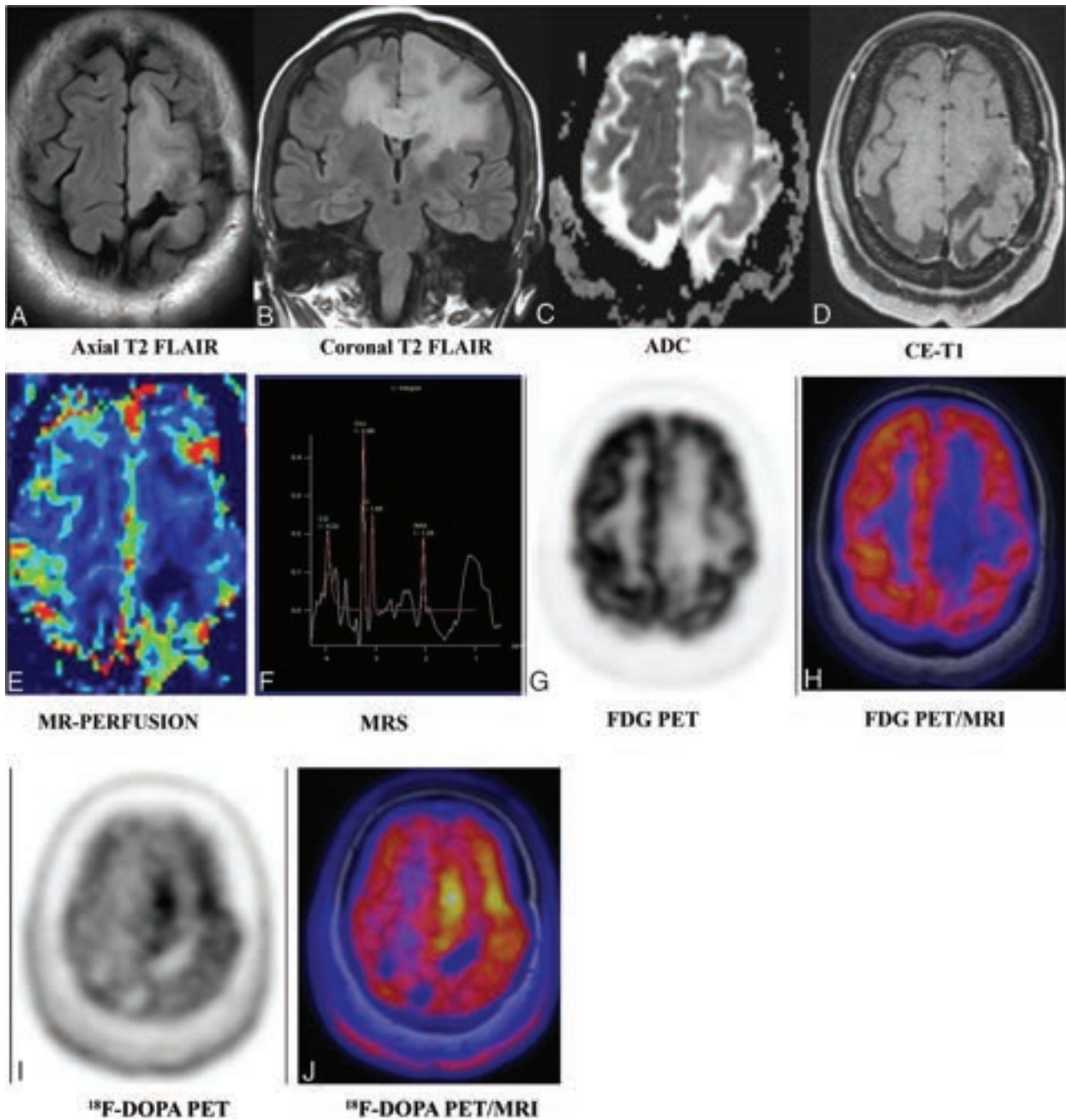


FIG 4. A 35-year-old man was initially diagnosed with left frontal lobe oligodendroglioma grade II, status post resection and chemoradiation in 2008. He underwent a follow-up [^{18}F] DOPA-PET MR imaging. T2 FLAIR axial (A) and coronal (B) images demonstrate a large cortical and subcortical area of abnormal T2-FLAIR hyperintensity in the left parasagittal frontal lobe extending to the left gangliocapsular area and the corpus callosum and across the midline in the right parietal region without apparent diffusion restriction (C), enhancement (D), and increased rCBV perfusion (E). Multivoxel MRS (F) shows increased Cho/Cr and Cho/NAA ratios (1.86 and 2.31, respectively). FDG-PET MR imaging (G and H) shows no appreciable FDG uptake. FDOPA-PET MR imaging shows areas of significant DOPA tracer uptake (maximum standard uptake value = 1.54 versus <1.0 as normal) more prominently in the left paramedian frontal region. FDOPA-avid, FDG-nonavid nonenhancing lesion in the left frontal region involving the corpus callosum with positive MR imaging correlates suggests active underlying residual/recurrent disease. This case again highlights the superiority of AATs over FDG and the importance of multiparametric MR imaging over individual sequences. AAT uptake in the absence of contrast enhancement and increased perfusion helped with the planning of surgery and radiation. CE indicates contrast-enhanced.

and epidermal growth factor receptor–mutated gliomas. Tumor regions with a human telomerase reverse transcriptase mutation had higher TBR and lower ADC values, while tumor protein P53 mutation showed lower TBR and higher ADC values. The 1p/19q

codeletion and epidermal growth factor receptor mutations had lower ADC, and *IDH1* mutations had higher TBR mean values.²⁵ FET-PET MR imaging predicted *ATRX*, *MGMT*, *IDH1*, and 1p19q mutations in 85%, 76%, 89%, and 98%, respectively.²⁶

Tumor Margin Delineation and Defining Tumor Extent for Radiation Therapy Planning. In radiation planning, accurate tumor delineation is essential to provide the maximum tumor dose and minimize treatment-related damage to uninvolved regions. Enhancing components on MR imaging are the usual target for target-volume definition, whereas a tumor may extend beyond areas of enhancement. Conventional MR imaging inadequately distinguishes edema, contrast-enhancing, non-contrast-enhancing, and infiltrating tumors. PET hotspots represent high tumor cell densities. In a recent biopsy-validated study, FET-PET revealed precise glioma extent, allowing personalized treatment planning.²⁷ FDOPA-PET-guided dose-escalated radiation therapy significantly improved the overall survival in methylated and progression-free survival in unmethylated GBMs.²⁸ In 30 patients with HGGs, rCBV and the permeability (K₂) map correlated with enhancing tumor volumes. FET-PET provided complementary information, suggesting that contrast-enhancing MR imaging underestimates the metabolically active tumor volume.²⁹ Tumor volumes were larger in FET-PET than in rCBV maps ($P < .001$), with low spatial similarity of both imaging parameters.³⁰ Similar results by Lohmann et al³¹ demonstrated larger metabolically active tumor volume by FET-PET than by contrast enhancement ($P < .001$) and lower spatial similarity. FET-PET resulted in a mean increase of 27% from clinical target volumes to biologic tumor volumes.³²

Immediate Postsurgical Residual Tumor Evaluation. The assessment of the early postoperative resection status in HGGs is necessary for surgical re-evaluation in the large residual disease. Early postoperative MR imaging may be ambiguous for residual tumors. In 25 patients with HGGs, FET-PET, MR imaging, and intraoperative assessment consistently showed complete resection in 48% of cases and residual disease in 24%.³³ A Prospective PET/MRI study correlated the MET accumulation in GBM patients before postoperative chemoradiation with time to recurrence. The median time to recurrence was significantly shorter in MET-positive than MET-negative patients (6.3 and 19 months, $P < .001$).³⁴ Rosen et al³⁵ evaluated the prognostic value of dynamic FET-PET in partially resected *IDH* wild-type astrocytic gliomas with minimal or absent contrast enhancement. Smaller pre-irradiation FET-PET tumor volumes correlated with a favorable progression-free survival (7.9 versus 4.2 months; $P = .012$) and overall survival (16.6 versus 9.0 months; $P = .002$). In contrast, the mean TBR and time-to-peak values were associated with only a longer progression-free survival ($P = .048$ and $P = .045$, respectively).

Disease and Treatment Monitoring: Differentiation between Tumor Recurrence and TRC. After initial glioma management, TRC are common and may mimic or coexist with tumor recurrence. RANO criteria based on T2-weighted, FLAIR, and contrast-enhancement changes are affected by BBB damage, which fails to differentiate tumor recurrence from treatment-related changes. In 20%–30% of patients, early postirradiation MR imaging exhibited increased enhancement, mimicking progression. However, it gradually disappeared without intervention.³⁶ TRC can appear as new sites of enhancement or an increased extent of enhancement. Multiparametric MRI has certain limitations in

cases of pseudoprogression within the first 12 weeks of therapy and in cases of radionecrosis after 12 weeks of treatment.³⁷ The recent RANO recommendation for AAT-PET also includes assessing the response to radiation in gliomas apart from target delineation, prognostication, and re-irradiation.³⁸ MET-PET was moderately specific (74%) and highly sensitive (97%) in detecting recurrence.³⁹ The sensitivity remained high (97%) and the specificity rose to 93% when MET-PET MR imaging was used.^{39,40} A large meta-analysis (33 studies, 1734 patients) evaluated FET, MET, and FDOPA tracers for tumor recurrence with a sensitivity of 0.88, 0.92, and 0.85 and a specificity of 0.78, 0.78, and 0.70, respectively.⁶ The meta-analysis supports the incorporation of FET and MET in the treatment evaluation of HGGs. The amount of literature on the efficacy of 3'-deoxy-3'-¹⁸F-fluorothymidine [¹⁸F-FLT] and FDOPA is insufficient for a conclusion.⁵

The FET-PET TBR and PWI-rCBV indicators performed moderately well in distinguishing progression from TRC in 104 patients ($P < .01$). A criterion of rCBV maximum of >2.85 allowed a correct diagnosis of progression in 44 patients with a positive predictive value of 100%. In the remaining 60 patients, progression and TRC were discriminated in 78% of patients.⁴¹ FET-PET is of significant clinical importance in diagnosing pseudoprogression related to chemoradiation. FET-PET performed a mean of 10 (SD, 7) days after the equivocal MR imaging findings showed a high accuracy of 87% to identify pseudoprogression, with an improved specificity of 100%.⁴² A combined analysis of arterial spin-labeled CBF and FDOPA uptake allowed high diagnostic performance in differentiating progression and pseudoprogression in treated gliomas.⁴³ Given the high sensitivity for identifying tumor progression, FET-PET MR imaging could change clinical management in nearly one-half of patients.¹⁴

Monitoring Treatment Response to Newer Drugs in Recurrent HGGs. AAT-PET can predict patient survival in both HGGs and LGGs treated with temozolomide. AAT-PET imaging reveals metabolic alterations in response to temozolomide earlier than morphologic alterations on MR imaging. Dynamic TAC patterns are helpful for diagnostic and prognostic purposes, particularly in distinguishing progression from TRC.⁴⁴ Bevacizumab is an anti-angiogenic chemotherapy drug targeting circulating vascular endothelial growth factor and lowering cerebrovascular permeability. It is an adjunctive therapy in recurrent HGGs and significantly reduces contrast enhancement, underestimating residual tumor evaluation. FET, MET, and FDOPA-PET combined with multiparametric MRI have shown promising results for improving accuracy in diagnosing tumor recurrence and detecting early treatment failure and TRC in patients with recurrent HGGs treated with bevacizumab.⁹ In a recurrent HGG in a patient on bevacizumab, the relationship between response to therapy on FET-PET and improved overall survival or progression-free survival is not well-understood. Compared with MR imaging, FET-PET could determine the failure of bevacizumab therapy 9–10.5 weeks earlier and a change in diagnosis or treatment planning in one-third of patients.⁴⁵

The response assessment after immunotherapy in gliomas continues to be a significant challenge due to the rising occurrence of pseudoprogression. In patients with recurrent HGGs

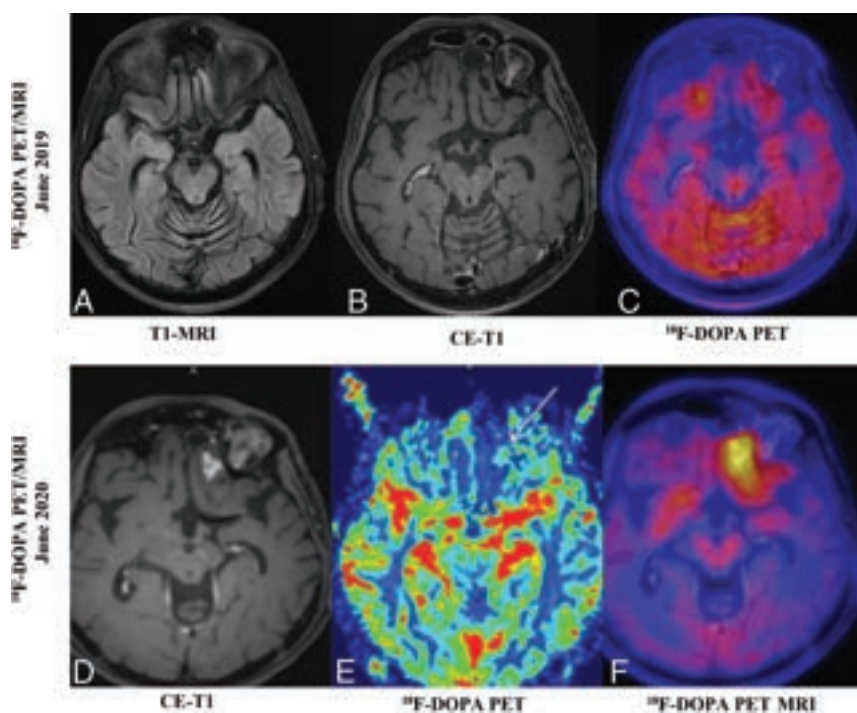


FIG 5. A 35-year-old man was treated for left frontal glioma (grade II), status post surgical resection and chemoradiation in 2009. He underwent a reoperation in February 2018 for tumor recurrence. In June 2019, [¹⁸F] DOPA PET MR imaging (A–C) showed a postresection surgical cavity in the left anterior parasagittal basifrontal region without nodular enhancement or any increased focal FDOPA uptake. There was no evidence of recurrence. In June 2020, follow-up [¹⁸F]-DOPA PET MR imaging (D and E) showed a new focal nodular enhancing lesion in the left basifrontal area (arrow) on the postcontrast T1-weighted image (D), with mildly increased rCBV perfusion (E) and corresponding increased FDOPA uptake on fused FET-PET MR imaging (F) (maximum standard uptake value = 3.9; lesion/striatal ratio; 1.38; <1.0 as normal), suggesting recurrence. The patient underwent a reoperation with recurrence found. This case also highlights the congruent findings on contrast-enhanced MR imaging and FDOPA-PET in differentiating TRC from recurrence. CE indicates contrast-enhanced.

treated with regorafenib (multikinase inhibitor), FET and DWI-ADC metrics can predict the overall survival, and could serve as semiquantitative independent biomarkers of response to treatment.⁴⁶ A recent study analyzed data from patients with GBM who received autologous dendritic cell vaccination therapy. In MR imaging for suspicion for GBM recurrence, FET-PET showed congruent tumor progression in 3/5 patients and TRC in the remaining 2/5.⁴⁷ AAT-PET may help to identify the personalized bevacizumab treatment dose to improve therapeutic efficacy. Tumor volumetric and ADC analyses of serial MR imaging scans from 67 patients and serial FET-TBRs from 31 patients revealed overall survival benefits from bevacizumab plus radiation therapy compared with radiation alone. A high FET-TBR of nonenhancing tumor portions during bevacizumab therapy was associated with an inferior overall survival on multivariate analysis (hazard ratio, 5.97; 95% CI, 1.16–30.8).⁴⁸

Role in Nonenhancing Tumors. Most LGGs do not grossly disrupt BBBs, and many HGGs have nonenhancing regions suboptimally evaluated on conventional MR imaging. In GBM, FLAIR changes adjacent to an enhancement are presumed to be related to edema, which alters radiation protocols. The Radiation

Therapy Oncology Group protocol suggests the possibility of microscopic disease in this region and includes it in the target volume with a lower prescribed radiation dose. In contrast, the European Society for Radiation Therapy and Oncology protocols do not specifically target this region. However, identifying this zone to precisely cover the target volume with the appropriate radiation dose is essential for treatment. AA-PET could image the nonenhancing areas better than conventional MR imaging or FDG (Fig 4).⁴⁹ In a biopsy-validated analysis, combined FDOPA-PET MR imaging detected high-grade subregions with an accuracy of 58% compared with 42% with contrast-enhanced MR imaging ($P = .03$). The hybrid technique leads to larger delineation volumes and better accuracy for detecting high-grade subregions.²⁰ In GBM, AA-PET MR imaging helps to clarify the nature of the suspected nonenhancing region (Figs 5 and 6). It improves delineation of the radiation therapy target, thus reducing undertreatment.³²

Future Perspectives: Newer Advances and Novel Radiotracers

Numerous non-AA tracers demonstrate uptake in gliomas, but the PET signal is frequently not solely attributed to the tumor cells. Glutamine-increased concentration in gliomas correlates with tumor proliferation and treatment resistance. The glutamine fluoro-analog, 4-[¹⁸F]-(2S,4R)-fluoroglutamine distinguishes proliferating gliomas from stable tumors.⁵⁰ The extracellular matrix, stromal cells, immune cells, and blood vessels comprise the tumor microenvironment contributing to tumorigenesis. New therapeutic approaches target tumor microenvironment cells, necessitating the discovery of relevant imaging biomarkers to identify individuals who benefit from such therapy.⁵¹ [¹⁸F]DPA-714(TSPO)-PET MR imaging is used to image the glioma-associated immunosuppressive tumor microenvironment for targeting immunotherapy, drug target engagement, and clinical response assessment.⁵²

Intratumoral hypoxia is associated with resistance to treatment and entails radiation to hypoxic subregions of tumors. [¹⁸F] fluoromisonidazole, a nitroimidazole derivative that images viable hypoxic cells, a biomarker of glioblastoma that correlates with prolonged overall survival⁵³ and distinguishes pseudoprogression from recurrence in patients with HGGs treated with pembrolizumab⁵⁴ [¹⁸F]-GE-180 (a novel TSPO ligand), is an imaging biomarker of tumor heterogeneity with improved binding affinity and a high TBR in glioblastoma. TSPO-PET can differentiate potentially aggressive forms of gliomas, graded according to the

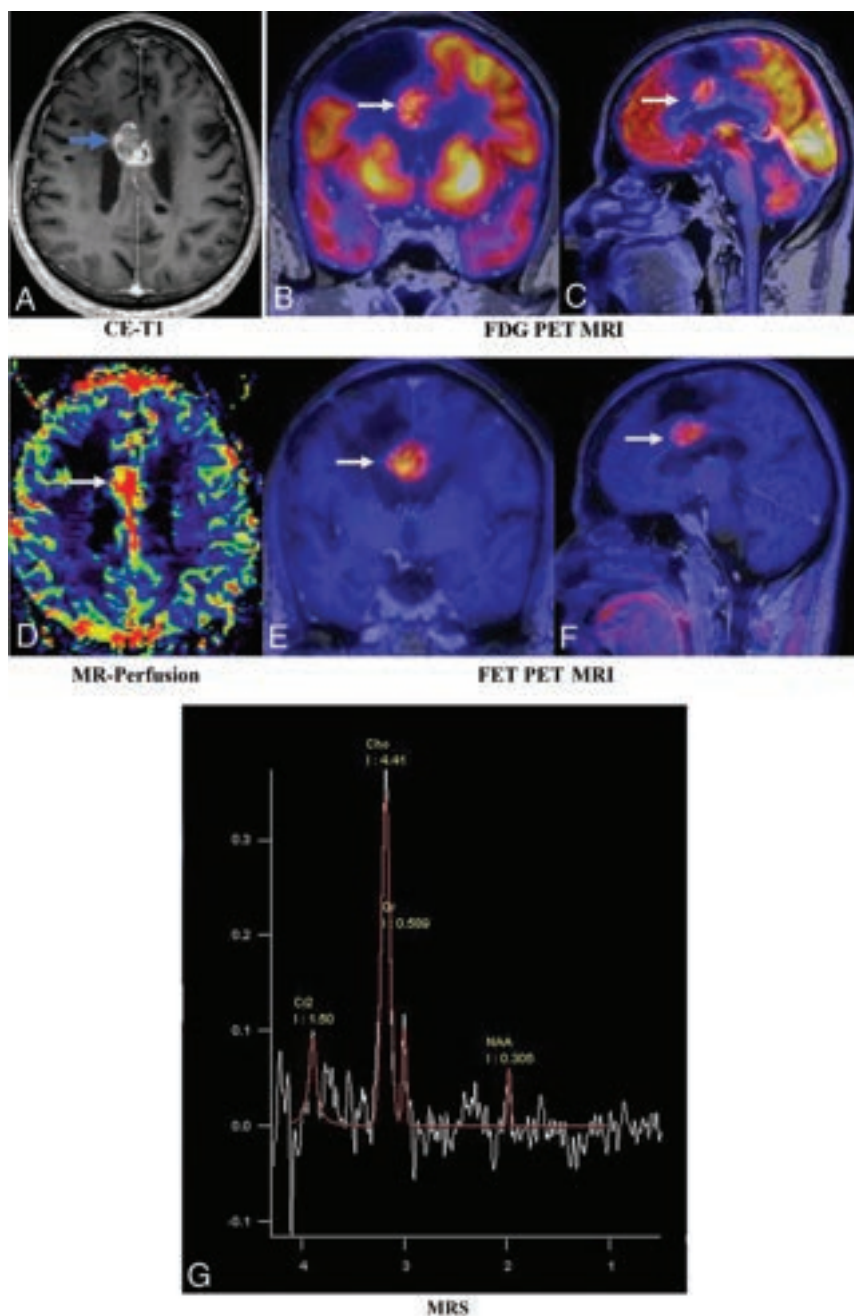


FIG 6. A 37-year-old man with a known diagnosis of oligodendroglioma, status post resection and chemoradiation. Postcontrast T1-weighted image (A, blue arrow) shows a recurrent enhancing lesion along the inferomedial aspect of the resection cavity of the right frontal region involving the body of the corpus callosum. Fused-PET MR images (B and C) show intralesional increased FDG slightly higher than in the white matter and lower than in the gray matter with increased rCBV perfusion (D, white arrows). Fused FET-PET MR images (E and F) show a relatively larger volume of a recurrent lesion, allowing better estimates of the extent of the lesion. Multivoxel MRS (G) shows an increased choline peak and decreased NAA peak. The pathologic diagnosis was a recurrence. This case highlights the superiority of AAT over FDG, congruent findings on MR imaging and FET-PET, and an excellent TBR, which were helpful in radiation therapy planning and re-surgical resection. CE indicates contrast-enhanced.

World Health Organization (WHO) classification, with a positive rate on PET of 100% among the HGGs.⁵⁵ The Arg-Gly-Asp peptide is an angiogenesis-targeting radiotracer that binds $\alpha v \beta 3$ integrins and monitors antiangiogenic therapies.⁵⁶ The fibroblast

activation protein gallium 68-labeled fibroblast activation protein inhibitor [⁶⁸Ga]FAPI shows high accumulation in *IDH* wild-type WHO grade IV gliomas and WHO grade III and IV gliomas compared with WHO grade II gliomas.⁵⁷ Although non-AA tracers are not specific for tumor cell imaging, they might still be used to better delineate tumor extent and, more important, as radiotheranostic agents. However, the results are very preliminary, and validation studies are required.

Application of Feature-Based PET MR Imaging Radiomics in Patients with Gliomas

Radiomics allows the voxel-level extraction of quantitative features from various diagnostic imaging integrated with clinical, histopathologic, and molecular factors to produce diagnostic, prognostic, or predictive mathematic models.⁵⁸ Several PET radiomics analyses have been performed in neuro-oncology with reasonable accuracy to predict the glioma grade and identify the *IDH* mutation and the patients with a high risk of progression after receiving first-line therapy. FET-PET MR imaging combined with textural analysis predicts *IDH* mutations at 93%.⁵⁹ The proposed machine learning model on MET-PET can predict grades of disease.⁶⁰ FET-radiomic features discriminated significantly between tumor and nontumor components of 32 patients with recurrent GBM. The texture feature showed the best performance for predicting time to progression and overall survival and localizing the site of recurrence. The authors postulated that FET-PET radiomics might help with prognostic evaluation and selecting patients with recurrent GBM who would benefit from re-irradiation.⁶¹ Further studies are needed to improve radiomics algorithms to personalize predictive and prognostic models and potentially support the medical decision process.

Cost-Effectiveness of Treatment Monitoring of Gliomas Using AAT-PET

It is crucial to ensure that financial resources are used as efficiently as possible, given the limited resources available for health care. Imaging techniques require substantial investment. They should preferably be used only when the extra value appears to justify the

expense. The known benefit of AAT-PET in patients with glioma is to prevent unnecessary treatment and its side effects. Joint recommendations state that AAT-PET MR imaging is appropriate for clinical use and FET-PET is the most useful for predicting treatment responses of glioblastomas.^{62,63} Despite the ubiquitous use of PET MR imaging, the FDA requires the treating institution to obtain an Investigational New Drug Application, which has prevented the mainstream adoption of AAT-PET into the neuro-oncology clinical algorithm in the United States.

Heinzel et al⁶⁴ evaluated the cost-effectiveness of FET-PET MR imaging-guided biopsy for diagnosing gliomas. FET-PET MR imaging resulted in an increase of 18.5% in the likelihood of a correct diagnosis. The incremental cost-effectiveness ratio for 1 additional accurate diagnosis was €6405 for the baseline scenario and €9114 for the scenario based on higher disease severity. Heinzel et al⁶⁵ investigated the cost-effectiveness of recurrent HGGs treated with bevacizumab and irinotecan. The authors suggested that the additional use of FET-PET in managing patients may be cost-effective. Baguet et al⁶⁶ evaluated the cost-effectiveness of a follow-up PET scan performed on patients with glioblastoma postsurgery and before temozolomide. The decision tree based on overall survival demonstrated that the number of nonresponders identified using PET was 57.14% higher than that with conventional MR imaging.

AATs need to be FDA-approved to become widely available and approved by the Centers for Medicare and Medicaid Services to be reimbursable. Cost-effective analyses of hybrid PET MR imaging scanners are still pending. Further work is needed to update treatment guidelines and to include more PET agents when appropriate, encouraging insurance companies to reimburse for these potentially valuable agents.⁶⁷ A simple-but-effective solution to the limited availability, use, and cost-effectiveness of the hybrid PET MR imaging remains to standardize the protocol for separate PET and MR imaging acquisitions.

Limitations of AATs

Combining PET and MR imaging is more patient-friendly than separate examinations and avoids the limitations of each imaging technique. With the development of PET MR imaging, it is now possible to swiftly and effectively study a variety of PET and MR imaging parameters. Significant hurdles include accessibility, the cost of PET MR imaging examinations, and the limited availability of the AATs. Uncertainty exists regarding the cost-effectiveness of PET MR imaging and the patients who will benefit from combined PET MR imaging. AATs have known limitations, with false-positive results in inflammation, infection, postsurgical regions, and postchemoradiation. Small tumor volumes may lead to false-negative results due to the partial volume effect. Acquisition of a baseline scan helps to compare pre- and post-treatment imaging findings. The estimation of TBR mean, TBR maximum, and BTV with AATs relies on reference brain parenchymal uptake. A decreased uptake due to atrophy, trauma, infarcts, and ischemia may lead to overestimating parameters. Initial dynamic FET images may show a reasonably high blood-pool uptake, and TAC in vascular structures may resemble tumor uptake. An increasing TAC may indicate inflammatory lesions, while a decreasing TAC may be seen in WHO grade II

oligodendroglial tumors.³ A significant proportion (30%) of grade II *IDH*-mutated gliomas do not exhibit considerable AAT uptake. A negative finding on AA-PET is insufficient to exclude LGGs.^{68,69}

CONCLUSIONS

In the current era of precision and personalized medicine, AAT-PET can provide additional insight beyond MR imaging for the clinical management of brain tumors (Online Supplemental Data). Furthermore, sufficient literature is available to demonstrate the utility of AAT-PET MR imaging in distinguishing recurrence from TRC in gliomas. There are several limitations in the existing literature, which may have impacted the diagnostic efficacy of the radionuclide tracers. Prospective validation studies of PET imaging criteria are needed to get beyond these restrictions and allow comparisons of direct results. Even though hybrid PET MR imaging is more patient-friendly and offers practical advantages, the cost-effectiveness and accessibility of these systems must be weighed against the additional effort involved in sequential examinations. As a result, it is projected that more effective therapy monitoring will be available in the upcoming years, which may be beneficial for glioma management.

Disclosure forms provided by the authors are available with the full text and PDF of this article at www.ajnr.org.

REFERENCES

1. Lin D, Wang M, Chen Y, et al. **Trends in intracranial glioma incidence and mortality in the United States, 1975-2018.** *Front Oncol* 2021;11:748061 CrossRef Medline
2. Ostrom QT, Gittleman H, Liao P, et al. **CBTRUS Statistical Report: primary brain and other central nervous system tumors diagnosed in the United States in 2010-2014.** *Neuro Oncol* 2017;19:v1-88 CrossRef Medline
3. Law I, Albert NL, Arbizu J, et al. **Joint EANM/EANO/RANO practice guidelines/SNMMI procedure standards for imaging of gliomas using PET with radiolabelled amino acids and [(18)F]FDG: version 1.0.** *Eur J Nucl Med Mol Imaging* 2019;46:540-57 CrossRef Medline
4. Soni N, Ora M, Mohindra N, et al. **Diagnostic performance of PET and perfusion-weighted imaging in differentiating tumor recurrence or progression from radiation necrosis in posttreatment gliomas: a review of literature.** *AJNR Am J Neuroradiol* 2020;41:1550-57 CrossRef Medline
5. de Zwart PL, van Dijken BR, Holtman GA, et al. **Diagnostic accuracy of PET tracers for the differentiation of tumor progression from treatment-related changes in high-grade glioma: a systematic review and metaanalysis.** *J Nucl Med* 2020;61:498-504 CrossRef Medline
6. Cui M, Zorrilla-Veloz RI, Hu J, et al. **Diagnostic accuracy of PET for differentiating true glioma progression from post treatment-related changes: a systematic review and meta-analysis.** *Front Neurol* 2021;12:671867 CrossRef Medline
7. Moreau A, Febvey O, Mognetti T, et al. **Contribution of different positron emission tomography tracers in glioma management: focus on glioblastoma.** *Front Oncol* 2019;9:9 CrossRef Medline
8. Lopes C, Pereira C, Medeiros R. **ASCT2 and LAT1 contribution to the hallmarks of cancer: from a molecular perspective to clinical translation.** *Cancers (Basel)* 2021;13:203 CrossRef Medline
9. Hughes KL, O'Neal CM, Andrews BJ, et al. **A systematic review of the utility of amino acid PET in assessing treatment response to bevacizumab in recurrent high-grade glioma.** *Neurooncol Adv* 2021;3:v3dab003 CrossRef Medline

10. Fuchs BC, Bode BP. **Amino acid transporters ASCT2 and LAT1 in cancer: partners in crime?** *Semin Cancer Biol* 2005;15:254–66 CrossRef Medline
11. Jansen NL, Suchorska B, Wenter V, et al. **Dynamic 18F-FET PET in newly diagnosed astrocytic low-grade glioma identifies high-risk patients.** *J Nucl Med* 2014;55:198–203 CrossRef Medline
12. Jansen NL, Graute V, Armbruster L, et al. **MRI-suspected low-grade glioma: is there a need to perform dynamic FET PET?** *Eur J Nucl Med Mol Imaging* 2012;39:1021–29 CrossRef Medline
13. Jansen NL, Schwartz C, Graute V, et al. **Prediction of oligodendroglial histology and LOH 1p/19q using dynamic [(18)F]FET-PET imaging in intracranial WHO grade II and III gliomas.** *Neuro Oncol* 2012;14:1473–80 CrossRef Medline
14. Brendle C, Maier C, Bender B, et al. **Impact of (18)F-FET PET/MRI on clinical management of brain tumor patients.** *J Nucl Med* 2022; 63:522–27 CrossRef Medline
15. Furtak J, Rakowska J, Szyberg T, et al. **Glioma biopsy based on hybrid dual time-point FET-PET/MRI: a proof of concept study.** *Front Neurol* 2021;12:634609 CrossRef Medline
16. Göttler J, Lukas M, Kluge A, et al. **Intra-lesional spatial correlation of static and dynamic FET-PET parameters with MRI-based cerebral blood volume in patients with untreated glioma.** *Eur J Nucl Med Mol Imaging* 2017;44:392–97 CrossRef Medline
17. Ort J, Hamou HA, Kernbach JM, et al. **(18)F-FET-PET-guided gross total resection improves overall survival in patients with WHO grade III/IV glioma: moving towards a multimodal imaging-guided resection.** *J Neurooncol* 2021;155:71–80 CrossRef Medline
18. Xiao J, Jin Y, Nie J, et al. **Diagnostic and grading accuracy of (18)F-FDOPA PET and PET/CT in patients with gliomas: a systematic review and meta-analysis.** *BMC Cancer* 2019;19:767 CrossRef Medline
19. Verger A, Filss CP, Lohmann P, et al. **Comparison of (18)F-FET PET and perfusion-weighted MRI for glioma grading: a hybrid PET/MR study.** *Eur J Nucl Med Mol Imaging* 2017;44:2257–65 CrossRef Medline
20. Girard A, Le Reste PJ, Metais A, et al. **Combining (18)F-DOPA PET and MRI with perfusion-weighted imaging improves delineation of high-grade subregions in enhancing and non-enhancing gliomas prior treatment: a biopsy-controlled study.** *J Neurooncol* 2021;155:287–95 CrossRef Medline
21. Osborn AG, Louis DN, Poussaint TY, et al. **The 2021 World Health Organization Classification of Tumors of the Central Nervous System: what neuroradiologists need to know.** *AJNR Am J Neuroradiol* 2022;43:928–37 CrossRef Medline
22. Song S, Wang L, Yang H, et al. **Static (18)F-FET PET and DSC-PWI based on hybrid PET/MR for the prediction of gliomas defined by IDH and 1p/19q status.** *Eur Radiol* 2021;31:4087–96 CrossRef Medline
23. Tatekawa H, Yao J, Oughourlian TC, et al. **Maximum uptake and hypermetabolic volume of 18F-FDOPA PET estimate molecular status and overall survival in low-grade gliomas: a PET and MRI study.** *Clin Nucl Med* 2020;45:e505–11 CrossRef Medline
24. Kim D, Chun JH, Kim SH, et al. **Re-evaluation of the diagnostic performance of (11)C-methionine PET/CT according to the 2016 WHO classification of cerebral gliomas.** *Eur J Nucl Med Mol Imaging* 2019;46:1678–84 CrossRef Medline
25. Cheng Y, Song S, Wei Y, et al. **Glioma imaging by O-(2-18F-fluoroethyl)-L-tyrosine PET and diffusion-weighted MRI and correlation with molecular phenotypes, validated by PET/MR-guided biopsies.** *Front Oncol* 2021;11:743655 CrossRef Medline
26. Haubold J, Demircioglu A, Gratz M, et al. **Non-invasive tumor decoding and phenotyping of cerebral gliomas utilizing multiparametric (18)F-FET PET-MRI and MR fingerprinting.** *Eur J Nucl Med Mol Imaging* 2020;47:1435–45 CrossRef Medline
27. Meyer HS, Liesche-Starnecker F, Mustafa M, et al. **(18)F FET PET uptake indicates high tumor and low necrosis content in brain metastasis.** *Cancers (Basel)* 2021;13:355 CrossRef Medline
28. Laack NN, Pafundi D, Anderson SK, et al. **Initial results of a Phase 2 trial of (18)F-DOPA PET-guided dose-escalated radiation therapy for glioblastoma.** *Int J Radiat Oncol Biol Phys* 2021;110:1383–95 CrossRef Medline
29. Dissaux G, Dissaux B, Kabbaj OE, et al. **Radiotherapy target volume definition in newly diagnosed high grade glioma using (18)F-FET PET imaging and multiparametric perfusion MRI: a prospective study (IMAGG).** *Radiother Oncol* 2020;150:164–71 CrossRef Medline
30. Filss CP, Galldiks N, Stoffels G, et al. **Comparison of 18F-FET PET and perfusion-weighted MR imaging: a PET/MR imaging hybrid study in patients with brain tumors.** *J Nucl Med* 2014;55:540–45 CrossRef Medline
31. Lohmann P, Stavrinou P, Lipke K, et al. **FET PET reveals considerable spatial differences in tumour burden compared to conventional MRI in newly diagnosed glioblastoma.** *Eur J Nucl Med Mol Imaging* 2019;46:591–602 CrossRef Medline
32. Hayes AR, Jayamanne D, Hsiao E, et al. **Utilizing 18F-fluoroethyl-tyrosine (FET) positron emission tomography (PET) to define suspected nonenhancing tumor for radiation therapy planning of glioblastoma.** *Pract Radiat Oncol* 2018;8:230–38 CrossRef Medline
33. Kläsner B, Buchmann N, Gempt J, et al. **Early [18F]FET-PET in gliomas after surgical resection: comparison with MRI and histopathology.** *PLoS One* 2015;10:e0141153 CrossRef Medline
34. Seidlitz A, Beuthien-Baumann B, Löck S, et al. **Final results of the Prospective Biomarker Trial PETra: [(11)C]-MET-accumulation in postoperative PET/MRI predicts outcome after radiochemotherapy in glioblastoma.** *Clin Cancer Res* 2021;27:1351–60 CrossRef Medline
35. Rosen J, Stoffels G, Lohmann P, et al. **Prognostic value of pre-irradiation FET PET in patients with not completely resectable IDH-wildtype glioma and minimal or absent contrast enhancement.** *Sci Rep* 2021;11:20828 CrossRef Medline
36. Ellingson BM, Chung C, Pope WB, et al. **Pseudoprogression, radionecrosis, inflammation or true tumor progression? Challenges associated with glioblastoma response assessment in an evolving therapeutic landscape.** *J Neurooncol* 2017;134:495–504 CrossRef Medline
37. Albert NL, Weller M, Suchorska B, et al. **Response Assessment in Neuro-Oncology Working Group and European Association for Neuro-Oncology recommendations for the clinical use of PET imaging in gliomas.** *Neuro Oncol* 2016;18:1199–208 CrossRef Medline
38. Galldiks N, Niyazi M, Grosu AL, et al. **Contribution of PET imaging to radiotherapy planning and monitoring in glioma patients: a report of the PET/RANO group.** *Neuro Oncol* 2021;23:881–93 CrossRef Medline
39. Deuschl C, Kirchner J, Poeppel TD, et al. **11C-MET PET/MRI for detection of recurrent glioma.** *Eur J Nucl Med Mol Imaging* 2018; 45:593–601 CrossRef Medline
40. D'Souza MM, Sharma R, Jaimini A, et al. **11C-MET PET/CT and advanced MRI in the evaluation of tumor recurrence in high-grade gliomas.** *Clin Nucl Med* 2014;39:791–98 CrossRef Medline
41. Steidl E, Langen KJ, Hmeidani SA, et al. **Sequential implementation of DSC-MR perfusion and dynamic [(18)F]FET PET allows efficient differentiation of glioma progression from treatment-related changes.** *Eur J Nucl Med Mol Imaging* 2021;48:1956–65 CrossRef Medline
42. Werner JM, Weller J, Ceccan G, et al. **Diagnosis of pseudoprogression following lomustine-temozolomide chemoradiation in newly diagnosed glioblastoma patients using FET-PET.** *Clin Cancer Res* 2021;27:3704–13 CrossRef Medline
43. Pellerin A, Khalifé M, Sanson M, et al. **Simultaneously acquired PET and ASL imaging biomarkers may be helpful in differentiating progression from pseudo-progression in treated gliomas.** *Eur Radiol* 2021;31:7395–405 CrossRef Medline
44. Prather KY, O'Neal CM, Westrup AM, et al. **A systematic review of amino acid PET in assessing treatment response to temozolomide in glioma.** *Neurooncol Adv* 2022;4:vdac008 CrossRef Medline

45. Harris RJ, Cloughesy TF, Pope WB, et al. **18F-FDOPA and 18F-FLT positron emission tomography parametric response maps predict response in recurrent malignant gliomas treated with bevacizumab.** *Neuro Oncol* 2012;14:1079–89 CrossRef Medline
46. Lombardi G, Spimpolo A, Berti S, et al. **PET/MR in recurrent glioblastoma patients treated with regorafenib: [(18F)FET and DWI-ADC for response assessment and survival prediction.** *Br J Radiol* 2022;95:20211018 CrossRef Medline
47. Kristin Schmitz A, Sorg RV, Stoffels G, et al. **Diagnostic impact of additional O-(2-[18F]fluoroethyl)-L-tyrosine ((18F)-FET) PET following immunotherapy with dendritic cell vaccination in glioblastoma patients.** *Br J Neurosurg* 2021;35:736–42 CrossRef Medline
48. Wirsching HG, Roelcke U, Weller J, et al. **MRI and (18)F-FET-PET predict survival benefit from bevacizumab plus radiotherapy in patients with isocitrate dehydrogenase wild-type glioblastoma: results from the randomized ARTE Trial.** *Clin Cancer Res* 2021;27:179–88 CrossRef Medline
49. Niyazi M, Brada M, Chalmers AJ, et al. **ESTRO-ACROP guideline “target delineation of glioblastomas.”** *Radiother Oncol* 2016;118:35–42 CrossRef Medline
50. Ekici S, Nye JA, Neill SG, et al. **Glutamine imaging: a new avenue for glioma management.** *AJNR Am J Neuroradiol* 2022;43:11–18 CrossRef Medline
51. Anderson NM, Simon MC. **The tumor microenvironment.** *Curr Biol* 2020;30:R921–25 CrossRef Medline
52. Zinnhardt B, Mütter M, Roll W, et al. **TSPO imaging-guided characterization of the immunosuppressive myeloid tumor microenvironment in patients with malignant glioma.** *Neuro Oncol* 2020;22:1030–43 CrossRef Medline
53. Leimgruber A, Hickson K, Lee ST, et al. **Spatial and quantitative mapping of glycolysis and hypoxia in glioblastoma as a predictor of radiotherapy response and sites of relapse.** *Eur J Nucl Med Mol Imaging* 2020;47:1476–85 CrossRef Medline
54. Barajas RF Jr, Ambady P, Link J, et al. **[(18)F]-fluoromisonidazole (FMISO) PET/MRI hypoxic fraction distinguishes neuroinflammatory pseudoprogression from recurrent glioblastoma in patients treated with pembrolizumab.** *Neurooncol Pract* 2022;9:246–50 CrossRef Medline
55. Unterrainer M, Fleischmann DF, Vettermann F, et al. **TSPO PET, tumour grading and molecular genetics in histologically verified glioma: a correlative (18)F-GE-180 PET study.** *Eur J Nucl Med Mol Imaging* 2020;47:1368–80 CrossRef Medline
56. Echavidre W, Picco V, Faraggi M, et al. **Integrin- $\alpha\beta 3$ as a therapeutic target in glioblastoma: back to the future?** *Pharmaceutics* 2022;14:1054 CrossRef Medline
57. Rohrich M, Loktev A, Wefers AK, et al. **IDH-wildtype glioblastomas and grade III/IV IDH-mutant gliomas show elevated tracer uptake in fibroblast activation protein-specific PET/CT.** *Eur J Nucl Med Mol Imaging* 2019;46:2569–80 CrossRef Medline
58. Lohmann P, Meißner AK, Kocher M, et al. **Feature-based PET/MRI radiomics in patients with brain tumors.** *Neurooncol Adv* 2020;2:iv15–21 CrossRef Medline
59. Lohmann P, Lerche C, Bauer EK, et al. **Predicting IDH genotype in gliomas using FET PET radiomics.** *Sci Rep* 2018;8:13328 CrossRef Medline
60. Russo G, Stefano A, Alongi P, et al. **Feasibility on the use of radiomics features of 11[C]-MET PET/CT in central nervous system tumours: preliminary results on potential grading discrimination using a machine learning model.** *Curr Oncol* 2021;28:5318–31 CrossRef Medline
61. Carles M, Popp I, Starke MM, et al. **FET-PET radiomics in recurrent glioblastoma: prognostic value for outcome after re-irradiation?** *Radiat Oncol* 2021;16:46 CrossRef Medline
62. Langen KJ, Galldiks N. **Update on amino acid pet of brain tumours.** *Curr Opin Neurol* 2018;31:354–61 CrossRef Medline
63. Langen K-J, Heinzel A, Lohmann P, et al. **Advantages and limitations of amino acid PET for tracking therapy response in glioma patients.** *Expert Rev Neurother*.2020;20:137–46 CrossRef Medline
64. Heinzel A, Stock S, Langen K-J, et al. **Cost-effectiveness analysis of FET PET-guided target selection for the diagnosis of gliomas.** *Eur J Nucl Med Mol Imaging* 2012;39:1089–96 CrossRef Medline
65. Heinzel A, Müller D, Langen KJ, et al. **The use of O-(2-18F-fluoroethyl)-L-tyrosine PET for treatment management of bevacizumab and irinotecan in patients with recurrent high-grade glioma: a cost-effectiveness analysis.** *J Nucl Med* 2013;54:1217–22 CrossRef Medline
66. Bague T, Verhoeven J, De Vos F, et al. **Cost-effectiveness of [18F] fluoroethyl-L-tyrosine for temozolomide therapy assessment in patients with glioblastoma.** *Front Oncol* 2019;9:9 CrossRef
67. Ehman EC, Johnson GB, Villanueva-Meyer JE, et al. **PET/MRI: Where might it replace PET/CT?** *J Magn Reson Imaging* 2017;46:1247–62 CrossRef Medline
68. Suchorska B, Giese A, Biczok A, et al. **Identification of time-to-peak on dynamic 18F-FET-PET as a prognostic marker specifically in IDH1/2 mutant diffuse astrocytoma.** *Neuro Oncol* 2018;20:279–88 CrossRef Medline
69. Zhang-Yin JT, Girard A, Bertaux M. **What does PET imaging bring to neuro-oncology in 2022? a review.** *Cancers (Basel)* 2022;14:879 CrossRef Medline

Usefulness of a Rim-Enhancing Pattern on the Contrast-Enhanced 3D-FLAIR Sequence and MRI Characteristics for Distinguishing Meningioma and Malignant Dural-Based Tumor

T. Panyaping, M. Punpichet, P. Tunlayadechanont, and O. Tritanon



ABSTRACT

BACKGROUND AND PURPOSE: Meningiomas are the most common type of extra-axial dural-based tumors; however, malignant dural-based tumors can mimic meningiomas on imaging. The aim of this study was to determine the efficacy of differentiating meningiomas from malignant dural-based tumors by using rim-enhancement patterns on a contrast-enhanced FLAIR sequence and MR imaging characteristics.

MATERIALS AND METHODS: This retrospective study included 102 patients with meningiomas and 31 patients with malignant dural-based tumors who underwent pretreatment MR imaging. The rim-enhancement patterns on contrast-enhanced FLAIR and MR imaging characteristics, including the dural tail sign, hyperostosis, bony destruction, leptomeningeal enhancement, peritumoral edema, T2-weighted signal intensity, and tumor enhancement were evaluated.

RESULTS: Complete rim enhancement of the tumor-brain interface on contrast-enhanced FLAIR (contrast-enhanced-FLAIR rim sign) was present in most meningiomas (91/102, 89.2%) and at significantly greater frequency than in malignant dural-based tumors (2/31, 6.5%) ($P < .001$). Complete contrast-enhanced FLAIR rim enhancement provided high sensitivity (89.2%), specificity (93.5%), and accuracy (90.2%) for diagnosing meningioma. Additionally, hyperostosis was an MR imaging characteristic that suggested a diagnosis of meningioma. In contrast, bony destruction with cortical breakthrough and leptomeningeal enhancement suggested malignant dural-based tumors. There were limitations of meningiomas of <2.0 cm or at cavernous sinus locations that did not demonstrate contrast-enhanced FLAIR rim enhancement.

CONCLUSIONS: The rim-enhancement pattern on contrast-enhanced FLAIR could help differentiate meningiomas and malignant dural-based tumors. The presence of complete rim enhancement on contrast-enhanced FLAIR was a robust predictive sign for meningioma.

ABBREVIATIONS: AUC = area under the curve; CE = contrast-enhanced; NPV = negative predictive value; PPV = positive predictive value; WHO = World Health Organization

Meningioma is the most common intracranial neoplasm and extra-axial tumor, representing up to 30% of all adult intracranial neoplasms.¹ The World Health Organization (WHO) classifies meningiomas on the basis of their histologic characteristics and recurrence risk as follows: grade I, benign (80%); grade II, atypical (18%); and grade III, anaplastic/malignant (2%).

Meningiomas typically have a dual blood supply in which the primary arterial feeders from dural branches or meningeal arteries largely supply the tumor core, generating a “sunburst pattern.” In large tumors, recruitment of pial supply from intracranial arteries to the peripheral parts of the tumor may be seen and provides some specific MR imaging features of rim enhancement on contrast-enhanced (CE) FLAIR images.^{2,3}

In 2003, Oguz and Cila⁴ investigated the enhancement patterns of meningiomas on CE-FLAIR images. Twenty-one meningiomas (70%) showed peripheral (rim) enhancement patterns, which is related to the dual (dural and pial) vascular supply to meningiomas more commonly seen in tumors of >2 cm in diameter. In 2005, Oner et al⁵ found that 85% of meningiomas of >2 cm showed peripheral enhancement on the CE-FLAIR sequence, confirming the dual vascular supply. In 2014, Enokizono et al⁶ revealed that

Received October 6, 2022; accepted after revision January 3, 2023.

From the Department of Diagnostic and Therapeutic Radiology, Faculty of Medicine, Ramathibodi Hospital, Mahidol University, Bangkok, Thailand.

Please address correspondence to Oranon Tritanon, MD, Department of Diagnostic and Therapeutic Radiology, Faculty of Medicine, Ramathibodi Hospital, Mahidol University, 270 Rama VI Rd, Ratchathewi, Bangkok 10400, Thailand; e-mail: Orantrita@gmail.com

Indicates open access to non-subscribers at www.ajnr.org

Indicates article with online supplemental data.

<http://dx.doi.org/10.3174/ajnr.A7780>

the rim-enhancement patterns on CE-FLAIR were strongly correlated with the presence of a dual vascular supply, which was evidenced by DSA, and classified the rim-enhancement patterns on CE-FLAIR into 4 grades by their extent from 0 (no rim visible) to 3 (rim visible over most of the tumor-brain interface). They also concluded that the rim-enhancement patterns on CE-FLAIR of meningioma could predict surgical cleavability and histologic tumor grade.

Meningiomas commonly present as incidental findings on brain imaging and are treated conservatively or surgically. However, approximately 2% of dural-based masses have imaging features that mimic meningiomas,⁷ including primary dural neoplasms, metastases, granulomatous diseases, various inflammatory diseases, and infections.⁸⁻¹¹ Thus, distinguishing between meningioma and its mimics is essential because clinical management and prognosis can differ significantly, especially for malignant dural-based tumors.

In 2017, Starr and Cha² proposed 5 key imaging features to differentiate meningioma mimics from meningiomas, including lack of a dural tail, which was present in 83.7% of meningioma mimics, marked T2 hyperintensity (45.9%), marked T2 hypointensity (43%), osseous destruction (40.5%), and leptomeningeal extension (21.6%). In 2021, Nagai Yamaki et al¹² proposed additional dural displacement signs to predict meningioma mimics.

To the best of our knowledge, no analytic study has used rim-enhancement patterns on CE-FLAIR to differentiate meningiomas and malignant dural-based tumors. Therefore, this study aimed to distinguish these tumors on the basis of rim-enhancement patterns on CE-FLAIR and MR imaging characteristics.

MATERIALS AND METHODS

Study Setting

This retrospective study included patients treated at the Department of Diagnostic and Therapeutic Radiology of Ramathibodi Hospital between January 2015 and May 2020. The study was approved by the Institutional Ethics Committee of Ramathibodi Hospital. Because of the retrospective nature of the study, the need for informed consent was waived.

Patient Selection

This study included 133 patients with histopathologic diagnoses of meningiomas (102 patients) or malignant dural-based tumors (31 patients) who underwent pretreatment MR imaging of the brain at the Department of Diagnostic and Therapeutic Radiology of Ramathibodi Hospital between January 2015 and May 2020. All patients underwent surgical resection, and histopathologic diagnoses were made by an experienced pathologist. The 102 meningiomas (1 meningioma per person) were subdivided into 3 groups according to the WHO grading scale: WHO I, WHO II, and WHO III. Demographic data of all patients were collected from medical records.

MR Imaging Protocols and Data Acquisition

All MR imaging scans were obtained using 1.5T and 3T scanners (Ingenuia; Philips Healthcare) with a standard head coil. The patients were imaged using a routine precontrast brain MR imaging protocol that included axial and sagittal T1WI, axial T2WI, axial SWI,

and DWI/ADC sequences. DWI was performed using a single-shot echo-planar imaging pulse sequence. Diffusion-sensitizing gradients were applied sequentially along the 3 orthogonal planes, and images were obtained at b-values of 0 and 1000 s/mm². ADC maps were generated for all patients using standard software. Routine MR imaging protocols with gadolinium (Gd) enhancement were obtained in CE-T1WI, CE-FLAIR, CE-3D T1 High Resolution Isotropic Volume Excitation (THRIVE), or BrainVIEW (Philips Healthcare). A standard dose (0.1 mmol/kg) of Gd-DTPA was injected at 1.8–2.0 mL/s in all patients using a standard length of IV tubing. After the Gd-DTPA had been injected, CE-3D FLAIR sequences were first performed in the sagittal plane with the following parameters: TR, 4800 ms; TE_{eff}, 330 ms; TI, 1650 ms; scan time, 5 minutes; FOV, 240 × 240 mm; matrix size, 368 × 210; and section thickness, 1.12 mm. Then, CE-3D THRIVE or BrainVIEW imaging was performed in the axial plane with TR, 5–7 ms; TE, 3–5 ms; flip angle, 12°; section thickness, 1 mm; and scan time, 2 minutes. Finally, CE T1-weighted imaging was performed with TR, 500 ms; TE, 10 ms; matrix size, 192 × 240; FOV, 240 × 240 mm; section thickness, 4 mm; and scan time, 2 minutes 15 seconds.

Imaging and Postprocessing Analysis

Axial CE-T1WI, sagittal CE-3D FLAIR, axial CE-3D THRIVE/BrainVIEW, axial T2WI, and axial DWI with ADC maps were acquired and evaluated in all patients. Multiplanar reconstruction was performed in axial, coronal, and sagittal views of the CE-FLAIR and CE-3D THRIVE/BrainVIEW images. All MR imaging findings were independently reviewed at the PACS workstation by 2 neuroradiologists with 10 and 9 years of experience in brain MR imaging. The neuroradiologists were blinded to patient data and pathologic diagnoses.

First, we evaluated the MR imaging findings including signal intensity on T2WI, dural tail (absent or present), osseous destruction (absent, marrow edema, cortex disruption, or cortical breakthrough), and hyperostosis (absent or present) on T2WI and CE-T1WI sequences. Then we defined the characteristics of rim enhancement at the tumor-brain interface as a rim with relatively high signal intensity on CE-FLAIR. We graded the rim enhancement patterns from 0 to 3 by their extent as 0, no rim visible; 1, 50% rim visible; 2, >50% rim visible but <100%; and 3, complete rim enhancement of the tumor-brain interface (100%) (Fig 1). There was no apparent discrepancy in demonstrating rim enhancement on CE-3D FLAIR images between 1.5T and 3T scanners by observation. Additionally, we evaluated leptomeningeal enhancement (absent or present) and graded peritumoral brain edema (0 to 2), which was defined as 0, no edema; 1, edema <2.0 cm radially from the tumor; and 2, edema ≥2.0 cm radially from the tumor. On CE-T1WI, we defined the contrast-enhancement pattern of the tumor as homogeneous or heterogeneous. Any discrepancies in interpretations of MR imaging findings were resolved by consensus.

Statistical Analysis

All statistical analyses were performed using STATA Version 15.1 software (StataCorp). The interobserver agreement in evaluating MR imaging characteristics was analyzed using κ analysis. A χ^2 test was used to ascertain the significance of differences in

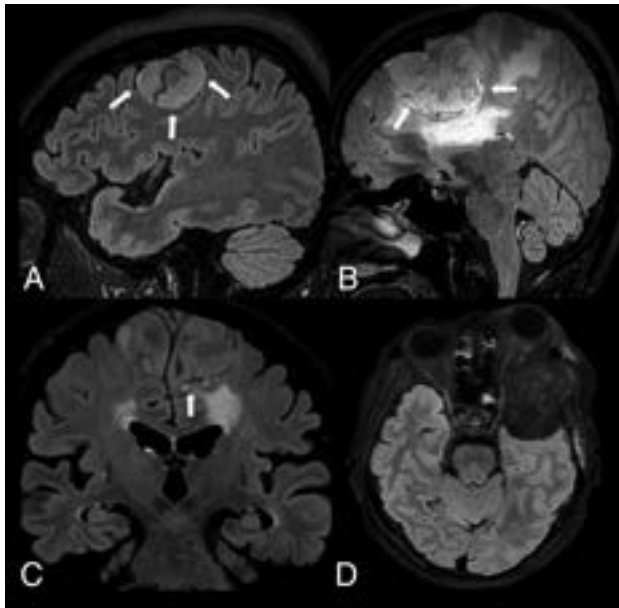


FIG 1. Four different rim-enhancement patterns at the tumor-brain interface on the CE-FLAIR sequence (arrows). A, Complete rim enhancement (CE-FLAIR rim sign). B, Rim enhancement of $\geq 50\%$ but $< 100\%$. C, Rim enhancement of $< 50\%$. D, No visible rim enhancement. The pathologic results of A, B, and C are meningioma, and D is plasmacytoma.

Table 1: Patient demographics and pathologic findings

Variables	Meningiomas (n = 102, 76.7%)	Malignant Dural-Based Tumors (n = 31, 23.3%)
Age (mean) (yr)	51.96 (SD, 10.69)	50.03 (SD, 20.81)
Sex		
Female	85 (83.3%)	15 (48.4%)
Male	17 (16.7%)	16 (51.6%)
Size (mean) (cm)	4.37 (SD, 1.91)	4.5 (SD, 2.2)
WHO grade		
I	72 (70.6%)	—
II	22 (21.6%)	—
III	8 (7.8%)	—
Location		
Convexity	24 (23.5%)	19 (61.2%)
Sphenoid wing	20 (19.6%)	3 (9.6%)
Petroclival	18 (17.6%)	1 (3.3%)
Parafalcine	13 (12.7%)	—
Cavernous sinus	9 (8.8%)	3 (9.6%)
Cerebellopontine angle	6 (5.8%)	1 (3.3%)
Suprasellar	9 (8.8%)	—
Foramen magnum	2 (1.9%)	—
Olfactory groove	1 (0.9%)	—
Orbit	—	3 (9.6%)
Prepontine	—	1 (3.3%)

Note:—The en dash (—) indicates none.

rim-enhancement patterns on CE-FLAIR and other MR imaging characteristics between meningiomas and malignant dural-based tumors and in the subgroup analysis of meningiomas graded WHO I, WHO II, and WHO III. *P* values $< .001$ were considered statistically significant differences. Furthermore, we calculated the sensitivity, specificity, positive predictive value (PPV), negative predictive value (NPV), and percentage accuracy of each MR imaging characteristic for differentiating between meningiomas and

malignant dural-based tumors. Combined MR imaging features in meningiomas and malignant dural-based tumors were also analyzed to predict the diagnosis.

RESULTS

Summary of Patient Demographics and Tumor Characteristics

There were 133 patients with 133 dural-based tumors (1 mass per patient), consisting of meningiomas (102 patients, 76.7%) and malignant dural-based tumors (31 patients, 23.3%). All patient demographics and tumor characteristics are shown in Table 1. All meningiomas in this study were > 2.0 cm in diameter. The 102 meningiomas were classified as WHO I (72/102, 70.6%), WHO II (22/102, 21.6%), and WHO III (8/102, 7.8%). The 31 dural-based masses were pathologically diagnosed as malignant dural-based tumors, as detailed in Table 2.

Summary of MR Imaging Findings between Meningiomas and Malignant Dural-Based Masses

Most meningiomas exhibited complete rim enhancement of the tumor-brain interface on CE-FLAIR sequences (91/102, 89.2%) (Fig 2), which was significantly higher than that in malignant dural-based tumors (2/31, 6.5%) ($P < .001$). Additionally, meningiomas frequently showed hyperostosis (76/102, 74.5%), marrow edema (76/102, 74.5%), and homogeneous enhancement on T1WI (75/102, 73.5%), features that were all significantly different compared with malignant dural-based tumors ($P < .001$), which demonstrated hyperostosis (0/31, 0%), marrow edema (6/31, 19.4%), and homogeneous enhancement on T1WI (9/31, 29%). In contrast, malignant dural-based tumors that demonstrated cortical breakthrough (21/31, 67.7%) and leptomeningeal enhancement (10/31, 32.3%), absence of a dural tail sign (6/31, 19.4%), hypointensity on T2WI (8/31, 25.8%), and heterogeneous enhancement on T1WI (22/31, 71%) were significantly different compared with meningiomas ($P < .001$), which showed cortical breakthrough (5/102, 4.9%), leptomeningeal enhancement (0/102, 0%), absence of a dural tail sign (2/102, 2%), hypointensity on T2WI (4/102, 3.9%), and heterogeneous enhancement on T1WI (27/102, 26.5%). A summary of the MR imaging findings of meningiomas and malignant dural-based tumors is presented in the Online Supplemental Data.

Characteristic MR Imaging Findings That Predict Meningiomas

Complete rim enhancement of the tumor-brain interface on the CE-FLAIR sequence demonstrated excellent sensitivity (89.2%), specificity (93.5%), PPV (97.8%), and NPV (72.5%) and had the highest accuracy (90.2%) for predicting meningioma. The interobserver agreement was excellent for interpreting rim-enhancement patterns on CE-FLAIR sequences, with a κ value = 0.902.

Furthermore, the analysis of $\geq 50\%$ CE-FLAIR rim enhancement demonstrated more excellent sensitivity (95.1%), specificity (93.5%), PPV (98%), NPV (85.3%), and accuracy (94.7%) for predicting meningioma with a perfect interobserver agreement (κ value = 1.0).

Hyperostosis also showed fair sensitivity (74.5%), excellent specificity (100.0%), and PPV (100.0%) and had high accuracy

(80.5%) for consideration of meningioma. The dural tail sign and marrow edema had high sensitivity but low specificity for predicting meningioma (Table 3).

Furthermore, complete or $\geq 50\%$ rim enhancement of the tumor-brain interface on the CE-FLAIR sequence (CE-FLAIR rim sign) plus hyperostosis demonstrated higher accuracy for diagnosing meningiomas of >2.0 cm (area under the curve [AUC] = 0.953).

Table 2: Characteristics of malignant dural-based tumors

Pathology	No. of Cases (n = 31)
Metastasis	18 (58%)
Adenoid cystic carcinoma	5
Lung (non-small cell)	3
Breast (invasive ductal carcinoma)	2
Squamous cell carcinoma at scalp	2
Urachal carcinoma	1
Thyroid (follicular carcinoma)	1
Mucoepidermoid carcinoma	1
Nasopharynx (SCCA)	1
Base of tongue (SCCA)	1
Colon (adenocarcinoma)	1
Plasmacytoma/multiple myeloma	6 (19.3%)
Ewing sarcoma	2 (6.4%)
Lymphoma (non-Hodgkin)	2 (6.4%)
Osteosarcoma	1 (3.4%)
Spindle cell carcinoma	1 (3.4%)
Atypical teratoid/rhabdoid tumor	1 (3.4%)

Note:—SCCA indicates squamous cell carcinoma.

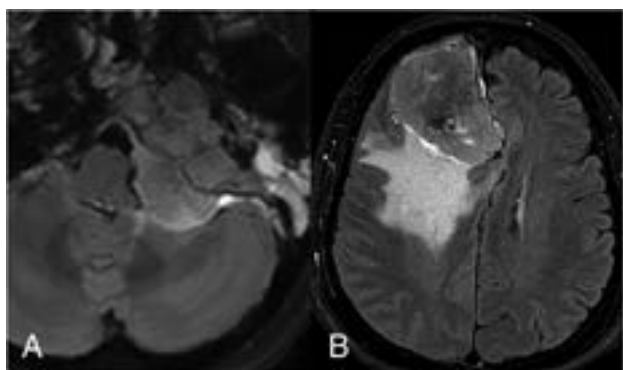


FIG 2. CE-FLAIR rim sign in meningiomas at the cerebellomedullary cistern (A) and parafalcine region (B).

Characteristic MR Imaging Findings That Predict Malignant Dural-Based Tumors

Cortical breakthrough demonstrated moderate sensitivity (67.7%) with high specificity (95.1%), PPV (80.8%), NPV (90.7%), and the best accuracy (88.7%) for consideration of malignant dural-based tumors. Leptomeningeal enhancement and lack of a dural tail demonstrated low sensitivity (32.3% and 19.4%, respectively) but high specificity (100.0% and 98.0%, respectively), PPV (100.0% and 75.0%, respectively), NPV (82.9% and 80.0%, respectively), and accuracy (84.2% and 79.7%, respectively) for predicting malignant dural-based tumors (Table 4).

A combination of aggressive MR imaging findings including leptomeningeal enhancement and cortical breakthrough was a strong predictive sign for malignant dural-based tumors (AUC = 0.911).

Subgroup Analysis of MR Imaging Findings and Comparisons between Meningiomas of WHO Grades I, II, and III

The frequency of cortical breakthrough was significantly higher in WHO grade III (4/8, 50%) meningiomas than in WHO grades I and II (1/94, 1%) ($P < .001$). WHO grade I and II meningiomas demonstrated homogeneous enhancement on T1WI (73/94, 77.6%) more often than WHO grade III meningiomas (2/8, 25%). A comparison of MR imaging findings of WHO grade I-III meningiomas is shown in the Online Supplemental Data.

DISCUSSION

Meningiomas are the most common form of intracranial neoplasms and extra-axial masses and show many specific MR imaging findings. However, approximately 2% of dural-based masses have imaging features that mimic meningiomas, specifically malignant dural-based tumors, which can be a diagnostic challenge.

During several recent years, a few studies have described rim-enhancement patterns on the CE-FLAIR sequence for diagnosing meningioma. However, no previous report in the literature has investigated the role of rim enhancement on CE-FLAIR to differentiate meningiomas and meningioma mimics. This is the first study to compare meningiomas with malignant dural-based tumors using rim-enhancement patterns on CE-FLAIR (or CE-FLAIR rim signs). In this study, the presence of a complete CE-FLAIR rim sign showed high sensitivity, specificity, PPV, and accuracy for predicting meningiomas. Most meningio-

Table 3: Characteristic MR imaging findings for predicting meningiomas

Variables	Sensitivity	Specificity	PPV	NPV	Accuracy
Dural tail sign	98.0%	19.4%	80.0%	75.0%	79.7%
Marrow edema	79.2%	33.3%	92.7%	13.0%	75.2%
Hyperostosis	74.5%	100.0%	100.0%	54.4%	80.5%
Complete rim enhancement on CE-FLAIR	89.2%	93.5%	97.8%	72.5%	90.2%
Homogeneous enhancement on T1WI	73.5%	71.0%	89.3%	44.9%	72.9%

Table 4: Characteristic MR imaging findings for predicting malignant dural-based tumors

Variables	Sensitivity	Specificity	PPV	NPV	Accuracy
Lack of dural tail	19.4%	98.0%	75.0%	80.0%	79.7%
Cortical breakthrough	67.7%	95.1%	80.8%	90.7%	88.7%
Leptomeningeal enhancement	32.3%	100.0%	100.0%	82.9%	84.2%
Heterogeneous enhancement on T1WI	71.0%	73.5%	44.9%	89.3%	72.9%
Hypointense signal on T2WI	53.3%	86.2%	66.7%	78.1%	75.0%

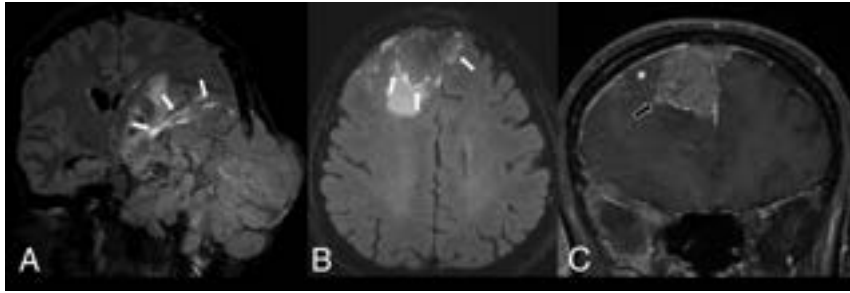


FIG 3. A, Anaplastic meningioma (WHO grade III). CE-FLAIR (A) sequence demonstrates a large extra-axial mass with cortical breakthrough involving the left middle skull base and left temporal skull with the CE-FLAIR rim sign (*white arrows*). Malignant soft-tissue tumor was the favored diagnosis in the initial report. The pathologic result is anaplastic meningioma (WHO grade III). A malignant dural-based mass on CE-FLAIR (B) and CE-T1WI fat suppression (C) sequences shows an extra-axial heterogeneously enhancing mass at the bilateral frontal convexities that had invaded the anterior-superior sagittal sinus and demonstrates the CE-FLAIR rim sign (*white arrows*), accompanied by focal leptomeningeal enhancement (*asterisk*) and adjacent brain parenchymal invasion (*black arrow*). Meningioma was the favored diagnosis in the initial report. The pathologic result was metastatic mucoepidermoid carcinoma.

mas of >2 cm demonstrated complete rim enhancement on CE-FLAIR, similar to the results presented by Oner et al⁵ (12/14, 85%). Furthermore, the presence of $\geq 50\%$ CE-FLAIR rim enhancement demonstrated more excellent sensitivity, specificity, and accuracy for predicting meningioma.

These characteristic MR imaging findings have been described as possibly related to the dual blood supply (meningeal and pial arterial supply) of meningiomas that is commonly seen in tumors of >2 cm in diameter (21/30, 70%).⁴ Because high Gd concentrations induce signal loss in the CE-FLAIR sequence, the high concentration of Gd in the central part of meningiomas that is due to the dominant meningeal supply can suppress the T1 effect and increase T2 shortening, resulting in relative signal loss or no increased signal; in contrast, the lower concentration of Gd in the tumor capsule due to relatively less vascularity related to the pial supply can enhance T1 effects and increase T1 shortening, resulting in peripheral contrast enhancement on CE-FLAIR.⁵ These findings can be observed in the CE-2D FLAIR technique in the previous studies and the CE-3D FLAIR technique in our study. In addition, the 3D-FLAIR technique has an advantage over 2D-FLAIR in multiplanar reconstruction, providing a better evaluation of the rim enhancement on CE-FLAIR.

All meningiomas in this study were >2.0 cm in diameter. Nonetheless, 4 meningiomas with no visible rim enhancement and 1 meningioma with $<50\%$ rim enhancement on CE-FLAIR were observed. All 4 meningiomas with nonvisible rim enhancement were located in the intracavernous sinuses and received vascular supply in various ways from the ICA (C3–C7 segments), ophthalmic artery, or intracranial branches of the external carotid artery without pial vascular supply except for those that extended beyond the cavernous sinus.¹³ Such findings represented a limitation of using CE-FLAIR rim signs to predict intracavernous meningiomas (Online Supplemental Data). The meningioma that demonstrated $<50\%$ CE-FLAIR rim enhancement was located at the cerebral convexity. The reduced rim enhancement of this lesion could be related to the relatively poor pial artery supply of the tumor.

Recent studies suggest that malignant dural-based masses receive vascular supply from various branches of the internal and external carotid arteries according to their cell types and locations.^{14–16} No pial vascular supply in the tumor capsule has been described for malignant dural-based masses. However, our study demonstrated 2 cases of malignant dural-based tumors (dural metastasis of squamous cell carcinoma and mucoepidermoid carcinoma) with complete rim enhancement on the CE-FLAIR sequence accompanied by aggressive imaging features, including adjacent leptomeningeal enhancement and brain parenchymal invasion. The CE-FLAIR rim sign of these lesions could be related to prominent pial arterial supply at the peripheral portion of the tumors (Fig 3).

In this study, bony hyperostosis demonstrated fair sensitivity and excellent specificity and PPV, with high accuracy for consideration of meningioma, consistent with findings in prior literature.¹⁷ However, lymphomas and immunoglobulin G4-related diseases can show hyperostosis that can mimic meningioma,^{18,19} but we did not observe this feature in this study.

A dural tail was a hallmark for meningioma, with almost 60% prevalence, but several dural-based masses also demonstrated this feature.^{20,21} The proliferation of meningiomas triggers an inflammatory reaction that results in dural thickening and enhancement. In this study, a dural tail was present in 98% of meningiomas and 80.6% of malignant dural-based tumors ($P < .001$), higher than what was previously reported for the prevalence of dural tails in meningioma mimics by Starr and Cha.² Furthermore, in our study, the lack of a dural tail demonstrated relatively low sensitivity but high specificity for predicting malignant dural-based tumors compared with the study by Starr and Cha.

The presence of cortical breakthrough in dural-based masses represents an aggressive feature with significant bone destruction, which is supposed to be found in malignant dural-based tumors and WHO grade III meningiomas and is very unusual in WHO grade I meningiomas.² Our study found that cortical breakthrough had moderate sensitivity, high specificity, good PPV and NPV, and the highest accuracy for consideration of malignant dural-based tumors, similar to the results of Starr and Cha.² However, there were 5 cases of meningiomas that demonstrated cortical breakthrough. All were anaplastic meningiomas (WHO III) with complete rim enhancement on CE-FLAIR sequences, features that could help suggest anaplastic or malignant meningioma rather than malignant dural-based tumors (Fig 3).

Additionally, leptomeningeal enhancement was an excellent predictive sign for malignant dural-based tumors and was not generally seen in meningiomas. Our study demonstrated adjacent leptomeningeal enhancement in metastases, lymphoma, atypical teratoid/rhabdoid tumor, and squamous cell carcinoma at the scalp, possibly related to the subarachnoid space and brain parenchymal invasion. Therefore, observing associated leptomeningeal

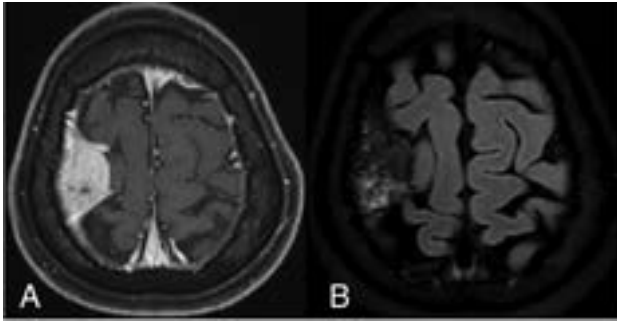


FIG 4. A, CE-T1WI fat suppression sequence demonstrates an extra-axial mass at the right frontoparietal convexity with a dural tail sign that resembles a meningioma. B, CE-FLAIR sequence. No rim enhancement on the tumor-brain interface is observed. Meningioma was the favored diagnosis in the initial report. The pathologic result was osteosarcoma.

enhancement could alert radiologists that a dural-based mass is unlikely to be a meningioma.²

Hypointensity on T2WI is a feature that is not commonly seen in meningiomas and generally indicates hypercellularity, large areas of calcification, or significant fibrous tissue in the tumor, which are variably present in meningioma mimics. In this study, 25.8% (8/31) of malignant dural-based tumors showed hypointensity on T2WI. They were metastases, plasmacytoma/multiple myeloma, and osteosarcoma (Fig 4). The frequency of hypointensity on T2WI was lower compared with the findings of Starr and Cha,² in which 43% of malignant dural-based tumors had hypointensity on T2WI. Homogeneous or heterogeneous enhancement on T1WI was variable in each tumor type and histologic subtype of meningioma.²²

Thus, combining these MR imaging findings could lead to high accuracy in differentiating meningioma and malignant dural-based tumors. Complete or $\geq 50\%$ rim enhancement of the tumor-brain interface on the CE-FLAIR sequence (the CE-FLAIR rim sign) plus hyperostosis demonstrated higher accuracy for diagnosing meningiomas of >2.0 cm (AUC = 0.953), except for those at an intracavernous location. However, CE-FLAIR rim signs were found in a few malignant dural-based masses, where they were accompanied by leptomeningeal enhancement and brain parenchymal invasion. Therefore, aggressive MR imaging findings including leptomeningeal enhancement and cortical breakthrough were strong predictive signs of malignant dural-based tumors (AUC = 0.911). In this study, cortical breakthrough was present in 4 cases of WHO grade III meningiomas. However, these cases also had complete CE-FLAIR rim signs, findings that were highly suggestive of meningioma with aggressive behavior. Regarding the results from our study, we have proposed the diagnostic framework for differentiating meningioma and malignant dural-based tumor, which is shown in the Online Supplemental Data.

Our study had some limitations, including its single-institution nature, no evaluation of tumors of <2.0 cm in diameter, and a small number of WHO grade III meningiomas. Further studies should include more patients, specifically with WHO grade III meningioma. Nevertheless, this study is the first step toward using rim-enhancement patterns on CE-FLAIR to predict meningioma

and differentiate such cases from malignant dural-based tumors. Future research could use rim-enhancement patterns on CE-FLAIR and other MR imaging findings to differentiate meningiomas and other benign dural-based masses such as hemangiopericytomas and infectious/inflammatory dural-based lesions, which can mimic each other and make diagnostics challenging.

CONCLUSIONS

Complete or $\geq 50\%$ rim enhancement on the CE-FLAIR sequence (CE-FLAIR rim sign) showed high accuracy for diagnosing meningiomas of >2.0 cm. Hyperostosis was another helpful MR imaging finding for predicting meningioma. Aggressive MR imaging findings including cortical breakthrough and leptomeningeal enhancement were strong predictive signs of malignant dural-based tumors.

Disclosure forms provided by the authors are available with the full text and PDF of this article at www.ajnr.org.

REFERENCES

- Osborn AG. *Brain Imaging, Pathology, and Anatomy*. 2nd ed. Elsevier; 2017:659–94
- Starr CJ, Cha S. **Meningioma mimics: five key imaging features to differentiate them from meningiomas.** *Clin Radiol* 2017;72:722–28 CrossRef Medline
- Kelly M. Tumors. In: Krings T, Geibprasert S, ter Brugge KG eds. *Case-Based Interventional Neuroradiology*. Thieme Medical Publishers; 2011:207–12
- Oguz KK, Cila A. **Rim enhancement of meningiomas on fast FLAIR imaging.** *Neuroradiology* 2003;45:78–81 CrossRef Medline
- Oner AY, Tokgöz N, Tali ET, et al. **Imaging meningiomas: is there a need for post-contrast FLAIR?** *Clin Radiol* 2005;60:1300–05 CrossRef Medline
- Enokizono M, Morikawa M, Matsuo T, et al. **The rim pattern of meningioma on 3D FLAIR imaging: correlation with tumor-brain adhesion and histological grading.** *Magn Reson Med Sci* 2014;13:251–60 CrossRef Medline
- Ghosal N, Dadlani R, Gupta K, et al. **A clinicopathological study of diagnostically challenging meningioma mimics.** *J Neurooncol* 2012;106:339–52 CrossRef Medline
- Smith AB, Horkanyne-Szakaly I, Schroeder JW, et al. **From the radiologic pathology archives: mass lesions of the dura: beyond meningioma-radiologic-pathologic correlation.** *Radiographics* 2014;34:295–312 CrossRef Medline
- Nayak L, Abrey LE, Iwamoto FM. **Intracranial dural metastases.** *Cancer* 2009;115:1947–53 CrossRef Medline
- Lee EK, Lee EJ, Kim MS, et al. **Intracranial metastases: spectrum of MR imaging findings.** *Acta Radiol* 2012;53:1173–85 CrossRef Medline
- Meyers SP, Hirsch WL Jr, Curtin HD, et al. **Chondrosarcomas of the skull base: MR imaging features.** *Radiology* 1992;184:103–08 CrossRef Medline
- Nagai Yamaki V, de Souza Godoy LF, Alencar Bandeira G, et al. **Dural-based lesions: is it a meningioma?** *Neuroradiology* 2021;63:1215–25 CrossRef Medline
- Schramm J. *Advances and Technical Standards in Neurosurgery*. Vol 43. Springer-Verlag; 2015:103–22
- Lyndon D, Lansley JA, Evanson J, et al. **Dural masses: meningiomas and their mimics.** *Insights Imaging* 2019;10:11 CrossRef Medline
- Hayt DB, Blatt CJ, Goldman SM, et al. **Hypervascular presentation of multiple myeloma involving the skull, demonstrated on encephaloscintigraphy.** *J Nucl Med* 1979;20:125–26 Medline
- Whitehead RE, Melhem ER, Kasznica J, et al. **Telangiectatic osteosarcoma of the skull base.** *AJNR Am J Neuroradiol* 1998;19:754–57 Medline

17. Siegelman ES, Mishkin MM, Taveras JM. **Past, present, and future of radiology of meningioma.** *Radiographics* 1991;11:899–910 CrossRef Medline
18. Paiva J, King J, Chandra R. **Extra-axial Hodgkin's lymphoma with bony hyperostosis mimicking meningioma.** *J Clin Neurosci* 2011;18:725–27 CrossRef Medline
19. Lin CK, Lai DM. **IgG4-related intracranial hypertrophic pachymeningitis with skull hyperostosis: a case report.** *BMC Surg* 2013;13:37 CrossRef Medline
20. Wilms G, Lammens M, Marchal G, et al. **Thickening of dura surrounding meningiomas: MR features.** *J Comput Assist Tomogr* 1989;13:763–68 CrossRef Medline
21. Wilms G, Lammens M, Marchal G, et al. **Prominent dural enhancement adjacent to nonmeningiomatic malignant lesions on contrast-enhanced MR images.** *AJNR Am J Neuroradiol* 1991;12:761–64 Medline
22. Kunimatsu A, Kunimatsu N, Kamiya K, et al. **Variants of meningiomas: a review of imaging findings and clinical features.** *Jpn J Radiol* 2016;34:459–69 CrossRef Medline

Parieto-Occipital Injury on Diffusion MRI Correlates with Poor Neurologic Outcome following Cardiac Arrest

E. Calabrese, S. Gandhi, J. Shih, M. Otero, D. Randazzo, C. Hemphill, R. Huie, J.F. Talbott, and E. Amorim



ABSTRACT

BACKGROUND AND PURPOSE: MR imaging of the brain provides unbiased neuroanatomic evaluation of brain injury and is useful for neurologic prognostication following cardiac arrest. Regional analysis of diffusion imaging may provide additional prognostic value and help reveal the neuroanatomic underpinnings of coma recovery. The purpose of this study was to evaluate global, regional, and voxelwise differences in diffusion-weighted MR imaging signal in patients in a coma after cardiac arrest.

MATERIALS AND METHODS: We retrospectively analyzed diffusion MR imaging data from 81 subjects who were comatose for >48 hours following cardiac arrest. Poor outcome was defined as the inability to follow simple commands at any point during hospitalization. ADC differences between groups were evaluated across the whole brain, locally by using voxelwise analysis and regionally by using ROI-based principal component analysis.

RESULTS: Subjects with poor outcome had more severe brain injury as measured by lower average whole-brain ADC ($740 [SD, 102] \times 10^{-6} \text{ mm}^2/\text{s}$ versus $833 [SD, 23] \times 10^{-6} \text{ mm}^2/\text{s}$, $P < .001$) and larger average volumes of tissue with ADC below $650 \times 10^{-6} \text{ mm}^2/\text{s}$ ($464 [SD, 469] \text{ mL}$ versus $62 [SD, 51] \text{ mL}$, $P < .001$). Voxelwise analysis showed lower ADC in the bilateral parieto-occipital areas and periolandic cortices for the poor outcome group. ROI-based principal component analysis showed an association between lower ADC in parieto-occipital regions and poor outcome.

CONCLUSIONS: Brain injury affecting the parieto-occipital region measured with quantitative ADC analysis was associated with poor outcomes after cardiac arrest. These results suggest that injury to specific brain regions may influence coma recovery.

ABBREVIATIONS: AUC = area under the curve; CPC = Cerebral Performance Category; PC = principal component; PCA = principal component analysis; PCAC = post-cardiac arrest coma; ROC = receiver operating characteristic; ROSC = return of spontaneous circulation; TTM = targeted temperature management; WLST = withdrawal of life-sustaining therapies

Cardiac arrest affects 600,000 patients annually in the United States despite substantial advances in resuscitation medicine.¹

Received July 28, 2022; accepted after revision January 3, 2023.

From the Department of Radiology and Biomedical Imaging (E.C., S.G., J.F.T.), Department of Neurology (J.S., M.O., D.R., C.H., E.A.), Weill Institute for Neurosciences, and Department of Neurological Surgery (R.H.), University of California, San Francisco, San Francisco, California; and Department of Radiology and Biomedical Imaging (S.G., J.F.T., E.A.), Zuckerberg San Francisco General Hospital, San Francisco, California.

This study was supported by the American Heart Association (20CDA35310297; 2020AMFDP), the National Institutes of Health (1K23NS119794), and the National Center for Advancing Translational Sciences, National Institutes of Health, through the University of California, San Francisco—Clinical Translation and Science Institute, grant No. ULI TR001872.

The contents of this study are solely the responsibility of the authors and do not necessarily represent the official views of the National Institutes of Health.

Please address correspondence to Edilberto Amorim, MD, Department of Neurology, Weill Institute for Neurosciences, University of California, San Francisco, Zuckerberg San Francisco General Hospital, 1001 Potrero Ave, Building 1, Suite 312, San Francisco, CA, 94110; e-mail: edilbertoamorim@gmail.com; @EdAmorimMD; @ecalabr

Indicates open access to non-subscribers at www.ajnr.org

Indicates article with online supplemental data.

<http://dx.doi.org/10.3174/ajnr.A7779>

For patients surviving initial resuscitation, mortality ranges from 75% to 88% for in-hospital and out-of-hospital cardiac arrests, respectively. Most deaths follow withdrawal of life-sustaining therapies (WLST) due to perceived poor neurologic prognosis after multimodal evaluation with serial examinations and ancillary testing. Determination of prognosis is, therefore, a key component of post-cardiac arrest care, and accurate evaluation of brain injury severity is critical to prevent premature WLST in post-cardiac arrest coma (PCAC) who have the potential to recover.

The inclusion of MR imaging, particularly DWI, in the multimodal neuroprognostication paradigm has gained traction in routine clinical care, particularly in the targeted temperature management (TTM) era.² The use of sedatives and neuromuscular blockade as well as metabolic changes with TTM may decrease the validity of previously established prognostication tools such as clinical examination, electroencephalography, and somatosensory-evoked potentials, while abnormalities on MR imaging are unlikely to be affected. Research-leveraging qualitative and quantitative MR imaging analysis has demonstrated utility for outcome predictions in post-cardiac arrest coma.³⁻¹⁶ However, MR imaging literature

for outcome prediction after cardiac arrest has been limited by variability in MR imaging scanning methodology, qualitative rather than quantitative assessment, and a focus on global rather than regional patterns of brain injury. While several prior studies have demonstrated that the presence of any acute brain injury is associated with poor outcome, relatively fewer studies have addressed regional brain injury patterns and their association with good-versus-poor clinical outcome.^{6,7,9,10,12-16}

The main purpose of this study was to quantitatively describe the regional neuroanatomic distribution of brain injury post-cardiac arrest using DWI. We found that both global brain injury and specifically injury to the parieto-occipital region were associated with severe neurologic impairment. These results provide important insights into the clinical and prognostic significance of regional brain injury patterns on diffusion-weighted MR imaging for post-cardiac arrest coma and address existing knowledge gaps in the importance of assessment of global-versus-regional brain injury.

MATERIALS AND METHODS

Patient Selection

This study was approved by the University of California San Francisco and Zuckerberg San Francisco General Hospital institutional review boards with a waiver of informed consent. Using electronic health record search tools, we identified all subjects treated at a single university-affiliated hospital between 2016 and 2021 for post-cardiac arrest coma ($n = 335$). For this study, post-cardiac arrest coma were defined as patients having a Glasgow Coma Scale score of ≤ 8 after return of spontaneous circulation (ROSC). We then identified patients who underwent inpatient brain MR imaging ($n = 105$) as part of a routine multimodal prognostic evaluation for patients who do not recover consciousness after the rewarming phase of TTM or by 48 hours following arrest. Exclusion criteria included patients with missing MR imaging sequences ($n = 1$), patients who did not complete TTM ($n = 2$), the presence of a significant unrelated abnormality on brain MR imaging such as hemorrhage or large-territory encephalomalacia ($n = 8$), or MR imaging acquired >7 days (168 hours) post-cardiac arrest. Poor outcome was defined as the inability to follow 1-step commands before hospital discharge on the basis of retrospective review of the electronic health record.

Clinical notes by the primary team, neurology, occupational therapy, and/or physical therapy were reviewed to determine the best clinical examination before discharge. The ability to follow commands was part of the standard evaluation from clinical providers, which includes evaluation of at least 1-step axial and appendicular commands (eg, show fingers, wiggle toes, or stick out tongue). Cerebral Performance Category (CPC) scores were recorded for all patients included in the analysis but were assessed only at the time of discharge and, therefore, did not capture patients who recovered consciousness and the ability to follow commands during hospitalization but subsequently died after WLST ($n = 3$ in this cohort). With the exception of these 3 patients, the good and poor outcome groups corresponded exactly to CPC 1–3 and CPC 4–5, respectively. Patients able to

follow commands were categorized as having good outcome and patients unable to follow commands as having poor outcome.

Image Acquisition

MR images were acquired on a single 3T MR scanner (Magnetom Skyra; Siemens). Imaging protocol included either a 6- or 12-direction DWI with $b = 1000 \text{ s/mm}^2$. ADC maps were generated automatically on the scanner. Additional DWI parameters included an FOV of $22 \times 22 \text{ cm}$, an image matrix of 192×192 , and section thickness of 4 mm (voxel resolution = $1.14 \times 1.14 \times 4 \text{ mm}$), section gap of 1 mm, section number range of 28–34, TR range of 4710–5520 ms, TE range of 64–74 ms, and number of excitations of 1. Representative examples of DWI and ADC images are provided in the Online Supplemental Data.

Image Preprocessing

DWI volumes were processed using custom software programmed in Python 3.8 using the Nipype 1.6 package (<https://github.com/nipy/nipype/releases/tag/1.6.0>) to interface with non-Python software. DWI volumes were converted to NIfTI format using `dcm2niix 1.0` (<https://github.com/rordenlab/dcm2niix/releases>) and then aligned to the Montreal Neurological Institute 152 brain atlas using multistep rigid, affine, and diffeomorphic automated image registration implemented using Advanced Normalization Tools (ANTs 2.3.5; <http://stnava.github.io/ANTs/>). Qualitative registration accuracy was manually evaluated for quality control. Resulting transforms were used to map patient ADC maps into the atlas space. Representative examples of DWI and ADC images before and after registration are included in the Online Supplemental Data.

ROI Extraction

A total of 124 bilateral cortical ($n = 96$) and subcortical ($n = 28$) ROIs were extracted from each patient's DWI volume using the Harvard-Oxford cortical and subcortical brain atlases, respectively. All structures were assessed in both the left and right hemispheres individually, and subcortical structures were also evaluated as a single bilateral ROI.

Quantitative ADC Analysis

Brain-wide ADC differences between outcome groups were assessed using 2 metrics established in previously published work: average whole-brain ADC and total volume of tissue with ADC less than $650 \times 10^{-6} \text{ mm}^2/\text{s}$ (ADC_{650}).⁸ Voxels with ADC values greater than $1100 \times 10^{-6} \text{ mm}^2/\text{s}$ were considered to represent CSF and were excluded. Regional mean ADC and ADC_{650} differences between groups were also assessed for each individual region in the Harvard-Oxford cortical and subcortical brain atlases.

Whole-Brain Injury Frequency Mapping

Whole-brain injury frequency maps were generated to allow visualization of common sites of injury for each outcome group. Brain injury was defined as all brain voxels with ADC less than $650 \times 10^{-6} \text{ mm}^2/\text{s}$. Binarized injury maps were generated for each patient and averaged within each outcome group. The output of this analysis was a single injury-frequency map for each outcome group, in which voxel values represent the proportion of patients in the outcome group with injury in that location.

Subject demographics stratified by outcome group

Variable	Follows Commands (n = 17)	Does Not Follow Commands (n = 64)	P Value
Age (mean) (yr)	55 (SD, 16)	57 (SD, 15)	.741
Female sex	4/17 (24%)	18/64 (28%)	.701
Race and ethnicity ^a			.757
Asian	4 (21%)	6 (9%)	
Black	3 (16%)	14 (22%)	
Hispanic	2 (11%)	6 (9%)	
Hawaiian	0 (0%)	2 (3%)	
Non-Hispanic white	2 (11%)	6 (9%)	
Unknown	8 (42%)	30 (47%)	
Time from ROSC to MR imaging (mean) (hr)	120 (SD, 26)	115 (SD, 27)	.496
Shockable rhythm	6/17 (35%)	12/64 (19%)	.145
Out-of-hospital cardiac arrest	14/17 (82%)	49/64 (77%)	.610
Time to ROSC (mean)	19 (SD, 14)	24 (SD, 14)	.182

^a Patient race and ethnicity do not add to 100% as some patients reported more than one race and ethnicity combination.

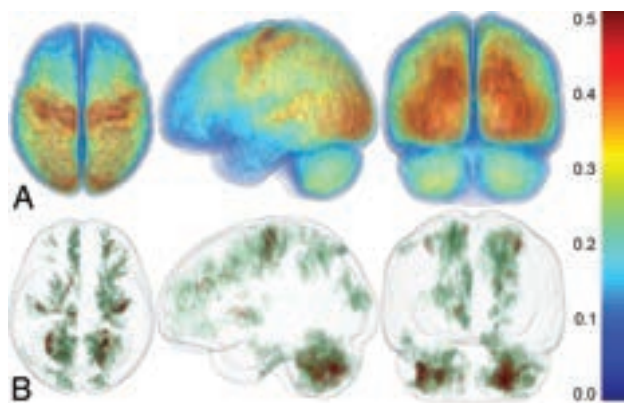


FIG 1. Frequency of hypoxic-ischemic brain injury in both outcome groups. Colorized 3D brain renderings show the frequency of injury (as defined by $ADC < 650 \times 10^{-6} \text{ mm}^2/\text{s}$) for the poor-outcome group (A) and the good outcome group (B), respectively. The color bar (right) indicates the frequency of injury across the whole brain. Note that regions with $<5\%$ injury frequency are transparent to allow better visualization of more frequently injured areas.

Voxelwise Quantitative ADC Analysis

Voxelwise ADC differences between outcome groups were assessed using threshold-free cluster enhancement implemented in FSL 6.0.2 (<http://www.fmrib.ox.ac.uk/fsl>). Statistical significance was determined as a family-wise error-corrected P value $< .05$. Several potentially confounding variables were included as confound regressors in the analysis: whole-brain average ADC, patient age, patient sex, and time to MR imaging (in hours).

ROI-Based Principal Component Analysis

Principal component analysis (PCA) was used to explore relationships between ROI-based injury and clinical outcome. The measure used for PCA was the percentage of brain parenchyma with ADC less than $650 \times 10^{-6} \text{ mm}^2/\text{s}$ for each ROI. A scree plot was generated to determine the percentage of variance accounted for by each principal component (PC). Variable loadings within each PC were thresholded at an absolute value of 0.5, and expert visual analysis of loading patterns for these strong loading variables was used to identify the underlying

construct of each PC. PC scores for each patient were then used for hypothesis testing. A backward regression that included PC scores and other clinical variables was used to determine significant predictors of poor outcome. The resulting significant predictors were included in a receiver operating characteristic (ROC) curve analysis to determine the sensitivity and specificity of these variables to predict poor outcome. PCA and ROC analyses were run using the *syndRomics* (<https://github.com/ucsf-ferguson-lab/syndRomics>) and *pROC* software packages in the R statistical framework (R Version 4.1.2; <http://www.r-project.org/>).¹⁷

Statistical Analysis

Continuous variables and categorical variables are reported as means (SD) and frequencies with percentages. The χ^2 test was used to compare categorical data. The 2-sample Student t test was used to compare continuous variables. The DeLong method was used to compare ROC curves. For all statistical tests, a P value $< .05$ was considered statistically significant. For the ROI analysis, a Bonferroni correction was used to control for multiple comparisons.

RESULTS

Subjects

We identified a total of 335 subjects: Two hundred fifty-four were excluded, and 81 were included in the analysis (Online Supplemental Data). Sixty-four of 81 (79%) subjects had poor outcomes. Demographic information for each outcome group is presented in the Table. There were no statistically significant differences in age, sex, race, and ethnicity; time to MR imaging; the presence of a shockable rhythm at presentation; location of cardiac arrest (in-hospital versus out-of-hospital); or time to ROSC. When we compared patients who were included versus excluded from the analysis, there was no statistically significant difference in the proportion of patients who had WLST or brain death (χ^2 P value = .12 and .89, respectively) (Online Supplemental Data).

Quantitative ADC Comparison between Outcome Groups

The poor outcome group had lower whole-brain mean ADC values ($740 [\text{SD}, 102] \times 10^{-6} \text{ mm}^2/\text{s}$ versus $833 [\text{SD}, 23] \times 10^{-6} \text{ mm}^2/\text{s}$, $P < .001$) and larger total ADC_{650} volumes ($464 [\text{SD}, 469] \text{ mL}$ versus $62 [\text{SD}, 51] \text{ mL}$, $P < .001$). Statistically significant differences in mean ADC and ADC_{650} by ROI (after Bonferroni correction) are presented in the Online Supplemental Data.

Whole-Brain Injury Mapping

Whole-brain ADC_{650} frequency maps were generated for each outcome group and are presented in Fig 1. The poor outcome group had a more severe and extensive pattern of brain injury most frequently involving the precentral gyri, precuneus, and cuneus (Fig 1A). The good outcome group (Fig 1B) showed a

relatively heterogeneous pattern of injury, with the most frequent areas of injury being the cerebellum, globi pallidi, and precentral gyri.

Voxelwise Analysis of Quantitative ADC Differences between Outcome Groups

Voxelwise analysis with threshold-free cluster enhancement was used to explore regional differences in ADC values between outcome groups without a priori anatomic constraints. Results of the voxelwise analysis are seen in Fig 2. Statistically significant clusters (after controlling for whole-brain average ADC, patient age, patient sex, and time from ROSC to MR imaging as confounding variables) were localized to the cuneus and precuneus.

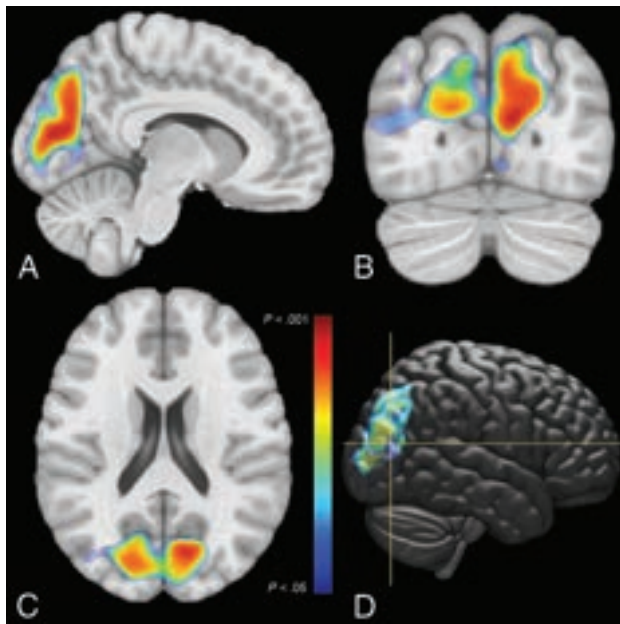


FIG 2. Results of voxelwise comparisons between outcome groups. Statistically significant voxels (family-wise error rate–corrected, $P < .05$) are shown as color overlays on orthogonal slices of the Montreal Neurologic Institute brain atlas (A–C). Color indicates the P value for the comparison (see the color bar). A volume-rendering of the P value from a lateral perspective is also shown, with dashed yellow lines indicating the plane of axial and coronal slices (D).

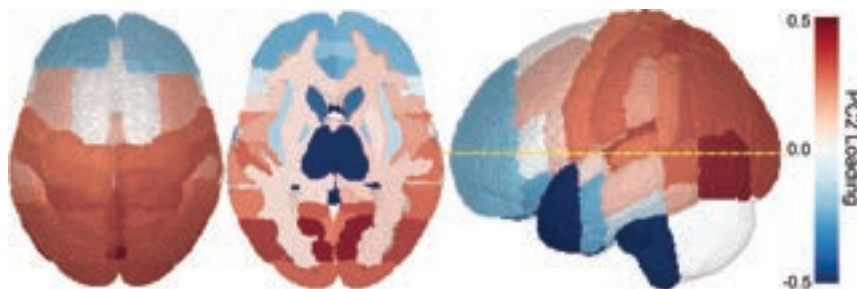


FIG 3. Loading values for PC2 from the PCA. Each cortical region from the Harvard Oxford brain atlas is colored according to its PC2 loading value. Red and blue loadings indicate opposite patterns of loading (red indicates positive correlation, blue indicates a negative correlation). The dashed yellow line on the lateral projection (right) indicates the plane of the axial section (center).

PCA of ROI-Based ADC Differences between Outcome Groups

PCA analysis of the percentage of brain parenchyma with ADC less than $650 \times 10^{-6} \text{ mm}^2/\text{s}$ for each ROI identified 2 PCs that accounted for $>95\%$ of the variance. PC loadings for PC1 and PC2 are included as Online Supplemental Data. All ROI-based variables loaded on PC1 in the same direction, indicating that they all contributed to the variance explained by this PC (79%). In contrast, ROI-based variables had variable loading contributions to the variance explained by PC2 (16%), with some variables (perirolandic and parieto-occipital ROIs) showing a positive correlation and others (anterior-frontotemporal and deep gray matter ROIs) showing a negative correlation (Fig 3).

ROC Analysis of Outcome Groups with PCA Results

ROC analysis for determining neurologic outcome on the basis of clinical and MR imaging features is presented in Fig 4. Using only the percentage of the whole brain with ADC less than $650 \times 10^{-6} \text{ mm}^2/\text{s}$ yielded a relatively high discriminative performance, with an ROC area under the curve (AUC) of 0.84. Whole-brain injury of 10% was 95% specific and 59% sensitive for poor outcome prediction, and whole-brain injury of 5% was 74% specific and 77% sensitive. ROC performance was similar using PC2 scores with an ROC AUC of 0.83. By comparison, the single best ROI-based predictor (average percentage of the cuneal cortex with ADC less than $650 \times 10^{-6} \text{ mm}^2/\text{s}$) yielded a similar performance with an ROC AUC of 0.89. An average cuneal injury of 5% was 94% specific and 75% sensitive. Combining PC scores with the location of arrest (in-hospital versus out-of-hospital) yielded the best performance with an ROC AUC of 0.91. Pair-wise comparison of ROC curves using the DeLong method revealed a statistically significant difference between the PC2 and PC1 + PC2 + arrest location curves ($P = .029$), with all other comparisons failing to reach statistical significance (Online Supplemental Data). ROC analysis using CPC scores rather than the ability to follow commands as the outcome metric is included as Online Supplemental Data.

DISCUSSION

Regional analysis of quantitative ADC showed that involvement of the cuneus, precuneus, and precentral gyrus was associated with poor outcomes post–cardiac arrest. Most important, whole-brain ADC frequency mapping revealed that injury to the precentral gyrus was more prominent in patients with poor outcome, but could also be present in patients with good outcome. However, injury to the parieto-occipital region was more specifically associated with poor outcomes as highlighted by both the PCA and voxelwise analyses, including when controlling for whole-brain ADC, which is expected to remove some of the variance explained by the severity of global brain injury. The percentage of ADC_{650} in the cuneus alone showed high performance for determining neurologic outcome, with a value of

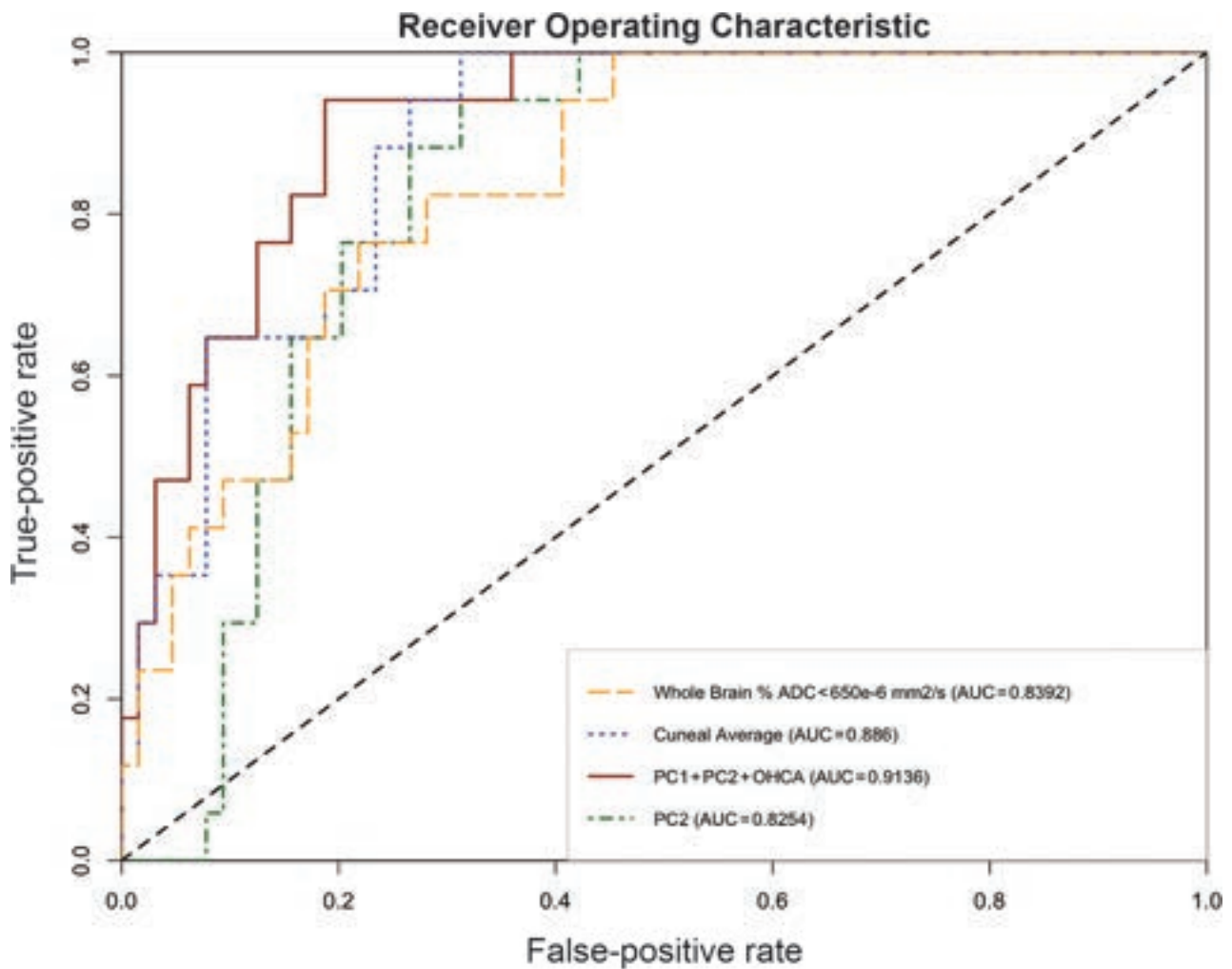


FIG 4. ROC analysis of different diffusion-weighted MR imaging–based variables for predicting outcome in patients with post–cardiac arrest coma. OHCA indicates out of hospital cardiac arrest.

5%, yielding 75% sensitivity and 94% specificity for poor outcome. These findings corroborate previous studies demonstrating that injury to this region is associated with poor outcomes in post–cardiac arrest coma; however, there has been limited prior work directly investigating regional injury correlates for poor clinical outcome in cardiac arrest and none using the PCA and voxelwise analyses presented here.^{9,10,15,18} Additional investigation is needed to determine whether injury to the parieto-occipital region is exclusively a marker of severe injury or a causal determinant of persistent coma post–cardiac arrest.

The posterior-medial cortex is part of the default mode network and is involved in regulation of consciousness and connectivity throughout the brain.^{19,20} Resting-state fMRI studies involving patients with both severe brain injury of distinct etiologies and various levels of consciousness showed that the degree of connectivity of the default mode network, in particular of the precuneus or posterior cingulate cortex, was directly proportional to the level of consciousness, with patients in a coma having lower connectivity.^{19,21–24} Our report adds to the post–cardiac arrest coma literature demonstrating that lower ADC values in the parieto-occipital region is associated with poor outcomes.^{9,11,12,15,20,25}

Injury to several other specific brain regions has also been associated with poor outcome; however, most studies pursued a descriptive approach that did not incorporate multivariable analytic models, which may help determine which regions are specifically useful for discriminating between good and poor outcomes independent of diffuse brain injury.

The regional vulnerability of the precuneus, cuneus lobes, and precentral gyrus following cardiac arrest is not well-understood. The precuneus, cuneus, visual cortex, and precentral gyrus are considered some of the most metabolically active regions in humans; therefore, this finding could be a consequence of metabolic demand mismatch in the context of hypoxic-ischemic brain injury and reperfusion injury following cardiac arrest.²⁶ An alternative vascular hypothesis is that the posterior circulation cannot provide sufficient cerebral blood flow during cardiopulmonary resuscitation and its limited autoregulatory response following return of spontaneous circulation and reperfusion may contribute to the increased vulnerability of these regions, similar to what is observed in posterior reversible encephalopathy syndrome.²⁷

The use of quantitative MR imaging can augment multimodal prognostication, and our study demonstrates the value of combining

clinical and neuroimaging information for outcome prediction. Several different clinical, laboratory, and electrophysiologic parameters are known to be associated with clinical outcomes in patients with cardiac arrest; however, most studies focused on imaging-based predictors have favored a global rather than region-specific analysis.²⁸ We showed that outcome determination using individual regions, whole brain, or a combination of specific regions using PCA had excellent performance, with AUCs ranging from 0.84 to 0.91. Our results are consistent with those in previous literature showing that the mean ADC as well as regional ADC₆₅₀ are helpful for prognostication in post-cardiac arrest coma.¹³⁻¹⁵ The specific cutoff for ADC₆₅₀ has not yet been defined, with a cutoff value of >10%–26% brain involvement being needed to achieve specificity for poor outcome prediction (ie, above 95%).^{4,5,8,14} In our study, 10% brain involvement with ADC₆₅₀ was 95% specific and 55% sensitive for predicting poor outcome, and 5% brain involvement was 74% specific and 77% sensitive. In addition, previous studies have shown that lower thresholds for ADC for such as 400 or 450 × 10⁻⁶ mm²/s yield higher ORs for predicting poor neurologic outcomes.^{6,8,16} Additional studies exploring the ADC parameter space using larger and more racially and ethnically diverse cohorts may help define global and regional thresholds with the best performance for outcome prediction.

Some of the variability in previously published data on the predictive value of DWI in patients with cardiac arrest could be secondary to differences in patient selection, variable timing of MR imaging, variable methodology, and differences in outcome selection. Given these limitations, in addition to limited access to quantitative DWI analysis techniques, we believe the results from regional analysis may be add important insight for clinical practice. Temporal variations in DWI appearance in patients after cardiac arrest have been established by multiple observational and quantitative studies, with the ability to predict outcome being best on MR imaging performed on days 3–5.^{6,13,15} These observations likely reflect both the well-described phenomenon of infarct pseudonormalization on DWI and the complex pathophysiology of anoxic injury, with a significant component of secondary injury caused by oxidative stress and neuronal excitotoxicity.²⁹ For these reasons, we excluded from our analysis patients with MR imaging performed >7 days following arrest; however, it remains unclear whether more stringent time-to-MR imaging limitations should be imposed for this type of study. Our study benefited from imaging acquisition in a single scanner with comparable protocols, which may have minimized some of the scanning-variability limitations.

There are several limitations of our study. This was a retrospective and single-center study that relied on documentation of a clinical examination documentation for outcome determination. While our outcome metric closely followed discharge CPC scores, it is, nonetheless, limited due to lack of standardization. In addition, at our institution the use of brain MR imaging is part of a multimodal prognostication protocol, together with other ancillary tests for patients who do not recover consciousness after TTM, possibly leading to a selection bias toward evaluating patients with more severe brain injury. While quantitative analysis of ADC data was not available for decision-making, clinicians were not blinded to qualitative MR imaging interpretation;

therefore, brain injury burden likely contributed to self-fulfilling prophecies related to WLST due to perceived poor neurologic prognosis.^{9,12,13} However, we did not detect any significant difference in the rates of WLST or brain death between patients who were included versus excluded in the analysis. Finally, the relatively small sample size and small proportion of patients with good outcome limit our ability to generalize findings or draw conclusions about when WLST should be considered. Larger and prospective studies focused on assessment of regional brain injury will be needed to confirm the association of parieto-occipital injury with poor clinical outcome.

CONCLUSIONS

Injury to the parieto-occipital region is associated with poor outcomes following cardiac arrest. Involvement of the precentral gyrus can be seen in both good and poor outcome groups; however, patients recovering from coma had a much lower burden of brain injury. Regional and voxelwise analysis of quantitative ADC may add value to multimodal neurologic prognostication in combination with other established predictors²⁸ and provide information about the neuroanatomic regions determining the potential for coma recovery.

Disclosure forms provided by the authors are available with the full text and PDF of this article at www.ajnr.org.

REFERENCES

1. Virani SS, Alonso A, Aparicio HJ, et al; American Heart Association Council on Epidemiology and Prevention Statistics Committee and Stroke Statistics Subcommittee. **Heart Disease and Stroke Statistics-2021 Update: a report from the American Heart Association.** *Circulation* 2021;143:e254–743 CrossRef Medline
2. Madden LK, Hill M, May TL, et al. **The implementation of targeted temperature management: an evidence-based guideline from the Neurocritical Care Society.** *Neurocrit Care* 2017;27:468–87 CrossRef Medline
3. An C, You Y, Park JS, et al. **The cut-off value of a qualitative brain diffusion-weighted image (DWI) scoring system to predict poor neurologic outcome in out-of-hospital cardiac arrest (OHCA) patients after target temperature management.** *Resuscitation* 2020;157:202–10 CrossRef Medline
4. Wouters A, Scheldeman L, Plessers S, et al. **Added value of quantitative apparent diffusion coefficient values for neuroprognostication after cardiac arrest.** *Neurology* 2021;96:e2611–18 CrossRef Medline
5. Bevers MB, Scirica BM, Avery KR, et al. **Combination of clinical exam, MRI and EEG to predict outcome following cardiac arrest and targeted temperature management.** *Neurocrit Care* 2018;29:396–403 CrossRef Medline
6. Reynolds AS, Guo X, Matthews E, et al. **Post-anoxic quantitative MRI changes may predict emergence from coma and functional outcomes at discharge.** *Resuscitation* 2017;117:87–90 CrossRef Medline
7. Kim J, Kim K, Suh GJ, et al. **Prognostication of cardiac arrest survivors using low apparent diffusion coefficient cluster volume.** *Resuscitation* 2016;100:18–24 CrossRef Medline
8. Hirsch KG, Mlynash M, Eyngorn I, et al. **Multi-center study of diffusion-weighted imaging in coma after cardiac arrest.** *Neurocrit Care* 2016;24:82–89 CrossRef Medline
9. Kim J, Kim K, Hong S, et al. **Low apparent diffusion coefficient cluster-based analysis of diffusion-weighted MRI for prognostication of out-of-hospital cardiac arrest survivors.** *Resuscitation* 2013;84:1393–99 CrossRef Medline
10. Kim J, Choi BS, Kim K, et al. **Prognostic performance of diffusion-weighted MRI combined with NSE in comatose cardiac arrest**

- survivors treated with mild hypothermia. *Neurocrit Care* 2012;17:412–20 CrossRef Medline
11. Choi SP, Park KN, Park HK, et al. **Diffusion-weighted magnetic resonance imaging for predicting the clinical outcome of comatose survivors after cardiac arrest: a cohort study.** *Crit Care* 2010;14:R17 CrossRef Medline
 12. Hirsch KG, Mlynash M, Jansen S, et al. **Prognostic value of a qualitative brain MRI scoring system after cardiac arrest.** *J Neuroimaging* 2015;25:430–37 CrossRef Medline
 13. Wijman CAC, Mlynash M, Caulfield AF, et al. **Prognostic value of brain diffusion-weighted imaging after cardiac arrest.** *Ann Neurol* 2009;65:394–402 CrossRef Medline
 14. Hirsch KG, Fischbein N, Mlynash M, et al. **Prognostic value of diffusion-weighted MRI for post-cardiac arrest coma.** *Neurology* 2020;94:e1684–92 CrossRef Medline
 15. Wu O, Sorensen AG, Benner T, et al. **Comatose patients with cardiac arrest: predicting clinical outcome with diffusion-weighted MR imaging.** *Radiology* 2009;252:173–81 CrossRef Medline
 16. Moon HK, Jang J, Park KN, et al. **Quantitative analysis of relative volume of low apparent diffusion coefficient value can predict neurologic outcome after cardiac arrest.** *Resuscitation* 2018;126:36–42 CrossRef Medline
 17. Torres-Espín A, Chou A, Huie JR, et al. **Reproducible analysis of disease space via principal components using the novel R package syndRomics.** *eLife* 2021;10:e61812 CrossRef Medline
 18. Snider SB, Fischer D, McKeown ME, et al. **Regional distribution of brain injury after cardiac arrest: clinical and electrographic correlates.** *Neurology* 2022;98:e1238–47 CrossRef Medline
 19. Vanhauzenhuysse A, Noirhomme Q, Tshibanda LJ, et al. **Default network connectivity reflects the level of consciousness in non-communicative brain-damaged patients.** *Brain* 2010;133:161–71 CrossRef Medline
 20. Li R, Utevsky AV, Huettel SA, et al. **Developmental maturation of the precuneus as a functional core of the default-mode network.** 2019;31:1506–19 CrossRef Medline
 21. Silva S, de Pasquale F, Vuillaume C, et al. **Disruption of posteromedial large-scale neural communication predicts recovery from coma.** *Neurology* 2015;85:2036–44 CrossRef Medline
 22. Koenig MA, Holt JL, Ernst T, et al. **MRI default mode network connectivity is associated with functional outcome after cardiopulmonary arrest.** *Neurocrit Care* 2014;20:348–57 CrossRef Medline
 23. Sair HI, Hannawi Y, Li S, et al; Neuroimaging for Coma Emergence and Recovery (NICER) Consortium. **Early functional connectome integrity and 1-year recovery in comatose survivors of cardiac arrest.** *Radiology* 2018;287:247–55 CrossRef Medline
 24. Wagner F, Hänggi M, Weck A, et al. **Outcome prediction with resting-state functional connectivity after cardiac arrest.** *Sci Rep* 2020;10:11695 CrossRef Medline
 25. Ryoo SM, Jeon S-B, Sohn CH, et al; Korean Hypothermia Network Investigators. **Predicting outcome with diffusion-weighted imaging in cardiac arrest patients receiving hypothermia therapy: multicenter retrospective cohort study.** *Crit Care Med* 2015;43:2370–77 CrossRef Medline
 26. Horwitz B, Duara R, Rapoport SI. **Intercorrelations of glucose metabolic rates between brain regions: application to healthy males in a state of reduced sensory input.** *J Cereb Blood Flow Metab* 1984;4:484–99 CrossRef Medline
 27. Anderson RC, Patel V, Sheikh-Bahaei N, et al. **Posterior reversible encephalopathy syndrome (PRES): pathophysiology and neuroimaging.** *Front Neurol* 2020;11:463 CrossRef Medline
 28. Sandroni C, D'Arrigo S, Cacciola S, et al. **Prediction of good neurological outcome in comatose survivors of cardiac arrest: a systematic review.** *Intensive Care Med* 2022;48:389–413 CrossRef Medline
 29. Sekhon MS, Ainslie PN, Griesdale DE. **Clinical pathophysiology of hypoxic ischemic brain injury after cardiac arrest: a “two-hit” model.** *Crit Care* 2017;21:90 CrossRef Medline

Validity Assessment of an Automated Brain Morphometry Tool for Patients with De Novo Memory Symptoms

F. Rahmani, S. Jindal, C.A. Raji, W. Wang, A. Nazari, G.G. Perez-Carrillo, M.M. Miller-Thomas, P. Graner, B. Marechal, A. Shah, M. Zimmermann, C.D. Chen, S. Keefe, P. LaMontagne, and T.L.S. Benzinger



ABSTRACT

BACKGROUND AND PURPOSE: Automated volumetric analysis of structural MR imaging allows quantitative assessment of brain atrophy in neurodegenerative disorders. We compared the brain segmentation performance of the AI-Rad Companion brain MR imaging software against an in-house FreeSurfer 7.1.1/Individual Longitudinal Participant pipeline.

MATERIALS AND METHODS: T1-weighted images of 45 participants with de novo memory symptoms were selected from the OASIS-4 database and analyzed through the AI-Rad Companion brain MR imaging tool and the FreeSurfer 7.1.1/Individual Longitudinal Participant pipeline. Correlation, agreement, and consistency between the 2 tools were compared among the absolute, normalized, and standardized volumes. Final reports generated by each tool were used to compare the rates of detection of abnormality and the compatibility of radiologic impressions made using each tool, compared with the clinical diagnoses.

RESULTS: We observed strong correlation, moderate consistency, and poor agreement between absolute volumes of the main cortical lobes and subcortical structures measured by the AI-Rad Companion brain MR imaging tool compared with FreeSurfer. The strength of the correlations increased after normalizing the measurements to the total intracranial volume. Standardized measurements differed significantly between the 2 tools, likely owing to differences in the normative data sets used to calibrate each tool. When considering the FreeSurfer 7.1.1/Individual Longitudinal Participant pipeline as a reference standard, the AI-Rad Companion brain MR imaging tool had a specificity of 90.6%–100% and a sensitivity of 64.3%–100% in detecting volumetric abnormalities. There was no difference between the rate of compatibility of radiologic and clinical impressions when using the 2 tools.

CONCLUSIONS: The AI-Rad Companion brain MR imaging tool reliably detects atrophy in cortical and subcortical regions implicated in the differential diagnosis of dementia.

ABBREVIATIONS: AD = Alzheimer disease; AIRC = AI-Rad Companion; CDR = Clinical Dementia Rating; DLB = dementia with Lewy bodies; FTD = frontotemporal dementia; FS = FreeSurfer; GDS = Geriatric Depression Scale; ICC = intraclass correlation coefficient; ILP = Individual Longitudinal Participant; OASIS = Open Access Series of Imaging Studies; TIV = total intracranial volume

Standard of care for any cognitive or memory issues includes structural MR imaging of the brain.¹ Beyond its utility to exclude anatomic or pathologic abnormalities, structural brain

MR imaging enables volumetric quantification of different brain structures that are affected by neurodegenerative diseases that cause cognitive impairment. FreeSurfer (FS; <https://surfer.nmr.mgh.harvard.edu/>) is the most commonly used volumetric analysis tool, using an automated ROI-based algorithm to generate thickness, surface areas, and volumes for 68 different cortical and subcortical regional volumes.^{2–4}

Due to the detailed scale of the FS output, it is often incorporated into further processing to summarize the results into meaningful metrics for different diagnostic purposes, namely dementia. One such pipeline is a 2-step processing pipeline consisting of FS Version 7.1.1 processing of structural T1 images followed by the Individual Longitudinal Participant (ILP) software Version 2.0 (herein and after referred to as the FS/ILP pipeline;⁵ for volumetric brain assessment. The time-exhaustive nature of this research-standard pipeline, which includes generation of the FS output (between 6 and 12 hours),

Received June 30, 2022; accepted after revision January 9, 2023.

From the Mallinckrodt Institute of Radiology, Division of Neuroradiology (F.R., S.J., C.A.R., W.W., A.N., G.G.P.-C., M.M.M.-T., C.D.C., S.K., P.L., T.L.S.B.) and Charles F. and Joanne Knight Alzheimer Disease Research Center (F.R., S.J., C.A.R., W.W., A.N., C.D.C., T.L.S.B.), Washington University in St. Louis, St. Louis, Missouri; Siemens Medical Solutions (P.G., B.M., M.Z.), Malvern, Pennsylvania; Advanced Clinical Imaging Technology (P.G., B.M., M.Z.), Siemens Healthcare, Lausanne, Switzerland; Department of Radiology (P.G., B.M., M.Z.), Lausanne University Hospital and University of Lausanne, Lausanne, Switzerland; LTS5, École Polytechnique Fédérale de Lausanne (P.G., B.M., A.S., M.Z.), Lausanne, Switzerland; and Siemens Healthcare (P.G., B.M., M.Z.), Erlangen, Germany.

Please address correspondence to Tammie L.S. Benzinger, MD, PhD, Mallinckrodt Institute of Radiology, Washington University School of Medicine in St. Louis, 510 South Kingshighway Boulevard, Campus Box 8131, St. Louis, MO 63110; e-mail: benzinger@wustl.edu; @BenzingerNeuro1; @tlsmit1

Indicates article with online supplemental data.

<http://dx.doi.org/10.3174/ajnr.A7790>

visual inspection, and potential manual editing and recalculation steps of the output, limits its applicability in high-throughput clinical settings. Siemens has developed the FDA-cleared AI-Rad Companion (AIRC; Siemens) brain MR software that enables volumetric quantification of main cortical and subcortical structures in a scale of a few minutes (herein after referred to as the AIRC tool). We therefore aimed to investigate the validity of the AIRC tool in a clinical context through the following: 1) assessment of the correlation, consistency, and agreement of volumetric measurements generated by the AIRC tool versus those produced by the FS/ILP pipeline; 2) assessment of the sensitivity of the AIRC output in the detection of volumetric abnormalities associated with neurodegenerative causes of dementia, compared with the output from the FS/ILP as a reference standard; and 3) assessment of the potential effect of any discrepant finding between the 2 tools on the final impression made by a radiologist.

MATERIALS AND METHODS

Participants

Participants were randomly selected from the Open Access Series of Imaging Studies 4 (OASIS-4) cohort, which is publicly accessible through the OASIS brain website: <https://central.xnat.org/>. Participants were included under the following circumstances: 1) They were referred for clinical assessment due to a de novo cognitive symptom, 2) were 45 years of age or older, and 3) had a structural T1-weighted MR imaging study within a maximum of 1 year of the initial assessment. Diagnosis of dementia was made on the basis of the clinical assessment and a battery of cognitive tests, including the Clinical Dementia Rating (CDR)⁶ and Mini-Mental State Examination.⁷ If dementia was present, an etiologic diagnosis was further determined on the basis of clinical practices for Alzheimer disease (AD), posterior cortical atrophy, dementia with Lewy bodies (DLB), frontotemporal dementia (FTD), and vascular cognitive impairment.^{8–11} This diagnosis was made by a neurologist clinician at the end of the recruitment visit and before any imaging assessment. Reflecting the proportion of each disease category in the OASIS-4 cohort, the current sample comprised a random selection of 15 individuals with AD, including 5 participants with early-onset AD; 10 participants with non-neurodegenerative conditions; such as subjective cognitive impairment in the absence of clinical dementia, mood disorders, polypharmacy, and sleep disorders; 5 with posterior cortical atrophy; 5 with DLB; 5 with FTD, and 5 with vascular cognitive impairment (Online Supplemental Data). The 15-item version of the Geriatric Depression Scale (GDS) was used to screen participants for the presence of depressive symptoms in which a cutoff score of 5 has shown 92% sensitivity (Online Supplemental Data).¹²

This study was conducted using a research agreement between Washington University School of Medicine in St. Louis and Siemens Medical Solutions USA and was reviewed and approved by the institutional review board of Washington University in Saint Louis School of Medicine (IRB No. 201912172).

Image Data Collection

The 3D T1WI MPRAGE and T2-weighted FLAIR images were acquired on a 3T scanner (Magnetom Skyra; Siemens) using a TR/TE = 2300/2.95 ms, TI = 900 ms, flip angle = 9°, section

thickness = 1 mm, and FOV = 256 × 256 for the T1WI scans, and a TR/TE = 900/81 ms, TI = 2500 ms, flip angle = 150°, section thickness = 5 mm, within a 256 × 256 FOV for FLAIR scans. SWI was performed in the same session and used the following parameters: TR/TE = 27/20 ms, flip angle = 15°, section thickness = 2.4 mm, FOV = 256 × 256.

In all subsequent analyses, the absolute volumes refer to raw estimates produced by each tool, normalized volumes refer to absolute volumes divided by their corresponding estimated total intracranial volume (TIV), and standardized volumes refer to *z* scores calculated by comparing the normalized volumes with their respective normative database.

AIRC Tool

The AIRC Brain MR tool creates brain morphometry reports using a T1WI MPRAGE series and through a tissue-wise segmentation model, resulting in a considerably reduced computation time (2–5 minutes) compared with other segmentation software such as FreeSurfer.^{3,13} This tool produces volumes of 25 different brain regions in both hemispheres (50 total) and compares them with age- and sex-matched normative data from a healthy population. Results are presented as a labeling report consisting of a label map showing the segmentation results (Fig 1A); a deviation report consisting of a deviation map and the corresponding standardized volumes for each region; and a list of evaluated volumes and their corresponding TIV-normalized measures displayed alongside the 10th–90th percentile normative ranges based on the participant's age and sex group. Regions with normative volumes that are outside this range are indicated by an asterisk (Fig 1B, -C).¹³ Once processed, a visual quality check of the labeling and deviation results is performed to ensure consistent delineation of different cortical and subcortical regions. All of the 45 scans passed this quality control.

Normative Range Analyses. The normative database for the AIRC tool consists of T1-weighted MR images of 303 healthy subjects, including 50.8% men (median age, 73.25 years; age range, 19–91 years). Scans were collected from 2 cohorts: 1) the Alzheimer Disease Neuroimaging Initiative (ADNI; <https://adni.loni.usc.edu/>) using standard protocols for participant selection and scanning protocol,^{14,15} and 2) Siemens collection of the MR imaging scans following the ADNI selection guidelines.

Normative ranges were calibrated on the respective healthy absolute volumes estimated by the AIRC using a log-linear regression model, taking into account the confounding effects of age and sex as covariates.¹³ The deviation map offers a color-coded preview of the amount of deviation based on *z* score estimates of each structure.¹³

The FS/ILP Pipeline

FS Segmentation. T1-weighted images were processed with FS Version 7.1.1 and resampled to 1 × 1 × 1 mm resolution for volumetric segmentation and cortical reconstruction.³ Regional volumes and cortical thicknesses were derived for 68 cortical and 40 subcortical regions in the left and right hemispheres after quality control of FS output through visual inspection.

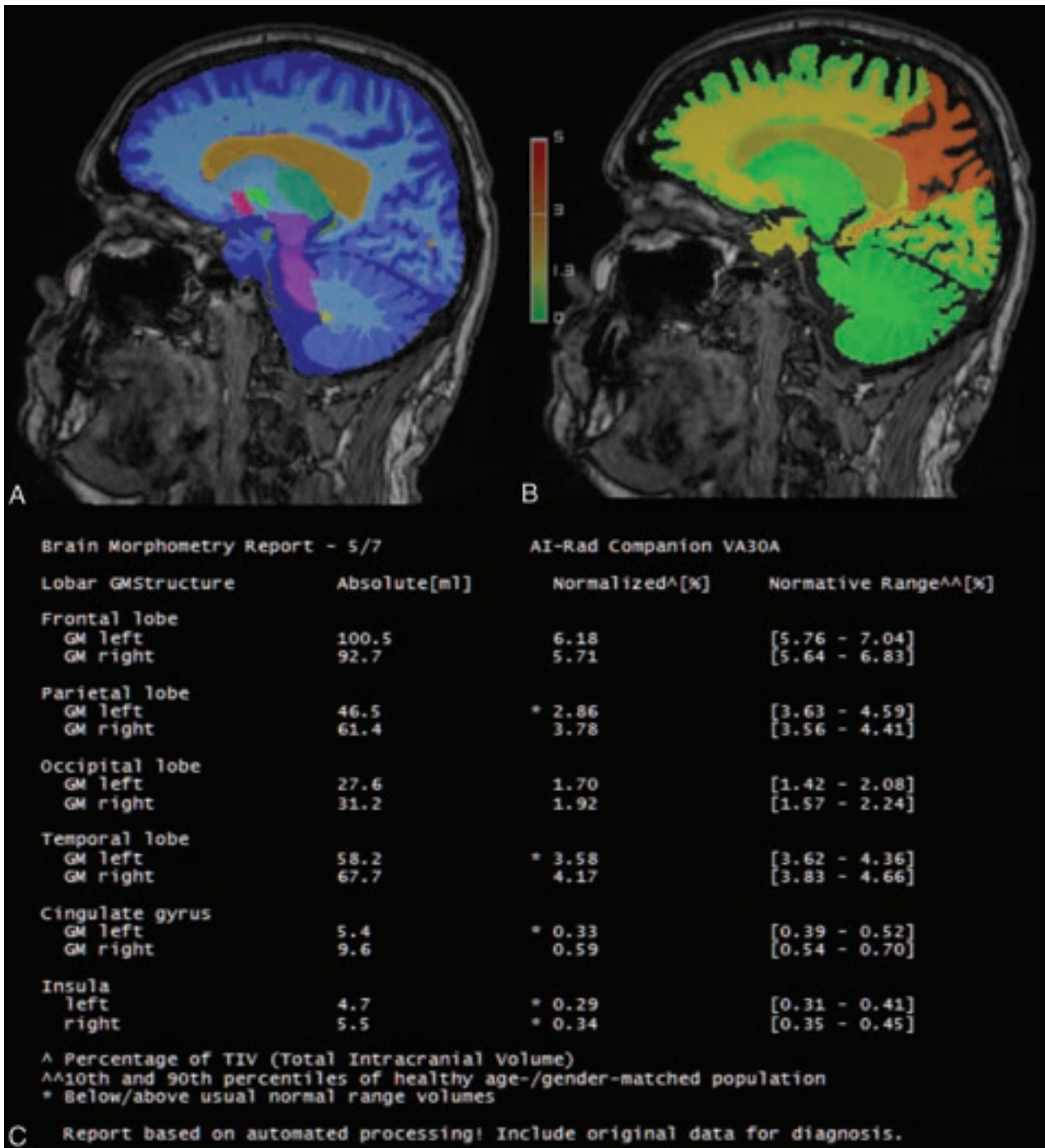


FIG 1. AIRC brain MR imaging tool volumetric output for a 60-year-old male participant with early-onset Alzheimer disease. Labeling map (A), deviation map (B), and 1 page of the numeric report (C). Asterisk indicate values outside the normative 10th–90th percentile range for participants age and sex.

Normative Range Analyses and ILP Report Generation. Once generated, FS volumes were compared with the ILP normative data sets consisting of T1-weighted MR imaging scans of 383 cognitively healthy participants assembled from 2 different sources: 1) 249 participants 38 to 88 years of age from the recently released publicly available data in OASIS-3,¹⁶ and 2) 134 mutation-negative participants 18 to 58 years of age from the control group of the Dominantly Inherited Alzheimer Network data set (<https://dian.wustl.edu/>; previously published as a Normal Aging Cohort by Koenig et al¹⁷).

The ILP pipeline calculates a number of summary metrics based on TIV-normalized volumes and cortical thicknesses from FS output: frontal lobe cortical thickness, parietal lobe cortical thickness, occipital lobe cortical thickness, left and right hippocampal volume, left and right FTD cortical thickness (a summary measurement of cortical regions affected by frontotemporal dementia), total lateral ventricular volume, and the ratio of lateral ventricular volume to cerebral volume (Online Supplemental Data). These summary metrics are then used to generate a regression model that demonstrates

age-adjusted ranges for these volumes and thicknesses using the ILP normative data sets, forming the ILP Report.⁵ With each T1WI scan processed through the FS/ILP pipeline, the above summary metrics are calculated and plotted on their corresponding ILP graph, in which the x-axis represents participants' ages and the y-axis shows the respective thickness or volume summary metric.

Analytical Approach and Statistics

Statistical analyses were performed by using R software Version 4.0.5 (<http://www.r-project.org/>). The purpose of these analyses was the following: 1) to assess the magnitude of the correlation, consistency, or agreement between measurements from each tool, and 2) to evaluate the sensitivity and specificity of the AIRC tool compared with FS/ILP as a reference standard. The Pearson correlation and intraclass correlation statistics were used to compare the absolute and normalized regional volumes and *z* scores derived from the FS/ILP and AIRC tools and their respective normative data sets. When necessary, a summation of various FS-based cortical segmentation volumes was calculated to match the lobar cortical volumes reported by the AIRC tool as detailed in the Online Supplemental Data.¹⁸ The Pearson correlation coefficient and intraclass correlation coefficients (ICCs) in agreement and consistency and their respective *P* values were calculated by using the “corr” and “icc” functions, respectively. Pearson correlation coefficient values of <0.3, between 0.3 and 0.5, and >0.5 were considered to indicate small, moderate, and large correlations, while ICC values <0.5, between 0.5 and 0.7, between 0.7 and 0.9, and >0.9 were considered to indicate poor, moderate, good, and excellent agreement or consistency.^{19,20} Additional details on the definition of these terms can be found in the Online Supplemental Data. Normal distribution of the variables was tested using the Kolmogorov-Smirnov goodness-of-fit test. *P* values < .05 after correction for multiple comparisons using the Benjamini-Hochberg false-discovery-rate correction rejected the null assumption.²¹ We further performed paired statistics to extract mean differences and the resulting effect sizes between volumes measured by each tool, as detailed in the Online Supplemental Data.

We compared the rates of detection of abnormal findings through comparison of final reports generated by each tool and by using the “chisq.test” function in R. The T1WI MPRAGE scans were evaluated by 3 board-certified neuroradiologists (W.W., C.A.R., and A.N.) with or without additional volumetric information provided by the AIRC or FS/ILP tools. Each participant was rated 3 times with 3 different methods, once using only the T1-weighted image (MPRAGE_Only), once after adding the FS/ILP output (MPRAGE+ILP), and once after adding the AIRC output (MPRAGE+AIRC). Raters independently assessed all 45 cases so that each participant was randomly evaluated by using one of the above 3 methods by each rater. The raters were asked to indicate radiologic impressions in a stepwise manner indicating the following: 1) whether there were any structural abnormalities related to the patient's cognitive symptoms, 2) whether the observed abnormalities were symmetric and lobar, and 3) whether the abnormalities pointed to a specific neurodegenerative entity (AD, posterior cortical atrophy, DLB, FTD, vascular cognitive impairment). The rate of compatibility between radiologic impressions and clinical diagnoses was calculated as

percentages for each method as detailed in the Online Supplemental Data and compared across methods using the “aov” and “TukeyHSD” functions in R.

RESULTS

The Online Supplemental Data demonstrate a summary of clinical and demographic features of the study population including their cognitive status assessed through CDR, CDR sum of boxes and the Mini-Mental State Examination scores, and the presence or absence of depressive symptoms based on the 15-item GDS score. The GDS score ranged between 0 and 6 across participants in all diagnosis groups, while participants with non-neurodegenerative causes for their cognitive symptoms were more likely to have a GDS score of ≥ 5 , compared with participants diagnosed with neurodegenerative conditions. Figure 2 demonstrates the results of comparisons between the 2 tools based on the absolute, normalized, and standardized regional volumes.

Absolute Volumes

There was a large, positive relationship (Pearson correlation coefficient) and excellent-to-good consistency (ICC-consistency) between measured absolute volumes of the brain, cerebellum, lateral ventricles, and putamen and between the AIRC tool and FS. Absolute volumes of the frontal, parietal, occipital, and temporal lobes and the hippocampal volumes demonstrated moderate-to-poor agreement (ICC-agreement) and consistency between by the AIRC tool and the FS/ILP pipeline. Thalamic absolute volumes demonstrated the weakest consistency between the 2 tools and no significant agreement (ICC-a) or correlation (ICC-c) (Fig 2).

Normalized Volumes

When we compared volumes normalized to the TIV, a large, positive correlation and moderate consistency were observed in both cortical and subcortical regional volumes between the 2 tools, while there was an increase in the correlation coefficients for most regions (Fig 2). Normalized brain, cerebellum, and lateral ventricular volumes demonstrated an excellent consistency and agreement when compared between the 2 tools. There was no significant agreement (ICC-a) in the normalized volumetric measurements of the bilateral frontal lobes, thalami, and putaminal regions (Fig 2).

Standardized Volumes

Once volumes were transformed to standardized *z* scores, correlation and consistency were moderate among *z* scores of the 4 main cortical lobes as well as the bilateral hippocampi (Fig 2). There was no significant agreement (ICC-a) in the regional *z* scores except in the bilateral pallidum, putamen, insula, and lateral ventricles (Fig 2).

Comparing the Diagnostic Utility of Outputs from the FS/ILP versus the AIRC Tools

We compared the performance of the AIRC tool and FS/ILP pipelines through comparison of the final report generated by the 2 tools. Cutoff points indicating abnormal regional values were either above +2 SDs (>97.5th percentile, for ventricular volumes and the ventricle/cerebrum ratio) and below -2 SDs (<2.5th percentile, for all other region/metrics) in the FS/ILP

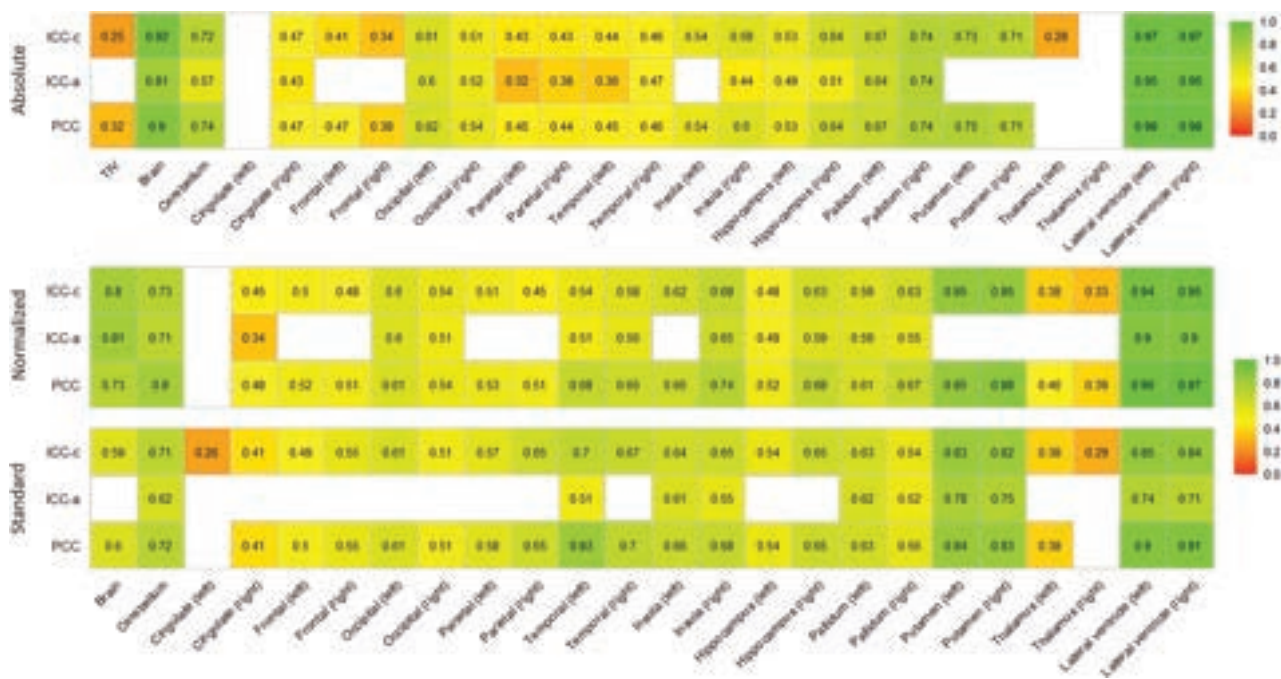


FIG 2. Comparing the Pearson and intraclass correlation between volumetric measurements produced by the AIRC-versus-FS/ILP tools. Panels demonstrate correlation coefficients for raw volumes (*top*), volumes normalized to TIV (*middle*), and standardized (*z* score) volumes (*bottom*). Blank cells demonstrate absence of statistically significant correlation between the 2 tools. ICC-c indicates Intraclass correlation coefficient-consistency; ICC-a, ICC-agreement; PCC, Pearson's correlation coefficient.

output, corresponding to >90th percentile (for ventricular volumes and the ventricle/cerebrum ratio) and <10th percentile (for all other region/metrics) in the AIRC tool output (Online Supplemental Data).

The Online Supplemental Data show a comparison between rates of detection of abnormal findings by the 2 tools, considering the FS/ILP pipeline as a reference standard. Note that in this step and for the main lobes (frontal, parietal, temporal, and occipital), volume-based *z* scores from the AIRC were compared with thickness-based *z* scores from the FS/ILP tool. This step was unlike the previous steps in which volumes generated by each tool were compared with each other. The AIRC tool had a high specificity in the detection of volumetric abnormalities, ranging from 90.6% in detecting enlarged lateral ventricles to 100% in detecting concurrent frontal and temporal atrophy (FTD thickness in FS/ILP output). Sensitivity ranged between 64.3% and 100%, with the lowest rate detected in the comparison between concurrent frontal and temporal lobe atrophy in the AIRC output and FTD thickness in the FS/ILP output. AIRC was 94.4% specific and 78% sensitive in the detection of hippocampal atrophy compared with the FS/ILP pipeline.

Equal Rate of Compatible Diagnoses Using the FS/ILP versus AIRC Tools

Each participant was independently evaluated 3 times, each time based on one of the following combinations of methods: MPRAGE_only, MPRAGE+FS/ILP, and MPRAGE+AIRC. Impressions made by the neuroradiologists were then compared with the diagnoses made by the clinician as the reference standard and marked as either compatible or incompatible (Online Supplemental Data).

Our findings indicated no difference in the rate of compatibility with clinical impressions among radiologic impressions made on the basis of the MPRAGE+ILP or MPRAGE+AIRC methods (χ^2 *P* value > .05). Even among participants with a known neurodegenerative diagnosis (35 of 45), there were no significant differences in the rate of detection of abnormality, symmetric and lobar atrophy, or the presence/absence of a neurodegenerative cause between 2 methods (Online Supplemental Data). Finally, we could not detect any difference in the rate of compatibility of the clinical diagnoses with the radiologic impressions made on the basis of either of the tools compared with the impressions made in the absence of quantitative volumetric assessment (based on the T1-weighted structural image [MPRAGE_only]).

DISCUSSION

We compared the AIRC brain MR imaging tool, a commercially available volumetric brain assessment software, with the standard publicly accessible FS/ILP pipeline. We used a sample of 45 individuals with a de novo memory symptom to investigate the effect of any potential discrepancy between the 2 tools. We found the following: 1) volumetric measurements produced by the FS/ILP and AIRC tools were largely correlated and moderately consistent in most cortical and subcortical structures, a relationship that improved in magnitude after normalization for TIV; 2) measurements were overall more consistent than having precise agreement; 3) agreement between standardized volumes was poor in most regions; 4) compared with the output of the FS/ILP pipeline as a reference standard, the AIRC algorithm had a high specificity in flagging regional atrophy; and 5) use of the AIRC-versus-FS/

ILP output did not result in any difference in the rate of detection of neurodegenerative changes by the neuroradiologist clinicians.

Similar to the Pearson correlation, ICC estimates the strength of the relationship between 2 continuous variables. However, the Pearson correlation does not take the rater bias, which is part of the systematic error, into account. This is an important element that sets correlation apart from agreement.²² As a result, the Pearson correlation is often paired with the intraclass correlation to optimize the detection of bias between the 2 different measurement tools. Optimized agreement requires not only a strong correlation but also low rater bias and, as a result, minimized systematic error between the 2 measurement tools. Therefore, and suggesting the presence of non-negligible bias between the 2 tools, we observed higher Pearson correlation coefficients compared with ICC-consistency and higher ICC-consistency compared with ICC-agreement for most structures, indicating the presence of rating bias among the tools (Fig 2).

Once standardized measurements were compared, the 4 main cortical lobes as well as the hippocampus demonstrated poor agreement between the FS/ILP pipeline and the AIRC tool. Because these large effect sizes are only seen in the *z* scores but not normalized volumes, they may be attributable to the differences in the composition of the normative cohort for each tool. These discrepancies might also reflect heuristic differences in the segmentation and labeling methods used by each tool. While the surface-based processing stream used by FS provides accurate delineation of white/gray matter and gray matter/CSF interfaces (Online Supplemental Data), AIRC tissue-based labeling often results in overestimation of cortical GM volumes compared with FS.^{3,12,23,24} Similarly, the AIRC often undersegments and hence provides lower absolute volumes for subcortical nuclei compared with FS (Online Supplemental Data).

Participants in the AIRC normative cohort were older compared with those in the OASIS-3 group (part of the FS/ILP normative cohort, 73.25 versus 55.7 years). As a result, the normative cohort used by the AIRC might be contaminated by individuals with incipient AD pathology. This possibility is not true for OASIS-3, in which participants were followed up and remained cognitively healthy in the 3 years after the enrollment scan, on the basis of the CDR status and amyloid PET cutoffs.^{5,25,26} Moreover, the AIRC normative cohort involves a relatively low number of individuals between 45 and 65 years of age, compared with OASIS-3 (approximately 20 versus 103). Because more than one-third of our participants were in this age range, the standardized score estimates made by the AIRC might be less reliable compared with those made by the FS/ILP pipeline. Given differences in normal databases, users should identify whether their patient population of interest overlaps with the age range of the normative database of any given software.

Most importantly and while FS can output both regional volumes and thicknesses, the ILP algorithm projects only percentiles calculated on the basis of regional thicknesses in the final output. Because the AIRC output is based on cortical volumes, the percentiles from the FS/ILP final report were not directly comparable with those in the AIRC report. As a result, the last step of comparing the 2 tools was to match the rate of abnormal *z* score/

percentile detection on the basis of the final reports (Online Supplemental Data).

The radiologist's evaluation of volumetric brain assessments is performed on the basis of a digital report detailing the patient's *z* score/percentile for each region compared with his or her age- and sex-specific normative range. For the main lobes, this evaluation is done on the basis of cortical thicknesses from the FS/ILP versus cortical volumes from the AIRC output which might be a source of measurement bias. Not surprisingly, most of the false-positive results (8 of the 10 region/participants)- i.e. detection of abnormality in the AIRC tool in the absence of abnormal finding in the FS/ILP output- were due to thresholding differences among the tools because the FS/ILP tool has a more conservative threshold for detection of abnormalities. As a future direction we recommend a comprehensive comparison of all available FDA-cleared programs on a common neuroimaging data set, given the large number of them and that similar studies have already been performed for AD fluid biomarkers.²⁷⁻²⁹ Finally, in developing the clinical applications of such volumetric tools additional diagnoses that were not investigated in this study, such as normal pressure hydrocephalus and primary progressive aphasia should also be considered.

While volumetric processing based on FS has been successfully used in both research and clinical settings for more than 2 decades, it lacks the time and resource efficacy in processing to permit clinical throughput in general and subspecialized radiology practices. One major driver of the long processing time and high memory usage is the reconstruction of white matter, pial, and dural surfaces, allowing FS to generate cortical thicknesses alongside cortical volumes. The AIRC output, being based on cortical volumes, has shown high sensitivity and specificity compared with the FS/ILP output, which is based on cortical volumes. On another note, rapid and accurate generation of these volumetric brain results are becoming increasingly important in high-throughput clinical settings. These features are provided by the AIRC tool due to the streamlined transfer of T1-weighted images from the PACS system, which facilitates the generation of results within several minutes and automated transfer of the results to the PACS system.

CONCLUSIONS

The AIRC brain MR tool detects volumetric changes in the main cortical lobes and subcortical regions implicated in the differential diagnosis of dementia, with sensitivity and specificity comparable with those of the FS/ILP pipeline as the reference standard. Given the much shorter processing time and streamlined user interface, the AIRC has the potential for similar comparisons in larger cohorts and further refinement of wider clinical use.

ACKNOWLEDGMENTS

We would like to thank Timothy Street and Russ Hornbeck for their critical contribution to resource management, especially software and IT support throughout this study.

Data used in this study and the normative data set used by the FS/ILP tool were in-part provided by the OASIS-4 and OASIS-3 cohorts, respectively (<https://central.xnat.org/>). This database is supported by the following grants: NIH P30AG066444, P50AG00561,

REFERENCES

- Knopman DS, DeKosky ST, Cummings JL, et al. **Practice parameter: diagnosis of dementia (an evidence-based review): Report of the Quality Standards Subcommittee of the American Academy of Neurology.** *Neurology* 2001;56:1143–53 CrossRef Medline
- Desikan RS, Ségonne F, Fischl B, et al. **An automated labeling system for subdividing the human cerebral cortex on MRI scans into gyral based regions of interest.** *Neuroimage* 2006;31:968–80 CrossRef Medline
- Fischl B. **FreeSurfer.** *Neuroimage* 2012;62:774–81 CrossRef Medline
- Raji CA, Ly M, Benzinger TL. **Overview of MR imaging volumetric quantification in neurocognitive disorders.** *Top Magn Reson Imaging* 2019;28:311–15 CrossRef Medline
- Owen CJ, Gordon B, Brier MR, et al. **The ILP: a new tool for evaluating preclinical Alzheimer's disease using volumetric MRI in a single participant.** *Alzheimers Dement* 2015;11:P697 CrossRef Medline
- Morris JC. **The Clinical Dementia Rating (CDR).** *Neurology* 1993;43:2412–14 CrossRef Medline
- Folstein MF, Folstein SE, McHugh PR. **"Mini-Mental State": a practical method for grading the cognitive state of patients for the clinician.** *J Psychiatr Res* 1975;12:189–98 CrossRef Medline
- McKhann GM, Knopman DS, Chertkow H, et al. **The diagnosis of dementia due to Alzheimer's disease: recommendations from the National Institute on Aging-Alzheimer's Association workgroups on diagnostic guidelines for Alzheimer's disease.** *Alzheimers Dement* 2011;7:263–69 CrossRef Medline
- McKeith IG, Boeve BF, Dickson DW, et al. **Diagnosis and management of dementia with Lewy bodies: Fourth Consensus Report of the DLB Consortium.** *Neurology* 2017;89:88–100 CrossRef Medline
- Rascovsky K, Hodges JR, Knopman D, et al. **Sensitivity of revised diagnostic criteria for the behavioural variant of frontotemporal dementia.** *Brain* 2011;134:2456–77 CrossRef Medline
- Skrobot OA, Black SE, Chen C, et al; VICESS group. **Progress toward standardized diagnosis of vascular cognitive impairment: guidelines from the Vascular Impairment of Cognition Classification Consensus Study.** *Alzheimers Dement* 2018;14:280–92 CrossRef Medline
- Lyness JM, Noel TK, Cox C, et al. **Screening for depression in elderly primary care patients: a comparison of the Center for Epidemiologic Studies-Depression Scale and the Geriatric Depression Scale.** *Arch Intern Med* 1997;157:449–54 Medline
- Schmitter D, Roche A, Maréchal B, et al; Alzheimer's Disease Neuroimaging Initiative. **An evaluation of volume-based morphometry for prediction of mild cognitive impairment and Alzheimer's disease.** *Neuroimage Clin* 2015;7:7–17 CrossRef Medline
- Wyman BT, Harvey DJ, Crawford K, et al; Alzheimer's Disease Neuroimaging Initiative. **Standardization of analysis sets for reporting results from ADNI MRI data.** *Alzheimers Dement* 2013;9:332–37 CrossRef Medline
- Jack CR, Bernstein MA, Fox NC, et al; ADNI Study. **The Alzheimer's Disease Neuroimaging Initiative (ADNI): MRI methods.** *J Magn Reson Imaging* 2008;27:685–91 CrossRef Medline
- LaMontagne PJ, Benzinger TLS, Morris JC, et al. **OASIS-3: longitudinal neuroimaging, clinical, and cognitive dataset for normal aging and Alzheimer disease.** *medRxiv* <https://www.medrxiv.org/content/10.1101/2019.12.13.19014902v1>. Accessed January 28, 2023
- Koenig LN, Day GS, Salter A, et al. **Select Atrophied Regions in Alzheimer disease (SARA): an improved volumetric model for identifying Alzheimer disease dementia.** *Neuroimage Clin* 2020;26:102248 CrossRef Medline
- Klein A, Tourville J. **101 labeled brain images and a consistent human cortical labeling protocol.** *Front Neurosci* 2012;6:171 CrossRef Medline
- Koo TK, Li MY. **A guideline of selecting and reporting intraclass correlation coefficients for reliability research.** *J Chiropr Med* 2016;15:155–63 CrossRef Medline
- Cohen J. *Statistical Power Analysis for the Behavioral Sciences*, 2nd ed. Routledge; 1998
- Benjamini Y, Hochberg Y. **Controlling the false discovery rate: a practical and powerful approach to multiple testing.** *Journal of the Royal Statistical Society: Series B (Methodological)* 1995;57:289–300 CrossRef
- Liu J, Tang W, Chen G, et al. **Correlation and agreement: overview and clarification of competing concepts and measures.** *Shanghai Arch Psychiatry* 2016;28:115–20 CrossRef Medline
- Fischl B, Sereno MI, Dale AM. **Cortical surface-based analysis, II: inflation, flattening, and a surface-based coordinate system.** *Neuroimage* 1999;9:195–207 CrossRef Medline
- Dale AM, Fischl B, Sereno MI. **Cortical surface-based analysis, I: segmentation and surface reconstruction.** *Neuroimage* 1999;9:179–94 CrossRef Medline
- Su Y, Flores S, Hornbeck RC, et al. **Utilizing the Centiloid scale in cross-sectional and longitudinal PiB PET studies.** *Neuroimage Clin* 2018;19:406–16 CrossRef Medline
- Su Y, Flores S, Wang G, et al. **Comparison of Pittsburgh compound B and florbetapir in cross-sectional and longitudinal studies.** *Alzheimers Dement (Amst)* 2019;11:180–90 CrossRef Medline
- Janelidze S, Teunissen CE, Zetterberg H, et al. **Head-to-head comparison of 8 plasma amyloid- β 42/40 assays in Alzheimer disease.** *JAMA Neurol* 2021;78:1375–82 CrossRef Medline
- Pemberton HG, Goodkin O, Prados F, et al; Alzheimer's Disease Neuroimaging Initiative. **Automated quantitative MRI volumetry reports support diagnostic interpretation in dementia: a multi-rater, clinical accuracy study.** *Eur Radiol* 2021;31:5312–23 CrossRef Medline
- Pemberton HG, Zaki LA, Goodkin O, et al. **Technical and clinical validation of commercial automated volumetric MRI tools for dementia diagnosis: a systematic review.** *Neuroradiology* 2021;63:1773–89 CrossRef Medline

Edge-Enhancing Gradient-Echo MP2RAGE for Clinical Epilepsy Imaging at 7T

S. Tao, X. Zhou, E. Greco, V. Gupta, B.E. Freund, E.M. Westerhold, A.M. Feyissa, W.O. Tatum, S. Grewal, V. Patel, and E.H. Middlebrooks

ABSTRACT

SUMMARY: The 3D edge-enhancing gradient-echo (EDGE) MR imaging sequence offers superior contrast-to-noise ratio in the detection of focal cortical dysplasia. EDGE could benefit from 7T MR imaging but also faces challenges such as image inhomogeneity and low acquisition efficiency. We propose an EDGE-MP2RAGE sequence that can provide both EDGE and T1-weighted contrast, simultaneously, improving data-acquisition efficiency. We demonstrate that with sequence optimization, EDGE images with sufficient uniformity and T1-weighted images with high gray-to-white matter contrast can be achieved.

ABBREVIATIONS: CNR = contrast-to-noise ratio; EDGE = edge-enhancing gradient-echo; FCD = focal cortical dysplasia; INV = inversion imaging

Focal cortical dysplasia (FCD) is the most commonly resected epileptogenic lesion in children and the third most common lesion in adults. A recently described MR imaging sequence, 3D-edge-enhancing gradient-echo (3D EDGE), offers superior contrast-to-noise (CNR) in the detection of FCD.^{1,2} However, the sequence has inherently low SNR and would theoretically be advantageous at 7T. However, 7T MR imaging presents unique challenges such as severe transmit B_1 field (B_1+) inhomogeneity, which can greatly compromise image-contrast uniformity. Additionally, the longitudinal T1s of brain tissues are prolonged at 7T, which requires a longer time for the longitudinal magnetization to recover. For EDGE, the longitudinal magnetization has a substantial impact on overall image contrast and SNR. Due to the prolonged T1, a longer TR may be necessary to improve the SNR and image uniformity, though it decreases data-acquisition efficiency and results in longer scan times.

We describe a new strategy to acquire the EDGE contrast to improve the acquisition efficiency. Because high-resolution, 3D T1-weighted imaging, such as an MPRAGE, is typically needed in an epilepsy MR imaging protocol, simultaneous acquisition of both T1-weighted and EDGE images in a single sequence can improve data-acquisition efficiency while allowing a longer TR to improve image uniformity and SNR. This acquisition strategy

is accomplished by integrating a second acquisition window into the EDGE sequence, resulting in an MP2RAGE sequence.³ In this study, we explore this strategy, EDGE-MP2RAGE, on clinical 7T MR imaging and show that it is capable of producing high-quality EDGE and T1-weighted images, which may be useful for clinical epilepsy imaging at 7T.

TECHNIQUE


EDGE is a magnetization-prepared fast gradient-echo sequence with its TI set at the time when the GM and WM longitudinal magnetizations have comparable signal intensity but opposite polarity, therefore offering a signal-cancellation effect at their boundaries (Fig 1A).² A long TR can lead to increased system idle time during which no data are acquired, increasing the overall scan time. Figure 1B demonstrates the proposed EDGE-MP2RAGE sequence, in which a second data-acquisition window with a different TI is added to the same TR following the EDGE acquisition. The 2 sets of raw inversion images (INV), INV 1 and 2, can be used to generate additional T1-weighted images similar to those in conventional MP2RAGE. Such an approach allows 2 image contrasts to be generated from the same TR, thereby improving data-acquisition efficiency while allowing a longer TR to be used to boost image SNR.

For a conventional MP2RAGE sequence, the TIs of the 2 acquisitions are typically optimized for the GM-WM CNR in the final T1-weighted images.³ With EDGE-MP2RAGE, however, sequence optimization is more complicated due to the requirement to adjust the INV1 to yield an EDGE contrast with sufficient SNR. Meanwhile, additional consideration is needed to improve the EDGE contrast uniformity across the brain, which can be compromised by the high B_1+ inhomogeneity at 7T.

Received August 15, 2022; accepted after revision January 3, 2023.

From the Departments of Radiology (S.T., X.Z., E.G., V.G., E.M.W., V.P., E.H.M.), Neurology (B.E.F., A.M.F., W.O.T.), and Neurosurgery (S.G., E.H.M.), Mayo Clinic, Jacksonville, Florida.

Please address correspondence to Shengzhen Tao, PhD, Mayo Clinic, Department of Radiology, 4500 San Pablo Rd, Jacksonville, FL 32224; e-mail: Tao.Shengzhen@mayo.edu

 Indicates article with online supplemental data.

<http://dx.doi.org/10.3174/ajnr.A7782>

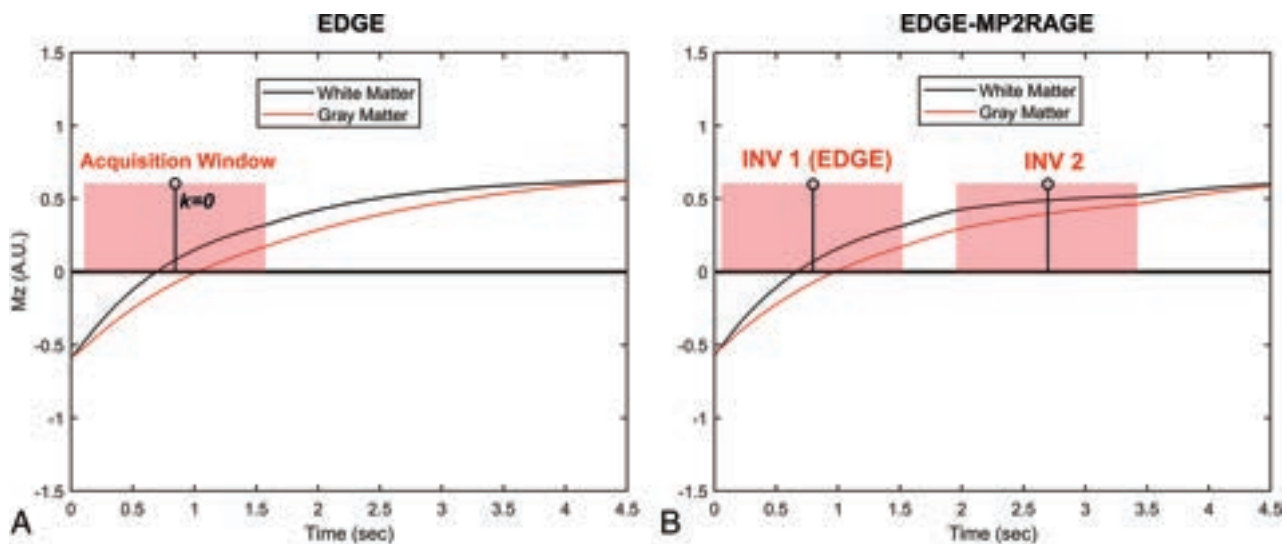


FIG 1. Examples of WM and GM longitudinal magnetizations (M_z) evolution in a repetition period (TR) for the EDGE (A) and EDGE-MP2RAGE (B) sequences. With EDGE contrast (A), the center of the data-acquisition window, which coincides with the k -space center (ie, $k = 0$), is placed when WM and GM have comparable signal intensity but opposite polarity. With EDGE-MP2RAGE (B), the first acquisition (ie, INV 1) is designed to provide the EDGE contrast. A.U. indicates arbitrary unit.

EDGE-MP2RAGE sequence parameters

Acquisition Plane	TR (Sec)	T ₁ /T ₂ (Sec)	FA ₁ /FA ₂	BW (Hz/px)	Acceleration	FOV (mm ²)	Matrix	Resolution (mm ³)
Sagittal	4.5	0.8/2.7	5°/4°	200	3×	230 × 230 × 154	296 × 296 × 192	0.8 × 0.8 × 0.8

Note:—FA indicates flip angle; BW, bandwidth.

The proposed EDGE-MP2RAGE accounts for these challenges by optimizing the sequence parameters to accomplish 2 objectives simultaneously, ie, to provide INV1 with EDGE contrast of sufficient SNR and image uniformity and to provide calculated T1-weighted images of sufficient GM-WM CNR. To achieve these objectives, we performed numeric simulations based on Bloch equations to determine the optimal pulse sequence parameters. The signal intensities of GM and WM in the INV1, INV2, and T1-weighted images were calculated on the basis of Bloch simulations, assuming different combinations of sequence parameters (ie, TI, TR, flip angle, echo spacing, and acquisition bandwidth). From this analysis, a group of parameter combinations that allow comparable GM/WM signal intensities in INV1 across a range of B_1+ inhomogeneity at 7T was determined.³ Finally, within this group, we selected the combination of parameters that were optimized simultaneously for both the SNR in the INV1 and the GM-WM CNR in the T1-weighted image.

The optimized sequence was then implemented on a clinical 7T Magnetom Terra MR imaging (Siemens) scanner with an 8Tx/32Rx head coil (Nova Medical) operating in single-transmit mode (TrueForm). Following an institutional review board-approved protocol, EDGE-MP2RAGE images were acquired on a healthy subject (a 17-year-old girl).

RESULTS

The Table shows the sequence parameters determined from the Bloch simulation analysis, which were designed assuming an isotropic resolution of 0.8 mm, giving a total scan time of 9 minutes. The full scan protocol can be found in the Online Supplemental Data.

Examples of EDGE (INV1) images acquired using the proposed EDGE-MP2RAGE sequences are shown in Fig 2, together with the T1-weighted images. The INV1 (A–C) show that WM and GM have comparable signal intensities, consistent with the EDGE contrast. For quantitative analysis, the cortical WM and GM signal intensities were measured from the EDGE images using ROIs across the brain in 3 orthogonal planes. The results show that the mean WM and GM signal levels are nearly identical (78 [SD, 12] versus 77 [SD, 10], respectively), confirming the visual analysis. Figure 2 also shows that high-quality T1-weighted images with good GM-WM contrast can be generated from the same acquisition. The EDGE image SNR, calculated as previously described for a single EDGE acquisition, measures 59.1 compared with approximately 30 reported for 3T EDGE.⁴

DISCUSSION

In this work, we developed and optimized a new EDGE-MP2RAGE sequence for use in MR imaging studies of epilepsy at 7T. Compared with lower fields, 7T allows higher-resolution imaging due to the high intrinsic SNR. However, due to the high B_1+ inhomogeneity and longer tissue T1 values, it is challenging to implement the EDGE contrast at 7T. To improve SNR and contrast uniformity, one can use a longer TR; however, this substantially reduces data-acquisition efficiency. By means of the EDGE-MP2RAGE sequence, an additional T1-weighted contrast can be generated from the same acquisition, and the average time spent on acquiring each contrast is effectively reduced by 50%, making it feasible to be implemented in clinical examinations. As demonstrated in the results section, EDGE contrast with

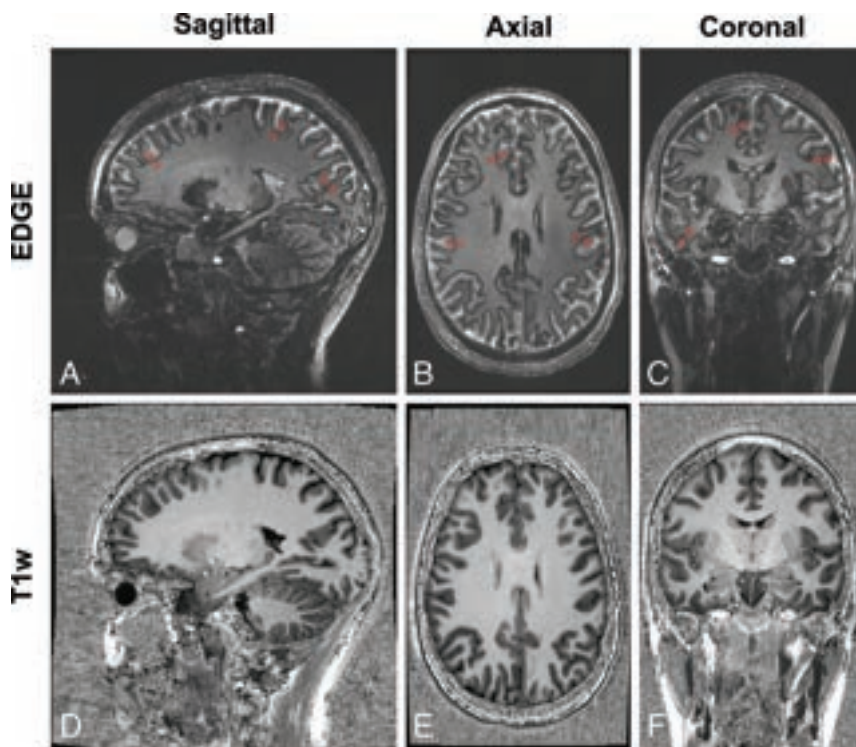


FIG 2. Examples of EDGE (INV 1, A–C) images and T1-weighted (T1w) images (D–F) acquired with the EDGE-MP2RAGE reformatted into sagittal, axial, and coronal planes. The ROI (red circles in A–C) for WM and GM signal intensity measurements are also shown.

acceptable image uniformity can be achieved with this approach using carefully selected sequence parameters despite well-known high B_1 inhomogeneity at 7T, and T1-weighted images with high GM-WM contrast can also be produced from the same acquisition. Note that the protocol described in this work is designed for 7T imaging and is not directly applicable to lower fields, such as 3T, because the longitudinal T_1 s of various brain tissues are different at other field strengths.

EDGE MR imaging has been shown to produce a substantial increase in CNR in the setting of FCD compared with traditional sequences such as MP2RAGE, FLAIR, and double inversion recovery.² The added SNR from 7T allows higher image resolution (0.8 versus 1.0 mm) while still achieving nearly twice the SNR of 3T EDGE. Additionally, a 3D T1-weighted image is also a hallmark of epilepsy protocols, allowing detailed assessment of brain anatomy. At 3T, the application of 2 TIs to generate an MP2RAGE image has been shown to be superior to MP2RAGE for evaluation of epilepsy.³

At 7T, the advantages of MP2RAGE over MPRAGE are even greater due primarily to the severe nonuniformities in the transmit field (B_1+), which is reduced in MP2RAGE.⁵ Within our framework, we have shown how the sequence parameters can be simultaneously optimized for EDGE contrast as part of the first TI image, while also optimizing the resulting T1-weighted image (also known as UNI image) of MP2RAGE.

One limitation of this study, however, is that a direct technical comparison between the new sequence and the standard ones has not been made, and this could be the object of future works.

CONCLUSIONS

We describe an optimized protocol for simultaneous EDGE-MP2RAGE imaging at 7T and show that this protocol could be useful for imaging drug-resistant focal epilepsy.

Disclosure forms provided by the authors are available with the full text and PDF of this article at www.ajnr.org.

REFERENCES

1. Abula Y, Abulimiti A, Liu Z, et al. **The role of the 3D-EDGE sequence at 3T MRI in the detection of focal cortical dysplasia: a technical case report and literature review.** *Neuropediatrics* 2022;53:436–39 CrossRef Medline
2. Middlebrooks EH, Lin C, Westerhold E, et al. **Improved detection of focal cortical dysplasia using a novel 3D imaging sequence: edge-enhancing gradient echo (3D-EDGE) MRI.** *Neuroimage Clin* 2020;28:102449 CrossRef Medline
3. Marques JP, Kober T, Krueger G, et al. **MP2RAGE, a self bias-field corrected sequence for improved segmentation and T1-mapping at high field.** *Neuroimage* 2010;49:1271–81 CrossRef Medline
4. Middlebrooks EH, Okromelidze L, Lin C, et al. **Edge-enhancing gradient echo with multi-image co-registration and averaging (EDGE-MICRA) for targeting thalamic centromedian and parafascicular nuclei.** *Neuroradiol J* 2021;34:667–75 CrossRef Medline
5. Oliveira IAF, Roos T, Dumoulin SO, et al. **Can 7T MPRAGE match MP2RAGE for gray-white matter contrast?** *Neuroimage* 2021;240:118384 CrossRef Medline

Leptomeningeal Interfoliar Enhancement on Vessel Wall MR Imaging as a Unique Radiologic Finding of Susac Syndrome

P. Cardozo, M. Marrodán, A. Gilmore, M.P. Fiol, and H. Chaves



ABSTRACT

SUMMARY: Susac syndrome is a rare disorder affecting the brain, retina, and inner ear, probably triggered by an immune-mediated endotheliopathy. Diagnosis is based on clinical presentation and ancillary test findings (brain MR imaging, fluorescein angiography, and audiometry). Recently, vessel wall MR imaging has shown increased sensitivity in the detection of subtle signs of parenchymal, leptomeningeal, and vestibulocochlear enhancement. In this report, we describe a unique finding identified using this technique in a series of 6 patients with Susac syndrome and discuss its potential value for diagnostic work-up and follow-up.

ABBREVIATIONS: SuS = Susac syndrome; VW-MRI = vessel wall MR imaging

Susac syndrome (SuS) is a rare disorder affecting the brain, retina, and inner ear.¹ Although the underlying pathogenesis is not clear, it is thought to be an immune-mediated endotheliopathy affecting precapillary arterioles, causing microvascular occlusion and multiple microinfarcts in involved territories.²

It predominantly affects young adults, particularly women.³ The classic clinical triad comprises encephalopathy, with or without focal neurologic deficits; sensorineural hearing loss; and visual disturbance secondary to branch retinal artery occlusions. However, the complete triad is present in only 13%–27% of patients at disease onset.³

SuS diagnosis is based on clinical presentation and evidence of brain, retinal, and vestibulocochlear involvement on brain MR imaging, fluorescein angiography, and audiometry.⁴ The main neuroimaging findings are multifocal, T2 FLAIR hyperintense white matter lesions with hallmark imaging patterns known as “snowballs,” “spokes,” “icicles,” and “string of pearls.”⁵ Fluorescein angiography shows arterial wall hyperfluorescence and branch retinal artery occlusions, and audiometry detects sensorineural hearing loss even in asymptomatic patients.^{4,5}

Vessel wall MR imaging (VW-MR imaging) is based on black-blood 3D T1-weighted sequences, enabling selective suppression of blood signal with high spatial resolution and a high contrast-to-noise ratio.⁶ Although initially developed to depict

intracranial vessel walls, it has demonstrated greater sensitivity in showing subtle leptomeningeal as well as parenchymal and vestibulocochlear enhancement, compared with gradient-echo and spin-echo sequences.^{7–9}


The aim of this study was to assess findings on contrast-enhanced VW-MR imaging in a cohort of patients with SuS. To this end, we reviewed institutional electronic medical records (between July 1, 2017, and October 1, 2022) in search of patients with definite or probable SuS according to the criteria proposed by Kleffner et al,¹⁰ who had at least 1 contrast-enhanced VW-MR imaging study acquired at any stage of the disease. Of the 6 patients included, 4 had definite and 2 had probable SuS diagnoses (3 women and 3 men; mean age, 36.3 years; age range, 19–57 years). All patients were subject to extensive work-up to exclude other possible conditions such as demyelinating syndromes, encephalitis, and vasculitis. VW-MR images were evaluated blinded to clinical data, by a fourth-year resident (P.C.) and a neuroradiologist (H.C.) with >10 years' experience, who has read >130 VW-MR imaging studies in the past 5 years.

Main demographic, clinical, and VW-MR imaging findings are summarized in the Online Supplemental Data. MR imaging scanner characteristics and T1-weighted vessel wall imaging sequence parameters are summarized in the Online Supplemental Data. Contrast enhancement on VW-MR imaging was visible in 5 patients, with different patterns and distributions (Fig 1 and Online Supplemental Data). In 4 patients, multiple, short, linear foci of leptomeningeal interfoliar enhancement were observed in both cerebellar hemispheres (Fig 2). Additionally, contrast enhancement was more conspicuous on VW-MR imaging compared with 3D-FLAIR and 3D gradient-echo T1-weighted images (Online Supplemental Data). In one patient who had

Received December 7, 2022; accepted after revision January 30, 2023.

From the Diagnostic Imaging (P.C., A.G., H.C.) and Neurology Departments (M.M., M.P.F.), Fleni, Buenos Aires, Argentina.

Please address correspondence to Hernan Chaves, MD, Fleni, Montañeses 2325, Ciudad Autónoma de Buenos Aires (C1428AQK), Argentina; e-mail: hchaves@fleni.org.ar

 Indicates article with online supplemental data.

<http://dx.doi.org/10.3174/ajnr.A7801>

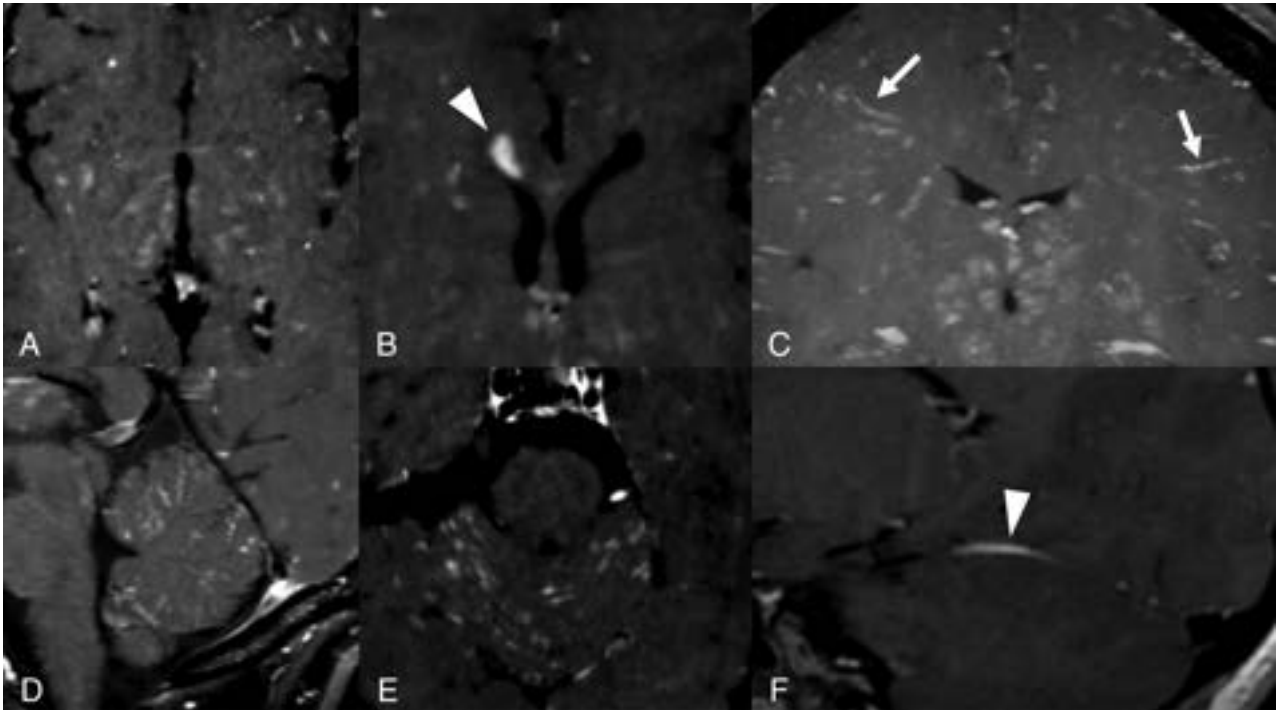


FIG 1. Different patterns of enhancement on VW-MR imaging: punctate (A), focal (*arrowhead*, B), perivascular (*arrows*, C), leptomeningeal (D and E), and pachymeningeal (*arrowhead*, F). Images A, B, D, and E correspond to patient 2, and C and F, to patient 1.

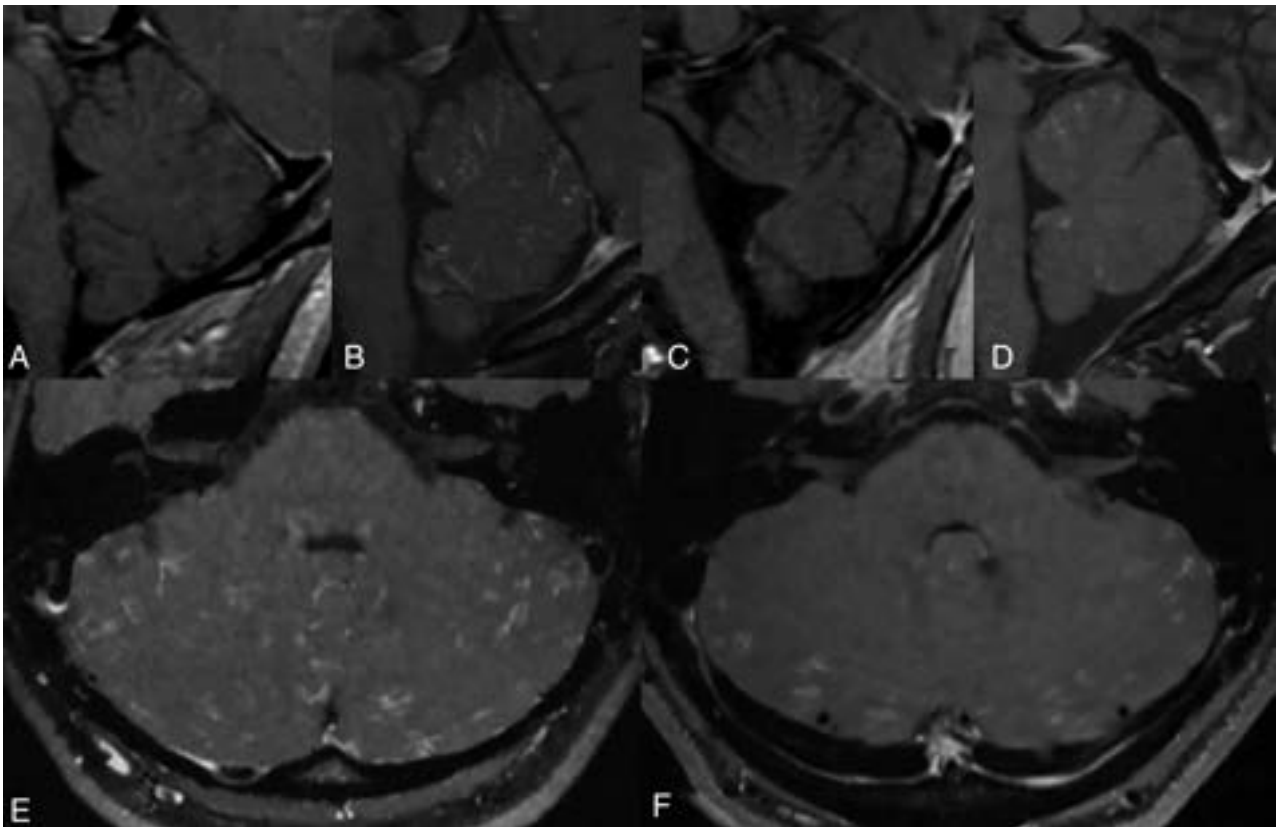


FIG 2. Interfoliar leptomeningeal enhancement on VW-MR imaging. Multiple thin, short, enhancing foci scattered along the folia of the cerebellar vermis and hemispheres. Patient 1 (A), patient 2 (B and E), patient 3 (C), and patient 6 (D and F).

treatment initiated before the MR imaging acquisition, no enhancement was detected, and in another patient, follow-up VW-MR imaging after 1 year of treatment showed complete remission of parenchymal and leptomeningeal enhancement observed at symptom onset (Online Supplemental Data).

DISCUSSION

Existing evidence describes classic neuroimaging features of SuS as white matter lesions, microinfarcts, and central callosal lesions. Gadolinium enhancement has also been considered a recurrent feature, presenting different patterns, including punctate or focal, and locations: perivascular, leptomeningeal, pachymeningeal, and cochleovestibular.^{11,12}

Although previous literature has demonstrated the higher reliability of contrast-enhanced FLAIR compared with contrast-enhanced T1, no study to date has examined the diagnostic performance of VW-MR imaging in patients with SuS.¹³⁻¹⁵ Only a limited number of reports have found that VW-MR imaging had higher sensitivity in distinguishing cases of SuS from other vascular conditions.^{11,12,16} Several authors have, however, described the greater sensitivity of VW-MR imaging compared with gradient-echo and spin-echo sequences for the detection of leptomeningeal and subtle parenchymal enhancement in other pathologies.⁷⁻⁹

Leptomeningeal enhancement is a recurrent feature of SuS. Most interesting, we detected a unique pattern of diffuse, infratentorial, interfoliar enhancement in 4 patients, not previously described in other conditions, consisting of multiple thin, short, enhancing foci scattered along the folia of the cerebellar vermis and hemispheres. Cerebellar leptomeningeal enhancement seen in meningitis or carcinomatosis differs from this pattern, tending to be more contiguous and/or thicker.

Additionally, a recent report by Baskin et al¹⁶ presented a case of gadolinium-enhancement resolution of VW-MR imaging after immunotherapy. We observed 2 similar cases, one with no enhancement on VW-MR imaging in a patient already receiving corticosteroid therapy and another in whom parenchymal and leptomeningeal enhancement resolved after immunosuppressive therapy.

No patient in this series or in other published reports showed arterial vessel wall enhancement, possibly because SuS affects small-caliber vessels (precapillary arterioles) not detected using current VW-MR imaging techniques.

Taken together, this evidence suggests that acute inflammation could be the pathologic substrate underlying VW-MR imaging findings, and leptomeningeal enhancement could represent a marker of disease activity. It remains unclear whether an association exists between this enhancement pattern and severity or even triggering of the disease.

On the basis of the increased sensitivity and presumed high specificity of VW-MR imaging, we believe that this imaging technique will improve both the SuS diagnosis and monitoring of treatment response during follow-up. Larger diagnostic accuracy studies will, however, be needed to confirm this hypothesis, given the limited number of patients included in our study.

Although evidence on VW imaging in SuS remains scarce, emerging data showing similar findings from different groups worldwide support the use of this sequence as a diagnostic tool for SuS.

Disclosure forms provided by the authors are available with the full text and PDF of this article at www.ajnr.org.

REFERENCES

1. Greco A, De Virgilio A, Gallo A, et al. **Susac's syndrome: pathogenesis, clinical variants and treatment approaches.** *Autoimmun Rev* 2014;13:814-21 CrossRef Medline
2. Susac JO, Egan RA, Rennebohm RM, et al. **Susac's syndrome: 1975-2005 microangiopathy/autoimmune endotheliopathy.** *J Neurol Sci* 2007;257:270-72 CrossRef Medline
3. Dörr J, Krautwald S, Wildemann B, et al. **Characteristics of Susac syndrome: a review of all reported cases.** *Nat Rev Neurol* 2013;9:307-16 CrossRef Medline
4. Marrodon M, Fiol MP, Correale J. **Susac syndrome: challenges in the diagnosis and treatment.** *Brain* 2021;145:858-71 CrossRef Medline
5. Rennebohm R, Susac JO, Egan RA, et al. **Susac's syndrome: update.** *J Neurol Sci* 2010;299:86-91 CrossRef Medline
6. Qiao Y, Steinman DA, Qin Q, et al. **Intracranial arterial wall imaging using three-dimensional high isotropic resolution black blood MRI at 3.0 Tesla.** *J Magn Reson Imaging* 2011;34:22-30 CrossRef Medline
7. Kato Y, Higano S, Tamura H, et al. **Usefulness of contrast-enhanced T1-weighted sampling perfection with application-optimized contrasts by using different flip angle evolutions in detection of small brain metastasis at 3T MR imaging: comparison with magnetization-prepared rapid acquisition of gradient echo imaging.** *AJNR Am J Neuroradiol* 2009;30:923-29 CrossRef Medline
8. Oh J, Choi SH, Lee E, et al. **Application of 3D fast spin-echo T1 black-blood imaging in the diagnosis and prognostic prediction of patients with leptomeningeal carcinomatosis.** *AJNR Am J Neuroradiol* 2018;39:1453-59 CrossRef Medline
9. Veiga M, Kuhweide R, Demaerel V, et al. **Labyrinthine enhancement on 3D black blood MR images of the brain as an imaging biomarker for cisplatin ototoxicity in (lung) cancer patients.** *Neuroradiology* 2021;63:81-90 CrossRef Medline
10. Kleffner I, Dörr J, Ringelstein M, et al; European Susac Consortium (EuSaC). **Diagnostic criteria for Susac syndrome.** *J Neurol Neurosurg Psychiatry* 2016;87:1287-95 CrossRef Medline
11. Yahyavi-Firouz-Abadi N, Kiczek M, Zeiler SR, et al. **Imaging features of Susac syndrome on high-resolution intracranial vessel wall MRI.** *Neurol Neuroimmunol Neuroinflamm* 2021;8:e994 CrossRef Medline
12. Lehman VT, Klaas JP, Makol A, et al. **High-resolution vessel wall imaging in Susac's syndrome.** *J Neurosurg Sci* 2019;63:235-36 CrossRef Medline
13. Coulette S, Lecler A, Saragoussi E, et al. **Diagnosis and prediction of relapses in Susac syndrome: a new use for MR postcontrast FLAIR leptomeningeal enhancement.** *AJNR Am J Neuroradiol* 2019;40:1184-90 CrossRef Medline
14. Bellanger G, Biotti D, Adam G, et al. **Leptomeningeal enhancement on post-contrast FLAIR images for early diagnosis of Susac syndrome.** *Mult Scler* 2022;28:189-97 CrossRef Medline
15. Engisch R, Titelbaum DS, Chilver-Stainer L, et al. **Susac's syndrome: leptomeningeal enhancement on 3D FLAIR MRI.** *Mult Scler* 2016;22:972-74 CrossRef Medline
16. Baskin J, Hardy TA, Law LY, et al. **Black blood MRI: endotheliopathy of Susac syndrome unmasked.** *Neurol Sci* 2021;42:325-27 CrossRef Medline

Identification of the Language Network from Resting-State fMRI in Patients with Brain Tumors: How Accurate Are Experts?

S.K. Gujar, K. Manzoor, J. Wongsripuemtet, G. Wang, D. Ryan, S. Agarwal, M. Lindquist, B. Caffo, J.J. Pillai, and H.I. Sair



ABSTRACT

BACKGROUND AND PURPOSE: Resting-state fMRI helps identify neural networks in presurgical patients who may be limited in their ability to undergo task-fMRI. The purpose of this study was to determine the accuracy of identifying the language network from resting-state-fMRI independent component analysis (ICA) maps.

MATERIALS AND METHODS: Through retrospective analysis, patients who underwent both resting-state-fMRI and task-fMRI were compared by identifying the language network from the resting-state-fMRI data by 3 reviewers. Blinded to task-fMRI maps, these investigators independently reviewed resting-state-fMRI ICA maps to potentially identify the language network. Reviewers ranked up to 3 top choices for the candidate resting-state-fMRI language map. We evaluated associations between the probability of correct identification of the language network and some potential factors.

RESULTS: Patients included 29 men and 14 women with a mean age of 41 years. Reviewer 1 (with 17 years' experience) demonstrated the highest overall accuracy with 72%; reviewers 2 and 3 (with 2 and 7 years' experience, respectively) had a similar percentage of correct responses (50% and 55%). The highest accuracy used ICA50 and the top 3 choices (81%, 65%, and 60% for reviewers 1, 2, and 3, respectively). The lowest accuracy used ICA50, limiting each reviewer to the top choice (58%, 35%, and 42%).

CONCLUSIONS: We demonstrate variability in the accuracy of blinded identification of resting-state-fMRI language networks across reviewers with different years of experience.

ABBREVIATIONS: BOLD = blood oxygen level–dependent; ICA = independent component analysis; rs = resting-state

Resting-state (rs) fMRI has emerged as a novel tool to analyze brain function. In contrast to traditional task-fMRI, no explicit task is required in rs-fMRI while blood oxygen level–dependent (BOLD) images are acquired. Owing to an assortment of naturally occurring fluctuations of BOLD activity in various regions of the brain, a set of intrinsic brain networks can be identified by examining spatially distinct, however temporally synchronous, BOLD signals at rest. The number of discrete brain networks is somewhat

arbitrary and depends on the specific threshold used to define a network; nevertheless, a relatively consistent set of major networks has been reliably demonstrated in many studies.¹


Although clinical use of rs-fMRI is currently not widespread, potentially partly due to the variability of brain networks when examined at the single-subject level,² there was considerable effort to translate this technique into clinical practice. Thus, the most promising use of rs-fMRI currently seems to be in the domain of presurgical brain mapping.³ While task-fMRI has been successfully used to identify critical brain regions for preoperative planning, task-fMRI requires compliance in performing behavioral paradigms necessary for determining brain activation. This compliance may be limited or absent in many cases, for example, in the pediatric population or in the elderly; in patients with language barriers, visual or hearing impairment, or cognitive/memory impairment that may preclude language task performance; or in those with physical debilitation limiting movement for performing motor tasks. Given the lack of a task, therefore, the use of rs-fMRI is attractive as an alternative technique to assess brain function. Furthermore, rs-fMRI may potentially require less time compared with task-fMRI to obtain comparable data.

Received October 28, 2021; accepted after revision January 4, 2023.

From the Division of Neuroradiology (S.K.G., K.M., J.W., D.R., S.A., J.J.P., H.I.S.), The Russell H. Morgan Department of Radiology and Radiological Science, Johns Hopkins University School of Medicine, Baltimore, Maryland; and Department of Biostatistics (G.W., M.L., B.C.), Department of Neurosurgery (J.J.P.), and The Malone Center for Engineering in Healthcare (H.I.S.), The Whiting School of Engineering, Johns Hopkins University, Baltimore, Maryland.

This work was supported by grant RSCH1420 from the grant program Radiological Society of North America (RSNA) Research & Education Foundation Carestream Health/RSNA Research Scholar Grant.

Please address correspondence to Haris I. Sair, MD, Johns Hopkins University School of Medicine, 600 North Wolfe St, Phipps B-112A, Baltimore, MD 21287; e-mail: hsair1@jhmi.edu; @hsairmd

 Indicates article with online supplemental data.
<http://dx.doi.org/10.3174/ajnr.A7806>

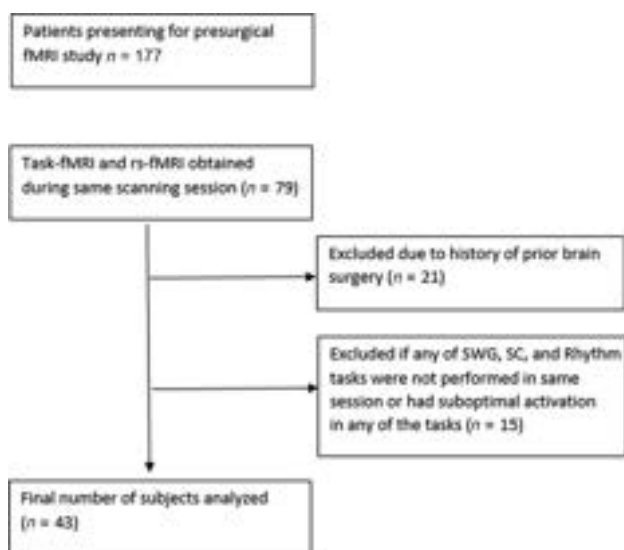


FIG 1. Flow diagram of inclusion and exclusion criteria. SWG indicates Silent Word Generation; SC, Sentence Completion.

As 1 example, rs-fMRI-derived motor networks have been shown to be comparable with motor regions activated during task-fMRI as well as motor regions identified during direct cortical stimulation.⁴ The concordance between rs-fMRI-derived language networks and task-fMRI-activated language regions is more variable. Earlier reports suggested moderate concordance;⁵ however, more recent reports have demonstrated high subject-level variability.^{6,7} While motor networks are relatively easily identified from rs-fMRI due to the relative invariance of the anatomic-functional relationship of the motor system across individuals, identification of the language network may be more challenging due to relatively high variance in localization of language areas across individuals⁸ and the similarity of elements of the language network to the spatial distribution of other networks such as the ventral attention network.⁹

If rs-fMRI is to be used as an alternative to task-fMRI, the accuracy of identification of the language network solely from rs-fMRI must be assessed when one is presented with multiple network correlation maps, ie, the output generated from commonly used methods of rs-fMRI analysis such as independent component analysis (ICA). While automated methods of network identification are currently being developed, we were interested in the ability of humans to correctly identify the language network. We examined the human accuracy of identifying subject-level rs-fMRI language networks using their task-fMRI language activation maps as the reference standard. We hypothesize that there is low accuracy in human identification of rs-fMRI language networks when language-related task-fMRI activation maps are unavailable.

MATERIALS AND METHODS

Participants

The radiology information system was interrogated for any patient who underwent fMRI for presurgical brain mapping between January 1, 2009, and July 1, 2015. Seventy-nine patients with intracranial neoplasms were identified for whom both language task-fMRI and rs-fMRI were available in the same

imaging session. Twenty-one patients had a history of an invasive intracranial procedure (surgery and/or biopsy) and were excluded to minimize confounding the effect of susceptibility. Because individual language paradigms commonly activate only subsets of the global language system, we included only patients who had completed 3 different language tasks (Silent Word Generation, Sentence Completion, and Rhyming) during the same session. Patients who had suboptimal activation on any 1 of the 3 language task-fMRIs, assessed subjectively as is routine in clinical fMRI cases, were excluded (15 patients). This exclusion was determined by lack of the expected localization of activation with excessive spurious activation in nonbrain regions with subject-specific statistical thresholding. After exclusion, data from 43 subjects were available for analysis (Fig 1).

Handedness

The Edinburgh Handedness Inventory was used to determine patient handedness.¹⁰

Imaging

Images were acquired on 3T Tim Trio MR imaging system (Siemens) using a 12-channel head matrix coil. For both task-fMRI and rs-fMRI, T2*-weighted BOLD images were acquired using 2D gradient-echo echo-planar imaging: TR = 2000 ms, TE = 30 ms, flip angle = 90°, FOV = 24 cm, acquisition matrix = 64 × 64 × 33, section thickness = 4mm, section gap = 1mm, interleaved acquisition. Instructions for rs-fMRI were the following: Keep your eyes closed, don't move, and don't think of anything in particular. One hundred eighty volumes were acquired for rs-fMRI (6 minutes). We also obtained 3D T1-weighted structural images: TR = 2300 ms, TI = 900 ms, TE = 3.5 ms, flip angle = 9°, FOV = 24 cm, acquisition matrix = 256 × 256 × 176, section thickness = 1 mm.

Task-fMRI Paradigms

As is routine at our institution, we instructed the patients and performed practice sessions outside the scanner before fMRI to ensure that patients understood the tasks. Real-time fMRI maps were monitored by the neuroradiologist administering the study to assess global data quality. Any task with suboptimal activation assessed subjectively was repeated per our protocol; for final analysis, the single best run of each task was chosen. The Prism Software Suite was used for stimulus presentation (Prism Clinical Imaging). A block design of either 30 (rhyming) or 20 (Silent Word Generation, Sentence Completion) seconds of alternative tasks and control blocks was used for an imaging time of 3 (Rhyming) or 4 minutes (Silent Word Generation, Sentence Completion).

Image Processing and Analysis

Statistical Parametric Mapping (SPM) Version 8 (<http://www.fil.ion.ucl.ac.uk/spm/software/spm12>) and custom Matlab (MathWorks) scripts were used to process the fMRI.

Task-fMRI

Task-fMRI underwent slice timing correction followed by motion correction. Images were normalized to a Montreal Neurological Institute-152 template and spatially smoothed using

a 6-mm full width at half maximum Gaussian kernel. A general linear model analysis was performed using a canonical hemodynamic response function convolved with the boxcar function for each task, without using model derivatives or global intensity normalization. A 128-second high-pass filter was used. An autoregressive was used to account for temporal autocorrelations. No confound matrix was used. A contrast design matrix set to detect activation across all 3 tasks compared with rest was used for each subject. SPM T-contrast maps were generated without clustering or multiple comparison correction, which is the approach that we use routinely for clinical language mapping because clustering is usually not necessary at the selected thresholds and correction for multiple comparisons would be too stringent for such single-subject language-activation analysis.

Rs-fMRI

Rs-fMRI underwent slice timing correction followed by motion correction. The ArtRepair toolbox (https://www.nitrc.org/projects/art_repair/)¹¹ was then used to detect volumes with large shifts in global average signal intensity related to scan-to-scan motion; both the outlier volumes and additional volumes recommended for de-weighting were tagged for subsequent removal from analysis (ie, for “scrubbing”). Rs-fMRI was linearly detrended, and following coregistration of rs-fMRI and T1-weighted images, physiologic nuisance regression of rs-fMRI was performed using component-based noise correction (CompCor method)¹² using signal extracted from eroded white matter and CSF masks. After bandpass filtering from 0.01 to 0.1 Hz, smoothing was performed with a 6-mm full width at half maximum Gaussian kernel. Finally, images tagged by ArtRepair were removed (scrubbed) from the rs-fMRI volumes.

The Group Independent Component Analysis of fMRI Toolbox (GIFT, Medical Image Analysis Lab, <http://mialab.mrn.org/software/gift>) was used to generate ICA maps for each subject using 20 (ICA20) and 50 (ICA50) target components, using the InfoMax algorithm with ICASSO¹³ set at 5 repeats. The language network was identified by first sorting the ICA components using multiple regression in GIFT, with the task-fMRI SPM T-maps as the reference template. Then, the component that demonstrated the highest spatial overlap with the task-fMRI maps localized to Broca and Wernicke activation was selected as the rs-fMRI language network. Of note, in all cases, there was 1 ICA component that best represented the primary language network for both ICA orders. This ICA component was labeled the rs-fMRI language network map for each subject.

Rs-fMRI Language Network Identification

Three participants independently reviewed the rs-fMRI ICA maps to identify the potential language network. All were blinded to the task-fMRI activation maps. The reviewers ranged in fMRI experience: 17 years (neuroradiologist), 7 years (neuroradiologist), and 2 years (neuroimaging postdoctoral researcher). Each of the raters had similar previous exposure to rs-fMRI and had experience in interpreting rs-fMRI network maps. Images were presented to each reviewer using the orthogonal viewer in FSLView (Version 3.1; <https://fsl.fmrib.ox.ac.uk/fsl/fslwiki/FslView/UserGuide>) with each subject’s rs-fMRI maps overlaid on their T1-weighted images. Review was performed independently

for ICA20 and ICA50. The reviewers were allowed to modify image contrast and thresholds. Reviewers ranked up to 3 top choices for the candidate rs-fMRI language map, as well as their confidence in their assessment ranging from 1 (highly confident) to 5 (not confident).

Statistical Tests

We aimed to discover the association between the probability of correct identification of the language network and some potential factors including the reviewers, ICA type, and each selection scenario.

We modeled this study using generalized linear mixed-effects models similar to studies of measurement reproducibility. Y_{ijkl} denoted the correctness of identification for subject i by reviewer j using ICA type k and top choices l . Y_{ijkl} takes values 1 or 0, indicating whether the identification is correct. The cross-sectional structure motivates the generalized mixed-effects model as follows:

$$\text{logit}(P(Y_{ijkl} = 1|u_i)) = \alpha + u_i + \beta_j + x_k + z_l + h_i \quad (1),$$

where the u_i is mutually independent normally distributed, $N(0, \sigma^2)$, random intercepts. The covariate β_j represents the fixed effect of reviewer j . The effect of ICA20 and ICA50 is denoted by x_1 and x_2 , respectively. The covariates z_1, z_2, z_3 denote the effect of 3 different selection scenarios (top 1 choice, top 2 choices, and top 3 choices). The term h_i denotes the handedness for subject i . To ensure the identifiability of the model, we introduced constraints $\beta_1 = 0, x_1 = 0, z_1 = 0$.

We performed likelihood ratio tests to investigate interaction terms between each pair of the fixed effects. The resulting tests were nonsignificant. We also found that the effect of ICA type and handedness does not help to improve the model fit, so the associated terms were excluded. In other words, there was no significant effect for the ICA type and handedness, given the other variables. We also performed the test for necessity of random intercept effect ($H_0 : \sigma^2 = 0$ versus $H_1 : \sigma^2 > 0$) by parametric bootstrapping. We found improvement in model fit (bootstrapped P value estimated to be 0) by fitting the model, accounting for the subject-specific random effects.

To further explore the association between the probability of correct identification and the confidence rating or the location of lesions, adjusted for the effect of each reviewer, ICA types, and selection scenarios, we fit a similar generalized mixed-effects model, accounting for these effects. Tumor location was recorded for involvement of the frontal lobe, parietal lobe, temporal lobe, occipital lobe, or deep (subcortical) areas, with additional specific tags for involvement of the left inferior frontal gyrus and right inferior frontal gyrus (either of them potentially involving the Broca areas) and of the left posterior temporal lobe and right posterior temporal lobe (either of them potentially involving the Wernicke areas).

The final model we fit is the following:

$$\text{logit}(P(Y_{ijkl} = 1|u_i)) = \alpha + u_i + \beta_j + z_l \quad (2),$$

where u_i follows the normal distribution, $N(0, \sigma^2)$, independently. This is the simplified version of model 1 after a sequence of

Table 1: Correctness percentage by reviewer and ICA target component

Reviewer	ICA Component	Top Choices	No. (% Correctness)	95% CIs
1	Overall		72.09%	66.12%–77.39%
1	20	Top 1	28 (65.12%)	49.01%–78.55%
1	20	Top 2	32 (74.42%)	58.53%–85.96%
1	20	Top 3	33 (76.74%)	61.00%–87.72%
1	50	Top 1	25 (58.14%)	42.21%–72.63%
1	50	Top 2	33 (76.74%)	61.00%–87.72%
1	50	Top 3	35 (81.40%)	66.08%–91.08%
2	Overall		50.39%	44.13%–56.63%
2	20	Top 1	16 (37.21%)	23.39%–53.28%
2	20	Top 2	23 (53.49%)	37.83%–68.53%
2	20	Top 3	24 (55.81%)	40.01%–70.59%
2	50	Top 1	15 (34.88%)	21.45%–50.99%
2	50	Top 2	24 (55.81%)	40.01%–70.59%
2	50	Top 3	28 (65.12%)	49.01%–78.55%
3	Overall		55.04%	48.74%–61.18%
3	20	Top 1	22 (51.16%)	35.68%–66.44%
3	20	Top 2	26 (60.47%)	44.45%–74.63%
3	20	Top 3	26 (60.47%)	44.45%–74.63%
3	50	Top 1	18 (41.86%)	27.37%–57.79%
3	50	Top 2	24 (55.81%)	40.01%–70.59%
3	50	Top 3	26 (60.47%)	44.45%–74.63%

Table 2: Difference in correctness percentages comparing the top choice with the top 2 and 3 choices

Reviewer	ICA	Pair Comparison	Number (Percentage Differences)	P Value ^a
1	20	Top 1 vs top 2	4 (8.30%)	.063
	20	Top 1 vs top 3	5 (11.63%)	.031 ^a
	20	Top 2 vs top 3	1 (2.33%)	.500
1	50	Top 1 vs top 2	8 (18.60%)	.004 ^a
	50	Top 1 vs top 3	10 (23.26%)	<.001 ^a
	50	Top 2 vs top 3	2 (4.65%)	.250
2	20	Top 1 vs top 2	7 (16.28%)	.008 ^a
	20	Top 1 vs top 3	8 (18.60%)	.004 ^a
	20	Top 2 vs top 3	1 (2.32%)	.500
2	50	Top 1 vs top 2	9 (20.93%)	.002 ^a
	50	Top 1 vs top 3	13 (30.23%)	<.001 ^a
	50	Top 2 vs top 3	4 (9.30%)	.063
3	20	Top 1 vs top 2	4 (9.30%)	.063
	20	Top 1 vs top 3	4 (9.30%)	.063
	20	Top 2 vs top 3	0 (0.00%)	1.0
3	50	Top 1 vs top 2	6 (13.95%)	.016 ^a
	50	Top 1 vs top 3	8 (18.60%)	.004 ^a
	50	Top 2 vs top 3	2 (4.65%)	.250

^a P value from the 1-sided sign test.

tests, as described above and will be used for inference and interpretation. From model 2, we can see that the probability of correct identification is associated with the subject-specific effect, reviewer-specific effect, and the selection scenarios.

A conditional logistic regression model given the subject-specific effect was constructed to explore the association between the probability of correct identification and the confidence rating adjusted for the effect of each reviewer and ICA type. No significant association resulted. To measure the concordance of rs-fMRI language network map identification among and within the 3 reviewers, we calculated intrarater and interrater κ statistics.

All statistical analyses were performed in R statistical and computing software, Version 3.6.2 (<http://www.r-project.org/>).

RESULTS

Patients included 29 men and 14 women with a mean age of 41 years (minimum 18 and maximum 69 years). Thirty-three patients are right-handed, 8 were left-handed, and 2 were ambidextrous.

Tables 1 and 2 illustrate the marginal association between correctness percentage and the reviewers, ICA type, and selection scenarios. Table 1 and the Online Supplemental Data demonstrate the percentage correct for each reviewer for ICA20 and ICA50, assessing their top choice (1), the top 2 choices (1 + 2), or the top 3 choices (1 + 2 + 3), with Fig 2 graphically depicting the overall comparisons. Reviewer 1, with 17 years of fMRI experience, demonstrated the highest overall accuracy with 72% (95% CI, 66.1%–77.4%) correct responses across all conditions. Reviewers 2 and 3, with 2 and 7 years of experience respectively, had overall similar percentages of correct responses (50% [95% CI, 44.1%–56.6%] and 55% [95% CI, 48.7%–61.2%]). For each reviewer, the highest accuracy was obtained using ICA50 and top 3 choices (81%, 65%, and 60% for reviewers 1, 2, and 3, respectively). Conversely, the lowest accuracy was also obtained using ICA50, however limiting each reviewer to the top choice (58%, 35%, and 42%).

Significant differences in accuracy were seen between selecting only the top choice versus selecting the top 3 choices (Table 2), with the exception of ICA20 for reviewer 3. In both ICA conditions and across all raters, no significant difference in accuracy was seen between the selection of the top 2 choices versus the top 3 choices.

When we compared the single top choice with the top 2 choices, mixed findings were noted between ICA orders and raters. Across the raters, inclusion of 3 choices compared with 1 choice improved the accuracy by 13% for ICA and 20% and 24% for ICA50. When examining the converse problem, whether ICA order increases accuracy, no significant difference was found for any of the reviewers in any of the 3 choice conditions (Online Supplemental Data). Figure 3 demonstrates, averaged across all subjects, the spatial distribution of task-fMRI language activation, correctly selected rs-fMRI language component, and incorrectly selected rs-fMRI.

κ statistics (Table 3) demonstrated an overall fair concordance between reviewer 1 and reviewers 2 and 3 ($\kappa = 0.35$ –0.40).

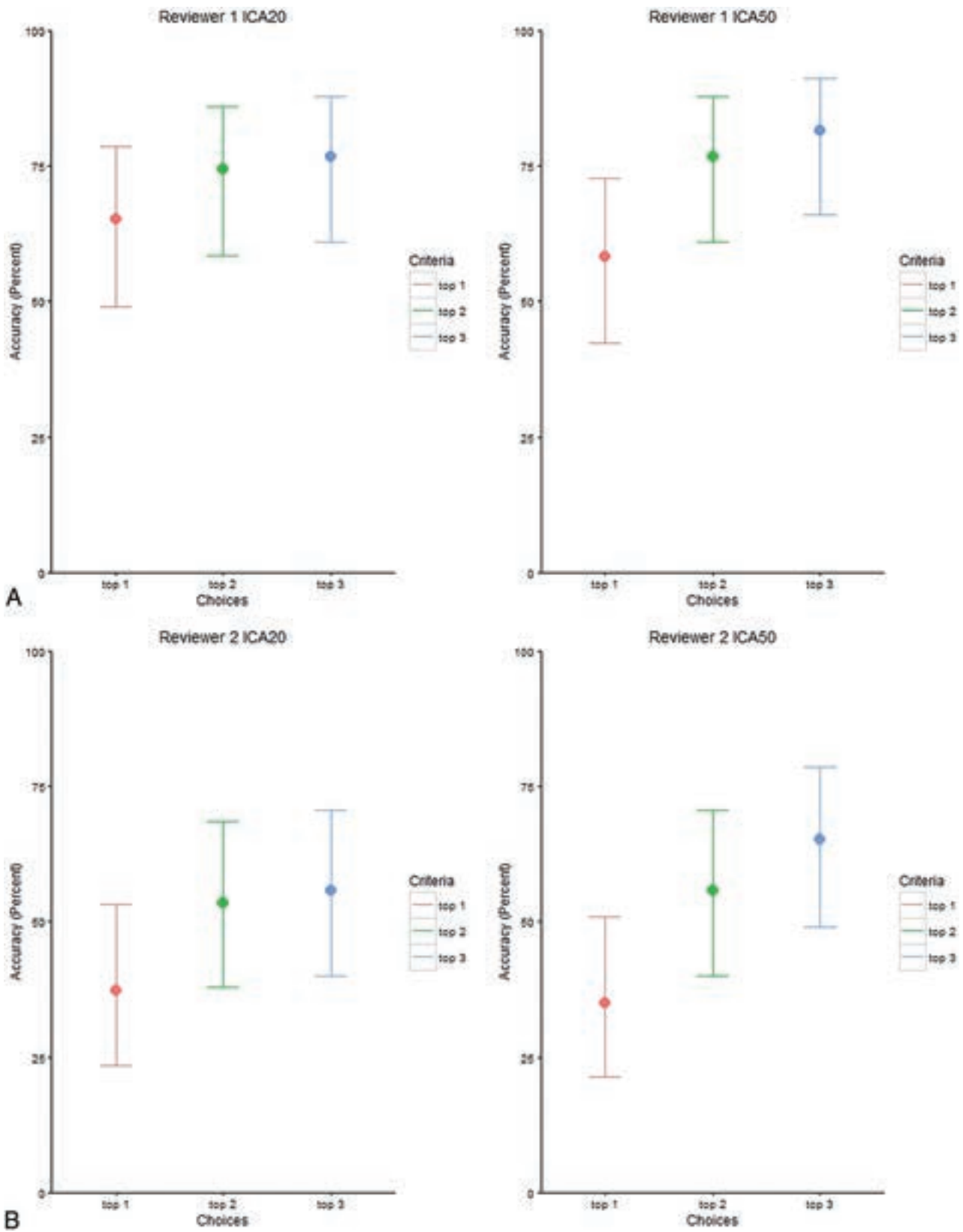


FIG 2. Correctness percentage by reviewer and ICA target components with their corresponding confidence intervals.

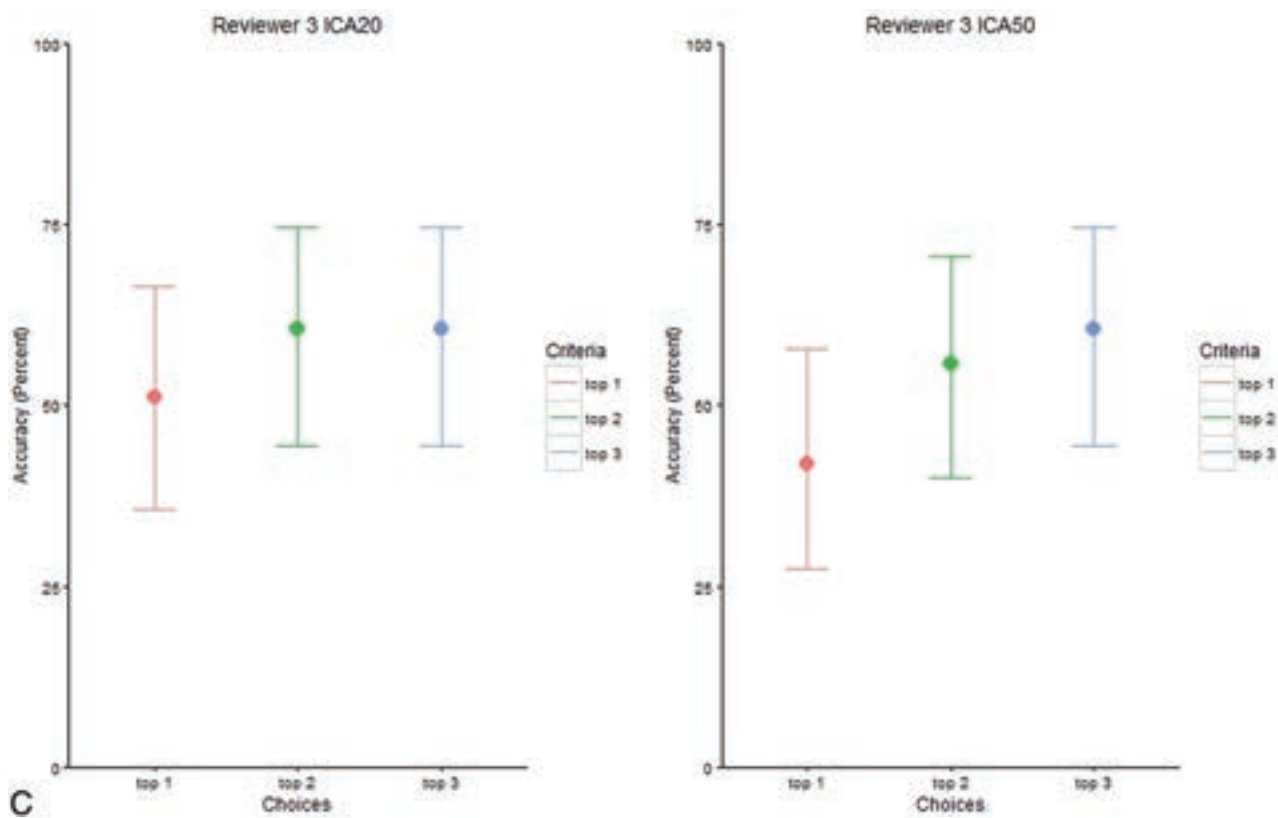


FIG 2. Continued.

Poor concordance was observed between reviewers 2 and 3 ($\kappa = 0.16$). When we limited analysis to the top choice, again reviewer 1 demonstrated fair concordance with reviewers 2 and 3 ($\kappa = 0.21$ – 0.47), and there was poor concordance between reviewers 2 and 3 ($\kappa = 0.028$). Similar findings were seen when analyzing the concordance of any of the top 3 choices (reviewer 1 versus 2 and 3 [$\kappa = 0.31$ – 0.42], and reviewer 2 versus 3 [$\kappa = 0.12$]).

On the basis of model 2, conditional on subject, the odds of correct identification for reviewer 2 were 0.26 (95% CI, 0.17–0.41) times the odds of reviewer 1, given the same selection scenario. Similarly, the OR of reviewer 3 against reviewer 1 was 0.34 (95% CI, 0.22–0.53), and the OR of reviewer 3 against reviewer 2 was 1.31 (95% CI, 0.86–1.99). Note that there was no significant difference between odds of reviewer 2 and reviewer 3, given the same selection scenario conditional on the subject.

From the same model, the odds of correct identification for selecting the top 2 choices were 2.39 (95% CI, 1.56–3.69) times the odds of the top 1 choice, given the same reviewer and conditional on subject. The OR of selecting the top 3 choices against the top 1 choice was 3.05 (95% CI, 1.98–4.76), and the OR of including the top 3 choices against the top 2 was 1.28 (95% CI, 0.83–1.98). The difference between the odds of selecting the top 3 and top 2 choices is not statistically significant.

Regarding the association between the probability of correct identification and the confidence rating or the location of lesions, the likelihood ratio test informs us that there is no

significant effect by the confidence rating and lesion locations (P value = .365).

DISCUSSION

Rs-fMRI is being increasingly used in the setting of presurgical brain mapping.^{3,14,15} Despite the potential subject level variability of data accuracy,^{6,7} nevertheless in select cases, rs-fMRI may be considered a viable option for presurgical brain mapping; indeed, at least 1 institution has included rs-fMRI in their presurgical brain mapping paradigm without obtaining task-fMRI.^{3,16} For this purpose, obtaining highly accurate intrinsic brain network data is paramount to avoid adverse outcomes following surgery.

Two widely used methods of rs-fMRI analysis are associated with unique limitations. Seed-based analysis necessitates placing ROIs in selected areas of the brain, depending on the network to be defined. The advantage of this method is that anatomy can guide placement of ROIs to target specific networks if clear landmarks for ROI placement are available, such as for the motor network. However, in the setting of presurgical language mapping, several confounds appear. First, primary language areas are more widely distributed anatomically across subjects;⁸ thus, placement of an ROI in the inferior portion of the pars opercularis, for example, may work for 1 patient but not another. Second, often there are anatomic distortions in expected language regions in patients with large brain lesions, making it difficult to determine the correct

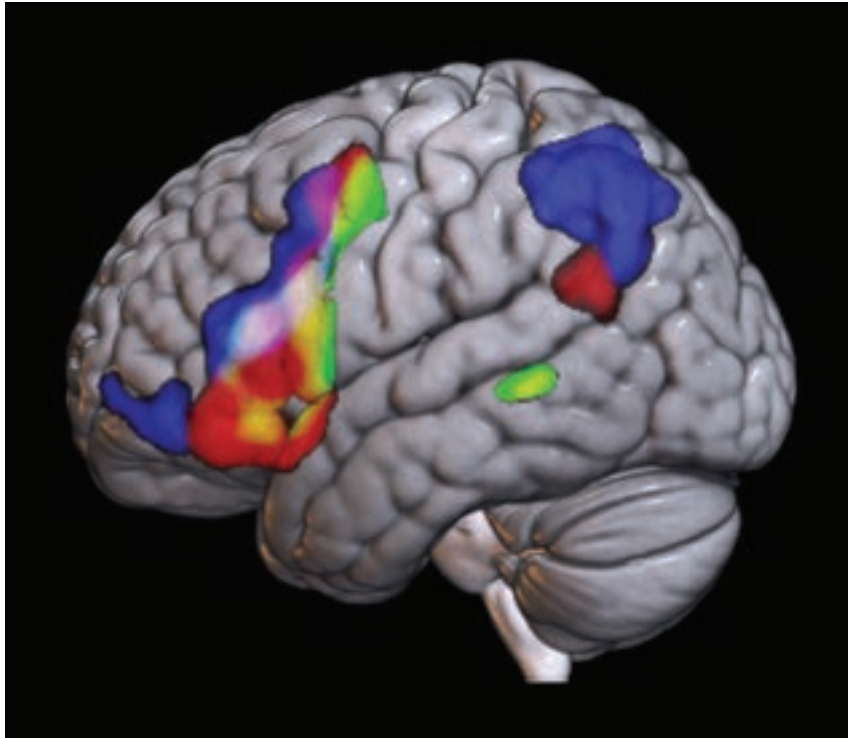


FIG 3. Comparison of task- versus rs-fMRI averaged across subjects. Green denotes average task-fMRI activation of the language system across all subjects. Red denotes the average spatial map of the rs-fMRI component correctly selected across subjects by all reviewers. Blue represents the average spatial map of the incorrectly selected rs-fMRI component across subjects by all reviewers. Overlays are additive: Yellow denotes overlapping voxels between green (task-fMRI) and red (correct rs-fMRI component). The white area in the inferior frontal gyrus along the inferior frontal sulcus denotes overlap across task-fMRI, incorrect rs-fMRI, and correct rs-fMRI. While some overlap is noted here, which may be a function of spatial smoothing, there is a clear distinction between the correct rs-fMRI versus incorrect rs-fMRI distribution.

Table 3: Interrater (between reviewers) κ statistic by top choice groups

Reviewer	1	2	3
Overall			
1	1.0	0.35	0.40
2	0.35	1.0	0.16
3	0.40	0.16	1.0
Top choice			
1	1.0	0.47	0.21
2	0.47	1.0	0.028
3	0.21	0.028	1.0
Top 2 choices			
1	1.0	0.37	0.37
2	0.37	1.0	0.27
3	0.37	0.27	1.0
Top 3 choices			
1	1.0	0.31	0.42
2	0.31	1.0	0.12
3	0.42	0.12	1.0

anatomic landmarks. Damage to primary language regions due to tumor infiltration or prior surgery may also cause reorganization of language networks,^{17,18} further limiting accurate ROI placement. Finally, neurovascular uncoupling may adversely

affect seed placement due to lack of expected BOLD fluctuations in network subregions.¹⁹

The alternative is to use a data-driven approach such as ICA. Here, rs-fMRI time-series typically at the voxel level is separated into maximally independent components. The resultant component maps each may represent one of the various intrinsic brain networks, or nuisance. To determine relevant maps, one may use automated methods such as template-matching; however as is the case with seed-based analysis in patients with large lesions, anatomic distortion or network reorganization may impede its accuracy. More commonly, relevant network maps are selected by visual inspection, taking into consideration potential changes in network topology.

Aside from (however related to) the problem of choosing the ideal number of target components in ICA (ie, ICA order), for which there is no clear paradigm,²⁰ the issue of categorizing networks derived from ICA can be especially challenging due to several factors. First, network maps do not necessarily break evenly across components, and using low ICA orders may cause merging of one or more networks (or even networks and noise), and using high ICA orders may result

in fragmentation of networks into subnetworks. For our study, using task-fMRI maps as the target, we found that a single component for ICA20 and ICA50 best matched the target, with no fragmentation at these levels of ICA orders. The general range of optimum ICA order is affected by several technical factors, including hardware, length of the scan, and postprocessing. The rs-fMRI output maps, therefore, may need to be evaluated in each unique experimental condition to optimize the general range of target ICA orders. At our institution for example, an ICA order of 50 appears to be ideal for use when rs-fMRI is included as part of the presurgical brain mapping protocol in addition to task-fMRI, the scanning of which is limited to 1 scanner. However, empirically, a higher target order has been necessary when the rs-fMRI protocol is used on a different scanner, at least partially due to differences in contrast to noise.

Despite having a relatively long clinical and research fMRI career of 17 years, the first rater's accurate identification of rs-fMRI language maps peaked at 72% across any condition; this fact should be noted by those who are using this method for research or clinical reasons. Limiting the choice to the best guess decreased accuracy to about 65%. With fewer years of

experience, the accuracy was overall not better than chance (50%). Caution, therefore, is advised when identification of language maps is a critical component of management, for example, to decide on an operative approach or the potential extent of tumor resection. Confirmation of the selected language component with additional methods (eg, task-fMRI or intraoperative mapping) would be critical.

Automated methods of network identification may, therefore, be necessary when task-fMRI is not available. Using a multilayer perceptron (a neural network), Mitchell et al²¹ demonstrated that reliable intrinsic brain networks could be characterized in 13 patients with distorted brain anatomy with electrocortical stimulation as the criterion standard. Further validation in larger sample sizes would be necessary to ensure that methods such as this have high reliability and reproducibility. Finally, a measure of inherent reliability of the rs-fMRI maps would be important to develop.

There are several limitations in our study. We used task-fMRI as the reference standard for ground truth, due to a lack of availability of consistent intraoperative mapping. While intraoperative mapping with direct cortical stimulation itself has specific limitations such as a potential lack of specificity, generally, it is considered superior to task-fMRI for functional localization.

We limited ICA orders to 20 and 50 empirically, on the basis of the optimum number of target components based on prior analysis of this data set. In this specific case, the language component was seen in a single component for both ICA20 and ICA50 as noted above. However, especially in lower ICA orders, rs-fMRI language networks may have been mixed with other networks, confounding the labeling of the ICA component to the correct network. In the setting of using data-driven approaches to ICA estimation (eg, as is implemented in the MELODIC tool in FSL, <https://fsl.fmrib.ox.ac.uk/fsl/fslwiki/MELODIC>) or setting the ICA order to an arbitrary higher number, mixing (due to low order) or fragmentation (due to higher order) may result in greater challenges in detecting the language network.

Finally, while potential distortion of language networks was addressed in this study, the contribution of technical and physiologic factors that result in further deviation of the networks from the expected appearance could introduce further difficulty in identification of the network. For example, the presence of hemorrhage or prior surgery may result in susceptibility artifacts masking certain components of the network. Similar loss of detection of network subcomponents may occur in the presence of neurovascular uncoupling.

CONCLUSIONS

We demonstrate the variability of the accuracy of blinded identification of rs-fMRI language networks across raters and different years of fMRI experience, using task-fMRI language activation maps as the reference. In addition to rs-fMRI-based brain mapping, additional confirmatory methods to supplement this information such as through task-fMRI or intraoperative stimulation may be necessary. Further work is needed to

determine the diagnostic utility of rs-fMRI using a more reliable criterion standard.

Disclosure forms provided by the authors are available with the full text and PDF of this article at www.ajnr.org.

REFERENCES

1. Barkhof F, Haller S, Rombouts SA. **Resting-state functional MR imaging: a new window to the brain.** *Radiology* 2014;272:29–49 CrossRef Medline
2. Airan RD, Vogelstein JT, Pillai JJ, et al. **Factors affecting characterization and localization of interindividual differences in functional connectivity using MRI.** *Hum Brain Mapp* 2016;37:1986–97 CrossRef Medline
3. Lee MH, Miller-Thomas MM, Benzinger TL, et al. **Clinical resting-state fMRI in the preoperative setting: are we ready for prime time?** *Top Magn Reson Imaging* 2016;25:11–18 CrossRef Medline
4. Qiu T, Yan C, Tang W, et al. **Localizing hand motor area using resting-state fMRI: validated with direct cortical stimulation.** *Acta Neurochir (Wien)* 2014;156:2295–302 CrossRef Medline
5. Tie Y, Rigolo L, Norton IH, et al. **Defining language networks from resting state fMRI for surgical planning: a feasibility study.** *Hum Brain Mapp* 2014;35:1018–30 CrossRef Medline
6. Sair HI, Yahyavi-Firouz-Abadi N, Calhoun VD, et al. **Presurgical brain mapping of the language network in patients with brain tumors using resting-state fMRI: comparison with task fMRI.** *Hum Brain Mapp* 2016;37:913–23 CrossRef Medline
7. Cochereau J, Deverdun J, Herbet G, et al. **Comparison between resting state fMRI networks and responsive cortical stimulations in glioma patients.** *Hum Brain Mapp* 2016;37:3721–32 CrossRef Medline
8. Sanai N, Mirzadeh Z, Berger MS. **Functional outcome after language mapping for glioma resection.** *N Engl J Med* 2008;358:18–27 CrossRef Medline
9. Corbetta M, Patel G, Shulman GL. **The reorienting system of the human brain: from environment to theory of mind.** *Neuron* 2008;58:306–24 CrossRef Medline
10. Oldfield RC. **The assessment and analysis of handedness: the Edinburgh Inventory.** *Neuropsychologia* 1971;9:97–113 CrossRef Medline
11. Mazaika P, Hoefft F, Glover G, et al. **Methods and software for fMRI analysis of clinical subjects.** *Neuroimage* 2009;47:S58 CrossRef
12. Behzadi Y, Restom K, Liau J, et al. **A component based noise correction method (CompCor) for BOLD and perfusion based fMRI.** *Neuroimage* 2007;37:90–101 CrossRef Medline
13. Himberg J, Hyvärinen A, Esposito F, et al. **Validating the independent components of neuroimaging time series via clustering and visualization.** *Neuroimage* 2004;22:1214–22 CrossRef Medline
14. Hsu A, Chen HS, Hou P, et al. **Presurgical resting-state functional MRI language mapping with seed selection guided by regional homogeneity.** *Magn Reson Med* 2020;84:375–83 CrossRef Medline
15. Leuthardt EC, Allen M, Kamran M, et al. **Resting-state blood oxygen level-dependent functional MRI: a paradigm shift in preoperative brain mapping.** *Stereotact Funct Neurosurg* 2015;93:427–39 CrossRef Medline
16. Leuthardt EC, Guzman G, Bandt SK, et al. **Integration of resting state functional MRI into clinical practice: a large single institution experience.** *PLoS One* 2018;13:e0198349 CrossRef Medline
17. Southwell DG, Hervey-Jumper SL, Perry DW, et al. **Intraoperative mapping during repeat awake craniotomy reveals the functional plasticity of adult cortex.** *J Neurosurg* 2016;124:1460–69 CrossRef Medline

18. Wang N, Zeng W, Chen L. **SACICA: a sparse approximation coefficient-based ICA model for functional magnetic resonance imaging data analysis.** *J Neurosci Methods* 2013;216:49–61 CrossRef Medline
19. Agarwal S, Sair HI, Airan R, et al. **Demonstration of brain tumor-induced neurovascular uncoupling in resting-state fMRI at ultrahigh field.** *Brain Connect* 2016;6:267–72 CrossRef Medline
20. Hui M, Li J, Wen X, et al. **An empirical comparison of information-theoretic criteria in estimating the number of independent components of fMRI data.** *PLoS One* 2011;6:e29274 CrossRef Medline
21. Mitchell TJ, Hacker CD, Breshears JD, et al. **A novel data-driven approach to preoperative mapping of functional cortex using resting-state functional magnetic resonance imaging.** *Neurosurgery* 2013;73:969–82; discussion 982–83 CrossRef Medline

Reconstruction of the Corticospinal Tract in Patients with Motor-Eloquent High-Grade Gliomas Using Multilevel Fiber Tractography Combined with Functional Motor Cortex Mapping

A. Zhylyka, N. Sollmann, F. Kofler, A. Radwan, A. De Luca, J. Gempt, B. Wiestler, B. Menze, A. Schroeder, C. Zimmer, J.S. Kirschke, S. Sunaert, A. Leemans, S.M. Krieg, and J. Pluim



ABSTRACT

BACKGROUND AND PURPOSE: Tractography of the corticospinal tract is paramount to presurgical planning and guidance of intraoperative resection in patients with motor-eloquent gliomas. It is well-known that DTI-based tractography as the most frequently used technique has relevant shortcomings, particularly for resolving complex fiber architecture. The purpose of this study was to evaluate multilevel fiber tractography combined with functional motor cortex mapping in comparison with conventional deterministic tractography algorithms.

MATERIALS AND METHODS: Thirty-one patients (mean age, 61.5 [SD, 12.2] years) with motor-eloquent high-grade gliomas underwent MR imaging with DWI (TR/TE = 5000/78 ms, voxel size = $2 \times 2 \times 2$ mm³, 1 volume at $b = 0$ s/mm², 32 volumes at $b = 1000$ s/mm²). DTI, constrained spherical deconvolution, and multilevel fiber tractography-based reconstruction of the corticospinal tract within the tumor-affected hemispheres were performed. The functional motor cortex was enclosed by navigated transcranial magnetic stimulation motor mapping before tumor resection and used for seeding. A range of angular deviation and fractional anisotropy thresholds (for DTI) was tested.

RESULTS: For all investigated thresholds, multilevel fiber tractography achieved the highest mean coverage of the motor maps (eg, angular threshold = 60°; multilevel/constrained spherical deconvolution/DTI, 25% anisotropy threshold = 71.8%, 22.6%, and 11.7%) and the most extensive corticospinal tract reconstructions (eg, angular threshold = 60°; multilevel/constrained spherical deconvolution/DTI, 25% anisotropy threshold = 26,485 mm³, 6308 mm³, and 4270 mm³).

CONCLUSIONS: Multilevel fiber tractography may improve the coverage of the motor cortex by corticospinal tract fibers compared with conventional deterministic algorithms. Thus, it could provide a more detailed and complete visualization of corticospinal tract architecture, particularly by visualizing fiber trajectories with acute angles that might be of high relevance in patients with gliomas and distorted anatomy.

ABBREVIATIONS: ADT = angular deviation threshold; CSD = constrained spherical deconvolution; CST = corticospinal tract; FAT = fractional anisotropy threshold; FOD = fiber orientation distribution; MLFT = multilevel fiber tractography; nTMS = navigated transcranial magnetic stimulation

Gliomas are the most prevalent malignant brain tumors in adults, and particularly anaplastic astrocytoma and glioblastoma as representatives of high-grade gliomas have poor prognoses.¹⁻³

Contemporary treatment combines neurosurgical tumor resection with extended focal radiation therapy and adjuvant chemotherapy.⁴⁻⁶ Specifically, a maximum extent of resection correlates to

Received May 15, 2022; accepted after revision January 17, 2023.

From the Department of Biomedical Engineering (A.Z., J.P.), Eindhoven University of Technology, Eindhoven, The Netherlands; Department of Diagnostic and Interventional Radiology (N.S.), University Hospital Ulm, Ulm, Germany; Helmholtz AI (F.K.), Helmholtz Zentrum Munich, Munich, Germany; Department of Diagnostic and Interventional Neuroradiology (N.S., F.K., B.W., C.Z., J.S.K.), School of Medicine, Klinikum rechts der Isar, TUM-Neuroimaging Center (N.S., C.Z., J.S.K., S.M.K.), Klinikum rechts der Isar, Image-Based Biomedical Modeling (F.K., B.M.), Department of Informatics, TranslaTUM (F.K., B.W.), Central Institute for Translational Cancer Research, and Department of Neurosurgery (J.G., A.S., S.M.K.), School of Medicine, Klinikum rechts der Isar, Technical University of Munich, Munich, Germany; Department of Radiology and Biomedical Imaging (N.S.), University of California, San Francisco, San Francisco, California; Department of Imaging and Pathology (A.R., S.S.), Translational MRI, and Department of Neurosciences (A.R., S.S.), Leuven Brain Institute, Katholieke Universiteit Leuven, Leuven, Belgium; Image Sciences Institute (A.D.L., A.L.) and Neurology Department (A.D.L.), University Medical Center Utrecht Brain Center, University Medical Center Utrecht, Utrecht, The Netherlands; and Department of Quantitative Biomedicine (B.M.), University of Zurich, Zurich, Switzerland.

A. Zhylyka and N. Sollmann have contributed equally to this work and share the first authorship.

Andrey Zhylyka received funding from the European Union's Horizon 2020 research and innovation program under the Marie Skłodowska-Curie grant agreement No. 765148. Bjoern Menze, Benedikt Wiestler, and Florian Kofler are supported through the SFB 824, subproject B12, supported by Deutsche Forschungsgemeinschaft through Technical University of Munich International Graduate School of Science and Engineering, GSC 81.

Please address correspondence to Andrey Zhylyka, MD, Eindhoven University of Technology, Biomedical Engineering, Rondon 70, Eindhoven, 5612AP, Netherlands; e-mail: a.zhylyka@tue.nl; @AnjensonZ; @NSollmann

Indicates open access to non-subscribers at www.ajnr.org

Indicates article with online supplemental data.

<http://dx.doi.org/10.3174/ajnr.A7793>

prolonged survival and improved quality of life.⁷⁻⁹ However, a maximum extent of resection needs to be weighed against the risk of surgery-related functional decline such as persistent paresis or aphasia, which may arise from tumor resection in or near functionally eloquent structures such as the motor or language cortex.^{10,11} Additionally, subcortical WM pathways such as efferent fibers that interconnect certain brain areas or course down to the periphery may need to be respected to avoid lasting functional deficits.^{12,13}

Imaging and mapping of brain function are essential for a maximum safe resection combined with a high extent of resection and a low-risk profile for permanent functional deterioration.^{6,14-16} In the preoperative setup, DWI with tractography is used for delineation of WM architecture, which can then be visualized and respected during tumor resection.^{17,18} Particularly, DTI-based tractography is commonly applied to reconstruct certain fiber tracts, relating to its comparatively wide availability and low false-positive rate.¹⁹ However, despite its frequent application in the preoperative work-up of patients with glioma, the technique has relevant shortcomings that render the accuracy of the method questionable.^{20,21} Specifically, major issues relate to potential underrepresentation of fiber branching or crossing fibers, which are difficult to resolve by DTI-based tractography.²²⁻²⁴ Alternatives to DTI-based tractography exist, including methods such as constrained spherical deconvolution (CSD)—tractography, which has shown improved specificity compared with DTI-based tractography, given that CSD-based tractography is determined by higher angular resolution and the possibility of also disentangling more complex fiber configurations.^{25,26} In CSD, multiple fibers passing through a voxel with distinct orientations can be estimated, depending on the fiber orientation distribution (FOD).^{25,26}

Multilevel fiber tractography (MLFT) has been developed from CSD-based tractography and similarly propagates fiber pathways on the basis of FOD peaks, with the main advancement that MLFT proposes that FOD peaks do not solely reflect crossing fibers but may also reflect high angular deviation of fibers or their branching.^{27,28} A previous study has demonstrated that MLFT improved reconstruction of the corticospinal tract (CST) in patients with motor-eloquent high-grade gliomas by generating fiber bundles with higher radial extent (ie, delineation of CST fanning with a wider range) compared with DTI as well as CSD-based deterministic CST tractography, thus potentially showing a more complete picture of the actual CST architecture.²⁷ Yet, without optimal seeding of the ROI for tractography, MLFT would be at considerable risk of reconstructing false-positive WM pathways, given that it can also include acute angles of fiber courses, which might be particularly frequently observed among patients with brain tumors due to the space-occupying effect that may lead to fiber diversion and compression.²⁷

The issue of optimal ROI seeding for CST reconstruction may be addressed by combining MLFT with preoperative functional mapping, such as navigated transcranial magnetic stimulation (nTMS). In essence, nTMS can target neurostimulation to the brain with subcentimeter precision and enables the spatial identification and demarcation of the motor cortex in relation to a lesion.^{29,30} Particularly, nTMS-based motor mapping has been frequently used in the preoperative setup and for guidance of intraoperative resection in patients with motor-eloquent brain

tumors.³⁰⁻³² The approach has been shown to result in cortical motor maps similar to those generated by intraoperative direct electrical stimulation as the reference standard for functional cortical mapping.³³⁻³⁵ More recently, combinations of tractography with nTMS have been used to establish function-based tractography of the CST, which is based on the definition of the nTMS-derived cortical motor map as an ROI.³⁶⁻⁴⁰

Against this background, the purpose of the present study was to combine MLFT for reconstruction of the CST with nTMS for enclosing the functional motor cortex in patients with motor-eloquent gliomas. We hypothesized that MLFT may show higher coverage of the nTMS motor map (ie, the highest percentage of fibers of the CST being connected to the motor cortex) compared with deterministic DTI-based and CSD-based tractography.

MATERIALS AND METHODS

Study Design and Patient Cohort

This study was approved by the local institutional review board (Ethikkommission Technische Universität München) and was conducted in accordance with the Declaration of Helsinki. The requirement for written informed consent for this study was waived due to the retrospective design.

Eligible patients were identified by chart review, covering the time interval from February 2019 to February 2020. Inclusion criteria were the following: 1) older than 18 years of age, 2) availability of preoperative 3T MR imaging, including diffusion-weighted sequences, 3) diagnosis of a high-grade glioma (based on imaging findings and later confirmation by histopathologic evaluation of biopsy probes or tumor tissue harvested during surgical resection), 4) suspected motor-eloquent tumor location according to preoperative MR imaging, and 5) availability of preoperative nTMS-based motor mapping of the tumor-affected hemisphere.

Overall, 31 patients (mean age, 61.5 [SD, 12.2] years; age range, 34.4–85.1 years; 12 women) matched the inclusion criteria and were considered for this study. Three patients were diagnosed with World Health Organization grade III gliomas, and 28 patients with World Health Organization grade IV gliomas, and the right hemisphere was affected by the tumor volume in 19 patients.

Data Acquisition

MR Imaging. Preoperative MR imaging was performed on two 3T scanners (Achieva dStream or Ingenia; Philips Healthcare) using a 32-channel head coil. The imaging protocol included a 3D FLAIR sequence (TR/TE = 4800/277 ms, 1-mm³ isotropic voxels covering the whole head), an axial T2-weighted sequence (TR/TE = 3396/87 ms, voxel size = 0.36 × 0.36 × 4 mm³), a diffusion-weighted sequence (TR/TE = 5000/78 ms, voxel size = 2 × 2 × 2 mm³, 1 volume at $b=0$ s/mm², 32 volumes at $b=1000$ s/mm²), and a 3D T1-weighted turbo field echo sequence (TR/TE = 9/4 ms, 1-mm³ isotropic voxels covering the whole head) without and with intravenous injection of a contrast agent using a dose of 0.2 mL per kg body weight of gadoteric acid (Dotagraf, 0.5 mmol/mL; Jenapharm).

nTMS. Preoperative motor mapping of the tumor-affected hemisphere was performed using nTMS (NBS system 4.3 or 5.0; Nexstim). For neuronavigation, the preoperatively acquired

contrast-enhanced 3D T1-weighted turbo field echo sequence was used. Motor mapping was performed according to a standardized protocol using a figure-of-eight stimulation coil and a biphasic pulse wave application.^{30,41} Both representations of upper and lower extremity muscles were mapped within the tumor-affected hemisphere using an intensity of 105%–110% of the individual resting motor threshold for the upper extremity and an intensity of at least 130% of the resting motor threshold for the lower extremity muscles.^{30,41} Motor-positive nTMS points were identified during post hoc analysis, which were required to show an amplitude of motor-evoked potentials of $\geq 50 \mu V$, with motor-evoked potential onset latencies within the typical ranges.^{30,42,43}

Image Segmentation and Processing of DWI Data. Before image segmentation, all MR imaging data were transferred to Montreal Neurological Institute space (with an isotropic voxel size of 1 mm^3). Given that commonly used parcellation pipelines may not produce robust segmentations in the presence of brain tumors, lesion filling was performed using the Virtual Brain Grafting toolkit (https://github.com/KUL-Radneuron/KUL_VBG/).^{44,45} This approach replaces the tumor volume with synthetic healthy tissue.⁴⁵

As a prerequisite for lesion filling, lesion segmentation was performed using the BraTS toolkit (<https://github.com/neuronflow/BraTS-Toolkit>).^{46,47} The BraTS toolkit was provided with T1-weighted images, both noncontrast and contrast-enhanced, as well as FLAIR and T2-weighted images, to perform the lesion segmentation.^{46,47} The segmentation differentiates between the tumor core (necrotic center and contrast-enhancing tumor parts) and FLAIR-hyperintense zones (edema/tumor infiltration).

All diffusion-weighted data sets were preprocessed by performing motion and eddy current corrections.⁴⁸ To estimate FODs, we used recursive calibration of the response function.⁴⁹ Given the number of acquired diffusion-weighted volumes, the order of spherical harmonics describing FODs was set to $L_{\text{maximum}} = 6$. All processing was performed in ExploreDTI (Version 4.8.6; <http://www.exploredti.com/>).

Because nTMS was performed as a separate acquisition, nTMS points had to be transferred to the space of the T1-weighted and diffusion imaging data sets, achieved by performing registration of the contrast-enhanced T1-weighted images to the masks containing all motor-positive nTMS points of the tumor-affected hemisphere. All nTMS points were enlarged using a hull of 2-mm radius by default to provide the final motor cortex seed mask.^{36,37} All image coregistrations and segmentations were visually inspected for quality and manually corrected, when necessary, by a trained neuroradiologist.

Tractography Algorithms. Three tractography algorithms were used for CST reconstruction: DTI-based tractography, CSD-based tractography, and MLFT. MLFT has been recently introduced and is a bundle-specific algorithm that reconstructs fiber bundles as multilevel structures.^{27,28} The algorithm requires seed and target regions (ie, the ipsilateral anterior pontine brainstem level and the nTMS-derived cortical motor map) and a maximum number of levels.^{27,28} At each iteration, streamline propagation is performed using a deterministic CSD-based algorithm. At the end of each iteration, FOD peaks of the points along pathways

that did not reach the target region are used as initial directions at the following iteration. Thus, the potential of the peaks to represent branches is explored.

The angular deviation threshold (ADT) is aimed at maintaining smoothness and physical plausibility of the fiber pathways because it prevents propagation into directions highly deviating from the previous step direction. However, the threshold may impact the accuracy of the reconstruction, depending on the voxel and angular resolution of the data. Thus, each tractography algorithm was run with 3 different ADTs, namely 20°, 45°, and 60°. For DTI-based tractography, 3 levels of the fractional anisotropy threshold (FAT) were used by setting the individual fractional anisotropy to a maximum value that enables reconstructing a minimum fiber course (ie, 100% FAT). For CSD-based tractography as well as MLFT, the FOD peak threshold was set to 0.08.^{27,28} The tractography step size was set to half the voxel size, and the number of iterations for MLFT was set to 2.

Statistical Analysis. Statistical testing was performed using SPSS (Version 26.0; SPSS Statistics for Windows; IBM) and the SciPy library (Version 1.3.1; <https://www.scipy.org>). The threshold for statistical significance was set at $\alpha = .05$.

To assess and compare reconstructions of the CST, we computed the ratio of the visited voxels of the nTMS mask to the reconstructed fibers for each parameter configuration (ADT = 20°, 45°, and 60°; FAT = 25%, 50%, and 75%) and algorithm (DTI-based tractography, CSD-based tractography, and MLFT). This computation provides an estimate of how much of the nTMS mask (ie, cortical motor-positive nTMS points) is covered and, consequently, how complete the reconstruction is according to the function-based reference (nTMS mask). Additionally, volumes of the reconstructed bundles were computed as the accumulated volume of all the voxels visited by at least 1 fiber pathway. Only the bundle part between the seed and target region was taken into account. To compare the nTMS coverage as well as the volumes of the reconstructions as obtained by the different algorithms depending on the FAT as well as ADT, we performed paired 1-sided Wilcoxon tests. Furthermore, the nTMS coverage achieved by the same algorithm at different ADT settings was compared using paired 2-sided Wilcoxon tests.

RESULTS

Tractography using MLFT was capable of reconstructing fiber bundles with higher volumes (on average 10,367, 19,567, and 26,485 mm^3 for ADTs of 20°, 45°, and 60°) than what was achieved by the DTI- and CSD-based algorithms, true for all used ADTs and FATs (Fig 1 and Online Supplemental Data). DTI-based tractography reconstructed statistically significant smaller bundles than CSD-based tractography at 25% ($P = .54, .99$, and 1 for 20°, 45°, and 60° ADT), 50% ($P = .97, 1$, and 1 for 20°, 45°, and 60° ADT) and 75% FAT ($P = 1$ for all ADTs) based on 1-sided Wilcoxon tests.

Compared with the other approaches, MLFT reconstructions of the CST achieved the highest coverage of the nTMS motor map, which amounted to 38.7%, 60.8%, and 71.8%, on average, for ADTs of 20°, 45°, and 60°, respectively (Fig 2 and Online Supplemental Data). MLFT also achieved higher coverage in

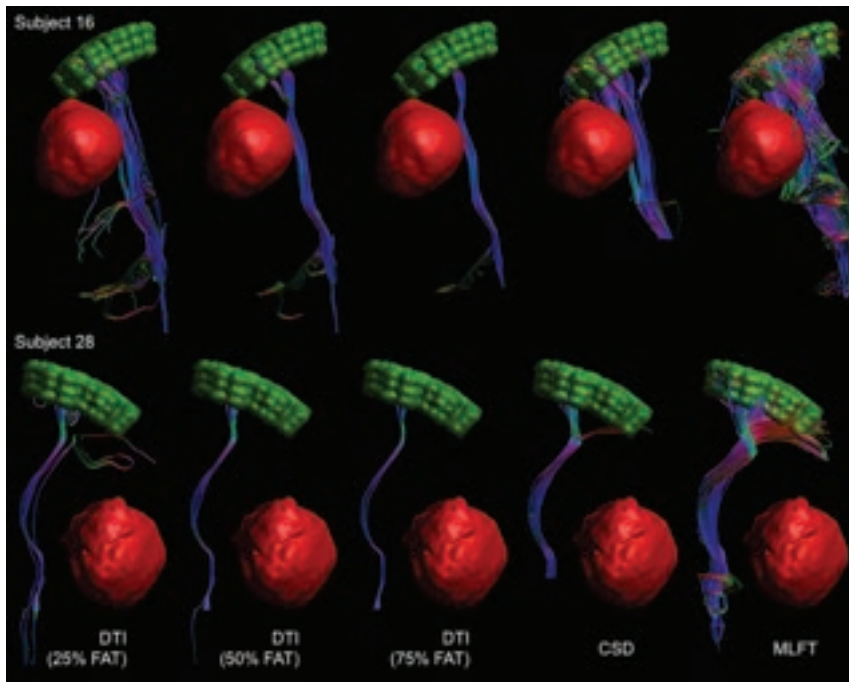


FIG 1. The nTMS-based motor map (green indicates single motor-positive nTMS points with a 2-mm hull) was used as the target region for reconstruction of the CST within the tumor-affected hemisphere (red indicates the tumor core). MLFT shows higher nTMS mask coverage compared with DTI- and CSD-based results, including cases of tumor-induced bundle deformation (subject No. 28).

case of tumor-induced bundle deformations (Fig 1). CSD-based tractography achieved higher coverage of the nTMS motor map than DTI-based tractography, regardless of the settings for ADT and FAT (Fig 2). This finding was also confirmed by comparing reconstructions obtained with the same ADTs with 1-sided Wilcoxon tests ($P > .95$ for all comparisons, Online Supplemental Data).

The change of the ADT led to statistically significant changes in nTMS motor map coverage ($P < .01$) based on 2-sided Wilcoxon tests, which can also be observed in an exemplary patient case (Fig 3). Only when using 75% FAT for DTI-based reconstruction was a statistically nonsignificant difference observed between reconstructions obtained with 20° and 60° ADT as well as 45° and 60° ADT.

DISCUSSION

We combined MLFT with motor mapping for CST reconstruction based on nTMS motor maps used for ROI placement in patients with motor-eloquent gliomas. Tractography results were compared against deterministic DTI-based and CSD-based tractography, given that these techniques are commonly used for clinical tractography in patients with brain tumors. The main findings are as follows: 1) MLFT enabled CST reconstruction with higher bundle volumes, and 2) MLFT yielded higher coverage of the nTMS motor map (ie, a higher percentage of the nTMS points reached by the reconstructed CST).

The MLFT algorithm we used was developed from CSD-based tractography, and it similarly reconstructs fiber pathways on the

basis of FOD peaks.^{27,28} However, in contrast to CSD-based tractography, MLFT suggests that FOD peaks may also be reflective of high angular deviation of fibers or their branching and may not only stem from fiber crossings.^{27,28} Hence, reconstruction of the CST with MLFT may produce bundles with higher radial extent; thus, the delineation of CST fanning with a wider range by also reconstructing fiber courses with acute angles becomes possible.^{27,28} Zhylyka et al²⁷ have shown this feature in a previous study among patients with motor-eloquent high-grade gliomas, but the motor cortex mask was defined using a parcellation mask of the precentral, postcentral, and paracentral gyri combined with a cross-section of the brainstem at the pontine level.

Given that MLFT may naturally reconstruct bundles with higher fiber count due to inclusion of fibers that course with acute angles, the potential risk of increasing the false-positive rate (ie, proportion of fibers that are visualized but do not connect to the actual

functional motor cortex) is present. Specifically, to avoid a high false-positive rate, MLFT would require well-defined ROI seeding, and if certain pathways do not connect to the ROI, the algorithm checks to see if any deviation at the previous reconstruction points would allow connection to the ROI, thus providing some control over specificity while potentially improving sensitivity.^{27,28} In this regard, motor maps from preoperative nTMS were used as the target ROIs, given that nTMS motor mapping has shown high agreement with intraoperative direct electrical stimulation as the reference standard for functional mapping in patients with brain tumor.³³⁻³⁵ Furthermore, nTMS has also been effectively combined with DTI-based tractography in the past, allowing DTI-based reconstruction of the CST using functional data for ROI seeding, which could improve tracking of fibers for preparation and guidance of tumor resection and stratification for perioperative functional deficits.^{36-39,50} In this context, compared with conventional seeding without functional data (eg, manual delineation of the brainstem for ROI generation), nTMS-based tractography of the CST has been shown to result in a lower number of aberrant tracts (ie, tracts not belonging to the CST), and it changed the surgical strategy in more than twice as many patients.^{38,50} Furthermore, detailed somatotopic CST reconstructions might become possible when using nTMS motor maps as ROIs, with greater spatial overlap between the motor cortex and the cortical end region of the CST compared with conventional anatomic seeding for tractography.⁴⁰

Reconstructions of the CST using MLFT showed the highest bundle volume for the CST, combined with the highest coverage of the nTMS motor map compared with deterministic DTI- or

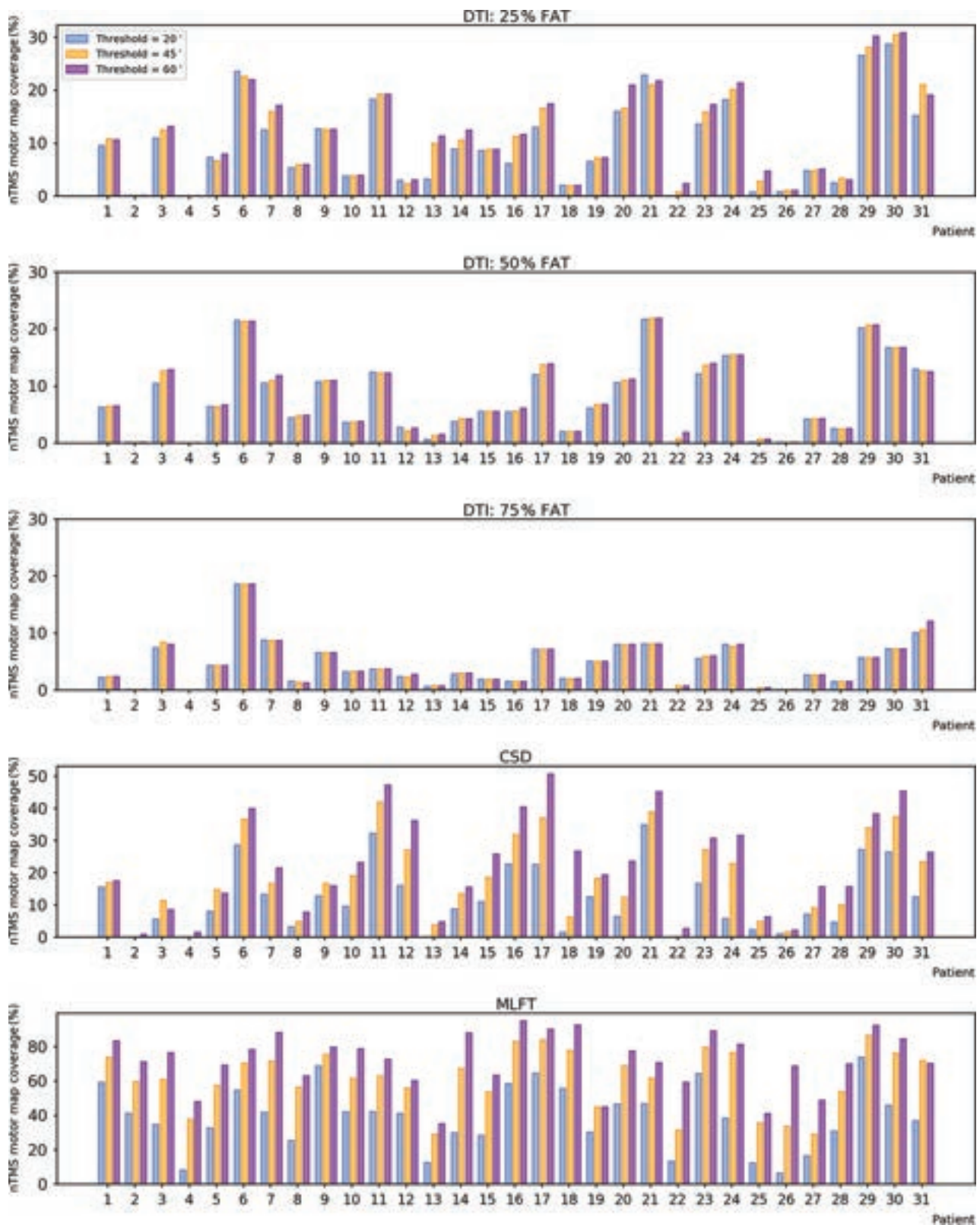


FIG 2. nTMS motor map coverage derived from CST reconstructed with DTI-based (with 25%, 50%, and 75% of the individual FAT), CSD-based, and MLFT tractography. Changes of ADTs appear to only have visible effect on the result of CSD-based tractography and MLFT.

CSD-based tractography. This result may indicate that a more complete reconstruction of the CST can be achieved with MLFT, which is most likely due to reconstruction of fibers with higher radial extents. Glioma may cause considerable deviation of CST

fibers, which may, in part, be lost to reconstruction when using DTI- or CSD-based approaches (Fig 1). The higher coverage of nTMS maps when applying MLFT could increase confidence because the fibers reconstructed from MLFT are actually

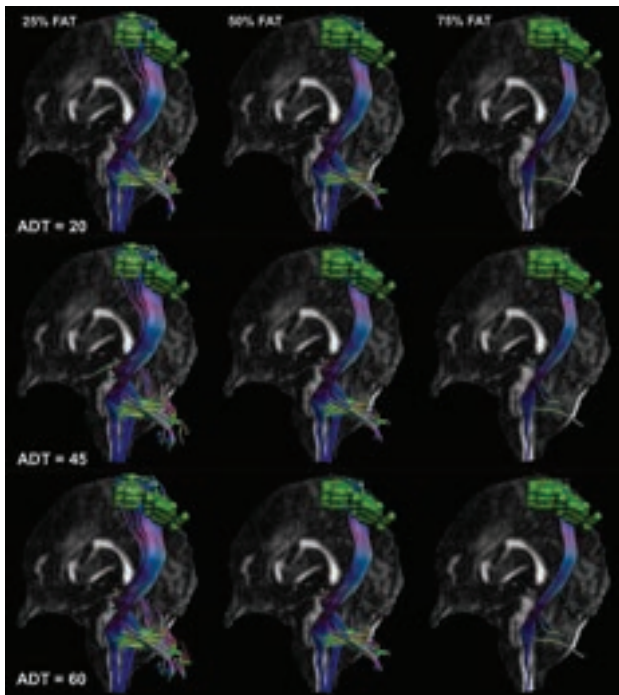


FIG 3. DTI-based reconstructions of the CST with the nTMS-based motor map (green indicates single motor-positive nTMS points with a 2-mm hull) with varied ADT (rows) and FAT levels in subject No. 30.

representative of the motor system (Fig 2), given that higher nTMS coverage is suggestive of more fibers being connected to the actual functional motor cortex. Of note, preoperatively enclosing the functional motor cortex with nTMS allows definition of its individual extent and location, which can be drastically aberrant to the structural landmark anatomy due to shifts related to the space-occupying effects and, most notably, due to plastic reshaping of functional motor representations in response to the presence and growth of glioma.⁵¹⁻⁵³

A more complete reconstruction of fibers belonging to the CST is of clinical merit when achieving an optimal onco-functional balance because their visualization could help avoid surgery-induced damage and, thus, occurrence of lasting perioperative paresis. Specifically, CST reconstruction with broader fanning by MLFT could also generate laterally coursing and marginal fibers, which could be at particular risk of damage when approaching a maximized extent of resection. The higher CST bundle volumes may likely also result in pathways with a smaller lesion-to-tract distance, having potential impact on resection planning. Previous work using nTMS motor mapping combined with DTI-based tractography of the CST has proposed the lesion-to-tract distance as a parameter for presurgical stratification of the risk of permanent motor function decline, with lower lesion-to-tract distances being associated with a higher risk for lasting deficits.^{36,37,39} Application of MLFT instead of DTI-based tracking might potentially allow refined results for lesion-to-tract distances, with a potential definition of more realistic lesion-to-tract distances that may facilitate improved surgical outcome in terms of the extent of resection and the patient's functional status.

A major limitation of this study is that tractography results were not confirmed by intraoperative direct electrical stimulation as the reference standard for functional mapping. Due to the retrospective character of this study, this confirmation was not possible but may be achieved in future studies. Hence, potential overrepresentations of fibers when using the MLFT algorithm cannot be fully excluded. Another limitation of MLFT relates to FOD accuracy, given that a high number of diffusion directions and high b-values are not routinely acquired for clinically used diffusion-weighted MR imaging sequences. As a consequence, the accuracy of the fitted diffusion models could be restricted because FODs have to be represented by lower-order spherical harmonics. Furthermore, the FOD algorithm used does not estimate separate response functions for different tissues.⁴⁹ However, using acquisitions with multiple diffusion-weightings (eg, multi-shell imaging) over the sequence we used would facilitate applying FOD algorithms that can differentiate multiple tissues.⁵⁴

CONCLUSIONS

Compared with routinely used deterministic DTI-based and CSD-based tractography of the CST, MLFT may enable CST reconstructions with a higher bundle volume paired with higher coverage of the functional motor cortex. Thus, MLFT could provide a more detailed visualization of CST architecture by also visualizing fiber courses with acute angles, which might be of particular relevance in patients with gliomas and distorted anatomy of the motor system. However, prospective confirmation of tractography results from MLFT by intraoperative direct electrical stimulation as the reference standard for functional mapping is required for validation purposes.

Disclosure forms provided by the authors are available with the full text and PDF of this article at www.ajnr.org.

REFERENCES

- Ostrom QT, Bauchet L, Davis FG, et al. **The epidemiology of glioma in adults: a state of the science review.** *Neuro Oncol* 2014;16:896–913 CrossRef Medline
- Ostrom QT, Cote DJ, Ascha M, et al. **Adult glioma incidence and survival by race or ethnicity in the United States from 2000 to 2014.** *JAMA Oncol* 2018;4:1254–62 CrossRef Medline
- Miller KD, Ostrom QT, Kruchko C, et al. **Brain and other central nervous system tumor statistics, 2021.** *CA Cancer J Clin* 2021;71:381–406 CrossRef Medline
- Stupp R, Mason WP, van den Bent MJ, et al; National Cancer Institute of Canada Clinical Trials Group. **Radiotherapy plus concomitant and adjuvant temozolomide for glioblastoma.** *N Engl J Med* 2005;352:987–96 CrossRef Medline
- Martínez-García M, Álvarez-Linera J, Carrato C, et al. **SEOM clinical guidelines for diagnosis and treatment of glioblastoma (2017).** *Clin Transl Oncol* 2018;20:22–28 CrossRef Medline
- Sanai N, Berger MS. **Surgical oncology for gliomas: the state of the art.** *Nat Rev Clin Oncol* 2018;15:112–25 CrossRef Medline
- Lacroix M, Abi-Said D, Fourney DR, et al. **A multivariate analysis of 416 patients with glioblastoma multiforme: prognosis, extent of resection, and survival.** *J Neurosurg* 2001;95:190–98 CrossRef Medline
- Brown PD, Maurer MJ, Rummans TA, et al. **A prospective study of quality of life in adults with newly diagnosed high-grade gliomas: the impact of the extent of resection on quality of life and survival.** *Neurosurgery* 2005;57:495–503 CrossRef Medline

9. Molinaro AM, Hervey-Jumper S, Morshed RA, et al. **Association of maximal extent of resection of contrast-enhanced and non-contrast-enhanced tumor with survival within molecular subgroups of patients with newly diagnosed glioblastoma.** *JAMA Oncol* 2020;6:495–503 CrossRef Medline
10. Duffau H, Mandonnet E. **The “onco-functional balance” in surgery for diffuse low-grade glioma: Integrating the extent of resection with quality of life.** *Acta Neurochir (Wien)* 2013;155:951–57 CrossRef Medline
11. Bush NAO, Chang SM, Berger MS. **Current and future strategies for treatment of glioma.** *Neurosurg Rev* 2017;40:1–14 CrossRef Medline
12. Stadlbauer A, Nimsky C, Buslei R, et al. **Diffusion tensor imaging and optimized fiber tracking in glioma patients: histopathologic evaluation of tumor-invaded white matter structures.** *Neuroimage* 2007;34:949–56 CrossRef Medline
13. Bello L, Gambini A, Castellano A, et al. **Motor and language DTI fiber tracking combined with intraoperative subcortical mapping for surgical removal of gliomas.** *Neuroimage* 2008;39:369–82 CrossRef Medline
14. Hervey-Jumper SL, Berger MS. **Maximizing safe resection of low- and high-grade glioma.** *J Neurooncol* 2016;130:269–82 CrossRef Medline
15. Villanueva-Meyer JE, Mabray MC, Cha S. **Current clinical brain tumor imaging.** *Clin Neurosurg* 2017;81:397–415 CrossRef Medline
16. Carrete LR, Young JS, Cha S. **Advanced imaging techniques for newly diagnosed and recurrent gliomas.** *Front Neurosci* 2022;16:787755 CrossRef Medline
17. Henderson F, Abdullah KG, Verma R, et al. **Tractography and the connectome in neurosurgical treatment of gliomas: the premise, the progress, and the potential.** *Neurosurg Focus* 2020;48:E6 CrossRef Medline
18. Yeh FC, Irimia A, de Almeida Bastos DC, et al. **Tractography methods and findings in brain tumors and traumatic brain injury.** *Neuroimage* 2021;245:118651 CrossRef Medline
19. Maier-Hein KH, Neher PF, Houde JC, et al. **The challenge of mapping the human connectome based on diffusion tractography.** *Nat Commun* 2017;8:1349 CrossRef Medline
20. Duffau H. **Diffusion tensor imaging is a research and educational tool, but not yet a clinical tool.** *World Neurosurg* 2014;82:e43–45 CrossRef
21. Azad TD, Duffau H. **Limitations of functional neuroimaging for patient selection and surgical planning in glioma surgery.** *Neurosurg Focus* 2020;48:E12 CrossRef Medline
22. Behrens TE, Berg HJ, Jbabdi S, et al. **Probabilistic diffusion tractography with multiple fibre orientations: what can we gain?** *Neuroimage* 2007;34:144–55 CrossRef Medline
23. Farquharson S, Tournier JD, Calamante F, et al. **White matter fiber tractography: why we need to move beyond DTI.** *J Neurosurg* 2013;118:1367–77 CrossRef Medline
24. Jeurissen B, Leemans A, Tournier JD, et al. **Investigating the prevalence of complex fiber configurations in white matter tissue with diffusion magnetic resonance imaging.** *Hum Brain Mapp* 2013;34:2747–66 CrossRef Medline
25. Tournier JD, Calamante F, Connelly A. **Robust determination of the fibre orientation distribution in diffusion MRI: non-negativity constrained super-resolved spherical deconvolution.** *Neuroimage* 2007;35:1459–72 CrossRef Medline
26. Jeurissen B, Leemans A, Jones DK, et al. **Probabilistic fiber tracking using the residual bootstrap with constrained spherical deconvolution.** *Hum Brain Mapp* 2011;32:461–79 CrossRef Medline
27. Zhylyka A, Sollmann N, Kofler F, et al. **Tracking the corticospinal tract in patients with high-grade glioma: clinical evaluation of multi-level fiber tracking and comparison to conventional deterministic approaches.** *Front Oncol* 2021;11:761169 CrossRef Medline
28. Zhylyka A, Leemans A, Pluim JP, et al. **Anatomically informed multi-level fiber tractography for targeted virtual dissection.** *Magn Reson Mater Phy* 2022 Jul 29. [Epub ahead of print] CrossRef Medline
29. Ruohonen J, Karhu J. **Navigated transcranial magnetic stimulation.** *Neurophysiol Clin* 2010;40:7–17 CrossRef Medline
30. Sollmann N, Krieg SM, Säisänen L, et al. **Mapping of motor function with neuronavigated transcranial magnetic stimulation: a review on clinical application in brain tumors and methods for ensuring feasible accuracy.** *Brain Sci* 2021;11:897 CrossRef Medline
31. Lefaucheur JP, Picht T. **The value of preoperative functional cortical mapping using navigated TMS.** *Neurophysiol Clin* 2016;46:125–33 CrossRef Medline
32. Haddad AF, Young JS, Berger MS, et al. **Preoperative applications of navigated transcranial magnetic stimulation.** *Front Neurol* 2021;11:628903 CrossRef Medline
33. Forster MT, Hattingen E, Senft C, et al. **Navigated transcranial magnetic stimulation and functional magnetic resonance imaging: advanced adjuncts in preoperative planning for central region tumors.** *Neurosurgery* 2011;68:1317–24 CrossRef Medline
34. Krieg SM, Shibani E, Buchmann N, et al. **Utility of presurgical navigated transcranial magnetic brain stimulation for the resection of tumors in eloquent motor areas: clinical article.** *J Neurosurg* 2012;116:994–1001 CrossRef Medline
35. Tarapore PE, Tate MC, Findlay AM, et al. **Preoperative multimodal motor mapping: a comparison of magnetoencephalography imaging, navigated transcranial magnetic stimulation, and direct cortical stimulation: clinical article.** *J Neurosurg* 2012;117:354–62 CrossRef Medline
36. Sollmann N, Wildschuetz N, Kelm A, et al. **Associations between clinical outcome and navigated transcranial magnetic stimulation characteristics in patients with motor-eloquent brain lesions: a combined navigated transcranial magnetic stimulation-diffusion tensor imaging fiber tracking approach.** *J Neurosurg* 2018;128:800–10 CrossRef Medline
37. Sollmann N, Zhang H, Fratini A, et al. **Risk assessment by presurgical tractography using navigated TMS maps in patients with highly motor- or language-eloquent brain tumors.** *Cancers (Basel)* 2020;12:1264 CrossRef Medline
38. Frey D, Strack V, Wiener E, et al. **A new approach for corticospinal tract reconstruction based on navigated transcranial stimulation and standardized fractional anisotropy values.** *Neuroimage* 2012;62:1600–09 CrossRef Medline
39. Rosenstock T, Grittner U, Acker G, et al. **Risk stratification in motor area-related glioma surgery based on navigated transcranial magnetic stimulation data.** *J Neurosurg* 2017;126:1227–37 CrossRef Medline
40. Conti A, Raffa G, Granata F, et al. **Navigated transcranial magnetic stimulation for “somatotopic” tractography of the corticospinal tract.** *Operative Neurosurgery* 2014;10:542–54; discussion 554 CrossRef Medline
41. Krieg SM, Lioumis P, Mäkelä JP, et al. **Protocol for motor and language mapping by navigated TMS in patients and healthy volunteers: workshop report.** *Acta Neurochir (Wien)* 2017;159:1187–95 CrossRef Medline
42. Säisänen L, Julkunen P, Niskanen E, et al. **Motor potentials evoked by navigated transcranial magnetic stimulation in healthy subjects.** *J Clin Neurophysiol* 2008;25:367–72 CrossRef Medline
43. Sollmann N, Bulubas L, Tanigawa N, et al. **The variability of motor evoked potential latencies in neurosurgical motor mapping by preoperative navigated transcranial magnetic stimulation.** *BMC Neurosci* 2017;18:5 CrossRef Medline
44. Fischl B. **FreeSurfer.** *Neuroimage* 2012;62:774–81 CrossRef Medline
45. Radwan AM, Emsell L, Blommaert J, et al. **Virtual brain grafting: enabling whole brain parcellation in the presence of large lesions.** *Neuroimage* 2021;229:117731 CrossRef Medline
46. Menze BH, Jakab A, Bauer S, et al. **The multimodal Brain Tumor Image Segmentation Benchmark (BRATS).** *IEEE Trans Med Imaging* 2015;34:1993–2024 CrossRef Medline
47. Kofler F, Berger C, Waldmannstetter D, et al. **BraTS Toolkit: translating BraTS brain tumor segmentation algorithms into clinical and scientific practice.** *Front Neurosci* 2020;14:125 CrossRef Medline

48. Mohammadi S, Möller HE, Kugel H, et al. **Correcting eddy current and motion effects by affine whole-brain registrations: evaluation of three-dimensional distortions and comparison with slicewise correction.** *Magn Reson Med* 2010;64:1047–56 CrossRef Medline
49. Tax CM, Jeurissen B, Vos SB, et al. **Recursive calibration of the fiber response function for spherical deconvolution of diffusion MRI data.** *Neuroimage* 2014;86:67–80 CrossRef Medline
50. Krieg SM, Buchmann NH, Gempt J, et al. **Diffusion tensor imaging fiber tracking using navigated brain stimulation: a feasibility study.** *Acta Neurochir (Wien)* 2012;154:555–63 CrossRef Medline
51. Southwell DG, Hervey-Jumper SL, Perry DW, et al. **Intraoperative mapping during repeat awake craniotomy reveals the functional plasticity of adult cortex.** *J Neurosurg* 2016;124:1460–69 CrossRef Medline
52. Conway N, Wildschuetz N, Moser T, et al. **Cortical plasticity of motor-eloquent areas measured by navigated transcranial magnetic stimulation in patients with glioma.** *J Neurosurg* 2017;127:981–91 CrossRef Medline
53. Gibb WR, Kong NW, Tate MC. **Direct evidence of plasticity within human primary motor and somatosensory cortices of patients with glioblastoma.** *Neural Plast* 2020;2020:8893708 CrossRef Medline
54. De Luca A, Guo F, Froeling M, et al. **Spherical deconvolution with tissue-specific response functions and multi-shell diffusion MRI to estimate multiple fiber orientation distributions (mFODs).** *Neuroimage* 2020;222:117206 CrossRef Medline

Persistent Opacification of the Woven EndoBridge Device: A Conebeam CT Analysis of the Bicêtre Occlusion Scale Score 1 Phenomenon

J. Caroff, S.D. Popescu, C. Mihalea, D.A. Popica, L. Ikka, S. Gallas, A. Ozanne, V. Chalumeau, J. Moret, J. Cortese, and L. Spelle



ABSTRACT

BACKGROUND AND PURPOSE: Some Woven EndoBridge devices present a persistent intradivice opacification at imaging follow-up, described as the Bicêtre Occlusion Scale Score 1 (BOSS 1) phenomenon. The clinical implications remain unknown. We aimed here to analyze the factors influencing this occurrence and to precisely describe the evolution of BOSS 1 with time using conebeam CT.

MATERIALS AND METHODS: We retrospectively analyzed a prospectively maintained Woven EndoBridge database at our tertiary center and included all patients with isolated BOSS 1 and BOSS 1 associated with small neck remnant (BOSS 1 + 2).

RESULTS: Two hundred sixty-seven aneurysms were treated with a Woven EndoBridge device between July 2012 and December 2021. Follow-up with DSA was available for 220 aneurysms (median, 5 months), among which BOSS 1 and 1 + 2 were found in 9.1% (20/220) (95% CI, 5.5%–12.7%). A second DSA follow-up (median, 17 months) was performed in 15 of these 20 aneurysms, which revealed that 40% had evolved to complete Woven EndoBridge occlusion, 33% showed a decreased persistent opacification, and 27% remained stable. BOSS 1 was significantly associated with postoperative antiplatelet medication, a lower aneurysm aspect ratio, and the use of the Woven EndoBridge 17 ($P < .05$). The average Woven EndoBridge shape modification was less pronounced in the BOSS 1 population ($P < .02$). None of the BOSS 1 or 1 + 2 aneurysms required retreatment or were associated with hemorrhage occurrence.

CONCLUSIONS: Isolated persistent flow inside the Woven EndoBridge device at follow-up is rare and notably associated with antiplatelet prescription. It seems to present a benign course in most cases.

ABBREVIATIONS: BOSS 1 = Bicêtre Occlusion Scale Score 1; CBCT = conebeam CT; FU = follow-up; WShM = WEB shape modification; WEB = Woven EndoBridge

The Woven EndoBridge (WEB; MicroVention) has been used in the treatment of wide-neck intracranial ruptured and unruptured aneurysms for >10 years.^{1–3} Once implanted within the aneurysmal sac, this device induces progressive thrombosis by disrupting the blood flow at the level of the neck. Flow decrease and stagnation of blood then trigger the thrombosis cascade inside the WEB, leading to aneurysm healing on endothelialization of the WEB struts.

In a small proportion of patients, this process appears either inhibited or very much delayed.^{4,5} Evidence of contrast filling inside the WEB at follow-up (FU) of such patients reflects a

persisting blood flow, yet the underlying mechanisms of this incomplete thrombosis remain unclear.

Such isolated persistent intra-WEB opacification is described as Bicêtre Occlusion Scale Score 1 (BOSS 1) (Fig 1).⁶ While this phenomenon appears in a relatively small number of cases,^{4,5} its immediate clinical impact or long-term evolution remains undetermined. In the literature, such cases have been referred to as adequate occlusion^{4–6} or sometimes as an aneurysm remnant.^{7,8} Our unique systematic use of conebeam CT (CBCT)⁹ during FU allowed us to conduct a precise analysis of this phenomenon.

MATERIALS AND METHODS

Ethical Statement

The French Ethical Committee for Research in Medical Imaging (CERIM) approved this study (institutional review board No. CRM2101–127). Informed consent was obtained for every patient.

Study Design and Population

We retrospectively analyzed demographic, clinical, and imaging data from patients prospectively included between July 2012 and December 2021 in a prospectively maintained WEB database.

Received October 26, 2022; accepted after revision January 3, 2023.

From the Department of Interventional Neuroradiology (J. Caroff, S.D.P., C.M., D.A.P., L.I., S.G., A.O., V.C., J.M., J. Cortese, L.S.), NEURI Brain Vascular Center, Bicêtre Hospital, Assistance Publique-Hôpitaux de Paris, Paris-Saclay University, Le Kremlin-Bicêtre, France; Paris-Saclay University Faculty of Medicine (L.S.), Le Kremlin-Bicêtre, France; and INSERM Unit 1176 (J. Caroff), INSERM Unit 1195 (J. Cortese, L.S.), Le Kremlin-Bicêtre, France. J. Caroff and S.D. Popescu contributed equally to this work.

Please address correspondence to Jildaz Caroff, MD, Department of Interventional Neuroradiology, NEURI Brain Vascular Center, Bicêtre Hospital, Assistance Publique Hôpitaux de Paris, 78 Rue du General Leclerc, 94270 Le Kremlin-Bicêtre, France; e-mail: jildaz.caroff@aphp.fr; @jildazz

<http://dx.doi.org/10.3174/ajnr.A7783>

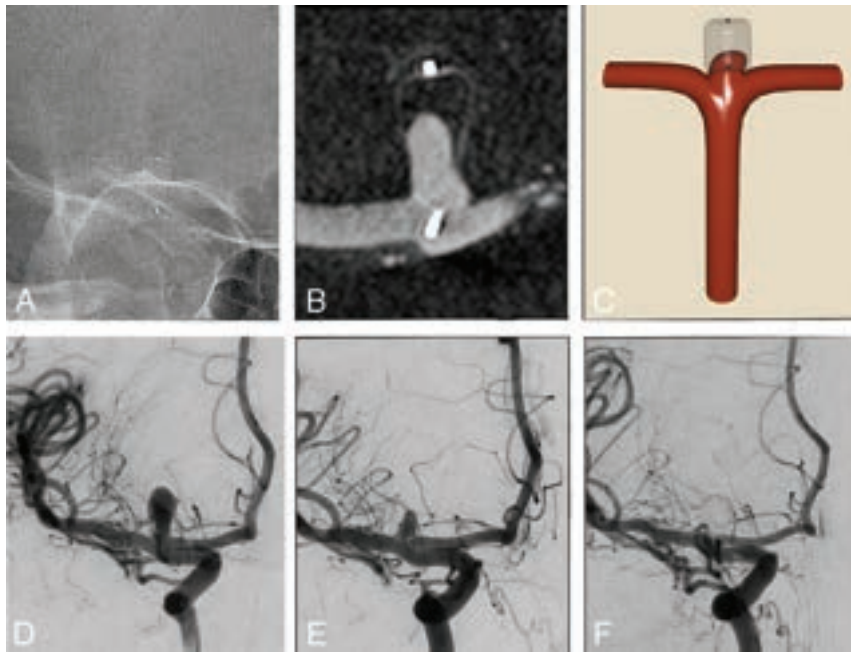


FIG 1. A saccular aneurysm of the right ICA terminus was treated with a WEB device (A and D). The 4-month DSA and VasoCT FU demonstrated a persistent intra-WEB opacification ie, BOSS 1 (B and E). The 1-year FU revealed complete occlusion of the aneurysm (F). Illustration of the BOSS 1 phenomenon (C).

Inclusion criteria were the following: patients with intracranial unruptured or ruptured aneurysms treated with a WEB device and who had at least 1 FU cerebral DSA, including CBCT, with 1 of the 2 following imaging features at first FU: an isolated residual opacification inside the WEB device (BOSS 1) or a small neck remnant + residual opacification inside the WEB device (BOSS 1 + 2).

All patients presenting with an aneurysm remnant + residual opacification inside the WEB device (BOSS 1 + 3) were excluded from the study.

Embolization Procedure and Medication Protocols

Each elective patient scheduled for embolization with the WEB was premedicated with dual antiplatelet therapy,¹⁰ for which the most frequently used combination was ticagrelor (90 mg twice daily) and aspirin (160 mg daily) on the day before the intervention. Ruptured aneurysms were not premedicated.

Following the intervention, only in cases of important WEB protrusion or adjuvant stent deployment was antiplatelet therapy prescribed at the operator's discretion.

DSA FU and Analysis

We systematically used both DSA and CBCT (SmartCT Vaso; Philips Healthcare) as imaging methods to assess the aneurysmal occlusion and intra-WEB opacifications.⁹ In general, the first follow-up DSA for ruptured aneurysms was performed 3 months after treatment, while for unruptured aneurysms, it was performed 6 months postembolization. Images were analyzed by 2 neuroradiologists, and discrepancies were resolved by discussion and agreement. Angiographic outcome was assessed on the basis of the BOSS scale.

For the purpose of this study, the BOSS 1 category was subdivided into 3 subtypes: BOSS 1^{33%}, referring to opacification of 1%–33% of the WEB device; BOSS 1^{66%} for 34%–66%; and BOSS 1^{100%} for 67%–100% at FU (Fig 2).

As previously described,¹¹ WEB shape modification (WShM) was quantitatively defined as a ratio (percentage) and was obtained by standardized measuring of the distance between the proximal and distal WEB markers on cross-sectional images obtained with conebeam CT performed after WEB detachment and again at last FU.

Statistical Analysis

Continuous variables were reported as the mean \pm standard deviation (SD) if normally distributed, or as the median (interquartile range), while categorical variables were expressed as a frequency (%). Confidence intervals were based on the Wald statistic. As appropriate, a χ^2 or Fisher exact test was used to evaluate

qualitative factors, and a Student *t* test or Wilcoxon *U* test to assess quantitative variables. *P* values < .05 were considered statistically significant. All statistical analyses were performed using R 3.6.1 for Windows (<https://cran.r-project.org/bin/windows/base/old/3.6.1/>).

RESULTS

BOSS 1 Assessment

A total of 267 aneurysms were treated with a WEB device between July 2012 and December 2021 (Table). A cerebral DSA FU was available in 220 of these cases (82%), 27.4% of which were ruptured aneurysms.

The BOSS 1 phenomenon was found in 20 cases (9.1%; 95% CI, 5.5%–12.7%) at first DSA FU (median, 5 months; interquartile range, 3–6 months). These were subdivided into BOSS 1^{33%} for 15%, BOSS 1^{66%} for 25%, and BOSS 1^{100%} for 60% (Fig 3).

More than 1 DSA was available for 75% of cases presenting with the BOSS 1 phenomenon (15/20). At the last FU (median, 16.9 months; interquartile range, 7–20 months), 40% of these BOSS 1 cases had evolved to complete WEB occlusion; BOSS 1 persisted in the remaining 60% (9/15), though the level of intra-device opacification had decreased in 60% (5/9) of these compared with the initial FU. At the last FU, persistent opacifications were subdivided into BOSS 1^{33%} for 44%, BOSS 1^{66%} for 33%, and BOSS 1^{100%} for 22%.

Factors Associated with BOSS 1 Persistence

Fifteen of the 20 patients (75%) presenting with the BOSS 1 phenomenon received an antiplatelet medication for at least 1 month after the intervention (11 single and 4 dual antiplatelet therapies). BOSS 1 was significantly associated with postoperative antiplatelet medication (OR = 3.52; 95% CI, 1.31–11.16; *P* < .02).

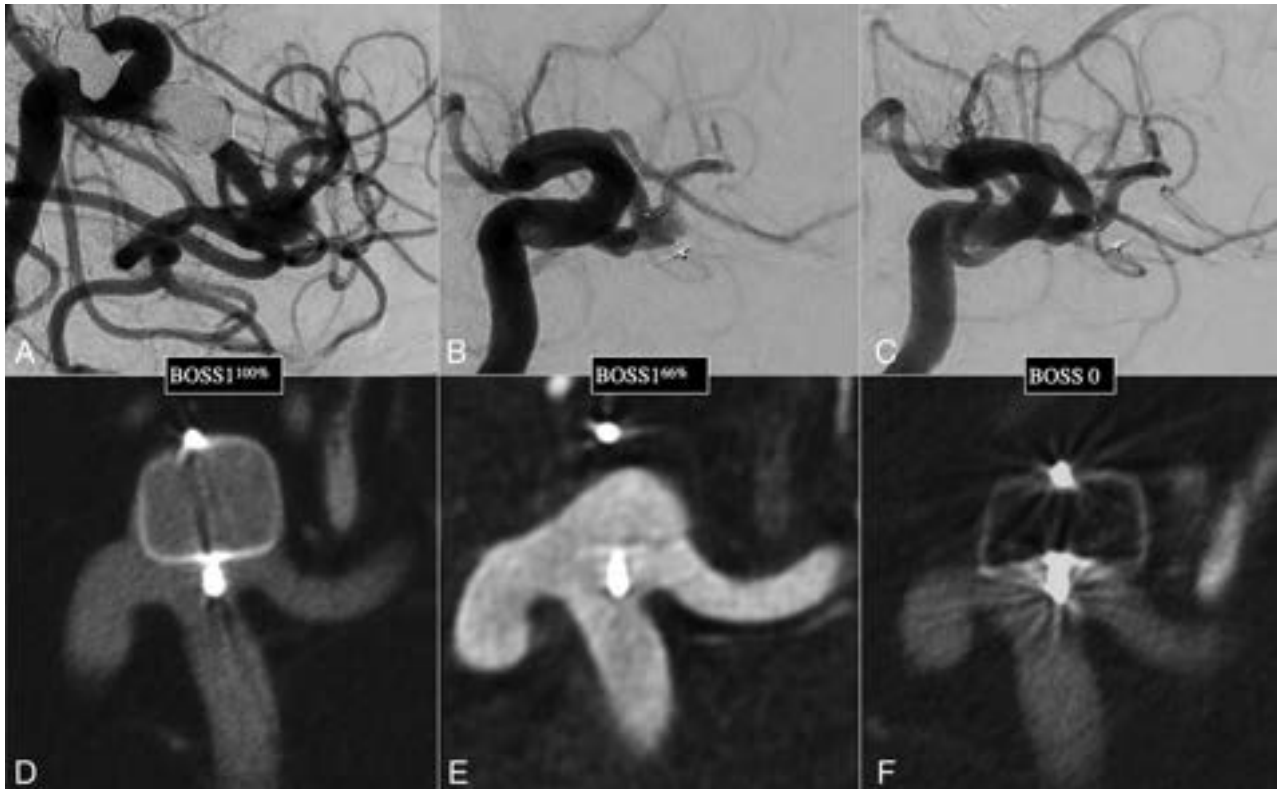


FIG 2. An MCA bifurcation aneurysm was treated with a WEB device. A progressive occlusion was depicted, from BOSS 1^{100%}, opacification of 67%–100% of the WEB volume (A and D), to BOSS 1^{66%}, opacification of 33%–66% of the WEB volume (B and E), and then BOSS 0, complete occlusion (C and F).

BOSS 1 phenomenon was also associated with use of the WEB 17 generation (OR = 3.33; 95% CI, 1.07–14.59; $P < .05$) and with the aneurysm aspect ratio (OR = 0.23; 95% CI, 0.06–0.75; $P < .02$).

The average WShM of 30% (95% CI, 9%–36%) at last FU was lower in the BOSS 1 and 1 + 2 scores compared with the 39% (95% CI, 21%–52%) in the other scores ($P < .02$).

None of the aneurysms presenting with BOSS 1 or 1 + 2 required retreatment, and no hemorrhage occurred during the FU period.

DISCUSSION

Here we have highlighted the unique capacity of VasoCT to analyze the BOSS 1 phenomenon; we believe it should be used systematically as the criterion standard technique to assess WEB treatment success.

Persistent filling of the WEB device cannot be assessed using MR imaging,¹² and the assessment is impossible in most cases with CT.¹³ Differentiating between aneurysm remnants and BOSS 1 is sometimes disputable, even using projection imaging (DSA), yet this distinction is fundamental to allow the correct management. Indeed, a retreatment should probably be considered in cases in which blood flow is depicted in the sac around the WEB. CBCT also allowed a precise quantitative assessment of intradiverticular opacification.⁹

Our series shows a relatively rare occurrence of the BOSS 1 phenomenon at early follow-up, with a rate of 9.1% (95% CI,

5.5%–12.7%). Previous smaller series have reported 6.3%–16% BOSS 1 rates at midterm FU.^{4,5}

Favorable Angiographic Evolution of BOSS 1

We observed a reduction in persistent opacification inside the WEB device between the first and last FU in 73% of cases, demonstrating a progressive thrombosis with time.

BOSS 1 remained at last FU in 60% of cases, but no patient experienced a worsening of angiographic status (ie, no evolution to BOSS 3) or aneurysmal rupture, and no BOSS 1 or 1 + 2 aneurysms required retreatment during the FU period. This result would suggest a benign course for this angiographic phenomenon.

Impact of Antiplatelet Therapy on BOSS 1

While the use of antiplatelet medication after WEB implantation has already been hypothesized to favor persistent opacification,⁷ here we have provided the first evidence of prolonged antiplatelet therapy (>1 week after the intervention) being significantly associated with an increased risk of BOSS 1 aneurysms at FU (OR = 3.52; 95% CI, 1.31–11.16). We believe that antiplatelet drugs can be responsible for delayed aneurysm thrombosis and neck endothelialization.

In our study, 75% of patients with BOSS 1 received an antiplatelet medication for at least 1 month after WEB placement (versus 45% in the control group). Concordantly, Nguyen et al⁴ reported dual antiplatelet therapy intake for at least 1 month postintervention in 7 of 8 patients with BOSS 1, and Nawka

Characteristics of patients, aneurysms, and treatments according to the initial angiographic follow-up^a

Characteristics	BOSS 1 (n = 20)	BOSS 0, 0', 2, 3, and 3 + 1 (n = 200)	P Value
Patient			
Age (mean) (yr)	56.8 (SD, 10.9)	55.7 (SD, 11.3)	.669
Female	14 (70)	129 (65)	.623
Current smoker	3/18 (17)	70/185 (38)	.074
Aneurysm			
Acutely ruptured	4 (20)	57 (29)	.418
Irregular	10 (50)	97 (49)	.90
Maximum diameter (mean) (mm)	6.4 (SD, 1.8)	6.4 (SD, 2.4)	.904
Height (mean) (mm)	4.8 (SD, 1.7)	5.3 (SD, 2.2)	.211
Neck (mean) (mm)	4.4 (SD, 1.6)	3.8 (SD, 1.2)	.113
Width (mean) (mm)	5.3 (SD, 1.5)	5.0 (SD, 1.8)	.448
Aspect ratio (height/neck) (mean)	1.11 (SD, 0.44)	1.38 (SD, 0.53)	.016
Width/neck ratio (mean)	1.23 (SD, 0.27)	1.31 (SD, 0.30)	.220
Location			
MCA	12 (60)	89 (44.5)	Ref ²³
AcomA	3 (15)	60 (30)	.137
TCarotid	3 (15)	9 (4.5)	.218
BA	0 (0)	17 (8.5)	.992
Other	2 (10)	25 (12.5)	.512
Treatment			
Type of WEB			
WEB-SL	16 (80)	152 (76)	Ref ²³
WEB-DL	1 (5)	13 (7)	.770
WEB-SLS	3 (15)	35 (18)	.754
WEB 17	17 (85)	126 (63)	.049
Additional stent	2 (10)	8 (4)	.227
Antiplatelet therapy (>1 week)	15 (75)	92 (46)	.013
WShM (%)	30 (9–36)	39 (21–52)	.014

Note:—AcomA indicates anterior communicating artery; TCarotid, internal carotid artery terminus; BA, basilar artery; WEB-SL, WEB single-layer; WEB-DL, WEB dual-layer; WEB-SLS, WEB single-layer sphere; BOSS 0, no residual flow inside the aneurysm or the WEB; 0', opacification of the proximal recess of the WEB; 1, residual flow inside the WEB; 2, neck remnant; 3, aneurysm remnant; 1 + 3, contrast agent media depicted inside and around the device.⁵

^aData are presented as number (%) for qualitative variables and as the mean (SD) or as the median (interquartile range) for quantitative variables (according to their distribution). Smoking status was missing for 17 patients.

et al⁵ reported antiplatelet therapy for at least 6 weeks in all patients with BOSS 1.

With the oversizing paradigm,¹¹ moderate WEB protrusions in the parent artery are more common, and operators tended to prescribe postoperative antiplatelet medications in those situations. Operators should, however, also consider the potential delay in aneurysmal thrombosis and endothelial repair caused by the antiplatelet therapy.^{14,15}

Other Predictive Factors of BOSS 1

Web 17 Generation. The latest generation of the WEB device (WEB 17) can be delivered through 0.017-inch microcatheters.¹⁶ The smaller-sized devices were achieved by reducing the number of wires used in braiding. While this change in design does not seem to modify the “adequate occlusion” rates,¹⁷ the higher porosity at the level of the neck could be responsible for higher BOSS 1 rates. In our series, this last generation of WEB was significantly associated with BOSS 1 occurrence, and 85% of BOSS 1 corresponded to WEB 17 devices.

Aspect Ratio. The aneurysm dimensions and conformation play an important role in BOSS 1 occurrence. In our study, lower aspect ratio aneurysms (ie, shallow aneurysms) were significantly associated with BOSS 1 at FU. We hypothesized that these aneurysms were more likely to have a delayed intra-aneurysm thrombosis due to the larger surface area of the WEB, requiring

endothelial cell covering in the neck region, similar to that observed with the negative impact of larger neck size on the angiographic outcomes of flow-diverter stents.¹⁸

Ruptured Aneurysms. We found no significant differences in terms of BOSS 1 occurrence between ruptured and unruptured aneurysms.¹⁹

WShM and BOSS 1

The mechanisms behind WShM are not well-understood, though clot retraction is suspected to be a major cause,²⁰ with a water hammer effect potentially acting as a minor associated cofactor.²¹

The thrombosis process inside the WEB is initially induced by flow disruption. After endothelialization of the WEB surface, the aneurysm is completely excluded from the circulation, and progressive collagen deposition and subsequent contraction occur.²²

We observed a significantly lower WShM among the BOSS 1 population compared with other categories, supporting the notion of an impact of clot formation on WEB retraction; the lower intra-WEB thrombus volumes could be hypothesized to lead to less retraction.

Limitations

We acknowledge some limitations in our study, the first being its retrospective and monocentric nature; however, we believe

Patient	1st FU		Last FU
20	1 - 33 %		NA
12	1 - 33 %	22 months →	0 %
1	1 - 33 %	12 months →	1 - 33 %
18	34 - 66 %	19 months →	0 %
6	34 - 66 %	20 months →	0 %
13	34 - 66 %	10 months →	0 %
15	34 - 66 %	10 months →	1 - 33 %
10	34 - 66 %	18 months →	34 - 66 %
2	67 - 100 %	27 months →	0 %
8	67 - 100 %	12 months →	0 %
7	67 - 100 %	18 months →	1 - 33 %
9	67 - 100 %	18 months →	1 - 33 %
17	67 - 100 %	26 months →	34 - 66 %
11	67 - 100 %	16 months →	34 - 66 %
5	67 - 100 %	17 months →	67 - 100 %
14	67 - 100 %	14 months →	67 - 100 %
3	67 - 100 %		NA
4	67 - 100 %		NA
16	67 - 100 %		NA
19	67 - 100 %		NA

FIG 3. Evolution of the degrees of WEB volume opacifications (in percentages) for all BOSS 1 aneurysms at early FU (median, 5 months) and at last follow-up (median, 17 months).

that our unique systematic use of VasoCT was mandatory to conduct the precise analysis presented. Second, the number of patients could be viewed as limited; however, we present here one of the largest series of patients presenting with the BOSS 1

rare phenomenon. Finally, the lack of very long-term FU prevents us from drawing any definite conclusions on the outcome of all patients with BOSS 1; however, our data provide evidence in favor of the progressive evolution toward occlusion.

CONCLUSIONS

Isolated persistent flow inside the WEB device at follow-up is rare and notably associated with antiplatelet prescription; it seems to present a benign course in most cases.

Disclosure forms provided by the authors are available with the full text and PDF of this article at www.ajnr.org.

REFERENCES

1. Liebig T, Kabbasch C, Strasilla C, et al. **Intrasaccular flow disruption in acutely ruptured aneurysms: a multicenter retrospective review of the use of the WEB.** *AJNR Am J Neuroradiol* 2015;36:1721–27 CrossRef Medline
2. Pierot L, Moret J, Barreau X, et al. **Safety and efficacy of aneurysm treatment with WEB in the cumulative population of three prospective, multicenter series.** *J Neurointerv Surg* 2018;10:553–59 CrossRef Medline
3. Arthur AS, Molyneux A, Coon AL, et al; WEB-IT Study Investigators. **The safety and effectiveness of the Woven EndoBridge (WEB) system for the treatment of wide-necked bifurcation aneurysms: final 12-month results of the pivotal WEB Intrasaccular Therapy (WEB-IT) Study.** *J Neurointerv Surg* 2019;11:924–30 CrossRef Medline
4. Nguyen HA, Soize S, Manceau PF, et al. **Persistent blood flow inside the Woven EndoBridge device more than 6 months after intracranial aneurysm treatment: frequency, mechanisms, and management: a retrospective single-center study.** *AJNR Am J Neuroradiol* 2020;41:1225–31 CrossRef Medline
5. Nawka MT, Lohse A, Bester M, et al. **Residual flow inside the Woven EndoBridge device at follow-up: potential predictors of the Bicester Occlusion Scale Score 1 Phenomenon.** *AJNR Am J Neuroradiol* 2020;41:1232–37 CrossRef Medline
6. Caroff J, Mihalea C, Tuilier T, et al. **Occlusion assessment of intracranial aneurysms treated with the WEB device.** *Neuroradiology* 2016;58:887–91 CrossRef Medline
7. Cognard C, Januel AC. **Remnants and recurrences after the use of the WEB intrasaccular device in large-neck bifurcation aneurysms.** *Neurosurgery* 2015;76:522–30; discussion 530 CrossRef Medline
8. Aguiar G, Caroff J, Mihalea C, et al. **WEB device for treatment of posterior communicating artery aneurysms.** *J Neurointerv Surg* 2022;14:362–65 CrossRef Medline
9. Caroff J, Mihalea C, Neki H, et al. **Role of C-arm VasoCT in the use of endovascular WEB flow disruption in intracranial aneurysm treatment.** *AJNR Am J Neuroradiol* 2014;35:1353–57 CrossRef Medline
10. Caroff J, Aubert L, Lavenu-Bombled C, et al; JENI Research Collaboration. **Antithrombotic therapies for neurointerventional surgery: a 2021 French comprehensive national survey.** *J Neurointerv Surg* 2022 Mar 28 [Epub ahead of print] CrossRef Medline
11. Caroff J, Cortese J, Girot JB, et al. **Woven EndoBridge device shape modification can be mitigated with an appropriate oversizing strategy: a VasoCT based study.** *J Neurointerv Surg* 2022;14:neurint-surg-2020-017232 CrossRef Medline
12. Nawka MT, Sedlacik J, Frölich A, et al. **Multiparametric MRI of intracranial aneurysms treated with the Woven EndoBridge (WEB): a case of Faraday's cage?** *J Neurointerv Surg* 2018;10:988–94 CrossRef Medline
13. Raoult H, Eugene F, Le Bras A, et al. **CT angiography for one-year follow-up of intracranial aneurysms treated with the WEB device: utility in evaluating aneurysm occlusion and WEB compression at one year.** *J Neuroradiol* 2018;45:343–48 CrossRef Medline
14. Bomberger RA, DePalma RG, Ambrose TA, et al. **Aspirin and dipyridamole inhibit endothelial healing.** *Arch Surg* 1982;117:1459–64 CrossRef Medline
15. Caroff J, King RM, Ughi GJ, et al. **Longitudinal monitoring of flow-diverting stent tissue coverage after implant in a bifurcation model using neurovascular high-frequency optical coherence tomography.** *Neurosurgery* 2020;87:1311–19 CrossRef Medline
16. Mihalea C, Caroff J, Pagiola I, et al. **Safety and efficiency of the fifth generation Woven EndoBridge device: technical note.** *J Neurointerv Surg* 2019;11:511–15 CrossRef Medline
17. Cortese J, Caroff J, Chalumeau V, et al. **Determinants of cerebral aneurysm occlusion after embolization with the WEB device: a single-institution series of 215 cases with angiographic follow-up.** *J Neurointerv Surg* 2022 Apr 15 [Epub ahead of print] CrossRef Medline
18. Paliwal N, Tutino VM, Shallwani H, et al. **Ostium ratio and neck ratio could predict the outcome of sidewall intracranial aneurysms treated with flow diverters.** *AJNR Am J Neuroradiol* 2019;40:288–94 CrossRef Medline
19. Spelle L, Herbretau D, Caroff J, et al. **CLinical Assessment of WEB device in Ruptured aneurYSms (CLARYS): 12-month angiographic results of a multicenter study.** *J Neurointerv Surg* 2022;14:807–14 CrossRef Medline
20. Pierot L. **Letter: WEB aneurysm treatment—occlusion stability and “compression.”** *Neurosurgery* 2015;77:E666–67 CrossRef Medline
21. Caroff J, Mihalea C, Da Ros V, et al. **A computational fluid dynamics (CFD) study of WEB-treated aneurysms: can CFD predict WEB “compression” during follow-up?** *AJNR J Neuroradiol* 2017;44:262–68 CrossRef Medline
22. Lee D, Yuki I, Murayama Y, et al. **Thrombus organization and healing in the swine experimental aneurysm model, Part I: a histological and molecular analysis.** *J Neurosurg* 2007;107:94–108 CrossRef Medline
23. Caroff J, Mihalea C, Klisch J, et al. **Single-layer WEBs: Intrasaccular flow disrupters for aneurysm treatment—feasibility results from a European study.** *AJNR Am J Neuroradiol* 2015;36:1942–6 CrossRef Medline

Embolic Agent Choice in Middle Meningeal Artery Embolization as Primary or Adjunct Treatment for Chronic Subdural Hematoma: A Systematic Review and Meta-analysis

J.C. Ku, A.A. Dmytriw, M.A. Essibayi, M.A. Banihashemi, J.E. Vranic, S. Ghozy, D. Altschul, R.W. Regenhardt, C.J. Stapleton, V.X.D. Yang, and A.B. Patel



ABSTRACT

BACKGROUND: Middle meningeal artery embolization is an emerging treatment option for chronic subdural hematomas.

PURPOSE: Our aim was to assess outcomes following middle meningeal artery embolization by different techniques, including in comparison with traditional surgical methods.

DATA SOURCES: We searched the literature databases from inception to March 2022.

DATA SELECTION: We selected studies reporting outcomes after middle meningeal artery embolization as a primary or adjunctive treatment for chronic subdural hematoma.

DATA ANALYSIS: We analyzed the risk of recurrence of chronic subdural hematoma, reoperation for recurrence or residual hematoma, complications, and radiologic and clinical outcomes using random effects modeling. Additional analyses were performed on the basis of whether middle meningeal artery embolization was used as the primary or adjunct treatment and by embolic agent type.

DATA SYNTHESIS: Twenty-two studies were included with 382 patients with middle meningeal artery embolization and 1373 surgical patients. The rate of subdural hematoma recurrence was 4.1%. Fifty (4.2%) patients underwent a reoperation for a recurrent or residual subdural hematoma. Thirty-six (2.6%) experienced postoperative complications. The rates of good radiologic and clinical outcomes were 83.1% and 73.3%, respectively. Middle meningeal artery embolization was significantly associated with decreased odds of subdural hematoma reoperation (OR = 0.48; 95% CI, 23.4–99.1; $P = .047$) compared with surgery. The lowest rates of subdural hematoma radiologic recurrence, reoperation, and complications were observed among patients receiving embolization with Onyx, whereas good overall clinical outcome occurred most commonly with combined polyvinyl alcohol and coils.

LIMITATIONS: A limitation was the retrospective design of studies included.

CONCLUSIONS: Middle meningeal artery embolization is safe and effective, either as a primary or adjunctive treatment. Treatment using Onyx seems to yield lower rates of recurrence, rescue operation, and complications whereas particles and coils produce good overall clinical outcomes.

ABBREVIATIONS: cSDH = chronic subdural hematoma; MMA = middle meningeal artery; PVA = polyvinyl alcohol; SDH = subdural hematoma

Chronic subdural hematomas (cSDHs) are a commonly encountered intracranial pathology, occurring in 1–20.6 per 100,000 person-years.¹ The incidence is expected to rise as the population ages worldwide. Surgical evacuation of the hematoma

via burr-hole or craniotomy has remained the mainstay of treatment for many years.¹ However, the rate of recurrence or residual hematoma requiring an additional operation has been reported to be as high as 36.4%.²

Recently, there has been increasing interest in using middle meningeal artery (MMA) embolization as a treatment option for

Received August 21, 2022; accepted after revision January 24, 2023.

From the Division of Neurosurgery (J.C.K.), Department of Surgery and Institute of Medical Science (M.A.B.), University of Toronto, Toronto, Ontario, Canada; Neuroendovascular Program (A.A.D., J.E.V., R.W.R., C.J.S., A.B.P.), Massachusetts General Hospital, Harvard Medical School, Boston, Massachusetts; Departments of Radiology (M.A.E., S.G.), Mayo Clinic, Rochester, Minnesota; Department of Neurosurgery (M.A.E., D.A.), Montefiore Medical Center, Albert Einstein College of Medicine, New York, New York; Nuffield Department of Primary Care Health Sciences and Department for Continuing Education (EBHC program) (S.G.), Oxford University, Oxford, UK; and Neurointerventional Program (A.A.D., V.X.D.Y.), Department of Clinical Neurological Sciences & Medical Imaging, Schulich School of Medicine, Western University, London, Ontario, Canada.

J.C. Ku, A.A. Dmytriw, and M.A. Essibayi equally contributed to this manuscript.

Please address correspondence to Adam A. Dmytriw, MD, MPH, MSc, Neuroendovascular Program, Massachusetts General Hospital, Harvard Medical School, 55 Fruit St, Boston, MA 02114; e-mail: admytriw@mgh.harvard.edu

Indicates article with online supplemental data.

<http://dx.doi.org/10.3174/ajnr.A7796>

cSDH, because it targets the suspected underlying pathophysiology of cSDH. Although the mechanisms of cSDH accumulation are not fully understood, neovascularization from the MMA is thought to play an important role in cSDH propagation.³ Following accumulation of blood, usually from minor trauma, in the potential subdural space, the influx of inflammatory cells and proliferation of damaged dural border cells lead to neomembrane formation,⁴ neovascularization of the outer membrane, and recruitment of MMA feeders connecting to these neovessels of the outer membrane. Furthermore, these neovessels are leaky and allow continued exudation of blood products, causing further blood accumulation.⁴ Embolizing the MMA to eliminate the blood supply and source of cSDH accumulation has been proposed as both a primary and adjunctive treatment for cSDH,⁵ particularly in the elderly who have medical comorbidities and are on antithrombotic medications. However, as an emerging treatment, differences in technical aspects of the procedure abound, including in the choice of embolic agent.³ Particles, liquid embolic agents, coils, and a combination of these agents have all been tried in MMA embolization with varying results. Currently, there is no FDA approval for any of these agents specifically for this indication, though several industry-sponsored prospective trials are currently underway (NCT04402632, NCT04816591, NCT04065113, NCT04410146; clinicaltrials.gov).

A previous meta-analysis reported low rates of recurrence, surgical rescue, and in-hospital complications associated with MMA embolization; indeed, they were lower than those associated with conventional treatment (either surgery or conservative management).⁵ However, the authors were unable to examine technical nuances such as the choice of embolization agent due to insufficient data, and their assessment of MMA embolization as a primary or adjunctive treatment was also self-reportedly limited.⁵ Since that time, several additional double-arm studies have been published. Our study aimed to provide an updated meta-analysis to assess the outcomes following MMA embolization, including traditional surgical evacuation, and determine whether specific technical nuances, such as the choice of embolization agent, affect the postprocedural outcomes.

MATERIALS AND METHODS

Search Strategy

The search protocol, including research questions and inclusion and exclusion criteria, was developed a priori according to the Preferred Reporting Items for Systematic Reviews and Meta-Analyses (PRISMA) guidelines.

We queried the Ovid MEDLINE, EMBASE, Web of Science, and Cochrane Library databases from inception to March 2022 to identify studies reporting outcomes in patients with cSDH treated with MMA embolization (Online Supplemental Data). In addition, the references of included publications were searched manually for other relevant studies. The following keywords were used in combination, “subdural hematoma,” “cSDH,” “SDH,” “middle meningeal artery,” “MMA,” and “embolization,” to identify relevant articles. The search was limited to articles studying humans with patients 18 years of age or older, and in English.

Studies were included if they were randomized or had an observational prospective or retrospective study design and reported outcomes following MMA embolization in patients with cSDH. There were no restrictions on the size of the cSDH or the clinical status of the patients for inclusion. Both single- and double-arm studies were included. Exclusion criteria included case reports, case series with less than 5 patients, review articles, conference abstracts, animal studies, and non-peer-reviewed publications.

Primary MMA embolization was defined as MMA embolization without surgery. Adjunct MMA embolization was defined as planned MMA embolization with surgery; this could occur before or following surgery, as long as the procedures occurred within 48 hours of each other.

Outcomes

Outcomes were initially analyzed as a single group including both MMA embolization alone and MMA embolization and surgery groups. Further subgroup analysis dividing outcomes between both groups and additionally by the embolization agent was performed.

The primary outcomes of interest were rates of cSDH recurrence and cSDH rescue surgery following MMA embolization. Recurrence was defined as the re-accumulation of cSDH, as defined by the study authors, with or without the need for repeat surgery. Reoperation was defined as the need for surgical evacuation (or re-evacuation) of the cSDH following MMA embolization, either due to recurrence of cSDH or unsatisfactory results from the index procedure.

The complication rate following MMA embolization was also collected, and this included procedural-related complications or general complications that occurred during the follow-up interval, as reported by the study authors. Radiologic outcome at last follow-up was collected and dichotomized as good or poor outcome. A good outcome included >50% hematoma resolution, <10-mm residual hematoma width, or improvement on the last CT scans as defined by the study authors. When available, change in hematoma volume or width between the initial and last follow-up CT was also collected. Clinical outcome was collected and dichotomized as good or poor outcome. A good outcome included MR spectroscopy 0–2, Glasgow Outcome Score 4–5, Glasgow Outcome Scale-Extended 5–8, and improvement in neurologic or functional status or neurologic deficit at the last follow-up.

Data Extraction

The following data were extracted from each study: study design, country of origin, patient eligibility, inclusion/exclusion criteria, sex and age of patients, medical comorbidities, presenting neurologic status, presenting size of the cSDH, indication for MMA embolization, primary or adjunctive use of MMA embolization, and embolic agent. In addition, the outcomes of recurrence rates, surgical rescue, complications, radiologic outcome, and clinical outcome were also extracted.

Evaluation of Quality and Risk-of-Bias Assessment for Individual Studies

The Newcastle-Ottawa Quality Assessment Scale Case-Control Studies tool was used after modification to assess the risk of bias in

our included studies. The quality of all eligible studies was evaluated independently and in duplicate by 2 reviewers (J.C.K. and M.A.E.), using the 2011 Oxford Center for Evidence-Based Medicine levels of evidence.

Statistical Analysis

All studies that reported outcomes following MMA embolization in patients with cSDH were pooled for meta-analysis of outcomes via pooled weighted proportions or pooled weighted means for continuous outcomes. The results were pooled using ORs in studies that compared outcomes in MMA embolization versus surgery versus conservative management. Additional analyses were performed for MMA embolization as a primary or adjunctive treatment and to compare embolization approaches.

The Q-statistics test and calculation of I^2 were used to assess heterogeneity between studies. P values $< .05$ and I^2 values of $>50\%$ were defined as significant heterogeneity between studies. Pair-wise and subgroup meta-analyses were performed using a random effects model using the Freeman-Tukey transformed proportion and the DerSimonian-Laird approach. A P value $< .05$ was set for statistical significance. Assessment for risk of publication bias was performed using the Egger regression test for funnel-plot asymmetry for all variables that included data from ≥ 10 studies. If the Egger regression test demonstrated that there was a significant risk of publication bias ($P < .05$), the trim-and-fill approach was used to calculate the adjusted value. The meta-analysis was performed by using the OpenMeta-Analyst open source software (<https://abstracts.cochrane.org/2010-keystone/openmeta-analyst-open-source-cross-platform-software-advanced-meta-analysis>) and the MAJOR tool (metafor package) of Jamovi R-based statistical software (<https://www.jamovi.org/>).

RESULTS

Search Results

The search strategy returned 536 total and 291 deduplicated results, as seen in the PRISMA diagram (Online Supplemental Data). Following abstract screening and full-text review, 22 articles were included for analysis (Online Supplemental Data),⁶⁻²⁷ totaling 382 patients who underwent MMA embolization, compared with 1373 patients who underwent surgery. Overall, 133 of 757 (17.6%) patients had bilateral SDHs. The mean follow-up ranged between 2 and 26.3 months among studies. Three studies did not report any information on follow-up (Online Supplemental Data).

Study Characteristics

All studies included for analysis were case series, retrospective reviews, or prospective studies compared with a retrospective cohort. There were no prospective randomized trials. All retrospective studies were graded as level 4, and prospective studies with historical controls were graded as level 3, based on the Oxford Center for Evidence-Based Medicine 2011 levels of evidence. The risk of bias was low in 7, moderate in 14 studies, and high in 1 study. Twenty studies were retrospective, and 2 were prospective. The smallest study included 5 patients, and the

largest included 138 patients (Online Supplemental Data). Thirteen studies with 457 patients reported the outcomes stratified by treatment technique, 9 studies with 243 patients reported outcomes of patients receiving embolization only, and 10 studies reported outcomes of 278 patients undergoing combined surgery and embolization. Nine studies with 431 patients had no outcomes separated by treatment technique. Overall, 7 studies reported the outcomes of patients receiving embolization with polyvinyl alcohol (PVA); 4, with *n*-BCA; 3, with PVA \pm coils; and 2, with Onyx (Medtronic) embolization.

Single-Arm Overall Outcomes

Overall, 397 of 421 (96%; 95% CI, 93.4%–98.7%) patients demonstrated intraprocedural complete embolization of the MMA (Online Supplemental Data). The rate of subdural hematoma (SDH) recurrence was 4.1% (95% CI, 2.8%–5.4%) in 50 of 898 patients following MMA embolization (both primary and adjunct treatment) (Online Supplemental Data). On person-time analysis, the rate of SDH recurrence over time was 0.6% (95% CI, 0.3%–1%) per month (Online Supplemental Data). Fifty of 888 patients (4.2%; 95% CI, 2.9%–5.5%) underwent a reoperation for a recurrent or residual SDH (Online Supplemental Data). Thirty-six of 890 patients (2.6%; 95% CI, 1.2%–3.9%) experienced postoperative complications (Online Supplemental Data). These included 2 groin complications (1 groin hematoma, 1 femoral artery occlusion), 3 procedural complications (rupture of the MMA, 1 transient bradycardia during embolization), 4 postprocedural infarcts (clinical or radiologic), 10 medical complications (urinary tract infection, pneumonia, deep vein thrombosis, pulmonary embolism), and 15 seizures or new neurologic deficits or complications otherwise not specified.

The rates of good radiologic and clinical outcomes were 83.1% (382 of 518; 95% CI, 74.6%–91.5%) and 73.3% (292 of 372; 95% CI, 60%–86.6%), respectively (Online Supplemental Data). On follow-up, the SDH volume decreased with a mean reduction of 54.2 mL (95% CI, 46.3–62 mL) (Online Supplemental Data) and a mean reduction in SDH width of 9.9 mm (95% CI, 7.5–12.2 mm) (Online Supplemental Data).

Embolization Alone versus Adjunct to Surgery

The rates of SDH recurrence were comparable between patients who received embolization only (6.3%; 95% CI, 3.3%–9.3%) and those who received a combination of embolization and surgery (5.3%; 95% CI, 2.7%–7.9%; $P = .976$). On person-time analysis, the risk of SDH recurrence during follow-up in the embolization-only group was 1.7% (95% CI, 0.7%–2.6%) per month compared with 0.3% in the combined embolization and surgery group (95% CI, 0%–0.6%; $P = .035$). SDH reoperation was required in 5.4% (95% CI, 2.6%–8.2%) of patients undergoing embolization alone and in 4.6% (95% CI, 2%–7.2%; $P = .912$) of patients with combined embolization and surgery. Eight (2.2%; 95% CI, 0.4%–4%) of 243 patients with embolization alone and 22 (5.5%; 95% CI, 1.5%–9.5%; $P = .025$) of 280 patients with combined embolization and surgery experienced postoperative complications. Good radiologic resolution was reported in 94.1% (95% CI, 84.8%–

100%) of embolization alone and in 92.1% (95% CI, 85.8%–98.5%; $P = .187$) of combined embolization and surgery cohorts. Rates of good clinical outcomes were similar in the embolization alone (81.2%; 95% CI, 66.7%–95.6%) and combined embolization and surgery groups (75.3%; 95% CI, 36%–100%; $P = .569$).

Embolization Comparing Agent Choice

SDH recurred with a rate of 4.7% (95% CI, 1.5%–8%) in patients treated with PVA, 3.5% (95% CI, 0%–8.1%) with *n*-BCA, 2.2% (95% CI, 0%–5.1%) with PVA ± coils, and 2% (95% CI, 0%–6.4%) in patients receiving Onyx. The SDH reoperation rate was 4.2% (95% CI, 1.2%–7.3%) for PVA, followed by 4.1% (95% CI, 1%–7.3%) for PVA ± coils, 3.7% (95% CI, 0%–8.2%) for *n*-BCA, and 2% (95% CI, 0%–6.4%) in patients receiving Onyx. The rate of complications was 5.6% (95% CI, 1.1%–10.1%) for PVA, 3% (95% CI, 0%–6.9%) for *n*-BCA, 2% (95% CI, 0%–6.4%) in patients receiving Onyx, and 1.4% (95% CI, 0%–3.7%) in patients receiving PVA ± coils. Good radiologic outcomes were similar comparing embolization agents (Onyx: 82%; 95% CI, 57%–100% versus PVA ± coils: 84.4%; 95% CI, 63.9%–100%). Rates of good clinical outcomes were 85.2% (95% CI, 68.1%–100%) for PVA ± coils, 78.5% (95% CI, 55.9%–100%) for *n*-BCA, and 75.7% (95% CI, 63.8%–87.5%) in patients receiving Onyx. Detailed outcomes by treatment technique and embolization agent are available in the Online Supplemental Data.

Pair-Wise Meta-analysis Outcomes

On a pair-wise meta-analysis, there was no significant difference between MMA embolization alone and combined surgery with MMA embolization in terms of SDH recurrence (OR = 0.36; 95% CI, 0.12–1.09; $P = .071$). MMA embolization alone significantly decreased the odds of SDH reoperation (OR = 0.48; 95% CI, 23.4–99.1; $P = .047$) compared with surgery alone. No other significant differences were noted in other safety, radiologic, and clinical outcomes. Detailed outcomes of the 2-arm meta-analysis by treatment technique and embolization agent is available in the Online Supplemental Data.

Heterogeneity and Risk of Bias

Among the results of single-arm meta-analysis, high heterogeneity ($I^2 > 50\%$) was noted in the following outcomes: good radiologic outcomes (85.03%), good clinical outcomes (92.37%), and SDH width decrease (93.99%). Among pair-wise meta-analysis outcomes comparing MMA embolization with combined MMA embolization and surgery, there were good radiologic ($I^2 = 94.51\%$) and good clinical ($I^2 = 51.01\%$) outcomes; and among those comparing MMA embolization with conservative treatment, SDH reoperation outcome ($I^2 = 88.16\%$) showed high heterogeneity. A sensitivity analysis was performed taking into consideration the embolization agent used or by exclusion of individual studies thought to be the source of heterogeneity. Grouping good radiologic outcomes by treatment type led to a decrease in I^2 to null, supporting this as a reason for the high heterogeneity (Online Supplemental Data). I^2 for good clinical outcomes decreased from 93.37% to 71.81% and 64.98% following stratification of outcomes by treatment and embolization agent, respectively. Three studies were identified as main sources of

heterogeneity, including Enriquez-Marulanda et al,¹⁰ Okuma et al,²⁰ and Waqas et al,²⁶ which may relate to their inclusion of different treatment approaches (both embolization and combined) and different embolization agents (PVA and PVA + coils). Following exclusion of these studies, I^2 decreased to 21.38%, and the rate of good clinical outcomes increased from 73.3% (95% CI, 60%–86.6%) to 87.8% (95% CI, 83.2%–92.5%). The low number of studies (2–3) included in the pair-wise meta-analyses (good radiologic and clinical outcomes after MMA embolization compared with a combined approach, SDH reoperation outcomes after MMA embolization versus conservative management, and SDH width outcomes) was thought to be the main source of heterogeneity.

Publication bias was determined to be present for only good radiologic outcomes (83.1%; 95% CI, 74.6%–91.5%; P value = .0023) (Online Supplemental Data). The adjusted outcome based on the trim-and-fill approach was 73.9% (95% CI, 59.1%–86.7%).

DISCUSSION

Our systematic review and meta-analysis summarize the most recent literature reporting MMA embolization for patients with cSDH in comparison with surgical interventions and draw attention to the importance of the choice of embolization agent for treatment success, in addition to the baseline patient clinical status, anatomic variations of the MMA, and experience of the neurointerventionalist. Most patients receiving MMA embolization achieved good clinical outcomes with an excellent rate of good radiologic outcomes and low recurrence and reoperation rates. There were no differences in outcomes comparing embolization-only and combined embolization with surgery except for reoperation and complication rates, which were significantly higher in the combined approach. Patients receiving embolization via PVA accompanied by coils had relatively improved radiologic (84.4%) and clinical outcomes (85.2%) but slightly higher reoperation rates (4.1%), whereas patients embolized with Onyx had the lowest rates of SDH recurrence (2%), reoperation (2%), and complications (2%).

Surgical evacuation of cSDH is associated with high rates of recurrence and complications.²⁸ Therefore, it may be a less desirable option for elderly patients with poor baseline clinical status and significant underlying comorbidities. On the other hand, it may also be unnecessary for patients with favorable clinical and radiologic status.²⁹ The use of less invasive treatment based on a better understanding of the pathophysiology of SDH will likely improve the outcomes. Thus, surgical evacuation may be reserved for those likely to benefit most, highlighting the need for optimization of treatment selection. Embolization of the MMA has gained considerable popularity in the past 2 decades.^{6,14,26} Most patients having undergone MMA embolization in this study achieved excellent clinical and radiologic outcomes, compared with the surgery cohort.

MMA embolization and surgery could have synergistic goals when used in a combined approach appropriately for patients with mass-effect symptoms. Surgery can alleviate those symptoms, whereas MMA embolization can decrease the recurrence of SDH. However, we did not observe a significant difference between the 2 approaches (MMA embolization alone versus MMA

embolization with surgery) in these outcomes. This result may be due to selection bias related to the retrospective nature of most of the included studies, in which patients undergo embolization alone or embolization with surgery based on their clinical presentation and the operator's decision-making. Furthermore, considerable heterogeneity exists in follow-up periods among studies, which was validated by the significant difference in the SDH recurrence rate per month between MMA embolization alone (1.7%/month) and combined embolization and surgery (0.3%/month). Thus, the combined approach might be associated with better radiologic outcomes but was not found to positively affect the clinical outcomes in this study. Unsurprisingly, this combined approach might add more morbidity related to the higher complication rates (5.5% reported compared with embolization alone (2.2%). The 2-stage nature of the combined approach explains the higher complication rate of embolization accompanied by surgery because each procedure has its own risks.

Reoperation rates were lower in the MMA embolization cohort compared with surgery alone, emphasizing the role of embolization in decreasing the overall morbidity in elderly patients and efficacy in the management of cSDH. Covariates, such as age, hematoma side (unilateral, bilateral), and other hematoma characteristics, and clinical comorbidities play a crucial role in the selection of the optimal treatment for cSDH. The choice of embolization agent is a crucial factor that was demonstrated to affect outcomes on the basis of experimental and a few observational studies. Shapiro et al,³ in a comprehensive review of the pathoanatomy of SDH, summarized the theoretic advantages and disadvantages of different embolization agents. PVA may have better penetration distally but higher recurrence rates compared with liquid agents, related to delayed recanalization. Liquid agents, such as Onyx or *n*-BCA, may be associated with a lower penetration profile but a more stable occlusion. Furthermore, coils are highly thrombogenic and can be deployed, commonly into the more proximal artery, along with PVA, leading to a more stable and permanent occlusion.

Operator experience and comfort level with a specific embolic agent also play a role in its safety and efficacy. Rates of radiologic and clinical outcomes of patients receiving MMA embolization were comparable among the embolization agents. However, high recurrence rates were reported after PVA alone but not with PVA and coils, emphasizing the benefit of combining agents to achieve better stability. Most interesting, reoperation was noted to be slightly higher in patients treated with PVA alone but also in those treated with PVA and coils. PVA was nonsignificantly associated with a slightly higher complication rate. This finding warrants further study but may be related to its higher risk of penetrating into collaterals, such as those to the ophthalmic artery. Across all agents, Onyx was associated with the lowest recurrence, reoperation, and complication rates.

Conservative care with observation and medical management may be preferable for patients with an asymptomatic presentation or those with very severe symptoms and poor baselines in which neither surgery nor MMA embolization is likely to offer benefit.³⁰ Catapano et al,³⁰ in a propensity-adjusted comparison of 35 patients receiving MMA embolization versus 196 patients treated conservatively, reported no difference in clinical outcomes; however, conservative treatment was much more commonly associated

with treatment failure (OR = 13; 95% CI, 1.7–99; $P = .01$) and incomplete hemorrhage resolution (OR = 5.4; 95% CI, 2.5–12; $P < .001$). Still, data available about outcomes of conservative management compared with MMA embolization are scarce, and further studies are warranted. Furthermore, treatment-selection criteria must be better defined on the basis of clinical status and radiographic characteristics. Thus, large multicenter cohort studies stratifying outcomes after these different approaches (MMA embolization, surgery alone, combined approach, and conservative approach) by anatomic characteristics of SDH and baseline clinical characteristics are needed to identify the patient-specific optimal treatment and develop clinical treatment guidelines.

Limitations

As with most systematic reviews and meta-analyses, this study was limited by the number of studies meeting the inclusion criteria and the quality of those studies. There were no randomized controlled trials. Nevertheless, this does represent the largest cohort of patients studied to date. Additionally, our meta-analysis showed considerable heterogeneity in several outcomes, particularly clinical and radiologic outcomes, which had additionally low report rates, with only 11 of 22 studies reporting their outcomes. This considerable heterogeneity was likely due to heterogeneous procedural details (embolization alone versus combined treatment, choice of different embolic agents), so while these outcomes provide a broad overview of the potential for MMA embolization, the outcomes from the additional analyses comparing agents may be more applicable to specific patient situations. There may also be substantial variations among individual studies with regard to treatment selection for MMA embolization versus surgery alone versus a combined approach. Patients undergoing surgery may have more severe symptoms based on cSDH mass effect requiring decompression. We were unable to assess the effect of this variable on postprocedural outcomes, and future clinical trials should consider this for patient treatment selection.

CONCLUSIONS

MMA embolization appears to be a safe and effective intervention for cSDH, either as a primary or adjunctive treatment. The combined approach may be best used for patients with large hemorrhages to alleviate mass effect while decreasing the risk of recurrence. PVA alone may have higher rates of recurrence, but the addition of coils with PVA improved stability rates. Embolization using Onyx seems to lead to lower rates of recurrence, rescue operations, and complications. Further large multicenter studies and randomized trials evaluating safety, radiologic outcomes, and clinical outcomes are warranted to better understand the characteristics associated with the benefit of different embolization agents and to set updated management guidelines for the treatment of cSDH.

Disclosure forms provided by the authors are available with the full text and PDF of this article at www.ajnr.org.

REFERENCES

1. Sahyouni R, Goshtasbi K, Mahmoodi A, et al. **Chronic subdural hematoma: a historical and clinical perspective.** *World Neurosurg* 2017;108:948–53 CrossRef Medline

2. Ridwan S, Bohrer AM, Grote A, et al. **Surgical treatment of chronic subdural hematoma: predicting recurrence and cure.** *World Neurosurg* 2019;128:e1010–23 CrossRef Medline
3. Shapiro M, Walker M, Carroll KT, et al. **Neuroanatomy of cranial dural vessels: implications for subdural hematoma embolization.** *J Neurointerv Surg* 2021;13:471–77 CrossRef Medline
4. Moshayedi P, Liebeskind DS. **Middle meningeal artery embolization in chronic subdural hematoma: implications of pathophysiology in trial design.** *Front Neurol* 2020;11:923 CrossRef Medline
5. Ironside N, Nguyen C, Do Q, et al. **Middle meningeal artery embolization for chronic subdural hematoma: a systematic review and meta-analysis.** *J Neurointerv Surg* 2021;13:951–57 CrossRef Medline
6. Al-Mufti F, Kaur G, Amuluru K, et al. **Middle meningeal artery embolization using combined particle embolization and n-BCA with the dextrose 5% in water push technique for chronic subdural hematomas: a prospective safety and feasibility study.** *AJNR Am J Neuroradiol* 2021;42:916–20 CrossRef Medline
7. Ban SP, Hwang G, Byoun HS, et al. **Middle meningeal artery embolization for chronic subdural hematoma.** *Radiology* 2018;286:992–99 CrossRef Medline
8. Carpenter A, Rock M, Dowlati E, et al. **Middle meningeal artery embolization with subdural evacuating port system for primary management of chronic subdural hematomas.** *Neurosurg Rev* 2022; 45:439–49 CrossRef Medline
9. Catapano JS, Ducruet AF, Nguyen CL, et al. **Middle meningeal artery embolization for chronic subdural hematoma: an institutional technical analysis.** *J Neurointerv Surg* 2021;13:657–60 CrossRef Medline
10. Enriquez-Marulanda A, Gomez-Paz S, Salem MM, et al. **Middle meningeal artery embolization versus conventional treatment of chronic subdural hematomas.** *Neurosurgery* 2021;89:486–95 CrossRef Medline
11. Fan G, Wang H, Ding J, et al. **Application of absolute alcohol in the treatment of traumatic intracranial hemorrhage via interventional embolization of middle meningeal artery.** *Front Neurol* 2020;11:824 CrossRef Medline
12. Hashimoto T, Ohashi T, Watanabe D, et al. **Usefulness of embolization of the middle meningeal artery for refractory chronic subdural hematomas.** *Surg Neurol Int* 2013;4:104 CrossRef Medline
13. Joyce E, Bounajem MT, Scoville J, et al. **Middle meningeal artery embolization treatment of nonacute subdural hematomas in the elderly: a multiinstitutional experience of 151 cases.** *Neurosurg Focus* 2020;49:E5 CrossRef Medline
14. Kan P, Maragkos GA, Srivatsan A, et al. **Middle meningeal artery embolization for chronic subdural hematoma: a multi-center experience of 154 consecutive embolizations.** *Neurosurgery* 2021;88:268–77 CrossRef Medline
15. Kim E. **Embolization therapy for refractory hemorrhage in patients with chronic subdural hematomas.** *World Neurosurg* 2017;101:520–27 CrossRef Medline
16. Link TW, Boddu S, Paine SM, et al. **Middle meningeal artery embolization for chronic subdural hematoma: a series of 60 cases.** *Neurosurgery* 2019;85:801–07 CrossRef Medline
17. Mureb MC, Kondziolka D, Shapiro M, et al. **DynaCT enhancement of subdural membranes after middle meningeal artery embolization: insights into pathophysiology.** *World Neurosurgery* 2020;139:e265–70 CrossRef Medline
18. Nakagawa I, Park HS, Kotsugi M, et al. **Enhanced hematoma membrane on DynaCT images during middle meningeal artery embolization for persistently recurrent chronic subdural hematoma.** *World Neurosurg* 2019;126:e473–79 CrossRef Medline
19. Ng S, Derraz I, Boetto J, et al. **Middle meningeal artery embolization as an adjuvant treatment to surgery for symptomatic chronic subdural hematoma: a pilot study assessing hematoma volume resorption.** *J Neurointerv Surg* 2020;12:695–99 CrossRef Medline
20. Okuma Y, Hirotsune N, Sato Y, et al. **Midterm follow-up of patients with middle meningeal artery embolization in intractable chronic subdural hematoma.** *World Neurosurg* 2019;126:e671–78 CrossRef Medline
21. Onyinzor C, Berlis A, Abel M, et al. **Efficacy and mid-term outcome of middle meningeal artery embolization with or without burr hole evacuation for chronic subdural hematoma compared with burr hole evacuation alone.** *J Neurointerv Surg* 2022;14:297–300 CrossRef Medline
22. Rajah GB, Waqas M, Dossani RH, et al. **Transradial middle meningeal artery embolization for chronic subdural hematoma using Onyx: case series.** *J Neurointerv Surg* 2020;12:1214–18 CrossRef Medline
23. Schwarz J, Carnevale JA, Goldberg JL, et al. **Perioperative prophylactic middle meningeal artery embolization for chronic subdural hematoma: a series of 44 cases.** *J Neurosurg* 2021 May 21. [Epub ahead of print] CrossRef Medline
24. Shotar E, Meyblum L, Premat K, et al. **Middle meningeal artery embolization reduces the post-operative recurrence rate of at-risk chronic subdural hematoma.** *J Neurointerv Surg* 2020;12:1209–13 CrossRef Medline
25. Tempaku A, Yamauchi S, Ikeda H, et al. **Usefulness of interventional embolization of the middle meningeal artery for recurrent chronic subdural hematoma: five cases and a review of the literature.** *Interv Neuroradiol* 2015;21:366–71 CrossRef Medline
26. Waqas M, Vakhari K, Weimer PV, et al. **Safety and effectiveness of embolization for chronic subdural hematoma: systematic review and case series.** *World Neurosurg* 2019;126:228–36 CrossRef Medline
27. Yajima H, Kanaya H, Ogino M, et al. **Middle meningeal artery embolization for chronic subdural hematoma with high risk of recurrence: a single institution experience.** *Clin Neurol Neurosurg* 2020;197:106097 CrossRef Medline
28. Almenawer SA, Farrokhyar F, Hong C, et al. **Chronic subdural hematoma management: a systematic review and meta-analysis of 34,829 patients.** *Ann Surg* 2014;259:449–57 CrossRef Medline
29. Scerrati A, Visani J, Ricciardi L, et al. **To drill or not to drill, that is the question: nonsurgical treatment of chronic subdural hematoma in the elderly: a systematic review.** *Neurosurg Focus* 2020;49: E7 CrossRef Medline
30. Catapano JS, Ducruet AF, Nguyen CL, et al. **A propensity-adjusted comparison of middle meningeal artery embolization versus conventional therapy for chronic subdural hematomas.** *J Neurosurg* 2021;135:1208–13 CrossRef Medline

Endovascular Recanalization of Symptomatic Chronic ICA Occlusion: Procedural Outcomes and Radiologic Predictors

C. Zhou, Y.-Z. Cao, Z.-Y. Jia, L.-B. Zhao, S.-S. Lu, H.-B. Shi, and S. Liu

ABSTRACT

BACKGROUND AND PURPOSE: Endovascular recanalization has been attempted in patients with symptomatic chronic ICA occlusion, however, the heterogeneity of recanalization outcomes and the perioperative complications present challenges for the clinical application. Our aim was to evaluate the safety and efficacy of endovascular recanalization for symptomatic chronic ICA occlusion and identify potential predictors for successful recanalization.

MATERIALS AND METHODS: This study included 47 consecutive patients with symptomatic chronic ICA occlusion who underwent endovascular recanalization at our institution. Patients' clinical information, radiologic characteristics, procedural results, and outcomes were recorded. Factors related to technical success were analyzed by univariate and multivariate analyses.

RESULTS: The technical success rate was 74.5% (35/47); 12.8% of patients (6/47) experienced intraoperative complications, but none had permanent neurologic deficits. Three months after recanalization, 21 of the 29 recanalized patients (72.4%) and 3 of the 10 failed patients (30.0%) demonstrated improved mRS scores. Restenosis or re-occlusion occurred in 12.9% of patients (4/31) with successful recanalization. Multivariate analysis showed that tapered or blunt stump ($P = .016$), distal ICA occlusion segment (below the cavernous segment versus at or above the ophthalmic segment, $P = .003$; at the cavernous or clinoid segment versus at or above the ophthalmic segment, $P = .027$), and radiologic occlusion to recanalization of ≤ 3 months ($P = .044$) were significantly associated with successful recanalization. Patients were assigned points according to the coefficients of the prediction model, and the technical success rates were 0%, 46.2%, 90.5%, and 100% in patients with 1, 2, 3, and 4 points, respectively.

CONCLUSIONS: Endovascular recanalization is a safe and effective treatment for symptomatic chronic ICA occlusion in selected patients. A residual stump, low levels of the distal ICA occlusion segment, and a short radiologic occlusion time were identified as positive predictors of technical success.

ABBREVIATIONS: AUC = area under the curve; CICA0 = chronic ICA occlusion; HR-MRI = high-resolution MR imaging

Most patients with chronic internal carotid artery occlusion (CICA0) can be treated successfully with aggressive medical management. However, some patients (6%–20%) remain at risk of recurrent TIA or ipsilateral ischemic stroke,^{1,2} which are mainly caused by impaired cerebral perfusion or a carotid stump embolism in the downstream circulation.^{3,4}

The optimal treatment for symptomatic CICA0 is unclear, especially in patients refractory to aggressive medical management.

According to previous research, surgical revascularization with extracranial–intracranial artery bypass is not superior to medical therapy in patients with hemodynamic impairment and does not reduce the risk of recurrent cerebrovascular events.^{5,6} Some studies have demonstrated that carotid endarterectomy can successfully revascularize a short extracranial ICA occlusion but is ineffective for long segmental and intracranial lesions.^{7,8} Hybrid surgery seems to compensate for these drawbacks, but it is associated with increased perioperative stroke and mortality rates because of the complicated postoperative management related to open surgery and intensive antiplatelet or anticoagulant protocols.⁹ In recent years, some case series on endovascular recanalization monotherapy have been published. However, the procedure is technically demanding, has varying success rates (ranging from 53.3% to 93.3%), and carries a high risk of perioperative complications, such as dissection, distal embolization, and hyperperfusion syndrome.^{10,11} Moreover, research is limited by the small number

Received August 31, 2022; accepted after revision January 24, 2023.

From the Departments of Interventional Radiology (C.Z., Y.-Z.C., Z.-Y.J., L.-B.Z., H.-B.S., S.L.) and Radiology (S.-S.L.), The First Affiliated Hospital of Nanjing Medical University, Nanjing, China.

C. Zhou, Y.Z. Cao, and S. Liu contributed equally to this work.

Please address correspondence to Sheng Liu, MD, PhD, Department of Interventional Radiology, The First Affiliated Hospital of Nanjing Medical University, 300 Guangzhou Rd, Nanjing, 210029, China; e-mail: liusheng@njmu.edu.cn

<http://dx.doi.org/10.3174/ajnr.A7804>

of cases; therefore, the preoperative radiologic predictors of successful recanalization for symptomatic CICA0 have not been thoroughly investigated.

Hence, we performed a retrospective study to evaluate the success rate and outcomes of endovascular recanalization for symptomatic CICA0 at our center. Furthermore, we identified potential radiologic predictors of successful recanalization, which will help clinicians select appropriate candidates for this procedure.

MATERIALS AND METHODS

Study Population

This study retrospectively analyzed 47 patients with symptomatic CICA0 who underwent endovascular recanalization at our institution from January 2018 to December 2021. All treatment choices were made according to the multidisciplinary consultation of the doctors in the neurology, neurosurgery, vascular surgery, and interventional radiology departments, along with the treatment wishes of patients and families. Chronic occlusion was considered as ≥ 4 weeks after onset. The inclusion criteria were as follows: 1) atherosclerotic CICA0, defined as 100% cross-sectional truncation of the vessel lumen observed by CTA or MRA and confirmed by DSA, 2) aggravation or recurrence of neurologic symptoms (TIA or stroke) despite aggressive medical treatment, and 3) hypoperfusion in the CICA0 territory confirmed by preoperative CTP or MR perfusion imaging. The following exclusion criteria were applied: 1) acute occlusion of the carotid artery; 2) asymptomatic lesions; 3) nonatherosclerotic or dissection occlusion, including Moyamoya disease, vasculitis, and trauma; 4) neurologic symptom aggravation or recurrence due to hemorrhagic transformation of infarction, a new infarction in the nonoccluded vessel territory, hypovolemia or systemic hypotension, heart and kidney insufficiency, severe infection, or high fever; 5) occurrence of a bleeding disorder in the past 3 months; and 6) allergies or contraindications to contrast media, heparin, or anesthesia. This study was approved by the ethics committee of our institution and conducted in accordance with the mandates of the Declaration of Helsinki (2008). Because of the retrospective nature of the study, the requirement for patients to provide informed consent was waived.

Clinical and Radiologic Assessment

Patients' clinical information, including the mRS score, was recorded. Two independent neuroradiologists performed all image assessments, and discrepancies were resolved by consensus. Brain CTP or MR perfusion was performed to evaluate cerebral hemodynamics and perfusion–diffusion mismatch. Cerebral hypoperfusion ipsilateral to the ICA occlusion was defined as delayed perfusion throughout the ipsilateral hemisphere with delayed TTP, increased MTT, and decreased regional CBF.¹² High-resolution MR imaging (HR-MRI) was used to analyze the occlusion etiology, proximal stump morphology, distal ICA occlusion segment, occlusion length, and luminal thrombosis. Several patients had poor-quality HR-MRI or did not have HR-MRI; these patients underwent preoperative vascular assessment by multiple simulated CTA images, which were reconstructed from the CTP images. Occlusion length was automatically calculated by the software after manual tracing of the longitudinal axis of the occluded vasculature.¹³ Segments of the

ICA were evaluated according to the classification criteria proposed by Bouthillier et al.¹⁴

Endovascular Treatment

Patients received aspirin, 100 mg/day, and clopidogrel, 75 mg/day, for at least 5 days before the procedure; subsequently, a thromboelastogram was used to evaluate platelet reactivity. Aspirin resistance was defined as $< 50\%$ inhibition of arachidonic acid–induced platelet aggregation, and clopidogrel resistance was defined as $< 30\%$ inhibition of adenosine diphosphate–induced platelet aggregation. No cases of aspirin resistance were observed, whereas 4 patients showed clopidogrel resistance and were treated with ticagrelor, 90 mg twice a day. All angiographic procedures and angioplasties were performed with the patient under general anesthesia by experienced neurointerventionalists. Intravenous heparin boluses were administered to maintain an activated clotting time of 250–300 seconds during the procedures.

Femoral access was achieved with an 8F sheath introducer and an 8F guiding catheter (Envoy, Codman Neuro) placed into the common carotid artery proximal to the occluded segment. Using roadmap guidance, the surgeon first attempted to pass a 0.035-inch Radifocus Guide Wire M (Terumo) in combination with a 4F vertebral angiographic catheter (Cordis) through the tapered stump or vulnerable area to the distal cervical ICA. Then, a 300-cm 0.014-inch exchange microwire (Transend or Synchro, Stryker) and an Echelon microcatheter (Medtronic) were used to advance further into the occluded segment and were navigated into the intracranial ICA. Thereafter, angiographic projections were performed to confirm the position of the microcatheter in the true lumen, assess the extent of the ICA thrombus, and confirm the patency of intracranial vessels. A SpiderFX embolic protection device (Medtronic) was typically used if short occlusions without tandem lesions and an adequate landing zone were identified. The Mo.Ma occlusion system (Medtronic) was sporadically used to protect against embolization in cases with suspected unstable thrombosis.

On the preoperative HR-MRI, high intraluminal signals on the unenhanced T1-sampling perfection with application-optimized contrasts by using different flip angle evolution (SPACE) sequence (Siemens) beyond the cervical occlusion site might have suggested intraluminal unstable thrombosis, and the procedure was commonly initiated by direct aspiration first. Otherwise, the procedure was initiated by predilation through the occlusive section with a small-diameter angioplasty balloon (2–3 mm), followed by closed-cell stent insertion, if appropriate. An open-cell stent was deployed for extremely tortuous vascular structures. A Wallstent (Boston Scientific), Precise stent (Cordis), or Protégé stent (Medtronic) was deployed for cervical ICAs. An Enterprise stent (Codman), LEO Plus stent (Balt), or Neuroform EZ stent (Stryker) was deployed for distal lesions.

If ≥ 2 stents were needed, they were deployed from the distal to the proximal region. The stent size was selected according to the proximal and distal diameters of the lesion and the length of the occluded segment. Postoperative angiography was performed to confirm patency and assess residual stenosis and distal perfusion. Post-balloon dilation was performed if residual stenosis within the stent was $> 50\%$. Successful recanalization was considered when

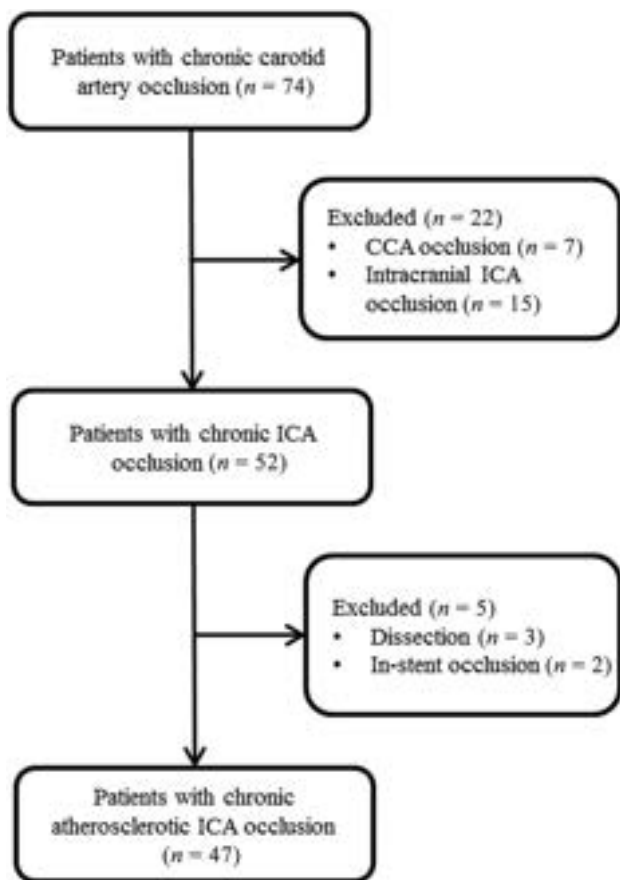


FIG 1. Patient flow diagram. CCA indicates common carotid artery.

the occlusion segment was stented with a final residual diameter stenosis of <30% and TICI grade 3 antegrade flow was established after intervention.

After the procedure, brain CT was performed immediately to rule out potential intracranial hemorrhage. Systolic blood pressure was strictly maintained at 100–120 mm Hg or decreased by 20% of the baseline value to prevent hyperperfusion syndrome. Regular dual-antiplatelet agents (aspirin, 100 mg/day, and clopidogrel, 75 mg/day), proper control of risk factors, and effective rehabilitation training were also prescribed.

Follow-up Outcomes

After discharge, dual-antiplatelet therapy was maintained for 3 months, and life-long aspirin or clopidogrel monotherapy was continued thereafter. Patients were also treated with statins and other medications to control risk factors. CTA or DSA was routinely performed 3 months after successful recanalization procedures and annually thereafter or when restenosis was suspected. Restenosis and re-occlusion were defined as a stenosis diameter of >50% and total occlusion of the target artery segment, respectively. Follow-ups were completed by clinic visits or telephone every 3 months until the end of April 2022. New neurologic deficits (TIA or stroke), intracranial hemorrhages, and deaths were recorded.

Statistical Analysis

All statistical analyses were performed with SPSS 25.0 (IBM). Categorical data are presented as counts and percentages. Continuous

data are expressed as the mean (SD) or as the median and interquartile range. Univariate analysis was performed by the Fisher exact or χ^2 tests for categorical data and 2-sample *t* tests or Mann-Whitney *U* tests for continuous data. To identify the factors independently associated with successful recanalization, we performed multivariable logistic regression; all variables with a *P* value of <.2 in the univariate analysis were included. ORs and their 95% confidence intervals were calculated. Then, a score-based prediction model was constructed with a regression coefficient–based scoring method. The points assigned to each variable were proportional to the regression coefficients of the variable rounded to the nearest integers. Statistical significance was set at a 2-sided *P* value of <.05.

RESULTS

Baseline Characteristics

A total of 47 patients (42 men; mean age, 63.6 [SD, 9.6] years) with symptomatic CICA/O were enrolled (Fig 1). Many patients had chronic comorbidities such as hypertension (66.0%), diabetes mellitus (34.0%), hyperlipidemia (10.6%), and cardiac disease (14.9%). In addition, 23 (48.9%) had a history of smoking, and 15 (31.9%) had a history of drinking. Preoperative vascular assessment by HR-MRI was performed in 38 patients (80.9%), and 9 patients (19.1%) were assessed by simulated multiple CTA images, which were reconstructed from the CTP images. The detailed patient characteristics and angiographic findings are presented in Table 1.

Procedural Outcomes and Follow-up

A total of 35 (74.5%) patients achieved successful recanalization. After the wires crossed the occlusion, embolic-protection devices were used in 34.3% (12/35) of patients: Ten patients received the SpiderFX device and 2 received the Mo.Ma occlusion system. The overall intraoperative complication rate was 12.8% (6/47); 1 patient had a slight subarachnoid hemorrhage followed by micro-wire perforation, 3 patients had asymptomatic dissection (2 of whom were treated with stent implantation), and 2 patients had distal embolization. Neither of the latter 2 patients exhibited new neurologic symptoms with successful mechanical thrombectomy. The rate of stroke or death within 30 days was 6.4% (3/47). One older adult patient died of massive reperfusion hemorrhage 1 day after the procedure. The other 2 patients developed new neurologic symptoms 2 and 10 days after their procedures (their mRS scores were 2 and 4, respectively). CTP revealed significant hypoperfusion on the recanalization side, and CTA showed in-stent thrombosis. The symptoms of both patients improved after emergency mechanical thrombectomy (local arterial thrombolysis combined with balloon dilation) and subsequent drug and rehabilitation treatment. No strokes or deaths occurred during hospitalization in the failed recanalization group.

The median follow-up period was 13.0 months (range, 2.3–51.8 months). At the 3-month follow-up, 21 of 29 patients having undergone recanalization (72.4%) with preoperative mRS scores of ≥ 1 showed improvement in their mRS scores, whereas only 3 of 10 patients (30.0%) with failed recanalization and preoperative mRS scores of ≥ 1 showed improvement in their mRS scores. Restenosis or re-occlusion occurred in 12.9% of recanalized

Table 1: Baseline characteristics of the studied patient population as stratified by failed or successful recanalization

Characteristics	Total (n = 47)	Successful (n = 35)	Failed (n = 12)	P Value
Mean age (yr)	63.6 (SD, 9.6)	64.3 (SD, 9.8)	61.8 (SD, 9.2)	.443
Male sex (No.) (%)	42 (89.4%)	31 (88.6%)	11 (91.7%)	1
Risk factors				
Hypertension (No.) (%)	31 (66.0%)	23 (65.7%)	8 (66.7%)	1
Diabetes mellitus (No.) (%)	16 (34.0%)	14 (40.0%)	2 (16.7%)	.263
Hyperlipidemia (No.) (%)	5 (10.6%)	4 (11.4%)	1 (8.3%)	1
Cardiac disease (No.) (%)	7 (14.9%)	6 (17.1%)	1 (8.3%)	.787
Smoking history (No.) (%)	23 (48.9%)	17 (48.6%)	6 (50.0%)	.932
Drinking history (No.) (%)	15 (31.9%)	12 (25.5%)	3 (25.0%)	.813
Neurologic symptoms				1
TIA (No.) (%)	8 (17.0%)	6 (17.1%)	2 (16.7%)	
Stroke (No.) (%)	39 (83.0%)	29 (82.9%)	10 (83.3%)	
Preoperative mRS score (median) (IQR)	1 (1–2)	1 (1–2)	1 (1–1)	.497
Radiologic characteristics				
Right-sided recanalization (No.) (%)	20 (42.6%)	16 (45.7%)	4 (33.3%)	.454
ICA stump morphology				.181
Tapered or blunt stump (No.) (%)	36 (76.6%)	29 (82.9%)	7 (58.3%)	
No stump (No.) (%)	11 (23.4%)	6 (17.1%)	5 (41.7%)	
Level of distal ICA occlusion segment				.004
Below the cavernous segment (No.) (%)	17 (36.2%)	16 (45.7%)	1 (8.3%)	
At the cavernous or clinoid segment (No.) (%)	21 (44.7%)	16 (45.7%)	5 (41.7%)	
At or above the ophthalmic segment (No.) (%)	9 (19.1%)	3 (8.6%)	6 (50%)	
Occlusion length ≤5cm (No.) (%)	12 (25.5%)	12 (34.3%)	0 (0%)	.049
Radiologic occlusion to recanalization ≤3 mo (No.) (%)	41 (87.2%)	32 (91.4%)	9 (75.0%)	.164

Note:—IQR indicates interquartile range.

Table 2: Multivariate analysis of factors influencing the successful recanalization^a

Characteristics	OR	95% CI for OR	β Coefficient	Points Assigned	P Value
Tapered or blunt stump (vs no stump)	25.8	1.8–364.7	3.251	1	.016
Level of distal ICA occlusion segment					
Below the cavernous segment (vs at or above the ophthalmic segment)	306.6	6.6–14,168.9	5.726	2	.003
At the cavernous or clinoid segment (vs at or above the ophthalmic segment)	11.4	1.3–98.0	2.434	1	.027
Radiologic occlusion to recanalization ≤3 mo (vs >3 months)	10.9	1.1–111.5	2.387	1	.044

^a The following variable was removed from the model: occlusion length ≤5 cm.

patients (4/31) who had follow-up imaging: Three presented with asymptomatic re-occlusion, and the other presented with symptomatic restenosis (recurrent dizziness). The latter patient received subsequent balloon dilation therapy. No recurrent TIA or stroke occurred in the other patients with successful recanalization during the clinical follow-up period. Of the 12 patients with failed recanalization, 3 patients (25.0%) experienced recurrent TIA or stroke and 1 patient with stroke died despite aggressive medical management.

Predictive Factors and Construction of a Scoring System

No significant differences were found in demographics, risk factors, or symptoms between the successful and failed recanalization groups. The distal ICA occlusion segment tended to be at a lower level in the successful recanalization group than in the failed recanalization group (technical success rates: below the cavernous segment, 94.1%; at the cavernous or clinoid segment, 76.2%; at or above the ophthalmic segment, 33.3%; $P = .004$). Multivariate analysis with logistic regression revealed that the following factors were significantly associated with successful recanalization: tapered or blunt stump (OR = 25.8; 95% CI, 1.8–364.7; $P = .016$), distal ICA occlusion segment (below the

cavernous segment versus at or above the ophthalmic segment) (OR = 306.6; 95% CI, 6.6–14,168.9; $P = .003$); at the cavernous or clinoid segment versus at or above the ophthalmic segment (OR = 11.4; 95% CI, 1.3–98.0; $P = .027$), and radiologic occlusion to recanalization of ≤3 months (OR = 10.9; 95% CI, 1.1–111.5; $P = .044$).

By means of the independent predictors obtained from multivariate analysis, a scoring system was created to predict the technical success rate of CICA O recanalization. Points for each variable were assigned as described in the materials and methods section (Table 2). Receiver operating characteristic curves were plotted to evaluate the predictive value of each factor and the combination of the 3 factors (Fig 2). The results demonstrated that the combination of the 3 factors had the highest efficacy for predicting successful recanalization (area under the curve [AUC] = 0.876). Furthermore, the technical success rates were 0%, 46.2%, 90.5%, and 100% in patients who were assigned 1, 2, 3, and 4 points, respectively (Fig 3). A representative case is presented in Fig 4.

DISCUSSION

Recently, several studies with small sample sizes have reported that endovascular recanalization is a feasible strategy to treat

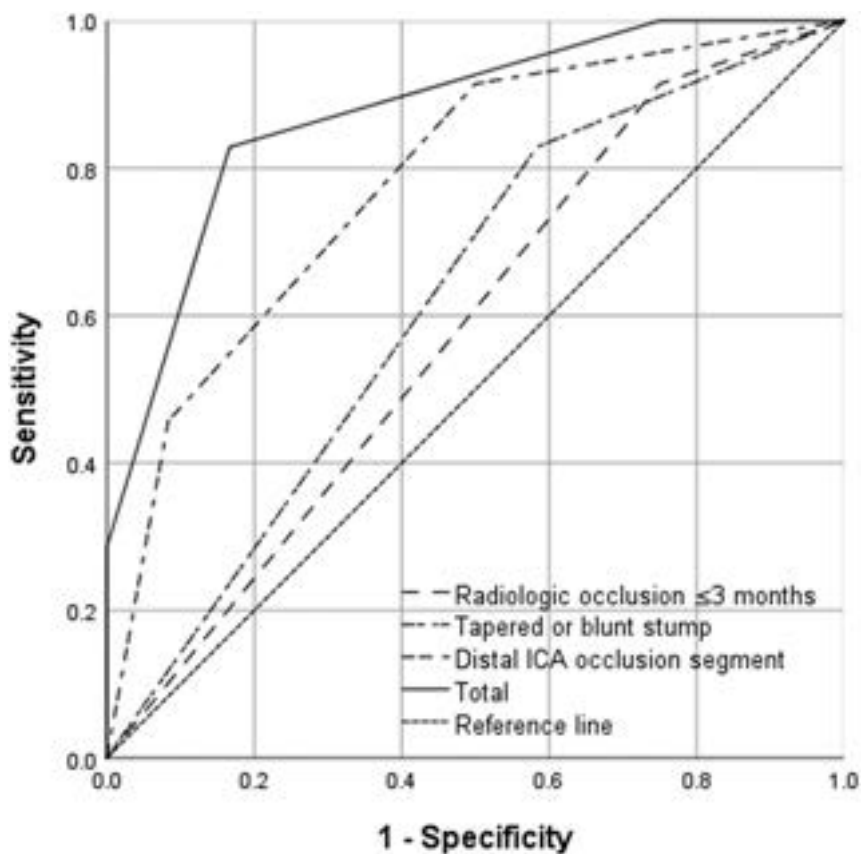


FIG 2. ROC curves were plotted to evaluate the predictive value of every factor (a tapered or blunt stump, the level of distal ICA occlusion segment, radiologic occlusion to recanalization of ≤ 3 months) and the combination of the 3 factors. The results show that the combination of these 3 factors showed the highest efficacy (AUC = 0.876). ROC indicates receiver operating characteristic.

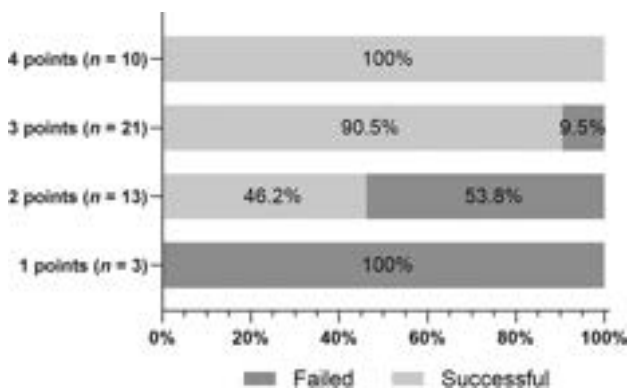


FIG 3. Effects of the presence of 1–3 predictive radiologic factors associated with failed or successful recanalization. The y-axis shows each group of patients with scores of 1, 2, 3, and 4 points; the actual number of patients is marked. The x-axis shows the percentage of patients who failed or succeeded in recanalization in each group. The technical success rates were 0%, 46.2%, 90.5%, and 100% in patients who were assigned 1, 2, 3, and 4 points, respectively.

symptomatic CICA0. However, the heterogeneity of recanalization outcomes and the perioperative complications presents challenges for the clinical application of endovascular recanalization.^{10,11} Our study observed an overall success rate of

endovascular recanalization of 74.5% (35/47); the intraoperative complication rate was 12.8%, and the morbidity and mortality rate within 30 days was 6.4%. Furthermore, CICA0 with stump (tapered or blunt), low levels of the distal ICA occlusion segment, and radiologic occlusion to recanalization of ≤ 3 months were associated with a greater chance of successful recanalization.

In previous studies, successful recanalization has been achieved in 53.3%–93.3% of patients with CICA0; this rate is related to the technical experience of the operators and the radiologic characteristics of the occlusion.^{10,11,15–17} Our study, which focused on symptomatic atherosclerotic cases, found that a tapered or blunt stump had a greater chance of successful recanalization compared with no stump; this finding is consistent with those of previous studies.^{15,16} In addition, we found that a longer duration of the occlusion was associated with a lower probability of successful recanalization: Technical success decreased from 78.0% to 50.0% when the radiologic occlusion time was increased from ≤ 3 months to > 3 months; the multivariate analysis also indicated that the occlusion duration played a significant role in recanalization.

Similar results were found in a meta-analysis by Cagnazzo et al,¹¹ which reported a successful endovascular recanalization rate of 70.2% for an occlusion duration of ≤ 3 months compared with 51.4% for an occlusion duration of > 3 months.

The length of the occlusion is a major determinant of successful recanalization due to the level of difficulty in identifying the vascular course and deviation from the vessel lumen when crossing a long occlusion.¹⁷ In previous studies, the length of the occlusion was mainly judged according to the distance between the site of the proximal occlusion and the retrograde reconstruction of the distal ICA segment by the collateral vessels on delayed angiographic images, which might be longer than the true length of the underlying thrombotic occluded lesion.^{16,18,19} HR-MRI can be used preoperatively to directly visualize and provide detailed information about occluded segments.²⁰ In the present study, we mainly classified the level of the distal ICA occlusion segment (Bouthillier segmentation) according to the preoperative HR-MRI and confirmed it by intraoperative angiograms; theoretically, this strategy is more accurate than the method of using delayed angiographic images. We found that low levels of the distal ICA occlusion segment were significantly associated with successful recanalization. Similar results were reported by Chao et al, who observed a higher technical success rate among “short-type” occlusions (occlusion length of ≤ 3 segments) compared with

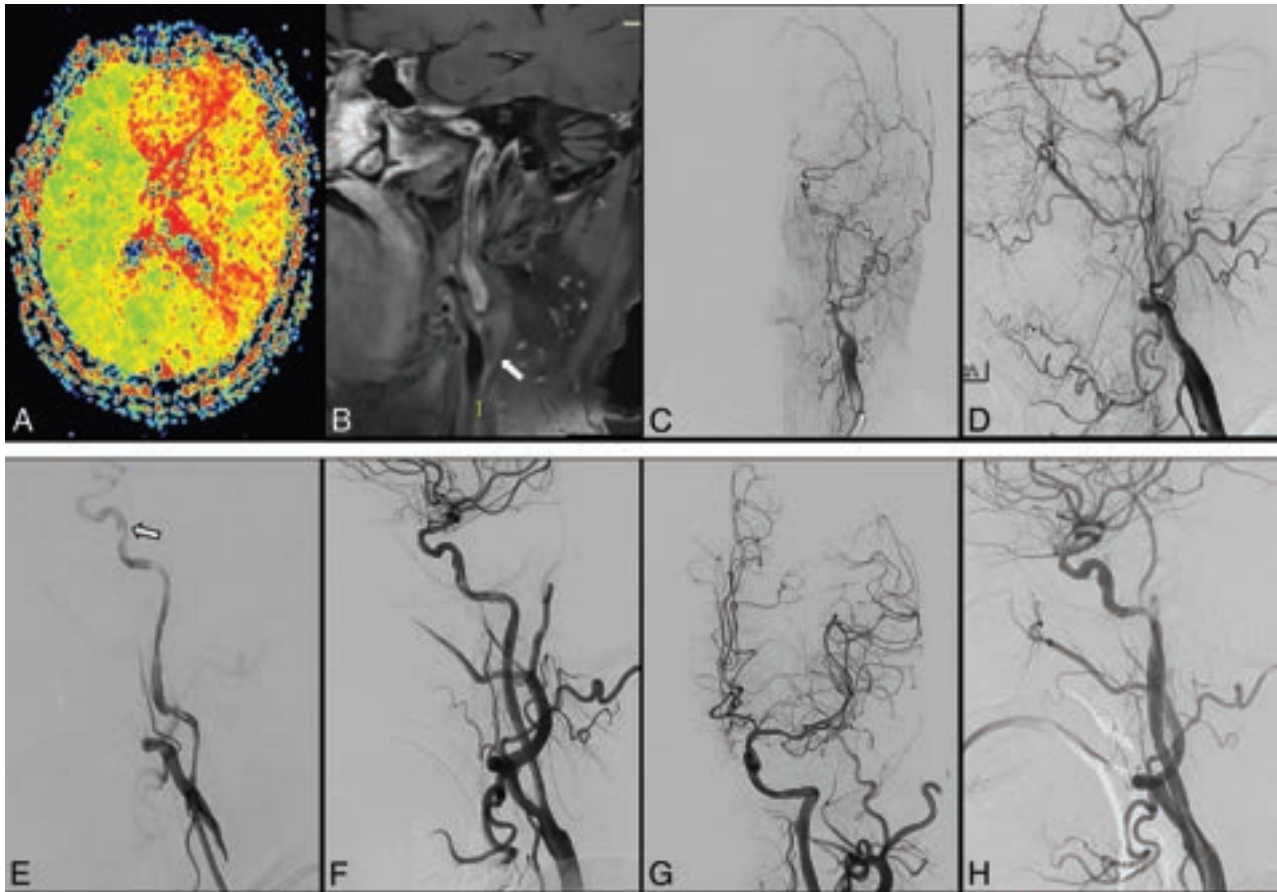


FIG 4. An elderly man presented with recurrent numbness and weakness in the right limb and was diagnosed with left ICA occlusion for >9 months. Preoperative perfusion-weighted imaging shows large areas of hypoperfusion (increased TTP, A) in the left hemisphere. HR-MRI scans (B) and angiographic results (C and D) confirm the occlusion of the C1 segment with no stump (arrow). The patient was assigned a score of 2 points before recanalization. After the microwire passed the occlusion site and was predilated with a 3 × 30 mm balloon, angiography (E) shows a long, rough vascular wall and regional dissection (arrow). Successful recanalization with good antegrade perfusion was achieved followed by the insertion of 1 Neuroform EZ stent (4.5 × 30 mm) and 2 Wallstent stents (7 × 40 mm and 9 × 30 mm, F and G). Angiographic results show patent stents at the 3-month follow-up (H).

“long-type” occlusions (93.3% versus 57.8%).¹⁵ Most surprising, we found that an occlusion length of ≤5 cm was not significantly associated with successful recanalization. A study by Hasan et al¹⁸ reported a 100% success rate in patients with an occlusion length of <5 cm in the cervical ICA, whereas the success rate was 50% for longer lesions. This outcome could be ascribed to several factors: first, carotid artery segment lengths are heterogeneous because of differences in sex, age, and other factors; second, the carotid artery is tortuous upward. Thus, neither DSA nor HR-MRI could accurately measure the length of the occlusion.

Chen et al¹⁶ developed a scoring system to predict the success rate of endovascular recanalization; the system was based on angiographic features and symptoms, such as a nontapered stump, distal carotid artery reconstitution at the communicating or ophthalmic segments, and the absence of neurologic events. However, their study was limited by heterogeneity and bias; 43.5% of patients were asymptomatic, and patients with intracranial occlusion and nonatherosclerotic or dissection occlusion were also included. Using the data obtained, we constructed an easy-to-operate 3-factor model to predict successful recanalization preoperatively. The 3 factors in the model were a tapered or

blunt stump, a distal ICA occlusion segment, and radiologic occlusion to recanalization of ≤3 months; these factors separately reflect CICA features in the different aspects discussed above. In the 47 patients included in our study, the model achieved high efficacy in risk stratification. Patients who received 1 point in this scoring system achieved no success in recanalization surgery (0/3), whereas all patients who received 4 points achieved successful recanalization (10/10).

Complications after recanalization have been reported in close to 18% of patients, with higher rates (approximately 25%) among patients with longer occlusions.^{18,21} In our study, the rate of intraoperative complications (such as dissection and perforation) was 12.8%, with no permanent neurologic deficits remaining after the operation. Distal embolization is a common complication of recanalization for CICA, with reported rates of up to 7.1%.^{15,18,19} In our study, 2 patients (2/47, 4.3%) demonstrated thrombus migration during the procedure; fortunately, no new symptoms or signs were observed after successful mechanical thrombectomy. Research has shown that atherosclerotic CICA is mainly caused by the superposition of thrombosis due to stenosis. Disrupting the thrombus by microcatheter or microguidewire

manipulation or compressing it during balloon dilation leads to a risk of thrombus migration.²² To stabilize the stenotic lesion and prevent distal embolization, we typically used a small-diameter balloon (2–3 mm) to perform predilation through the occlusive section first, followed by closed-cell stent insertion, if appropriate. Nevertheless, embolic protection measures should be performed to prevent embolism during recanalization procedures. However, the deployment of distal embolic protection devices, such as SpiderFX, is difficult when passing through the target vessels because of the long fibrotic or thrombotic lesion and tortuous vascular anatomy that is often found in chronic total occlusion.^{15,18,19} This issue is evidenced by the low application rate (34.3%, 12/35) of embolic protection devices in our study. The application of proximal protection devices that work through flow reversal, such as the Mo.Ma occlusion system, may be a beneficial supplementary technique to prevent distal embolization;²³ however, studies with large sample sizes are needed to confirm the results in patients with CICA0.

The successful recanalization of CICA0 leads to the resolution of the penumbra and the normalization of TTP or MTT, and it eventually contributes to the improvement of mRS scores following the procedure.¹² In 2 other studies on endovascular therapy,^{24,25} significant improvements in neurologic deficits and cognitive function were observed 3–6 months after the recanalization procedure. Similarly, in our study, most patients (72.4%) with successful recanalization showed improvement in their mRS scores at the 3-month follow-up compared with baseline, whereas few patients (30%) with failed recanalization showed improvement in the mRS scores. One recanalized patient (1/34, 2.9%) developed recurrent dizziness due to in-stent restenosis, whereas 3 patients with failed recanalization (3/12, 25.0%) experienced recurrent TIA or stroke during follow-up. Although we could not use preoperative and postoperative mRS scores alone to measure the operative success of this intervention, the combination of the improvement in mRS scores associated with successful recanalization and the reduction in recurrent cerebrovascular events demonstrates the safety and efficacy of this procedure.

The present study has several limitations. First, it is a retrospective study with a modest sample size, which might interfere with the statistical analysis, and it may have contained correlative variables. Therefore, further prospective studies with large sample sizes are needed to verify the results. Second, the lack of follow-up imaging data for some patients might limit the evaluation of the overall restenosis/re-occlusion rate. Finally, few studies have focused on the mural and intraluminal thrombus signals on HR-MRI; thus, further studies are needed to identify potential predictors of successful recanalization.

CONCLUSIONS

For symptomatic CICA0, endovascular recanalization is safe and effective in selected patients and may improve neurologic symptoms while reducing the recurrence rate of TIA or stroke in the midterm. A tapered or blunt stump, low levels of the distal ICA occlusion segment, and a short radiologic occlusion time were identified as independent predictors of technical success. Although additional prospective randomized trials with large cohorts are necessary to confirm our results, the scoring

system we constructed can help facilitate and improve preoperative case selection for recanalization.

Disclosure forms provided by the authors are available with the full text and PDF of this article at www.ajnr.org.

REFERENCES

1. Grubb RL, Powers WJ. **Risks of stroke and current indications for cerebral revascularization in patients with carotid occlusion.** *Neurosurg Clin N Am* 2001;12:473–87 CrossRef Medline
2. Morris-Stiff G, Teli M, Khan PY, et al. **Internal carotid artery occlusion: its natural history including recanalization and subsequent neurologic events.** *Vasc Endovascular Surg* 2013;47:603–07 CrossRef Medline
3. Sundaram S, Kannoth S, Thomas B, et al. **Collateral assessment by CT angiography as a predictor of outcome in symptomatic cervical internal carotid artery occlusion.** *AJNR Am J Neuroradiol* 2017;38:52–57 CrossRef Medline
4. Lall A, Yavagal DR, Bornak A. **Chronic total occlusion and spontaneous recanalization of the internal carotid artery: natural history and management strategy.** *Vascular* 2021;29:733–41 CrossRef Medline
5. Powers WJ, Clarke WR, Grubb RL, et al; COSS Investigators. **Extracranial-intracranial bypass surgery for stroke prevention in hemodynamic cerebral ischemia: the Carotid Occlusion Surgery Study randomized trial.** *JAMA* 2011;306:1983–92 CrossRef Medline
6. Grubb RL, Powers WJ, Clarke WR, et al; Carotid Occlusion Surgery Study Investigators. **Surgical results of the carotid occlusion surgery study.** *J Neurosurg* 2013;118:25–33 CrossRef Medline
7. Paty PS, Adeniyi JA, Mehta M, et al. **Surgical treatment of internal carotid artery occlusion.** *J Vasc Surg* 2003;37:785–88 CrossRef Medline
8. Hrbáčõ T, Beneš V, Širůcõek P, et al. **Safety and efficacy of surgical treatment of carotid stump syndrome: pilot study.** *Ann Vasc Surg* 2012;26:797–801 CrossRef Medline
9. Stewart LM, Spangler EL, Sutzko DC, et al. **Carotid endarterectomy with concomitant distal endovascular intervention is associated with increased rates of stroke and death.** *J Vasc Surg* 2021;73:960–67.e1 CrossRef Medline
10. Myrcha P, Głowiczki P. **A systematic review of endovascular treatment for chronic total occlusion of the internal carotid artery.** *Ann Transl Med* 2021;9:1203 CrossRef Medline
11. Cagnazzo F, Lefevre PH, Derraz I, et al. **Endovascular recanalization of chronically occluded internal carotid artery.** *J Neurointerv Surg* 2020;12:946–51 CrossRef Medline
12. Huang CC, Chen YH, Lin MS, et al. **Association of the recovery of objective abnormal cerebral perfusion with neurocognitive improvement after carotid revascularization.** *J Am Coll Cardiol* 2013;61:2503–09 CrossRef Medline
13. Hou Z, Yan L, Zhang Z, et al. **High-resolution magnetic resonance vessel wall imaging-guided endovascular recanalization for non-acute intracranial artery occlusion.** *J Neurosurg* 2021 Dec 3. [Epub ahead of print] CrossRef Medline
14. Bouthillier A, van Loveren HR, Keller JT. **Segments of the internal carotid artery: a new classification.** *Neurosurgery* 1996;38:425–32 CrossRef Medline
15. Chao L, Qingbin M, Haowen X, et al. **Imaging predictors for endovascular recanalization of non-acute occlusion of internal carotid artery based on 3D T1-SPACE MRI and DSA.** *Front Neurol* 2021;12:692128 CrossRef Medline
16. Chen YH, Leong WS, Lin MS, et al. **Predictors for successful endovascular intervention in chronic carotid artery total occlusion.** *JACC Cardiovasc Interv* 2016;9:1825–32 CrossRef Medline
17. Cao G, Hu J, Tian Q, et al. **Surgical therapy for chronic internal carotid artery occlusion: a systematic review and meta-analysis.** *Updates Surg* 2021;73:2065–78 CrossRef Medline
18. Hasan D, Zanaty M, Starke RM, et al. **Feasibility, safety, and changes in systolic blood pressure associated with endovascular revascularization of symptomatic and chronically occluded cervical internal carotid artery using a newly suggested radiographic**

- classification of chronically occluded cervical internal carotid artery: pilot study.** *J Neurosurg* 2018;130:1468–77 CrossRef Medline
19. Mo L, Ma G, Dai C, et al. **Endovascular recanalization for symptomatic subacute and chronically occluded internal carotid artery: feasibility, safety, a modified radiographic classification system, and clinical outcomes.** *Neuroradiology* 2020;62:1323–34 CrossRef Medline
 20. Tang M, Yan X, Gao J, et al. **High-resolution MRI for evaluation of the possibility of successful recanalization in symptomatic chronic ICA occlusion: a retrospective study.** *AJNR Am J Neuroradiol* 2022;43:1164–71 CrossRef Medline
 21. Lee CW, Lin YH, Liu HM, et al. **Predicting procedure successful rate and 1-year patency after endovascular recanalization for chronic carotid artery occlusion by CT angiography.** *Int J Cardiol* 2016;221:772–76 CrossRef Medline
 22. Yang Y, Liu X, Wang R, et al. **A treatment option for symptomatic chronic complete internal carotid artery occlusion: hybrid surgery.** *Front Neurosci* 2020;14:392 CrossRef Medline
 23. Tiwari A, Bo R, Sivakumar K, et al. **Safety and efficacy of flow reversal in acute and elective carotid angioplasty and stenting using the Mo. Ma device with short-term follow-up.** *Interv Neurol* 2020;8:196–205 CrossRef Medline
 24. Lin MS, Chiu MJ, Wu YW, et al. **Neurocognitive improvement after carotid artery stenting in patients with chronic internal carotid artery occlusion and cerebral ischemia.** *Stroke* 2011;42:2850–54 CrossRef Medline
 25. Fan YL, Wan JQ, Zhou ZW, et al. **Neurocognitive improvement after carotid artery stenting in patients with chronic internal carotid artery occlusion: a prospective, controlled, single-center study.** *Vasc Endovascular Surg* 2014;48:305–10 CrossRef Medline

MRI for Cushing Disease: A Systematic Review

M. Castle-Kirszbaum, S. Amukotuwa, P. Fuller, T. Goldschlager, A. Gonzalvo, J. Kam, C.Y. Kow, M.D. Shi, and S. Stuckey



ABSTRACT

BACKGROUND: MR imaging is key in the diagnostic work-up of Cushing disease. The sensitivity of MR imaging in Cushing disease is not known nor is the prognostic significance of “MR imaging–negative” disease.

PURPOSE: Our aim was to determine the overall sensitivity and prognostic significance of MR imaging localization of Cushing disease.

DATA SOURCES: We performed a systematic review of the MEDLINE and PubMed databases for cohort studies reporting the sensitivity of MR imaging for the detection of adenomas in Cushing disease.

STUDY SELECTION: This study included 57 studies, comprising 5651 patients.

DATA ANALYSIS: Risk of bias was assessed using the methodological index for non-randomized studies criteria. Meta-analysis of proportions and pooled subgroup analysis were performed.

DATA SYNTHESIS: Overall sensitivity was 73.4% (95% CI, 68.8%–77.7%), and the sensitivity for microadenomas was 70.6% (66.2%–74.6%). There was a trend toward greater sensitivity in more recent studies and with the use of higher-field-strength scanners. Thinner-section acquisitions and gadolinium-enhanced imaging, particularly dynamic sequences, also increased the sensitivity. The use of FLAIR and newer 3D spoiled gradient-echo and FSE sequences, such as spoiled gradient-echo sequences and sampling perfection with application-optimized contrasts by using different flip angle evolutions, may further increase the sensitivity but appear complementary to standard 2D spin-echo sequences. MR imaging detection conferred a 2.63-fold (95% CI, 2.06–3.35-fold) increase in remission for microadenomas compared with MR imaging–negative Cushing disease.

LIMITATIONS: Pooled analysis is limited by heterogeneity among studies. We could not account for variation in image interpretation and tumor characteristics.

CONCLUSIONS: Detection on MR imaging improves the chances of curative resection of adenomas in Cushing disease. The evolution of MR imaging technology has improved the sensitivity for adenoma detection. Given the prognostic importance of MR imaging localization, further effort should be made to improve MR imaging protocols for Cushing disease.

ABBREVIATIONS: ACTH = adrenocorticotropic hormone; CD = Cushing disease; CRH = corticotropin-releasing hormone; GE = gradient-echo; MINORS = methodological index for non-randomized studies; RARE = rapid acquisition with relaxation excitement; SE = spin-echo; SPGR = spoiled gradient-echo sequences; SPACE = sampling perfection with application-optimized contrasts by using different flip angle evolutions

Cushing disease (CD) is associated with reduced quality of life¹ and excess mortality.² MR imaging of the sellar region

identifies most cases of Cushing disease; however, up to 40% of cases are “MR imaging–negative,” though the exact proportion has not been definitively established.^{3–5}

Received February 1, 2022; accepted after revision October 11.

From the Departments of Neurosurgery (M.C.-K., T.G., J.K., C.Y.K.), Radiology (S.A.), Endocrinology (P.F.), and Surgery (M.C.-K., T.G.), Monash Health, Melbourne, Australia; Hudson Institute (P.F.), Melbourne, Australia; Department of Neurosurgery (A.G., J.K.), Austin Hospital, Melbourne, Australia; Barwon Health (M.D.S.), Geelong, Australia; and Department of Radiology (S.S.), Peter MacCallum Cancer Centre, Melbourne, Australia.

Please address correspondence to Mendel Castle-Kirszbaum, MBBS, PhD, Department of Neurosurgery, Monash Health, Melbourne Australia, 246 Clayton Rd, Clayton VIC, Australia 3168; e-mail: mdckjournal@gmail.com

Indicates article with online supplemental data.

<http://dx.doi.org/10.3174/ajnr.A7789>

Surgeons rely on MR imaging to identify the surgical target, guide surgical planning and technique, and avoid complications. Foremost, adenoma localization facilitates selective adenectomy, which is associated with the highest rate of cure.^{6,7} In MR imaging–negative Cushing disease, the surgeon is required to make multiple incisions into the gland in search of adenoma tissue or perform a hemi- or subtotal hypophysectomy;⁸ both are associated with a higher rate of complications and a lesser rate of cure.^{9,10} Surgical exploration and hemi-hypophysectomy may be

guided by inferior petrosal sinus sampling, but this procedure is invasive, not without risk, and correctly lateralizes eccentric tumors in only 69% of cases.¹¹

Improved MR imaging detection of adenomas in CD would avoid delays in treatment, streamline surgery, reduce the need for inferior petrosal sinus sampling, minimize iatrogenic gland and stalk injury, obviate the need for hypophysectomy, and increase the chance of surgical cure.¹² We sought to systematically review the literature on MR imaging in CD to establish the rate of MR imaging–negative disease, the patient and imaging protocol factors that determine MR imaging sensitivity, and the association of MR imaging localization with rates of biochemical remission after surgery.

Primer of MR Imaging for CD

MR imaging of the pituitary gland is notoriously challenging due to its anatomy. The pituitary gland sits in the sella at the confluence of the nasal, orbital, and cranial regions,^{13,14} medial to the lateral sellar compartment (cavernous sinus, a part of the extradural neuraxial compartment).¹⁵

A number of artifacts degrade sellar MR imaging. Due to its small size, partial volume effects from adjacent structures such as the ICA, sphenoid sinus air, or cavernous sinus fat may mimic microadenomas. A thin-section, high in-plane resolution, multiplanar acquisition is hence essential.¹⁶ Tissue inhomogeneity is also problematic; changes in magnetic susceptibility at air- and bone–soft tissue interfaces also distort the local magnetic field and cause artifacts, particularly at higher field strengths. Chemical shift artifacts may occur in the setting of fat infiltration of the dorsum sellae or cavernous sinus and may require fat-suppressed imaging. Pulsatile flow in the adjacent ICA,¹⁷ significantly enlarged intercavernous sinuses, or turbulent CSF in the suprasellar cistern may also cause artifacts. Finally, patients with Cushing syndrome may have an empty sella,¹⁸ which may reduce imaging sensitivity through either direct compression or altering the dynamics of contrast within the normal gland.¹⁹

Standard MR images are pre- and post intravenous gadolinium T1-weighted spin-echo (SE) or rapid acquisition with relaxation enhancement (RARE), eg, FSE/TSE, acquired in the coronal and sagittal planes, and coronal T2-weighted FSE with a section thickness of ≤ 3 mm. Volumetric acquisitions are now preferred because these provide thin slices and minimize partial volume effects and have the ability to create multiplanar reformats. Volumetric sequences are usually gradient-echo (GE) or RARE-based. Pituitary adenomas are typically T2-hyperintense and T1-hypointense to the normal gland precontrast; however, they may have a variety of signal characteristics and are often (frustratingly) isointense and imperceptible.

Enhancement is typically delayed compared with the normal gland, with slower wash-in and washout phases.²⁰ Adenomas, therefore, typically enhance less than the normal pituitary gland in early postcontrast images but display greater enhancement on delayed imaging. The reason is not clear but may relate to poor permeability of the pseudocapsule, reduced vessel density,²¹ or a predominance of small vessels within the tumor neovasculature.²² These enhancement characteristics are exploited by dynamic image acquisitions, in which the point of maximal-intensity

difference during wash-in is sought. Multiple (usually 6) sets of coronal T1-weighted images (either 2D or 3D, SE, FSE or GE) are acquired at 10-second intervals immediately following contrast administration. Delayed imaging, 30–60 minutes after contrast administration, may also be performed to take advantage of the relatively slow contrast washout within adenomas. FLAIR imaging is more sensitive to paramagnetic contrast enhancement than T1-weighted images and may, therefore, be preferred in this setting.²³ Spoiled gradient-echo sequences (SPGR) offer greater soft-tissue contrast and allow faster acquisition (minimizing motion/vascular pulsation artifacts) than standard SE sequences.²⁴ They are also often acquired with thinner slices. However, the SNR may be inferior to that in SE sequences, increasing the rate of false-positive findings, and susceptibility artifacts are also increased. 3D variable flip-angle FSE sequences, such as sampling perfection with application-optimized contrasts by using different flip angle evolutions (SPACE sequence; Siemens), allow thin-section imaging in reasonable acquisition times, reducing partial volume and motion artifacts.²⁵ These FSE sequences are resistant to susceptibility artifacts compared with 3D GE sequences. They may also be particularly useful for laterally based tumors because the signal intensity of slow-flowing blood (eg, in the cavernous sinus)²⁶ is high, while flow voids are maintained in fast-flowing carotids.²⁷ High spatial-resolution balanced spoiled steady-state free precession sequences, such as CISS, are predominantly heavily T2-weighted images that have a high SNR and are relatively insensitive to motion. Acquired without contrast, they may provide complementary findings to standard SE sequences by identifying microcystic or more T2-hyperintense regions in otherwise silent lesions and are suitable for patients with contraindications to intravenous gadolinium.

MATERIALS AND METHODS

A systematic review was performed in accordance with the Preferred Reporting Items for Systematic reviews and Meta-Analyses (PRISMA) statement.²⁸ A systematic search of the MEDLINE and PubMed electronic databases from their date of inception to September 2021 was conducted using the search string: (Magnetic Resonance Imaging OR MRI OR MR) AND (Cushing(s) Disease OR Corticotroph Adenoma OR Corticotrope Adenoma OR ACTH-Dependent Cushing(s) Syndrome).

Inclusion criteria were defined as the following: 1) randomized and nonrandomized controlled trials and cohort studies that reported the sensitivity of MR imaging for the detection of pituitary adenomas in Cushing disease; 2) documentation of an acceptable “reference standard” diagnosis of Cushing disease (histology or remission after surgery); and 3) written in English. Studies of multiple tumor types in which data specific to CD could not be extracted, studies of imaging modalities in which data specific to MR imaging could not be extracted, and single case reports were excluded.

Data Collection

Data extraction included study year, study size, patient age, surgical status, surgery type, adenoma size, cure rates, and MR imaging protocol. Results were stratified, when possible, by patient age, study year, tumor size, and MR imaging characteristics.

Risk of bias in individual studies was assessed using the methodological index for non-randomized studies (MINORS).²⁹

Meta-analysis of proportions was performed using the random-effects model for overall sensitivity. Pooled analysis was performed for subgroup analysis, and the Fisher exact test was used to compare pooled dichotomous data. Statistical significance was defined as $P < .05$. Heterogeneity between studies included in the meta-analysis of proportions was measured using the I^2 statistic. Analysis was performed using R 4.1.1 (<http://www.r-project.org/>).

RESULTS

Fifty-seven studies were identified from the systematic search of the literature (Online Supplemental Data), comprising 5651 patients (Online Supplemental Data). Risk of bias was assessed by the MINORS criteria and is presented in the Online Supplemental Data. The literature consisted mostly of case series and small retrospective cohort studies, spanning 1988–2021. Magnet field strength was reported in 36 (63.2%) studies, with most using standard-field-strength MR imaging (1T–3T), whereas 1 study used 7T imaging. MR imaging sequences were reported in 43 (75.4%) studies. The most used sequences included T1-weighted SE (100%, 43/43), T2-weighted SE (55.8%, 24/43), dynamic postcontrast studies (48.8%, 21/43), and SPGR (44.2%, 19/43). In all studies, the diagnosis of CD was established by either surgical findings or, in the absence of histology, biochemical remission after surgery.

Overall Sensitivity

In patients with CD, MR imaging had an overall sensitivity of 73.4% (95% CI, 68.8%–77.7%) and there was significant heterogeneity between studies ($I^2 = 92.1%$) (Online Supplemental Data). In studies that included only microadenomas, the overall sensitivity was 71.8% (95% CI, 63.0%–79.2%) and there was significant heterogeneity between studies ($I^2 = 82.0%$). In studies that included both macroadenomas and microadenomas, the sensitivity for detecting microadenomas was similar (70.0%; 95% CI, 64.9%–74.7%; $I^2 = 91.7%$) to that in studies of exclusively microadenomas ($P = .85$). Combined, the sensitivity of MR imaging for all microadenomas was 70.6% (95% CI, 66.2%–74.6%; $I^2 = 89.7%$). Compared with all patients with CD, the sensitivity of MR imaging for detecting microadenomas was significantly lower when assessing either studies of exclusively microadenomas (OR = 1.18, $P = .03$) or microadenomas within all studies (OR = 1.22, $P < .001$).

Study Year

Studies were categorized by year of publication into 1 of 3 epochs: pre-2000; 2000–2010; or post-2010. When the sensitivity of MR imaging was provided for different epochs within a study, data were separated into the relevant era. The sensitivity of MR imaging in the pre-2000 epoch was similar to that in the 2000–2010 epoch (60.5% versus 57.8%, $P = .89$). The post-2010 era had greater sensitivity than the pre-2000 (80.1% versus 60.5%, $P < .001$) and the 2000–2010 (80.1% versus 57.8%, $P < .001$) eras.

Patient Age

Two studies exclusively analyzed pediatric patients, while 12 studies exclusively analyzed adults. One additional study stratified results by patient age, and the data were included in the relevant

age group. MR imaging had greater sensitivity in adults with CD than in children (70.9% versus 52.5%, $P < .001$).

Field Strength

Twenty studies were performed using a single magnet field strength, while an additional 5 studies stratified results by field strength. Overall, there was a trend toward increasing sensitivity with increasing field strength. Compared with a standard field strength of 1.5T, scans performed at 3T identified significantly more adenomas (81.7% versus 73.6%, OR = 1.60, $P = .03$).

Comparisons with low-strength (eg, 0.5T) and higher-strength (eg, 7T) magnets were limited by the small sample size. Three studies assessed the same cohort of patients on 1.5T and 3T scanners,^{30–32} for a total of 28 patients. 3T field strength tended to be more sensitive (60.7% versus 35.7%, $P = .10$). The single study comparing 1.5T and 7T images also tended toward greater sensitivity with higher field strengths (81.3% versus 43.8%, $P = .07$).³³

Section Thickness

Thirty-two studies reported MR imaging sequence details, including minimum section thickness. Section thickness was categorized into 3 groups: >2 , ≤ 1 , and 1.1–2 mm. Compared with MR imaging protocols in which the thinnest cuts were >2 mm, those with slices of 1.1–2 mm (65.6% versus 58.1%, $P = .01$) and ≤ 1 mm (83.7% versus 58.1%, $P < .001$) were significantly more sensitive.

Because studies of <1 mm were more likely to have dynamic imaging, a separate analysis was performed excluding studies with dynamic contrast-enhanced sequences. Fine-section (≤ 1 mm) imaging improved the sensitivity of MR imaging even in the absence of dynamic sequences compared with either 1.1- to 2-mm slices ($P = .02$) or >2 -mm slices ($P = .03$).

MR Imaging Sequences

Thirty-nine studies reported sensitivity for specific MR imaging sequences. Compared with noncontrast T1 SE sequences, routine postgadolinium T1 SE sequences trended toward greater sensitivity but did not reach statistical significance. However, dynamic image acquisition improved the sensitivity of gadolinium-enhanced T1-weighted SE sequences significantly (78.6% versus 58.8%, $P < .001$). The sensitivity of dynamic sequences improved between the 2000 and 2010 era and the post-2010 era (52.8% versus 81.4%, $P < .001$). Spoiled gradient-echo sequences (most commonly SPGR) also demonstrated increased sensitivity compared with postcontrast T1-weighted SE images (69.8% versus 58.8%, $P < .001$). 3D FSE sequences (eg, SPACE) similarly demonstrated greater sensitivity than postcontrast 2D T1-weighted SE studies (82.1% versus 58.8%, $P < .001$).

Given that the sensitivity of each sequence is dependent on many factors including the characteristics of the population being tested, section thickness, and magnet strength (see above), a separate analysis was performed that included only studies with direct comparisons of MR images obtained on the same population on the same scanners.

Similar to the initial analysis, there was no significant difference between noncontrast and postcontrast 2D T1-weighted SE sequences (46.8% versus 62.2%, $P = .19$). Again, dynamic image acquisition improved the sensitivity of gadolinium-enhanced 2D

Effect of MR imaging detection on surgical outcome

	Remission	Persistent	%	P Value	OR (95% CI)
All adenomas					
MR imaging+	1968	445	81.6	<.001	1.40 (1.16–1.68)
MR imaging–	710	224	76.0	REF	REF
Microadenomas					
MR imaging+	1129	203	84.8	<.001	2.63 (2.06–3.35)
MR imaging–	324	153	67.9	REF	REF

Note:—REF indicates reference value; +, detected; –, not detected.

T1-weighted SE sequences (64.8% versus 47.3%, $P = .006$). There was no difference between SPGR and dynamic sequences (60.1% versus 67.3%, $P = .21$); however, SPGR demonstrated improved sensitivity in comparison with postcontrast 2D T1-weighted SE sequences (55.3% versus 38.6%, $P < .001$). Single studies demonstrated greater sensitivity of postcontrast 3D fast FSE sequences (eg, T2-SPACE) compared with dynamic acquisitions ($P = .01$)³⁴ and postcontrast 2D T1-weighted SE sequences ($P < .001$).³⁵ The addition of FLAIR sequences to SPGR increased the sensitivity of MR imaging, though overall numbers were small.²³ T2-CISS sequences in isolation were similarly as sensitive as postcontrast 2D T1-weighted SE sequences; however, both sequences identified particular adenomas that the other did not, suggesting these sequences are complementary.³⁶

Significance of MR Imaging Localization for Postoperative Remission

Postoperative biochemical remission data were available in 23 studies. Overall, patients with adenomas identifiable on MR imaging had a greater rate of postoperative biochemical remission (81.6% versus 76.0%, $P < .001$) (Table). Given that macroadenomas are more likely to be invasive and some may be giant and not amenable to gross total resection, a separate analysis was performed in microadenoma studies. Data pertaining only to microadenomas could be extracted from 16 studies. The strong predictive effect of MR imaging visibility on remission rates was maintained (84.8% versus 67.9%, $P < .001$). There was no difference in remission rates in MR imaging–negative disease between epochs.

DISCUSSION

Key Results

MR imaging identifies 73% of all adenomas and 71% of microadenomas in patients with CD. Sensitivity has improved with time due to greater spatial resolution (including finer section thickness) and scanning at higher field strengths, which allows high-resolution imaging with greater SNR. The increase in detection rates may, however, come at the cost of increased false-positives. Dynamic imaging and advanced 3D MR imaging techniques (SPGR, SPACE) may improve the sensitivity over conventional 2D SE sequences alone; however, they are likely complementary rather than interchangeable. MR imaging detection is a strong predictor of remission.

Generalizability

Perhaps the most important factor determining the sensitivity of MR imaging is how the images are interpreted. Experienced

radiologists and pituitary surgeons do not have perfect agreement among themselves^{33,37} or each other.³⁸ Dynamic³⁷ and higher-field-strength studies³³ tend to demonstrate less agreement, likely due poorer specificity related to artifacts and the more heterogeneous appearance of the gland at higher resolution. The MR pulse sequences and high-field-strength (7T) imaging described in this review may not be available in all centers.

Limitations

Significant ($I^2 = 90\%$) heterogeneity between studies limits the strength of our conclusions. The sensitivity of MR imaging is determined by many factors outside the acquisition, such as image interpretation and tumor characteristics, which will differ among cohorts. The factors analyzed in the study are inherently interrelated, with higher-field-strength scanners, advanced sequences, and thinner-section acquisitions more common in later decades. Improvements in scanner technology extend beyond field strength. With time, matrix size (ie, in-plane resolution) has increased, as has the number and design of head coils (ie, channels), resulting in higher-resolution imaging with improved signal. These specifications were rarely reported; comparison by field strength alone may oversimplify interscanner differences. Although increasing spatial resolution and advanced sequences may improve sensitivity, the effect on specificity has not been consistently reported. The false-positive rate may exceed 20% in some series,³⁹ and clinicians should be cognizant of the potential for a greater rate of false-positive results with fine-section acquisitions, higher-field-strength magnets, and more advanced pulse sequences.³⁸

The Future

Perfectly sensitive sellar imaging would facilitate a totally noninvasive work-up of CD and high rates of surgical cure. Steps toward this goal have already been taken; however, there remains room for improvement. CD-specific MR imaging protocols have been proposed,^{40,41} using dynamic imaging, SPGR, and volumetric FSE sequences, which are supported by our data. The benefits of higher-field-strength magnets are promising but may be limited by amplified artifacts from skull base pneumatization and bone-soft tissue interfaces. Nevertheless, the single study that compared 1.5T and 7T acquisitions demonstrated almost twice the sensitivity with higher-field-strength imaging. Gadolinium dose is a further variable to be optimized,⁴² with half-dose acquisitions demonstrating improved sensitivity. These advances are promising but need to be weighed against the potential increased rate of false-positive results. Future studies should universally report false-positive findings.

Intraoperative MR imaging is increasingly recognized as a valuable adjunct to increase the extent of resection of macroadenomas in specialist centers,⁴³ especially as field strength improves.⁴⁴ The role of intraoperative MR imaging in microadenoma surgery has not been established but may be limited by air and blood artifacts

from the operation. Endosphenoïdal coils may dramatically augment SNR but are currently experimental.⁴⁵

Current MR imaging protocols appear particularly insensitive for detecting dural invasion, which has prognostic significance.⁴⁶ Preoperative detection would facilitate consideration of resection of the medial wall of the cavernous sinus, theoretically increasing the chance of cure.⁴⁷

PET using [¹⁸F] fluoroethyl-L-tyrosine and ¹¹C-methionine may localize MR imaging-ocult lesions.⁴⁸ Response to corticotropin-releasing hormone (CRH) stimulation can predict PET-positive adenomas,⁴⁹ and PET detection can be further improved by CRH stimulation.⁵⁰ Although PET may be less sensitive than advanced MR imaging sequences in isolation,⁴⁹ it can help confirm equivocal MR imaging findings and may be fused to volumetric MR imaging acquisitions for intraoperative stereotaxis. Recently, ⁶⁸Ga-tagged CRH has been demonstrated to localize CD adenomas with impressive accuracy;⁵¹ however, its role in adenomas that fail to respond to CRH stimulation (approximately 10%) is unclear.

CONCLUSIONS

MR imaging detects between two-thirds and three-quarters of adenomas causing CD. MR imaging localization significantly improves outcome in patients with CD; in microadenomas, it increases the chance of remission by almost 20%. We have illustrated the patient and imaging factors that influence detection rates. These findings will help guide improvements in MR imaging protocols to maximize the chance of cure, thus improving quality of life and longevity for patients with CD. More precision in MR imaging protocols is required in this era of precision medicine.

ACKNOWLEDGMENT

The first author (M.C.-K.) is undertaking a higher degree funded by an Australian Government Research Training Program Scholarship.

Disclosure forms provided by the authors are available with the full text and PDF of this article at www.ajnr.org.

REFERENCES

1. Castle-Kirszbaum M, Wang YY, King J, et al. **Quality of life following endoscopic surgical management of pituitary adenomas.** *Neurosurgery* 2022;90:81–91 CrossRef Medline
2. Ntali G, Asimakopoulou A, Siamatras T, et al. **Mortality in Cushing's syndrome: systematic analysis of a large series with prolonged follow-up.** *Eur J Endocrinol* 2013;169:715–23 CrossRef Medline
3. Chowdhury IN, Sinai N, Oldfield EH, et al. **A change in pituitary magnetic resonance imaging protocol detects ACTH-secreting tumours in patients with previously negative results.** *Clin Endocrinol (Oxf)* 2010;72:502–06 CrossRef Medline
4. Batista D, Courkoutsakis NA, Oldfield EH, et al. **Detection of adrenocorticotropin-secreting pituitary adenomas by magnetic resonance imaging in children and adolescents with Cushing disease.** *J Clin Endocrinol Metab* 2005;90:5134–40 CrossRef Medline
5. Patronas N, Bulakbasi N, Stratakis CA, et al. **Spoiled gradient recalled acquisition in the steady state technique is superior to conventional postcontrast spin echo technique for magnetic resonance imaging detection of adrenocorticotropin-secreting pituitary tumors.** *J Clin Endocrinol Metab* 2003;88:1565–69 CrossRef Medline

6. Jagannathan J, Smith R, DeVroom HL, et al. **Outcome of using the histological pseudocapsule as a surgical capsule in Cushing disease: clinical article.** *J Neurosurg* 2009;111:531–39 CrossRef Medline
7. Lonser RR, Wind JJ, Nieman LK, et al. **Outcome of surgical treatment of 200 children with Cushing's disease.** *J Clin Endocrinol Metab* 2013;98:892–901 CrossRef Medline
8. Cristante J, Lefournier V, Sturm N, et al. **Why we should still treat by neurosurgery patients with Cushing disease and a normal or inconclusive pituitary MRI.** *J Clin Endocrinol Metab* 2019 May 14 [Epub ahead of print] CrossRef Medline
9. Dai C, Feng M, Sun B, et al. **Surgical outcome of transsphenoidal surgery in Cushing's disease: a case series of 1106 patients from a single center over 30 years.** *Endocrine* 2022;75:219–27 CrossRef Medline
10. Lonser RR, Nieman L, Oldfield EH. **Cushing's disease: pathobiology, diagnosis, and management.** *J Neurosurg* 2017;126:404–17 CrossRef Medline
11. Wind JJ, Lonser RR, Nieman LK, et al. **The lateralization accuracy of inferior petrosal sinus sampling in 501 patients with Cushing's disease.** *J Clin Endocrinol Metab* 2013;98:2285–93 CrossRef Medline
12. Feng M, Liu Z, Liu X, et al. **Diagnosis and outcomes of 341 patients with Cushing's disease following transsphenoid surgery: a single-center experience.** *World Neurosurg* 2018;109:e75–80 CrossRef Medline
13. Rhoton AL. **The sellar region.** *Neurosurgery* 2002;51:S335–74 Medline
14. Castle-Kirszbaum M, Uren B, Goldschlager T. **Anatomical variation for the endoscopic endonasal transsphenoidal approach.** *World Neurosurg* 2021;156:111–19 CrossRef Medline
15. Parkinson D. **Extradural neural axis compartment.** *J Neurosurg* 2000;92:585–88 CrossRef Medline
16. Bonneville JF, Bonneville F, Cattin F, et al. **MRI of the Pituitary Gland.** Springer-Verlag International Publishing; 2016
17. Castle-Kirszbaum M, Maingard J, Lim RP, et al. **Four-dimensional magnetic resonance imaging assessment of intracranial aneurysms: a state-of-the-art review.** *Neurosurgery* 2020;87:453–65 CrossRef Medline
18. Manavela MP, Goodall CM, Katz SB, et al. **The association of Cushing's disease and primary empty sella turcica.** *Pituitary* 2001;4:145–51 CrossRef Medline
19. Himes BT, Bhargav AG, Brown DA, et al. **Does pituitary compression/empty sella syndrome contribute to MRI-negative Cushing's disease? A single-institution experience.** *Neurosurg Focus* 2020;48:E3 CrossRef Medline
20. Milki Y, Matsuo M, Nishizawa S, et al. **Pituitary adenomas and normal pituitary tissue: enhancement patterns on gadopentetate-enhanced MR imaging.** *Radiology* 1990;177:35–38 CrossRef Medline
21. Viacava P, Gasperi M, Acerbi G, et al. **Microvascular density and vascular endothelial growth factor expression in normal pituitary tissue and pituitary adenomas.** *J Endocrinol Invest* 2003;26:23–28 CrossRef Medline
22. Perez-Millan MI, Berner SI, Luque GM, et al. **Enhanced nestin expression and small blood vessels in human pituitary adenomas.** *Pituitary* 2013;16:303–10 CrossRef Medline
23. Chatain GP, Patronas N, Smirniotopoulos JG, et al. **Potential utility of FLAIR in MRI-negative Cushing's disease.** *J Neurosurg* 2018;129:620–28 CrossRef Medline
24. Pui MH, Fok EC. **MR imaging of the brain: comparison of gradient-echo and spin-echo pulse sequences.** *AJR Am J Roentgenol* 1995;165:959–62 CrossRef Medline
25. Wang J, Wu Y, Yao Z, et al. **Assessment of pituitary micro-lesions using 3D sampling perfection with application-optimized contrasts using different flip-angle evolutions.** *Neuroradiology* 2014;56:1047–53 CrossRef Medline
26. Baumert B, Wörtler K, Steffinger D, et al. **Assessment of the internal craniocervical ligaments with a new magnetic resonance imaging sequence: three-dimensional turbo spin echo with variable flip-angle distribution (SPACE).** *Magn Reson Imaging* 2009;27:954–60 CrossRef Medline
27. Watanabe Y, Makidono A, Nakamura M, et al. **3D MR cisternography to identify distal dural rings: comparison of 3D-CISS and 3D-SPACE sequences.** *Magn Reson Med Sci* 2011;10:29–32 CrossRef Medline

28. Moher D, Liberati A, Tetzlaff J, et al; for the PRISMA Group. **Preferred reporting items for systematic reviews and meta-analyses: the PRISMA statement.** *BMJ* 2009;339:b2535–53 CrossRef Medline
29. Slim K, Nini E, Forestier D, et al. **Methodological index for non-randomized studies (MINORS): development and validation of a new instrument.** *ANZ J Surg* 2003;73:712–16 CrossRef Medline
30. Erickson D, Erickson B, Watson R, et al. **3 Tesla magnetic resonance imaging with and without corticotropin releasing hormone stimulation for the detection of microadenomas in Cushing's syndrome.** *Clin Endocrinol (Oxf)* 2010;72:793–99 CrossRef Medline
31. Kim LJ, Lekovic GP, White WL, et al. **Preliminary experience with 3-Tesla MRI and Cushing's disease.** *Skull Base* 2007;17:273–77 CrossRef Medline
32. Stobo DB, Lindsay RS, Connell JM, et al. **Initial experience of 3 Tesla versus conventional field strength magnetic resonance imaging of small functioning pituitary tumours.** *Clin Endocrinol (Oxf)* 2011;75:673–77 CrossRef Medline
33. de Rotte AA, Groenewegen A, Rutgers DR, et al. **High-resolution pituitary gland MRI at 7.0 Tesla: a clinical evaluation in Cushing's disease.** *Eur Radiol* 2016;26:271–77 CrossRef Medline
34. Wu Y, Cai Y, Rui W, et al. **Contrast-enhanced 3D-T2-weighted SPACE sequence for MRI detection and localization of adrenocorticotropin (ACTH)-secreting pituitary microadenomas.** *Clin Endocrinol (Oxf)* 2022;96:578–88 CrossRef Medline
35. Zhang K, Shen M, Qiao N, et al. **Surgical outcomes and multidisciplinary management strategy of Cushing's disease: a single-center experience in China.** *Neurosurg Focus* 2020;48:E7 CrossRef Medline
36. Lang M, Habboub G, Moon D, et al. **Comparison of constructive interference in steady-state and T1-weighted MRI sequence at detecting pituitary adenomas in Cushing's disease patients.** *J Neurol Surg B Skull Base* 2018;79:593–98 CrossRef Medline
37. Tabarin A, Laurent F, Catargi B, et al. **Comparative evaluation of conventional and dynamic magnetic resonance imaging of the pituitary gland for the diagnosis of Cushing's disease.** *Clin Endocrinol (Oxf)* 1998;49:293–300 CrossRef Medline
38. Grober Y, Grober H, Wintermark M, et al. **Comparison of MRI techniques for detecting microadenomas in Cushing's disease.** *J Neurosurg* 2018;128:1051–57 CrossRef Medline
39. Yogi-Morren D, Habra MA, Faiman C, et al. **Pituitary MRI findings in patients with pituitary and ectopic ACTH-dependent Cushing syndrome: does a 6-mm pituitary tumor size cut-off value exclude ectopic ACTH syndrome?** *Endocr Pract* 2015;21:1098–103 CrossRef Medline
40. Vitale G, Tortora F, Baldelli R; A.B.C. Group, et al. **Pituitary magnetic resonance imaging in Cushing's disease.** *Endocrine* 2017;55:691–99 CrossRef Medline
41. Bashari WA, Gillett D, MacFarlane J, et al. **Modern imaging in Cushing's disease.** *Pituitary* 2022;25:709–12 CrossRef Medline
42. Portocarrero-Ortiz L, Bonifacio-Delgadillo D, Sotomayor-González A, et al. **A modified protocol using half-dose gadolinium in dynamic 3-Tesla magnetic resonance imaging for detection of ACTH-secreting pituitary tumors.** *Pituitary* 2010;13:230–35 CrossRef Medline
43. Coburger J, König R, Seitz K, et al. **Determining the utility of intraoperative magnetic resonance imaging for transphenoidal surgery: a retrospective study: clinical article.** *J Neurosurg* 2014;120:346–56 CrossRef Medline
44. Jones PS, Swearingen B. **Intraoperative MRI for pituitary adenomas.** *Neurosurg Clin N Am* 2019;30:413–20 CrossRef Medline
45. Chittiboina P, Talagala SL, Merkle H, et al. **Endosphenoidal coil for intraoperative magnetic resonance imaging of the pituitary gland during transphenoidal surgery.** *J Neurosurg* 2016;125:1451–59 CrossRef Medline
46. Lonser RR, Ksendzovsky A, Wind JJ, et al. **Prospective evaluation of the characteristics and incidence of adenoma-associated dural invasion in Cushing disease.** *J Neurosurg* 2012;116:272–79 CrossRef Medline
47. Cohen-Cohen S, Gardner PA, Alves-Belo JT, et al. **The medial wall of the cavernous sinus, Part 2: selective medial wall resection in 50 pituitary adenoma patients.** *J Neurosurg* 2018;131:131–40 CrossRef Medline
48. Berkmann S, Roethlisberger M, Mueller B, et al. **Selective resection of Cushing microadenoma guided by preoperative hybrid 18-fluoroethyl-L-tyrosine and 11-C-methionine PET/MRI.** *Pituitary* 2021;24:878–86 CrossRef Medline
49. Chittiboina P, Montgomery BK, Millo C, et al. **High-resolution (18)F-fluorodeoxyglucose positron emission tomography and magnetic resonance imaging for pituitary adenoma detection in Cushing disease.** *J Neurosurg* 2015;122:791–97 CrossRef Medline
50. Boyle J, Patronas NJ, Smirniotopoulos J, et al. **CRH stimulation improves (18)F-FDG-PET detection of pituitary adenomas in Cushing's disease.** *Endocrine* 2019;65:155–65 CrossRef Medline
51. Walia R, Gupta R, Bhansali A, et al. **Molecular imaging targeting corticotropin-releasing hormone receptor for corticotropinoma: a changing paradigm.** *J Clin Endocrinol Metab* 2021;106:e1816–26 CrossRef Medline

Increased Labyrinthine T1 Postgadolinium Signal Intensity Is Associated with the Degree of Ipsilateral Sensorineural Hearing Loss in Patients with Sporadic Vestibular Schwannoma

J.P. Welby, J.C. Benson, C.M. Lohse, M.L. Carlson, and J.I. Lane

ABSTRACT

BACKGROUND AND PURPOSE: Vestibular schwannomas are benign, generally slow-growing tumors, commonly presenting with hearing loss. Alterations in the labyrinthine signal are seen in patients with vestibular schwannoma; however, the association between imaging abnormalities and hearing function remains poorly defined. The purpose of this study was to determine whether labyrinthine signal intensity is associated with hearing in patients with sporadic vestibular schwannoma.

MATERIALS AND METHODS: This was an institutional review board–approved retrospective review of patients from a prospectively maintained vestibular schwannoma registry imaged in 2003–2017. Signal-intensity ratios of the ipsilateral labyrinth were obtained using T1, T2-FLAIR, and postgadolinium T1 sequences. Signal-intensity ratios were compared with tumor volume and audiometric hearing threshold data including pure tone average, word recognition score, and American Academy of Otolaryngology–Head and Neck Surgery hearing class.

RESULTS: One hundred ninety-five patients were analyzed. Ipsilateral labyrinthine signal intensity including postgadolinium T1 images was positively correlated with tumor volume (correlation coefficient = 0.17, $P = .02$). Among signal-intensity ratios, postgadolinium T1 was significantly positively associated with pure tone average (correlation coefficient = 0.28, $P < .001$) and negatively associated with the word recognition score (correlation coefficient = -0.21 , $P = .003$). Overall, this result correlated with impaired American Academy of Otolaryngology–Head and Neck Surgery hearing class ($P = .04$). Multivariable analysis suggested persistent associations independent of tumor volume with pure tone average (correlation coefficient = 0.25, $P < .001$) and the word recognition score (correlation coefficient = -0.17 , $P = .02$) but not hearing class ($P = .14$). No consistent significant associations were noted between noncontrast T1 and T2-FLAIR signal intensities and audiometric testing.

CONCLUSIONS: Increased ipsilateral labyrinthine postgadolinium signal intensity is associated with hearing loss in patients with vestibular schwannoma.

ABBREVIATIONS: CC = correlation coefficient; IQR = interquartile range; PTA = pure tone average; SIR = signal-intensity ratio; VS = vestibular schwannoma; WRS = word recognition score; AAO-HNS = American Academy of Otolaryngology–Head and Neck Surgery

Sporadic vestibular schwannomas (VSs) are the third most common primary adult brain neoplasm and arise from the vestibular portions of cranial nerve VIII, potentially causing asymmetric sensorineural hearing loss, tinnitus, dizziness, and, less commonly, trigeminal symptoms or hydrocephalus.¹ Previously only severe symptomatic cases were detected, but increased use of MR imaging has led to improved diagnosis of VS. During the past half-century, the diagnosis of VS has increased approximately 14-fold, with the incidence in the United States currently reported to be 4.2 cases

per 100,000 person-years.^{1,2} Overall, as detection has improved, there has been a shift in practice so that most patients with small tumors are conservatively observed for tumor growth before intervention. Because tumor control and facial nerve outcomes are generally good for small tumors regardless of treatment technique, hearing loss and quality of life considerations have come to the forefront in this population.

The mechanisms underlying VS-associated sensorineural hearing loss remain largely unknown. Research has explored direct mass effect and compression of the cochlear nerve, vascular compromise mainly of the terminal labyrinthine branch of anterior inferior cerebellar artery, alterations in BBB permeability, CSF circulation, and local inflammation causing compositional changes within the endolymphatic/perilymphatic space.^{3–5} Furthermore, the associations between plausible pathologic explanations and imaging phenotypes with hearing loss in VS remain unknown.

Received November 30, 2022; accepted after revision January 31, 2023.

From the Departments of Radiology (J.P.W., J.C.B., J.I.L.), Quantitative Health Sciences (C.M.L.), and Otorhinolaryngology (M.L.C.), Mayo Clinic, Rochester, Minnesota.

Please address correspondence to John P. Welby, MD, Mayo Clinic, 200 1st St SW, Rochester, MN 55905; e-mail: Welby.John@mayo.edu

<http://dx.doi.org/10.3174/ajnr.A7800>

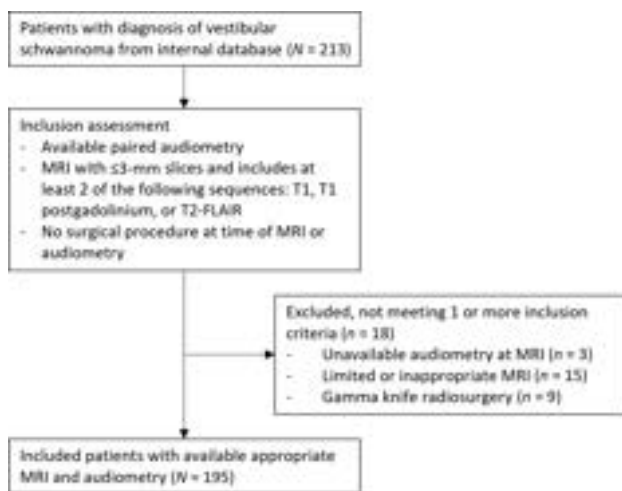


FIG 1. Patient selection flow chart.

For understanding these pathologies and their relationship with hearing, several advances have been made in MR imaging. Delayed contrast has been used as a marker for increased BBB permeability. While early work using 1.5T MR imaging found no significant signal increases within the cochlea with delayed contrast among healthy controls,⁶ subsequent work demonstrated normal enhancement detectable using 3D-FLAIR and delayed techniques.⁷ In patients with VS, contrast enhancement has been seen in the ipsilateral affected cochlea,⁸ with additional work demonstrating increased signal intensity and associations with reduced hearing.^{8,9}

Identifying the radiologic manifestations of hearing loss is important toward guiding management and developing novel strategies to mitigate hearing loss. With increasing radiologic sensitivity, methods in predicting early pathoetiological markers or clinically relevant hearing-associated imaging characteristics remain understudied. Given this paucity of knowledge, we sought to determine whether labyrinthine signal intensity is associated with VS-related hearing loss.

MATERIALS AND METHODS

Study Participation, Imaging, and Audiometry

An institutional review board–approved (protocol 15–008224) retrospective cross-sectional review was completed of patients from a prospectively maintained VS registry, imaged between 2003 and 2017, as previously described in an investigation of tumor volume and hearing outcomes in VS ($n = 213$).^{10,11} Informed consent was waived, given minimal risk. Patient selection is outlined as follows and in Fig 1.

The first available dedicated inner ear MR imaging with paired audiometric data was used. All available imaging including outside imaging was included for possible analysis. T1, T2-FLAIR, and postgadolinium T1 sequences were used as available. Patients with unavailable audiometry, MR imaging with slices of >3 mm, ≥ 2 nonavailable/nonacquired sequences, or a history of intervention such as gamma knife radiosurgery preceding appropriate imaging or audiometric testing were excluded.

ROIs, including the vestibule and cochlea, were manually drawn to obtain mean signal intensities of the labyrinthine structures by

J.P.W., similar to ROIs in a prior study.⁹ Labyrinthine ROI signal-intensity ratios (SIRs) were normalized to the contralateral labyrinthine structures using the equation mean ipsilateral/contralateral intensity to account for sequence and technique variability (Fig 2A). Additional comparisons using maximal intensities and normalization to the pons were explored but not ultimately used given above noted variability.

SIRs were then paired with the nearest audiometric hearing threshold data including pure tone average (PTA), word recognition score (WRS), and American Academy of Otolaryngology–Head and Neck Surgery (AAO-HNS) hearing class for analysis by C.M.L., as previously described.¹² Briefly, PTA was defined as the average dB threshold heard across 0.5-, 1-, 2-, and 3-kHz frequencies with substitutions at 2 and 4 kHz when appropriate.¹³ WRS represents the percentage of correctly repeated monosyllabic words at a fixed volume threshold. Less-than-perfect speech comprehension is defined as WRS $<90\%$. AAO-HNS hearing class combines PTA and WRS into 4 classes, A, B, C, or D, of increasing hearing deficits.¹² Broadly, class A represents normal/good hearing; B, mild impairment/serviceable; and C/D, severe impairment/nonserviceable with near to nonmeasurable hearing. Comparisons were made with available VS volumetric analysis as previously described in a prior investigation of tumor volume and hearing ($n = 193$).¹⁰

Statistical Methods

Statistical analyses were performed by C.M.L. Continuous features were summarized with means and SDs if approximately normally distributed and with medians and interquartile ranges (IQRs, 25th percentile to 75th percentile) otherwise; categorical features were summarized with frequencies and percentages. Univariable associations of interest were evaluated using the Pearson and Spearman rank correlation coefficients (CCs) and 2-sample *t* and Wilcoxon rank-sum tests. Associations of select SIRs with audiometric features after multivariable adjustment for tumor volume were explored using partial Pearson and Spearman rank correlation coefficients and adjusted means from linear regression models. For the linear regression models, tumor volume was transformed to the natural log scale to satisfy the underlying assumption of normality. Statistical analyses were performed using SAS, Version 9.4 (SAS Institute) and R statistical and computing software, Version 4.0.3 (<http://www.r-project.org/>). All tests were 2-sided, and *P* values $< .05$ were considered statistically significant.

RESULTS

A total of 195 patients with sporadic VS and SIRs from MRIs obtained between 2003 and 2017 comprised the study cohort following exclusion of 18 patients (Fig 1). Dedicated inner ear MR imaging was performed at a median of 154 days (IQR, 0–241 days) from the original diagnostic MR imaging. Of the subjects, 77 patients had an audiogram available from the same date as the MR imaging, 63 had an audiogram from a median of 13 days (IQR, 4–66 days) before the MR imaging, and 55 had an audiogram from a median of 18 days (IQR, 1–98 days) after the MR imaging, representing an assessment of ipsilateral hearing paired with the MR imaging under study. Demographics, audiometric features, and MR imaging features are summarized in Table 1.

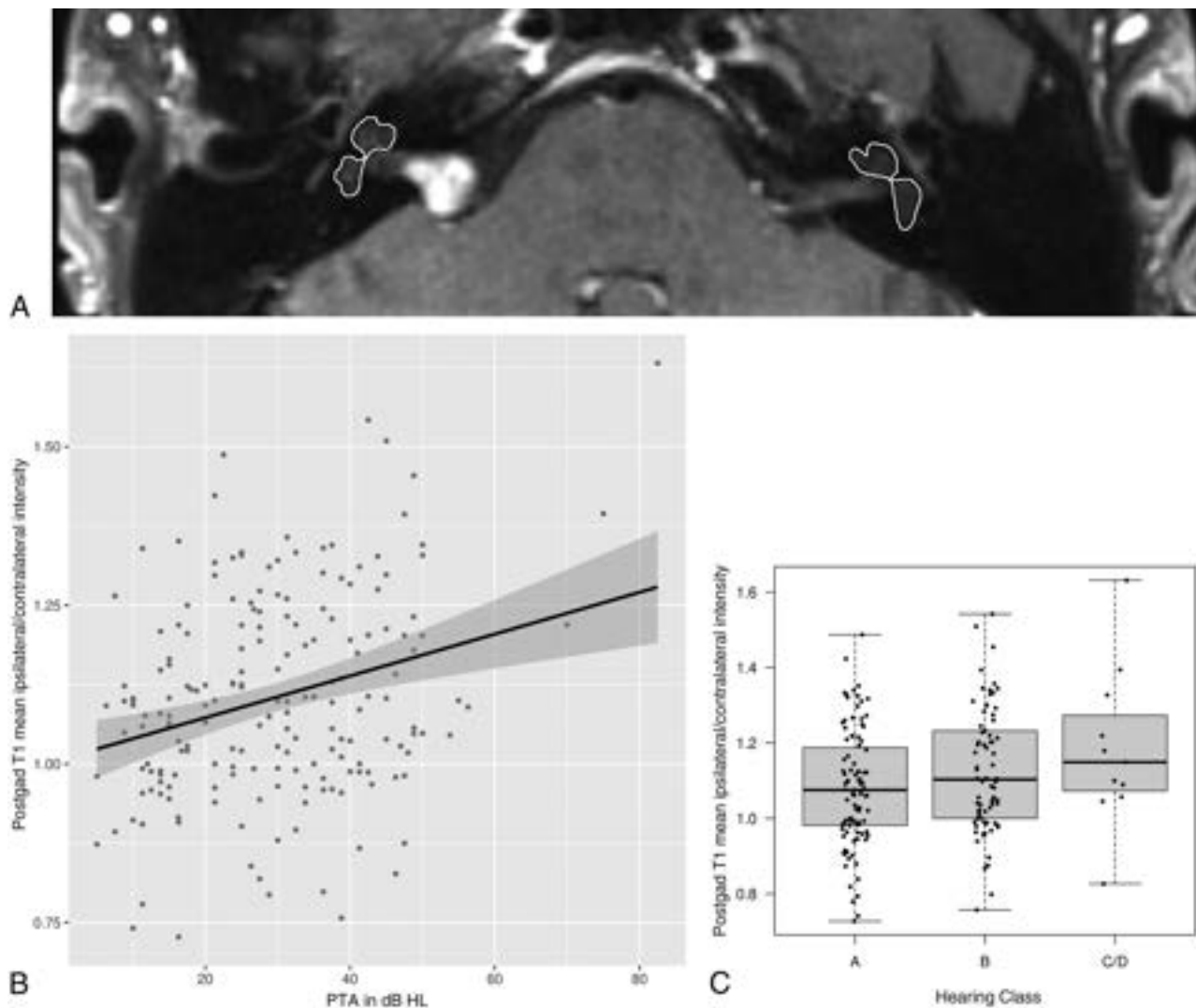


FIG 2. Postgadolinium T1 signal intensity and hearing impairment. A, Representative axial postgadolinium T1 MR imaging and ROIs used for analysis. Increased PTA (B) and worse AAO-HNS hearing classification grades (C) are associated with increased relative signal intensity. HL indicates hearing loss; postgad, postgadolinium.

Sample sizes for features with missing data are indicated in parentheses in Table 1. Note that the 213 patients initially eligible for study had serviceable hearing (ie, AAO-HNS hearing class A/B) on the diagnostic MRI.¹⁰ However, not all diagnostic MRIs were available for SIR assessment; thus, some patients had progressed to nonserviceable hearing at the time of the paired audiogram. Overall, the patient population demonstrated normal-to-mildly-impaired hearing, with 94% of patients demonstrating serviceable hearing: 54% of patients ($n = 100$) having class A and 40% ($n = 75$) having class B. Two notable observed MR imaging features include increased FLAIR mean ipsilateral/contralateral intensity (mean, 1.424 [SD, 0.389]) in addition to postgadolinium T1 mean ipsilateral/contralateral labyrinth intensity (mean, 1.102 [SD, 0.160]).

SIRs demonstrated statistically significant positive correlations with tumor volume, as shown in Table 2. Of note, mean SIRs were significantly associated with tumor volume on both pre- and postgadolinium T1-weighted sequences in addition to FLAIR.

Associations of SIRs, in addition to tumor volume, with ipsilateral hearing, including PTA, WRS, and hearing class, are summarized in Tables 3 and 4. Postgadolinium T1 mean SIR normalized to the contralateral side was significantly positively correlated with PTA ($CC = 0.28$; $P < .001$; Table 3 and Fig 2B) and significantly negatively correlated with WRS ($CC = -0.21$; $P = .003$; Table 3), indicating that larger SIRs were associated with worse hearing and speech comprehension. When we combined both PTA and WRS, hearing class worsened with increasing postgadolinium T1 mean SIRs normalized to the contralateral side, with mean SIRs of 1.080, 1.125, and 1.184 for patients with hearing class A, B, and C/D, respectively ($P = .04$; Table 4 and Fig 2C).

Associations of postgadolinium T1 mean SIRs normalized to the contralateral side with audiometric features after multivariable adjustment for tumor volume were also explored. Although associations of these select SIRs with audiometric features were attenuated after multivariable adjustment, some remained statistically significant. Specifically, the partial Pearson correlation coefficient for the association of postgadolinium T1 mean

ipsilateral/contralateral intensity with PTA after adjusting for tumor volume was 0.25 ($P < .001$). The partial Spearman rank correlation coefficient for associations with WRS was -0.17 ($P =$

.02). Mean levels of postgadolinium T1 mean ipsilateral/contralateral intensity for patients with 100% and $<100\%$ WRS after adjusting for tumor volume were 1.068 and 1.127, respectively ($P = .01$). Mean levels of postgadolinium T1 mean ipsilateral/contralateral intensity for patients with hearing class A, B, and C/D after adjusting for tumor volume were 1.083, 1.121, and 1.166, respectively ($P = .14$).

Table 1: Summary of study cohort (n = 195)

Demographics ^a	
Age at MR imaging (yr)	59 (12)
Sex	
Female	114 (58)
Male	81 (42)
Ipsilateral audiometric features ^a	
PTA in dB HL (n = 188)	29 (14)
WRS (n = 193) (%)	95 (85–100)
WRS $<90\%$ (n = 193)	58 (30)
Hearing class (n = 186)	
A	100 (54)
B	75 (40)
C	2 (1)
D	9 (5)
Ipsilateral MR imaging features ^a	
Volume (n = 193) (cm ³)	0.118 (0.049–0.338)
Mean ipsilateral/contralateral intensity	
T1	1.106 (0.177)
FLAIR (n = 76)	1.424 (0.389)
Postgadolinium	1.102 (0.160)

Note:—HL indicates hearing loss.

^a Continuous features are summarized with means if approximately normally distributed and with median (IQR) otherwise; categoric features are summarized with No. (%).

Table 2: Associations of SIRs with tumor volume (n = 193)

SIRs	CCs ^a	P Values ^a
Mean ipsilateral/contralateral intensity		
T1	0.16	.02
FLAIR (n = 76)	0.39	$<.001$
Postgadolinium T1	0.17	.02

^a CCs and P values are for associations with tumor volume.

Table 3: Associations of MR imaging features with PTA (n = 188) and WRS (n = 193)

MR Imaging Features	CCs ^a	P Values ^a
PTA		
Volume (n = 186) (cm ³)	0.25	$<.001$
Mean ipsilateral/contralateral intensity		
T1	0.18	.02
FLAIR (n = 73)	0.07	.5
Postgadolinium T1	0.28	$<.001$
WRS		
Volume (n = 191) (cm ³)	-0.25	$<.001$
Mean ipsilateral/contralateral intensity		
T1	-0.09	.2
FLAIR (n = 76)	-0.16	.17
Postgadolinium T1	-0.21	.003

^a CCs and P values are for associations with PTA and WRS.

Table 4: Associations of MR imaging features with hearing class (n = 186)

MR Imaging Features ^a	Hearing Class			P Values ^a
	A (n = 100)	B (n = 75)	C/D (n = 11)	
Volume (n = 184) (cm ³)	0.102 (0.046–0.273)	0.131 (0.055–0.440)	0.356 (0.242–0.539)	.006
Mean ipsilateral/contralateral intensity				
T1	1.082 (0.190)	1.122 (0.162)	1.184 (0.169)	.07
FLAIR (n = 73)	1.437 (0.380)	1.359 (0.406)	1.697 (0.144)	.7
Postgadolinium T1	1.080 (0.153)	1.125 (0.162)	1.184 (0.211)	.04

^a Features are summarized with median (IQR, tumor volume) or mean (SD). P values from Spearman rank correlation coefficients are for associations with hearing class.

DISCUSSION

In the present study, we found that signal intensity of the VS-affected labyrinthine structures is associated with the degree of hearing impairment. Specifically, we found that normalized SIRs of the ipsilateral cochlea and vestibule to the contralateral ear on T1-weighted postgadolinium MR imaging are associated with increased PTA, decreased WRS, and an overall impaired AAO-HNS hearing class at near-baseline imaging and hearing time points.

Contrast-enhanced MR imaging of the inner ear has become standard protocol for internal auditory canal assessment in VS. More recently, delayed contrast techniques have been increasingly suggested as an indirect method to assess contrast deposition in endolymph/perilymph and, thus, BBB permeability changes. Here, we found that there is a significant association between increased contrast-enhanced signal intensity and hearing loss with non-delayed techniques. Notably, a prior study did not observe this finding, possibly secondary to limitations with a reduced sample of patients and available audiometry.⁸ The present study found these effects at early time points and less severe hearing deficits including minimally decreased PTA and largely class A hearing relative to prior studies.^{8,9} Future longitudinal study is needed to determine whether these findings are stably associated with hearing trajectory or if there is any inherent variability with VS progression. Work determining whether the findings summarized herein can be extrapolated to individual prognosis will be key. Currently, we do not suggest that quantitative or qualitative inclusion of these findings is ready for standard implementation in clinical-radiologic practice. Such studies exploring the temporal progression of often qualitatively subtle findings will be important in expanding the methodology by which patients are selected for VS treatment and counseled regarding prospects of retaining useful hearing.

Recent studies have focused on using FLAIR imaging, and more recently 3D-FLAIR, as a method to identify presumed inflammatory proteins within the labyrinth associated with VS. While these data fit with current data suggesting increased non-contrast-enhanced FLAIR intensity in the affected labyrinthine

ear, we did not find a significant association between observed increased FLAIR signal intensities and hearing outcomes. There are several possible reasons for this result. There were a relatively limited number of appropriate FLAIR sequences available for analysis secondary to using the earliest imaging available for each patient. Given the timeframe of the study, there were even fewer 3D-FLAIR studies that have been posited to decrease confounding CSF flow artifacts.¹⁴ Most important, while other work has investigated the use of noncontrast FLAIR, finding increased signal within the ipsilateral VS-affected cochlea,^{15,16} associations between noncontrast labyrinthine FLAIR signal and hearing outcomes have been mixed.^{8,17,18} Findings of separate analyses investigating T2 sequences and hearing outcomes have been similarly varied.¹⁹⁻²¹ More recently, hearing loss associated with increased labyrinthine signal has been observed with contrast-enhanced 3D-FLAIR studies.^{8,9} Unfortunately, the early time points and limited availability of contrast-enhanced 3D-FLAIR imaging precluded inclusion in the present study. Future work exploring the technical advantages of contrast-enhanced 3D-FLAIR may improve the sensitivity to signal alterations within the labyrinth.

Prior studies have demonstrated variable associations between increased VS size and poor baseline hearing.^{10,22} Moreover, hearing loss usually ensues even without detectable tumor growth.²³ The current study found that increased tumor size, using volumetric 3D segmentation, is associated with increased SIR. Furthermore, by means of multivariable analysis to adjust for tumor volume, associations of increased SIRs with T1-weighted contrast-enhanced imaging and increased PTA or decreased WRS remained. Thus, these findings suggest that the mechanism driving hearing loss in VS may be independent of tumor size. Most important, however, the degree or independence of variables including tumor volume, signal intensity, and hearing outcomes are unknown. Overall, it is likely that the process of VS-related hearing loss is multifaceted, including vascular compromise, mass effect, BBB permeability, and local inflammation predisposing to hearing loss. Further work assessing these with multifactorial methods will be of increasing importance for directing focused therapies to mitigate hearing loss.

This study has limitations. In a tertiary care center, the present cohort is subject to an increased chance of referral bias.²⁴ Imaging studies spanned 14 years and included other institutions and thus varied techniques, protocols including contrast timing and sequence acquisition, scanners, and magnet strengths. MR imaging appropriate for assessment was frequently performed following presumptive VS diagnosis; baseline audiometric data are, thus, paired with the closest congruent MR imaging. Although the current study examined ipsilateral VS-associated hearing loss with signal-intensity normalization to the contralateral ear, no audiometric comparisons with the contralateral ear were made. Comparisons between T1 and T1 postgadolinium imaging could not be assessed secondary to technique variability. Combined contributions of intrinsic T1 measured with T1 postgadolinium signal intensities and associations with hearing cannot be excluded and, in fact, are likely, given prior research identifying proteinaceous accumulation and VS-associated hearing impairment.^{4,5} Prospective study isolating contributors longitudinally would be useful. As

described above, no contrast-enhanced 3D-FLAIR studies were included for analysis.

CONCLUSIONS

Contrast-enhanced T1 signal intensities of VS-affected labyrinthine structures are associated with hearing loss. Determining the radiologic manifestations of sensorineural hearing loss will be helpful for patient counseling, guiding therapeutic management, and development of novel strategies to mitigate or attenuate progression of sensorineural hearing loss.

Disclosure forms provided by the authors are available with the full text and PDF of this article at www.ajnr.org.

REFERENCES

1. Marinelli JP, Lohse CM, Carlson ML. **Incidence of vestibular schwannoma over the past half-century: a population-based study of Olmsted County, Minnesota.** *Otolaryngol Head Neck Surg* 2018;159:717–23 CrossRef Medline
2. Reznitsky M, Petersen MM, West N, et al. **Epidemiology of vestibular schwannomas: prospective 40-year data from an unselected national cohort.** *Clin Epidemiol* 2019;11:981–86 CrossRef Medline
3. Floc'h JL, Tan W, Telang RS, et al. **Markers of cochlear inflammation using MRI.** *J Magn Reson Imaging* 2014;39:150–61 CrossRef Medline
4. Hannan CJ, Lewis D, O'Leary C, et al. **The inflammatory microenvironment in vestibular schwannoma.** *Neurooncol Adv* 2020;2:vdaa023 CrossRef Medline
5. Lassaletta L, Calvino M, Morales-Puebla JM, et al. **Biomarkers in vestibular schwannoma-associated hearing loss.** *Front Neurol* 2019;10:978 CrossRef Medline
6. Naganawa S, Koshikawa T, Nakamura T, et al. **High-resolution T1-weighted 3D real IR imaging of the temporal bone using triple-dose contrast material.** *Eur Radiol* 2003;13:2650–58 CrossRef Medline
7. Naganawa S, Komada T, Fukatsu H, et al. **Observation of contrast enhancement in the cochlear fluid space of healthy subjects using a 3D-FLAIR sequence at 3 Tesla.** *Eur Radiol* 2006;16:733–37 CrossRef Medline
8. Yamazaki M, Naganawa S, Kawai H, et al. **Increased signal intensity of the cochlea on pre- and post-contrast enhanced 3D-FLAIR in patients with vestibular schwannoma.** *Neuroradiology* 2009;51:855–63 CrossRef Medline
9. Bowen AJ, Carlson ML, Lane JL. **Inner ear enhancement with delayed 3D-FLAIR MRI imaging in vestibular schwannoma.** *Otol Neurotol* 2020;41:1274–79 CrossRef Medline
10. Patel NS, Huang AE, Dowling EM, et al. **The influence of vestibular schwannoma tumor volume and growth on hearing loss.** *Otolaryngol Head Neck Surg* 2020;162:530–37 CrossRef Medline
11. Lees KA, Tombers NM, Link MJ, et al. **Natural history of sporadic vestibular schwannoma: a volumetric study of tumor growth.** *Otolaryngol Head Neck Surg* 2018;159:535–42 CrossRef Medline
12. **Committee on Hearing and Equilibrium guidelines for the evaluation of hearing preservation in acoustic neuroma (vestibular schwannoma).** *Otolaryngol Head Neck Surg* 1995;113:179–80 CrossRef Medline
13. Gurgel RK, Popelka GR, Oghalai JS, et al. **Is it valid to calculate the 3-kilohertz threshold by averaging 2 and 4 kilohertz?** *Otolaryngol Head Neck Surg* 2012;147:102–04 CrossRef Medline
14. Naganawa S, Koshikawa T, Nakamura T, et al. **Comparison of flow artifacts between 2D-FLAIR and 3D-FLAIR sequences at 3 T.** *Eur Radiol* 2004;14:1901–08 CrossRef Medline
15. Osawa I, Kozawa E, Tanaka S, et al. **Signal and morphological changes in the endolymph of patients with vestibular schwannoma on non-contrast 3D FLAIR at 3 Tesla.** *BMC Med Imaging* 2021;21:135 CrossRef Medline

16. Bhadelia RA, Tedesco KL, Hwang S, et al. **Increased cochlear fluid-attenuated inversion recovery signal in patients with vestibular schwannoma.** *AJNR Am J Neuroradiol* 2008;29:720–23 CrossRef Medline
17. Kim DY, Lee JH, Goh MJ, et al. **Clinical significance of an increased cochlear 3D fluid-attenuated inversion recovery signal intensity on an MR imaging examination in patients with acoustic neuroma.** *AJNR Am J Neuroradiol* 2014;35:1825–29 CrossRef Medline
18. Yoshida T, Sugiura M, Naganawa S, et al. **Three-dimensional fluid-attenuated inversion recovery magnetic resonance imaging findings and prognosis in sudden sensorineural hearing loss.** *Laryngoscope* 2008;118:1433–37 CrossRef Medline
19. van de Langenberg R, de Bondt BJ, Nelemans PJ, et al. **Predictors of volumetric growth and auditory deterioration in vestibular schwannomas followed in a wait and scan policy.** *Otol Neurotol* 2011;32:338–44 CrossRef Medline
20. Luong PQ, Cabrera CI, Patil N, et al. **MRI T2-weighted cochlear intensity as a predictor of hearing loss with vestibular schwannoma patients.** *Ann Otol Neurotol* 2021;4:19–25 CrossRef
21. van Linge A, Borsboom GJ, Wieringa MH, et al. **Hearing loss progresses faster in patients with growing intracanalicular vestibular schwannomas.** *Otol Neurotol* 2016;37:1442–48 CrossRef Medline
22. Brown A, Early S, Vasilijic S, et al. **Sporadic vestibular schwannoma size and location do not correlate with the severity of hearing loss at initial presentation.** *Front Oncol* 2022;12:836504 CrossRef Medline
23. Luryi AL, Babu S, Bojrab DI, et al. **Progression of hearing loss in observed non-growing vestibular schwannoma.** *Otol Neurotol* 2022;43:e767–72 CrossRef Medline
24. Saba ES, Marinelli JP, Lohse CM, et al. **Quantifying tertiary referral center bias in vestibular schwannoma research.** *Otol Neurotol* 2020;41:258–64 CrossRef Medline

Diagnostic Utility of 3D Gradient-Echo MR Imaging Sequences through the Filum Compared with Spin-Echo T1 in Children with Concern for Tethered Cord

F. Rafiee, W.A. Mehan, S. Rincon, S. Rohatgi, O. Rapalino, and K. Buch

ABSTRACT

BACKGROUND AND PURPOSE: Fatty intrathecal lesions are a cause of tethered cord, and detection of these on spinal MR imaging is paramount. Conventional T1 FSE sequences are the mainstay of detecting fatty elements; however, 3D gradient-echo MR images, volumetric interpolated breath-hold examination/liver acquisition with volume acceleration (VIBE/LAVA), are popular, given the increased motion resistance. We sought to evaluate the diagnostic accuracy of VIBE/LAVA compared with T1 FSE for detection of fatty intrathecal lesions.

MATERIALS AND METHODS: In this retrospective, institutional review board–approved study, 479 consecutive pediatric spine MRIs obtained to evaluate cord tethering between January 2016 and April 2022 were reviewed. Inclusion criteria were patients who were 20 years of age or younger who underwent spine MRIs containing both axial T1 FSE and VIBE/LAVA sequences of the lumbar spine. The presence or absence of fatty intrathecal lesions was recorded for each sequence. If fatty intrathecal lesions were present, anterior-posterior and transverse dimensions were recorded. VIBE/LAVA and T1 FSE sequences were evaluated on 2 separate occasions (VIBE/LAVAs first followed by T1 FSE several weeks later) to minimize bias. Basic descriptive statistics compared fatty intrathecal lesion sizes on T1 FSEs and VIBE/LAVAs. Receiver operating characteristic curves were used to determine minimal fatty intrathecal lesion size detectable by VIBE/LAVA.

RESULTS: Sixty-six patients were included, with 22 having fatty intrathecal lesions (mean age, 7.2 years). T1 FSE sequences revealed fatty intrathecal lesions in 21/22 cases (95%); however, fatty intrathecal lesions on VIBE/LAVA were detected in 12/22 patients (55%). Mean anterior-posterior and transverse dimensions of fatty intrathecal lesions measured larger on T1 FSE compared with VIBE/LAVA sequences (5.4×5.0 mm versus 1.5×1.6 mm, respectively; P values = .039 anterior-posterior; .027 transverse).

CONCLUSIONS: While T1 3D gradient-echo MR images may have decreased the acquisition time and are more motion-resistant than conventional T1 FSE sequences, they are less sensitive and may miss small fatty intrathecal lesions.

ABBREVIATIONS: AP = anterior-posterior; FIL = fatty intrathecal lesion; LAVA = liver acquisition with volume acceleration; RL = transverse; ROC = receiver operating characteristic; TCS = tethered cord syndrome; VIBE = volumetric interpolated breath-hold examination

Tethered cord syndrome (TCS) is a progressive neurologic condition that develops because of excessive tension on the spinal cord often related to the presence of a filar lesion. If untreated, patients may incur ischemic injury and diminished nerve conduction followed by motor and sensory deficits.^{1,2} Early detection with MR imaging and early surgical intervention are of paramount importance for preserving the quality of life in affected children.^{1,3-5} Filar lesions include deposition of abnormal fatty

tissue within the filum terminale and intradural/intrathecal lipomas, which can lead to impaired cord ascent and excessive stress on the conus.⁶

MR imaging is the mainstay for detection of abnormal conus position, characterization of findings suggestive of TCS, and pre-surgical planning.⁷⁻⁹ Fatty intrathecal lesions (FILs), including both fatty fila and intraspinal lipomas, have traditionally been detected on T1 FSE sequences.¹⁰ Gewirtz et al¹¹ published a series of fast MR imaging protocols for pediatric spine imaging using T2-weighted HASTE, T1-weighted TSE, and T2-weighted STIR sequences. The authors concluded that this set of MR images can identify spinal dysraphisms and other intraspinal anomalies. Sankhe et al¹² evaluated the utility of the CISS sequence for the detection of TCS, concluding that CISS is superior for detecting tethering elements, given the excellent spatial resolution and high

Received October 31, 2022; accepted after revision January 9, 2023.

From the Department of Radiology, Massachusetts General Hospital, Harvard Medical School, Boston, Massachusetts.

Please address correspondence to Karen Buch, MD, Harvard Medical School, Department of Radiology, Massachusetts General Hospital, 55 Fruit St, Boston, MA 02114; e-mail: kbuch@partners.org
<http://dx.doi.org/10.3174/ajnr.A7791>

contrast between CSF and soft-tissue structures. However, the CISS acquisition time is much longer than that of the T2 sequences and is less sensitive for the detection of fat elements. Despite these prior publications, the best fast sequence for detection of FILs is yet to be determined.^{11,13} In most radiologists' practices, T1-weighted images are the mainstay of the MR images in detecting fat elements in spinal anomalies.¹⁴

Recently, there has been an emphasis on fast-acquisition sequences, which are more resistant to motion artifacts, a feature that is particularly desirable for pediatric imaging. As a 3D T1-weighted gradient-echo sequence, volumetric interpolated breath-hold examination (VIBE) reduces the motion artifacts by its unique *k*-space sampling scheme.^{15,16} This sequence generates T1-weighted images but uses a spoiled gradient-echo sequence with ultrashort TRs and has shown lower signal-to-noise ratios compared with spin-echo imaging in prior studies.¹⁶⁻¹⁸ VIBE/liver acquisition with volume acquisition (LAVA) has been shown to be superior to T1-weighted FSE for the detection of pediatric spinal leptomeningeal lesions, owing to its shorter acquisition time and fewer motion artifacts related to respiration, cardiac motion, vessel pulsation, and CSF flow.¹⁹ Because there is a lack of consensus on the best way to evaluate TCS, we sought to compare the diagnostic utility of the VIBE/LAVA sequence for the detection of FILs in the pediatric age group with an FSE T1 pulse sequence. We hypothesized that the VIBE/LAVA will not be as sensitive for the detection of FILs compared with conventional T1 FSE sequences and may miss small FILs.

MATERIALS AND METHODS

This was an institutional review board–approved, retrospective study performed at a single institution. Using a keyword database search, we identified sequential pediatric MR imaging spine studies performed to evaluate cord tethering at our institution during a 6-year period spanning January 2016 to April 2022. Inclusion criteria were the following: 1) patients younger than 20 years of age undergoing spine MR imaging for clinically suspected TCS, and 2) MR imaging acquisition including both conventional T1 FSE and VIBE/LAVA sequences through the lumbar spine. Patients were excluded if the imaging was degraded by motion artifacts that precluded a diagnostic assessment.

MR imaging examinations of the spine were performed on either a 1.5T (Signa HDxt; GE Healthcare) or 3T platform (Magnetom Prisma Fit; Siemens). Acquired sequences used in this study included sagittal and axial T1 FSE sequences, T2WI, and axial ultrafast spoiled gradient-echo sequences known as VIBE on Siemens scanner and LAVA on GE scanner. In our study, we use the term VIBE/LAVA to address the T1-weighted 3D gradient-echo MR images from both vendors.

For the 1.5T GE platform, the MR imaging parameters for axial T1 FSE were as follows: TE = 11.696 ms, TR = 623 ms, section thickness = 3, matrix = 384 × 256, FOV = 100, scan time = 2.1 minutes, number of excitations = 1, flip angle = 90°, echo-train length = 3. The same parameters for axial LAVA were TE = 2.516 ms, TR = 5.072 ms, section thickness = 3 mm, matrix = 320 × 224, FOV = 100 mm, scan time = 2.25 minutes, number of excitations = 0.74, echo-train length = 1, flip angle = 15°.

For the 3T Siemens platform, the MR imaging parameters for axial T1 FSE were as follows: TE = 10 ms, TR = 545 ms, section thickness = 3, matrix = 256 × 230, FOV = 100, scan time = 1.7 minutes, number of excitations = 1, flip angle = 120°, turbo factor = 3. The same parameters for axial VIBE were TE = 1.61 ms, TR = 4.16 ms, section thickness = 1, matrix = 256 × 256, FOV = 100, scan time = 1.7 minutes, number of excitations = 2, turbo factor = 1, flip angle = 15°.

All MR imaging examinations were evaluated using Visage 7, Version 7.1.9c (Visage Imaging). The presence of a FIL was defined as a T1-hyperintense structure extending along the course of the filum terminale. FILs included both fatty fila as well as intradural lipomas. Each MR imaging was independently evaluated by 2 radiologists who were blinded to the clinical and surgical outcomes: 1) a pediatric neuroradiologist with 5 years of experience, and 2) a radiologist (K.B.) with >5 years of practice. For each patient, we recorded the following data: 1) basic demographic information including age, sex, presenting signs and symptoms, 2) the presence/absence of a FIL as determined on conventional T1 FSE, and 3) the presence/absence of a FIL as seen on VIBE/LAVA sequences (Figs 1 and 2).

To avoid a potential source of bias, we reviewed the T1 FSE and VIBE/LAVA sequences at 2 separate points in time. During both rounds of review, the readers were blinded to the radiology report, clinical history, and assessment for FILs on other sequences. The VIBE/LAVA sequence was assessed during the first round, and at least 2 weeks later, the conventional T1 FSE sequences were reviewed. For both the conventional T1 FSE sequence and the VIBE/LAVA sequence, if a FIL was present, the maximal axial anterior-posterior (AP) and transverse (RL) measurements were recorded as measured in the axial plane. Craniocaudal dimensions were measured as the number of vertebral body segments spanned.

Statistical Analysis

All statistical analyses were performed using SPSS, Version 28.0.0 (IBM). Independent *t* tests were used to compare the AP and RL diameters of FILs seen on T1 FSE sequences, which were also detected on VIBE/LAVA sequences, compared with FILs seen only on T1 FSE and not on VIBE/LAVA sequences.

A paired *t* test was used to compare the AP and RL measurements of FILs detected on VIBE/LAVA sequences with the corresponding measurements on T1 FSE sequences. Independent and paired *t* tests were similarly used for calculating the correlation between the craniocaudal extension of the FIL in both sequences.

Finally, to find a cutoff value for FIL size in which VIBE/LAVA can detect the lesion with an acceptable sensitivity and specificity, we illustrated the performance of a classification model at all classification thresholds by drawing a receiver operating characteristic (ROC) curve.

Interrater agreement between the radiologists was determined in both the FIL dimension and craniocaudal extension measurements, by calculating the intraclass correlation coefficient.

RESULTS

A total of 479 patient examinations performed between January 2016 and April 2022 were reviewed. A total of 66 patients (0–20 years of age) met the inclusion criteria. Of these 66 patients, 22 patients

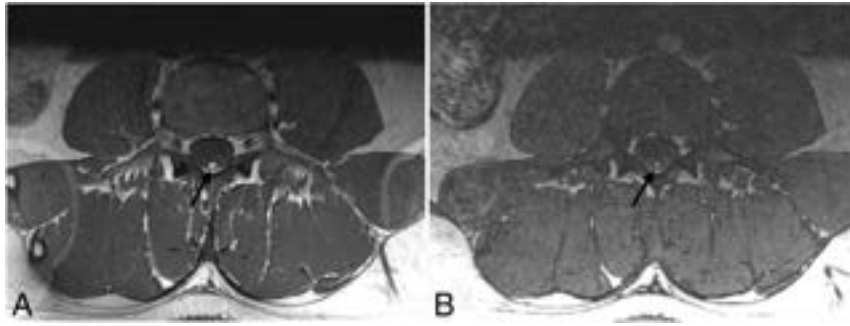


FIG 1. Different acquisitions of T1-weighted MR imaging on the axial planes of the lumbar region at the level of the L4–L5 intervertebral disc in an 18-year-old patient. *A*, T1 FSE sequence shows the dark-signal thecal sac containing the barely visible hypo- to iso-signal intensity cauda equina nerve roots and a round midline intradural lesion (*black arrow*) with bright signal intensity located posteriorly in the spinal canal at the expected anatomic site of the filum terminale, consistent with a FIL. Phase wrap-around artifacts are noted on both sides of the image. *B*, A radiofrequency spoiled 3D gradient-echo sequence known as VIBE of the same patient study at the same level shows a similar bright-signal intradural structure (*black arrow*), the FIL. Note the smaller AP and RL dimensions of the FIL compared with the T1 FSE sequence (*A*). The cauda equina nerve roots are well-demarcated as opposed to the T1 FSE sequence (*A*). VIBE/LAVA can underrate the AP and RL diameters of the FILs.

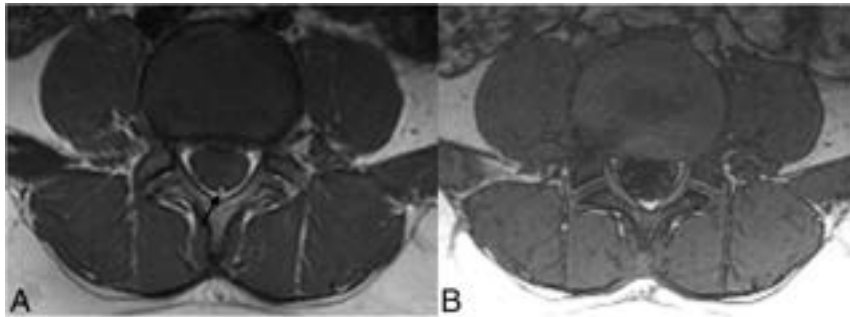


FIG 2. Different acquisitions of T1-weighted MR imaging on the axial plane through the lumbar region at the L4–L5 intervertebral disc in a 10-year-old boy. *A*, A T1 FSE sequence shows a tiny, round, midline intradural lesion (*black arrow*) with bright signal intensity located posteriorly in the spinal canal at the expected anatomic site of the filum terminale, consistent with a FIL. *B*, VIBE of the same patient at the same level shows iso-signal intensity nerve roots of the cauda equina traversing the spinal canal. Although the window level and width are adjusted for better detection of bright lesions, the VIBE sequence failed to reveal the FIL. Note the smaller AP and RL dimensions of the FIL compared with the case in Fig 3. The VIBE sequence is less sensitive in the detection of small FILs and can miss such lesions.

Table 1: Presenting sign and/or symptoms

Indication for MR Imaging	Total	FIL +ve	FIL –ve
Sacral abnormality	16 (24.2%)	9 (40.9%)	7 (16%)
Urinary dysfunction	10 (15.1%)	5 (22.7%)	5 (11.3%)
Bowel dysfunction	8 (12.1%)	2 (9%)	6 (13.6)
Scoliosis	7 (10.6%)	2 (9%)	5 (11.3%)
Lower-extremity weakness	6 (9%)	1 (4.5%)	5 (11.3%)
Back pain	6 (9%)	1 (4.5%)	5 (11.3%)
Other ^a	13 (19.5%)	2 (9%)	11 (25%)
Total	66	22	44

Note:—FIL +ve indicates positive detection of a FIL; FIL –ve, negative detection of a FIL.

^a Other indications for MR imaging include abnormal gait, Chiari I malformation, abnormal findings on spine sonography, and vertebral defects, anal atresia, cardiac defects, tracheo-esophageal fistula, renal anomalies, and limb abnormalities (VACTERL).

had imaging findings consistent with a FIL on at least 1 sequence (either the conventional T1 FSE and/or the VIBE/LAVA).

The mean age in our cohort was 7.2 years (range, 2 days to 18.5 [SD, 5.7] years). For patients with FILs, the mean age was

6.8 years (range, 2 days- to 18.5 [SD, 6.3] years). The cohort included 33 males and 33 females.

The most common presenting sign in the affected group was an asymptomatic sacral region abnormality detected by physical examination (40.9%). These sacral region abnormalities included a visible sacral dimple, a palpable sacral mass, or a gluteal cleft asymmetry. Urinary dysfunction (22.7%), bowel dysfunction (9%), back pain (4.5%), lower extremity weakness (4.5%), and scoliosis (9%) were the most common symptoms (Table 1). Two patients (9%) underwent spinal imaging due to other medical conditions and had atypical symptoms for TCS.

T1 FSE sequences revealed FILs in 21/22 patients (95.4%), whereas VIBE/LAVA sequences detected FILs in 12/22 patients (54.5%) (Table 2 and Figs 1 and 2). At surgery, 21/22 (95.5%) of these cases had gross fatty elements found to be consistent with FILs. One of the patients with no imaging sign of FILs on either sequence (T1 FSE and VIBE/LAVA) underwent an operation for a tethered cord release, and fibrofatty tissue was evident at histopathology.

For cases with a suspected FIL on both T1 FSE and the VIBE/LAVA sequences, the mean AP and RL diameters were 5.40 and 5.02 mm, respectively.

For cases with a suspected FIL on T1 FSE sequences on which no intrinsically T1-bright focus was identified on the VIBE/LAVA sequence, the mean AP and RL diameters were 1.47 and

1.64 mm, respectively (Table 2). These dimensions demonstrate the lower size limit for detectable FILs on the VIBE/LAVA sequence (independent *t* test, *P* value = .039 for AP and .027 for RL dimensions) (Fig 2).

Not only were we not able to detect smaller FILs on VIBE/LAVA sequences, we also found that FILs measured smaller on VIBE/LAVA sequences compared with conventional T1 FSE sequences (Fig 1). As stated previously, the mean AP and RL diameters of FILs in T1 FSE images were 5.40 and 5.02 mm, respectively; however, the mean AP and RL diameters of the FILs as measured on the corresponding VIBE/LAVA images were 4.85 and 4.57 mm. These measurement differences were statistically significant (paired *t* test, *P* value = .003 for AP and <.001 for RL diameters), noting that the VIBE/LAVA sequence underestimates the actual size of the FILs (Fig 1).

By setting a cutoff point of 1.45 mm for FIL AP diameter, the VIBE/LAVA sequence detected FILs with a sensitivity of 75%

Table 2: Number, size, and extent of FIL each sequence detected

Sequence	FIL +ve	FIL +ve Mean AP	FIL +ve Mean RL	FIL +ve Mean CC
+T1 FSE and +VIBE/LAVA, measured in T1 FSE	21/22 (95.4)	5.4	5	3.8
+T1 FSE and +VIBE/LAVA, measured in VIBE/LAVA	12/22 (54.5)	4.9	4.6	2.2
+T1 FSE and -VIBE/LAVA, measured in T1 FSE	9/21 (42.9)	1.5	1.6	2.5

Note:—RL indicates right-left dimension; CC, craniocaudal dimension; FIL +ve, positive detection of a FIL; FIL -ve, negative detection of a FIL.

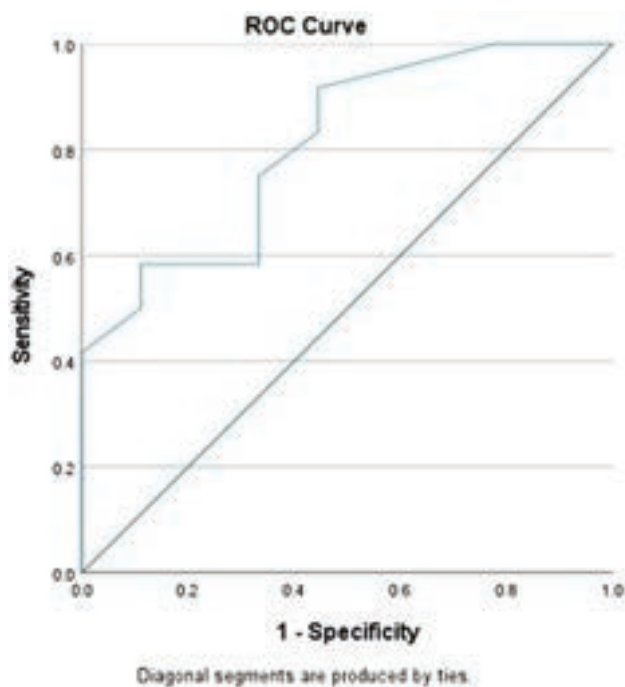


FIG 3. ROC curve for FIL AP diameter (area under the curve = 0.810, *P* value = .017).

and a specificity of 66.7% (ROC area under the curve = 0.810, *P* value = .017) (Fig 3). Considering the same sensitivity and specificity for the RL diameter, the cutoff point of 1.90 mm was optimal for this measurement (ROC area under the curve = 0.815, *P* value = .016) (Fig 4).

In addition to the size, we also compared the craniocaudal lengths of the FILs between the 2 sequences. The mean lengths of the FILs on the T1 FSE and VIBE/LAVA sequences were 3.75 and 2.17 vertebral levels, respectively. T1 FSE revealed larger craniocaudal extensions of FILs compared with the VIBE/LAVA sequence (paired *t* test, *P* value < .001).

The mean craniocaudal extent of FILs on the T1 FSE images of patients with positive findings on VIBE/LAVA was 1.3 levels longer than in those with negative findings. However, this difference was not statistically significant (independent *t* test, *P* value = .057).

The interrater reliability was measured by calculating the intraclass correlation coefficient. The intraclass correlation coefficient for the AP and RL diameter measurements for the T1 FSE sequences were 0.93 and 0.99, respectively, which are consistent with an excellent reliability. Similarly, we calculated the intraclass correlation coefficients for the same measurements for the VIBE/LAVA

sequences, which were 0.89 for AP and 0.98 for RL, consistent with good and excellent reliability, respectively.

The intraclass correlation coefficients in measuring the FIL craniocaudal extension were 0.86 and 0.83 for T1 FSE and VIBE/LAVA sequences, respectively, indicating a good interrater reliability of these measurements.

DISCUSSION

The detection of FILs, either related to a fatty filum or an intrathecal lipoma, is clinically important for the assessment of suspected tethered cord. These congenital abnormalities impair spinal cord ascent and cause excessive stress on the conus.^{6,7} Early detection and surgical intervention can help to alleviate symptoms and promote normal development in children.²⁰

T1 FSE sequences have long been considered the criterion standard for the detection of fatty elements in the spine.¹⁴ More recently, there has been an emphasis on the development of accelerated/fast sequences, leading to the development of fast, more motion-resistant sequences with decreased CSF pulsation artifacts, including 3D T1-weighted gradient-echo sequences such as VIBE/LAVA.²¹ However, to date, few studies have investigated their role in the detection of FILs in pediatric spine imaging.

In 2013, Murakami et al²² were the first to use the 3D T1-weighted spoiled gradient-echo sequence to detect lumbosacral lipoma and thickened filum terminales. The authors concluded that 3D T1 gradient-echo was superior to the conventional T1-weighted sequence in detecting thickened filar anomalies. The 3D T1 gradient-echo was able to localize the intrathecal lipoma in more section slices and clearly demarcated the filum terminal contour, allowing more accurate filum terminale diameter measurements.²²

Our study sought to compare the utility of the VIBE/LAVA sequence with that of the conventional T1 FSE sequence for the detection of FILs. We found that FILs on VIBE/LAVA sequences were only detectable 54.5% of the time compared with 95.4% of the time on the conventional T1 FSE sequences. We found that FILs measuring approximately 1.5 mm in the axial plane could be detected on conventional T1 FSE sequences but not on the VIBE/LAVA sequences.

Moreover, FIL measurements made on VIBE/LAVA sequences were consistently smaller compared with those of the conventional T1 FSE sequences. In our study cohort, we had 1 patient who did not demonstrate evidence of a FIL on both the conventional T1 FSE sequence and the VIBE/LAVA sequence but had fatty elements identified at histopathology following a tethered cord release operation. This finding is supported in the literature noting microfatty elements in the filum terminale that were radiographically occult.^{23,24}

There are several limitations to this study. The first being its retrospective nature. A retrospective design was utilized as we used the histopathology findings from tethered cord release surgery to validate the presence of fatty intrathecal tissue to validate the

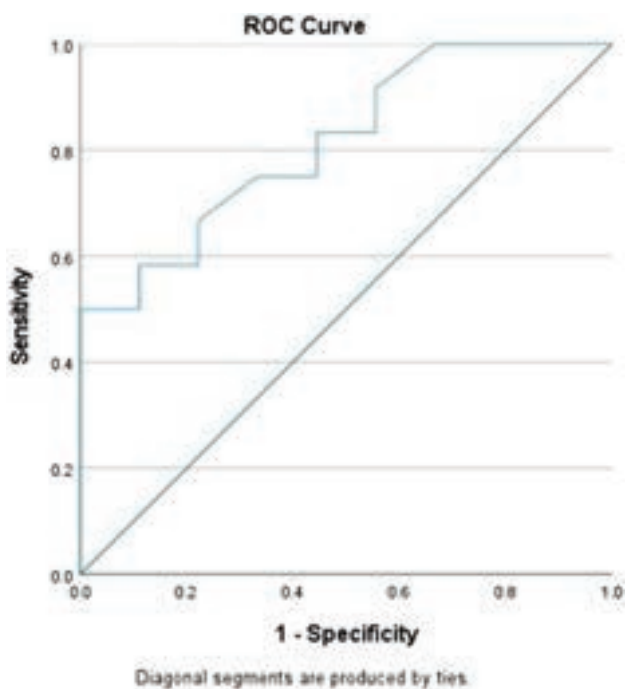


FIG 4. ROC curve for FIL RL diameter (area under the curve = 0.815, P value = .016).

findings on the conventional T1 FSE sequences and VIBE/LAVA sequences. Additionally, this study cohort was relatively small; however, we did have enough statistical power to perform our analyses (the calculated minimum number of subjects that needed to be enrolled to have 80% statistical power with $\alpha = .05$ was 16). The focus of this study is narrow in scope, being directed at the detection of fatty intrathecal components. We recognize that there are numerous other intrathecal and filar abnormalities that may result in a tethered cord. We thought that the narrow focus of this study emphasizes the importance of performing T1 FSE sequences over VIBE/LAVA sequences for the detection of small FILs.

CONCLUSIONS

The results of our study demonstrate improved sensitivity for detecting FILs on conventional T1 FSE sequences over the VIBE/LAVA sequences. While the VIBE/LAVA sequences are attractive to use, given motion resistance and decreased acquisition time, small FILs may be missed, potentially leading to delayed diagnosis and treatment.

Disclosure forms provided by the authors are available with the full text and PDF of this article at www.ajnr.org.

REFERENCES

- Lew SM, Kothbauer KF. Tethered cord syndrome: an updated review. *Pediatr Neurosurg* 2007;43:236–48 CrossRef Medline
- Solmaz I, Izi Y, Albayrak B, et al. Tethered cord syndrome in childhood: special emphasis on the surgical technique and review of the literature with our experience. *Turk Neurosurg* 2011;21:516–21 Medline
- Sanchez T, John RM. Early identification of tethered cord syndrome: a clinical challenge. *J Pediatr Health Care* 2014;28:e23–33 CrossRef Medline
- Gharedaghi M, Samini F, Mashhadinejad H, et al. Orthopedic lesions in tethered cord syndrome: the importance of early diagnosis and treatment on patient outcome. *Arch Bone Jt Surg* 2014;2:93–97 Medline
- Chern JJ, Dauser RC, Whitehead WE, et al. The effect of tethered cord release on coronal spinal balance in tight filum terminale. *Spine (Phila Pa 1976)* 2011;36:E944–49 CrossRef Medline
- Gupta A, Rajshkhar V. Fatty filum terminale (FFT) as a secondary tethering element in children with closed spinal dysraphism. *Childs Nerv Syst* 2018;34:925–32 CrossRef Medline
- Al-Omari MH, Eloqayli HM, Qudseih HM, et al. Isolated lipoma of filum terminale in adults: MRI findings and clinical correlation. *J Med Imaging Radiat Oncol* 2011;55:286–90 CrossRef Medline
- Rohrschneider WK, Forsting M, Darge K, et al. Diagnostic value of spinal US: comparative study with MR imaging in pediatric patients. *Radiology* 1996;200:383–88 CrossRef Medline
- Tortori-Donati P, Rossi A, Biancheri R, et al. Magnetic resonance imaging of spinal dysraphism. *Top Magn Reson Imaging* 2001;12:375–409 CrossRef Medline
- Mehta DV. Magnetic resonance imaging in paediatric spinal dysraphism with comparative usefulness of various magnetic resonance sequences. *J Clin Diagn Res* 2017;11:TC17–22 CrossRef Medline
- Gewirtz JL, Skidmore A, Smyth MD, et al. Use of fast-sequence spine MRI in pediatric patients. *J Neurosurg Pediatr* 2020;26:676–81 CrossRef Medline
- Sankhe S, Dang G, Mathur S, et al. Utility of CISS imaging in the management of tethered cord syndrome. *Childs Nerv Syst* 2021;37:217–23 CrossRef Medline
- Khalatbari H, Perez FA, Lee A, et al. Rapid magnetic resonance imaging of the spine in neonates with spinal dysraphism. *World Neurosurg* 2020;144:e648–59 CrossRef Medline
- Zugazaga Cortazar A, Martin Martinez C, Duran Feliubadalo C, et al. Magnetic resonance imaging in the prenatal diagnosis of neural tube defects. *Insights Imaging* 2013;4:225–37 CrossRef Medline
- Park JE, Choi YH, Cheon JE, et al. Three-dimensional radial VIBE sequence for contrast-enhanced brain imaging: an alternative for reducing motion artifacts in restless children. *AJR Am J Roentgenol* 2018;210:876–82 CrossRef Medline
- Wetzel SG, Johnson G, Tan AG, et al. Three-dimensional, T1-weighted gradient-echo imaging of the brain with a volumetric interpolated examination. *AJNR Am J Neuroradiol* 2002;23:995–1002 Medline
- Koh E, Walton ER, Watson P. VIBE MRI: an alternative to CT in the imaging of sports-related osseous pathology? *Br J Radiol* 2018;91:20170815 CrossRef Medline
- Bangiyev L, Raz E, Block TK, et al. Evaluation of the orbit using contrast-enhanced radial 3D fat-suppressed T1 weighted gradient echo (Radial-VIBE) sequence. *Br J Radiol* 2015;88:20140863 CrossRef Medline
- Cho HH, Choi YH, Cheon JE, et al. Free-breathing radial 3D fat-suppressed T1-weighted gradient-echo sequence for contrast-enhanced pediatric spinal imaging: comparison with T1-weighted turbo spin-echo sequence. *AJR Am J Roentgenol* 2016;207:177–82 CrossRef Medline
- Cools MJ, Al-Holou WN, Stetler WR Jr, et al. Filum terminale lipomas: imaging prevalence, natural history, and conus position. *J Neurosurg Pediatr* 2014;13:559–67 CrossRef Medline
- Kralik SF, O'Neill DP, Kamer AP, et al. Radiological diagnosis of drop metastases from paediatric brain tumours using combination of 2D and 3D MRI sequences. *Clin Radiol* 2017;72:902e913–19 CrossRef Medline
- Murakami N, Morioka T, Hashiguchi K, et al. Usefulness of three-dimensional T1-weighted spoiled gradient-recalled echo and three-dimensional heavily T2-weighted images in preoperative evaluation of spinal dysraphism. *Childs Nerv Syst* 2013;29:1905–14 CrossRef Medline
- Tu A, Steinbok P. Occult tethered cord syndrome: a review. *Childs Nerv Syst* 2013;29:1635–40 CrossRef Medline
- Rezaee H, Tavallai A, Keykhosravi E, et al. Effect of untethering on occult tethered cord syndrome: a systematic review. *Br J Neurosurg* 2022;36:574–82 CrossRef Medline

Neuroimaging Features of Biotinidase Deficiency

A. Biswas,^{1,2} C. McNamara,^{1,2} V.K. Gowda,^{1,2} F. Gala,^{1,2} S. Sudhakar,^{1,2} J. Sidpra, M.S. Vari,^{1,2} P. Striano,^{1,2} S. Blaser,^{1,2} M. Severino,^{1,2} S. Batzios, and^{1,2} K. Mankad^{1,2}



ABSTRACT

SUMMARY: Biotinidase deficiency is an autosomal recessive condition caused by pathogenic variants in the *BTD* gene. Resultant deficiency of free biotin leads to impaired activity of the enzyme carboxylase and related neurologic, dermatologic, and ocular symptoms. Many of these are reversible on treatment, but early recognition and commencement of biotin supplementation are critical. This practice is especially important in countries where routine neonatal screening for biotinidase deficiency is not performed. In this report comprising 14 patients from multiple centers, we demonstrate the MR imaging patterns of this disorder at various age groups. Knowledge of these patterns in the appropriate clinical context will help guide early diagnosis of this treatable metabolic disorder.

Biotin is a water-soluble B-complex vitamin and is a coenzyme for 4 carboxylase enzymes that participate in gluconeogenesis, amino acid catabolism, and fatty acid synthesis.¹⁻³ The enzyme biotin holocarboxylase synthetase covalently attaches biotin to specific apocarboxylases. Proteolytic degradation of these carboxylases results in the release of biocytin and biotinyl peptides, from which free biotin is released by the enzyme biotinidase.⁴ Free biotin is then recycled back into the pool for use by holocarboxylases.^{5,6} Biotinidase also plays a role in cleaving biotin from dietary protein-bound biotin.⁷ Biotinidase deficiency is, therefore, characterized by an overall deficiency of free biotin and consequent defective carboxylase activity.⁸ Inherited as an autosomal recessive condition, biotinidase deficiency is caused by pathogenic variants in the *BTD* gene (Online Mendelian Inheritance in Man 609019).

Neurologic symptoms of untreated biotinidase deficiency include seizures, encephalopathy, developmental delay, vision

loss, hearing loss, ataxia, and myelopathy, and these depend on the age at presentation.^{3,9,10} Non-neurologic features are also common, including alopecia, skin rash, and conjunctivitis. Treatment with biotin generally results in reversal of symptoms, except in cases of established hearing loss, optic atrophy, and moderate-severe developmental delay, with possible permanent deficits. Similarly, treatment with biotin before the development of clinical manifestations can prevent symptoms from developing. For this reason, routine neonatal screening for biotinidase deficiency is now performed in many countries, leading to decreased disease manifestation in these populations. In countries that lack adequate screening, however, early identification of the disease and initiation of treatment is of vital importance to prevent long-term sequelae.

Several case reports have described imaging features of biotinidase deficiency such as diffuse white matter signal changes and signal abnormalities involving the fornices, hippocampal formations, brainstem, optic pathway, and spinal cord, and these appear to be dependent on the age at presentation. In this series comprising 14 cases from multiple centers, we aimed to detail the imaging features of biotinidase deficiency presenting in various age groups.

CASE SERIES

Local institutional ethics board approval was obtained from each collaborating hospital (The Hospital for Sick Children, Toronto, Ontario, Canada; Great Ormond Street Hospital for Children, London, UK; Indira Gandhi Institute of Child Health, Bengaluru, India; Bai Jerbai Wadia Hospital for Children, Mumbai, India; and Istituto di Ricovero e Cura a Carattere Scientifico Istituto

Received September 26, 2022; accepted after revision January 4, 2023.

From the Department of Diagnostic Imaging (A.B., S. Blaser), The Hospital for Sick Children, Toronto, Ontario, Canada; Departments of Neuroradiology (A.B., C.M., S.S., J.S., K.M.) and Paediatric Metabolic Medicine (S. Batzios), Great Ormond Street Hospital for Children, National Health Service Foundation Trust, London, UK; Developmental Biology and Cancer Section (J.S.), University College London Great Ormond Street Institute of Child Health, London, UK; Department of Pediatric Neurology (V.K.G.), Indira Gandhi Institute of Child Health, Bengaluru, Karnataka, India; Department of Radiodiagnosis (F.G.), Bai Jerbai Wadia Hospital, Mumbai, Maharashtra, India; and Pediatric Neurology and Muscular Diseases Unit (M.S.V., P.S.) and Neuroradiology Unit (M.S.), Istituto di Ricovero e Cura a Carattere Scientifico Istituto Giannina Gaslini, Genoa, Italy.

S. Batzios and K. Mankad are joint senior authors.

Please address correspondence to Asthik Biswas, MD, Department of Neuroradiology, Great Ormond Street Hospital for Children NHS Foundation Trust, Great Ormond St, London, WC1N 3JH, UK; e-mail: asthikbiswas@gmail.com; @stikkman11

Indicates article with online supplemental data.

<http://dx.doi.org/10.3174/ajnr.A7781>

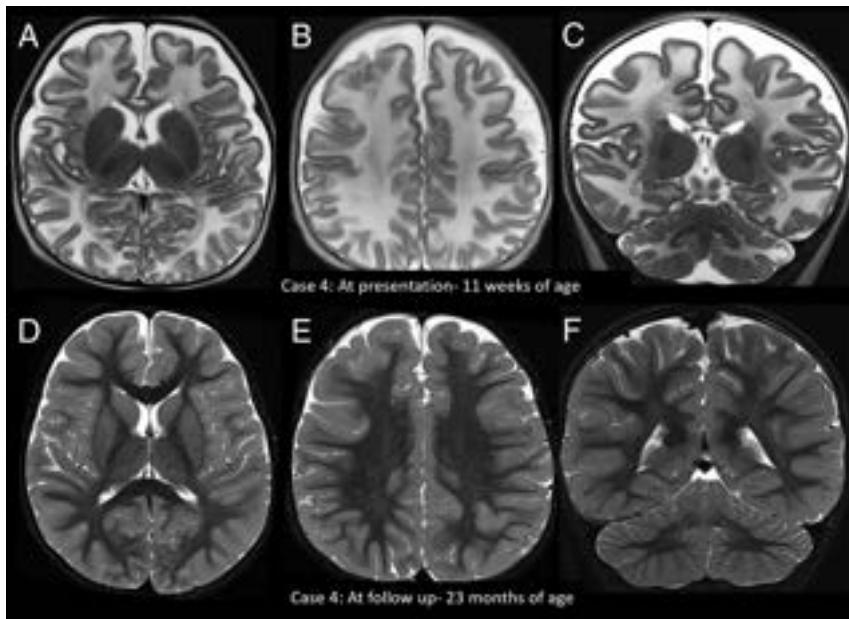


FIG 1. Imaging appearance and follow-up in the early infantile age group. Axial (A and B) and coronal (C) T2-weighted images in patient 4 at 11 weeks of age at the acute stage show diffuse white matter T2 hyperintensity. D–F, The findings fully resolved on treatment with biotin.

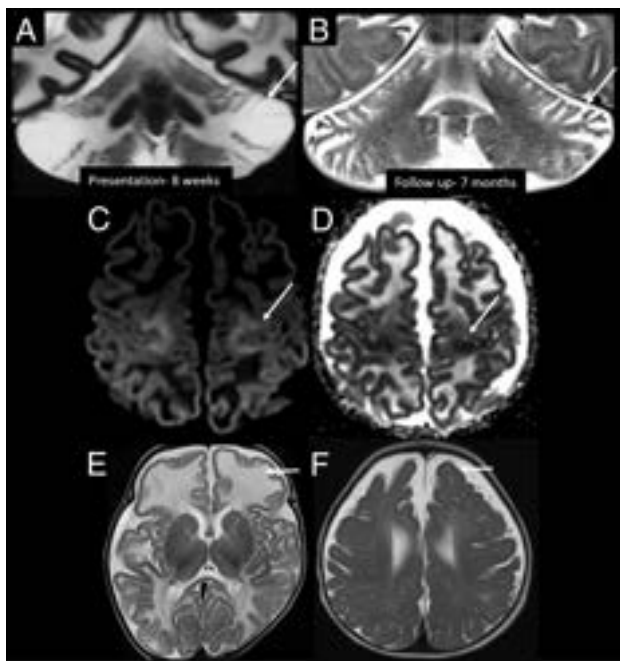


FIG 2. Other imaging patterns in the early infantile age group. Coronal T2-weighted images in patient 10 at 8 weeks of age show predominant superior and inferior semilunar lobule involvement in the acute stage (A, arrow), with atrophy on follow-up MR imaging (B, arrow). C and D, Axial DWI and ADC image in patient 4 at 11 weeks of age show perirolandic restricted diffusion (arrows). Axial T2-weighted image of patient 3 in the acute stage (10 weeks of age) (E) shows predominant involvement of the frontal lobes (arrow). Axial T2-weighted image of patient 10 (F) on the follow-up image at 7 months of age shows frontal-predominant atrophy (arrow).

Giannina Gaslini, Genoa, Italy). Clinical, laboratory, and imaging information of 14 patients with acute presentation of biotinidase deficiency (7 males, 7 females), ranging from 2 months to 14 years of age, were retrospectively reviewed.

All MR images were acquired on a 1.5 or 3T scanner, with MR imaging sequences performed as per each hospital's local protocol. All MR images included axial and sagittal T1-weighted, axial T2-weighted, axial or coronal FLAIR, and axial DWI sequences of the brain. MR spectroscopy was available in 1 patient, and a contrast-enhanced T1-weighted sequence was available in 1 patient. Noncontrast imaging of the cervical spine was available in 3 patients and of the whole spine in 3 patients. Spine sequences included sagittal and axial T2-weighted images, with or without T1-weighted sequences.

Clinical and MR Imaging Findings

Demographic, clinical, and imaging findings of the 14 patients are summarized in the Online Supplemental Data.

Early Infantile Group (Presentation < 3 Months of Age)

Seven patients (5 male infants, 2 female infants) presented at ages ranging from 8 to 12 weeks of life (median, 10 weeks; interquartile range, 9–11 weeks), with seizures being the presenting symptom in all patients. Other features that were seen variably included developmental delay ($n = 4$), hypotonia ($n = 3$), hearing loss ($n = 3$), failure to thrive ($n = 2$), encephalopathy ($n = 1$), vision loss ($n = 1$), hyperventilation ($n = 1$), vomiting ($n = 1$), skin rash ($n = 1$), and alopecia ($n = 1$).

MR imaging in all 7 patients demonstrated diffuse cerebral and cerebellar T2 hyperintensity and swelling (Fig 1). In 2 patients (patients 3 and 10), the frontal lobe white matter was predominantly swollen compared with other regions (Fig 2). In 2 patients (patients 4 and 10), there was striking predominant involvement of the superior and inferior semilunar lobules of the cerebellum (Fig 2). Other imaging features included T2 hyperintensity at the medullary pyramids ($n = 3$, patients 4, 7, and 10) and perirolandic restricted diffusion ($n = 3$, patients 3, 4, and 7) (Fig 2).

All patients were treated with biotin with doses ranging from 5 to 20 mg/day (median, 10 mg/day; interquartile range, 10–20 mg/day). Imaging following initiation of treatment was available in patients 4, 7, and 10 (at 2 years, 4 years, and 6 months of age, respectively), all of which showed resolution of swelling and signal abnormalities. Sequelae were only noted in patient 10 who showed frontal predominant cerebral atrophy and atrophy of the cerebellar semilunar lobules (Fig 2). On clinical follow-up, 3 patients (patients 1, 7, and 10) had sensorineural hearing loss, 2 (patients 1 and 5) had learning difficulties, and 1 (patient 10) had quadriplegia and strabismus.

Early Childhood Group (Presentation between 18 and 24 Months of Age)

Three patients (2 girls, 1 boy) presented at ages ranging from 18 to 24 months of age. All 3 patients had developmental delay and

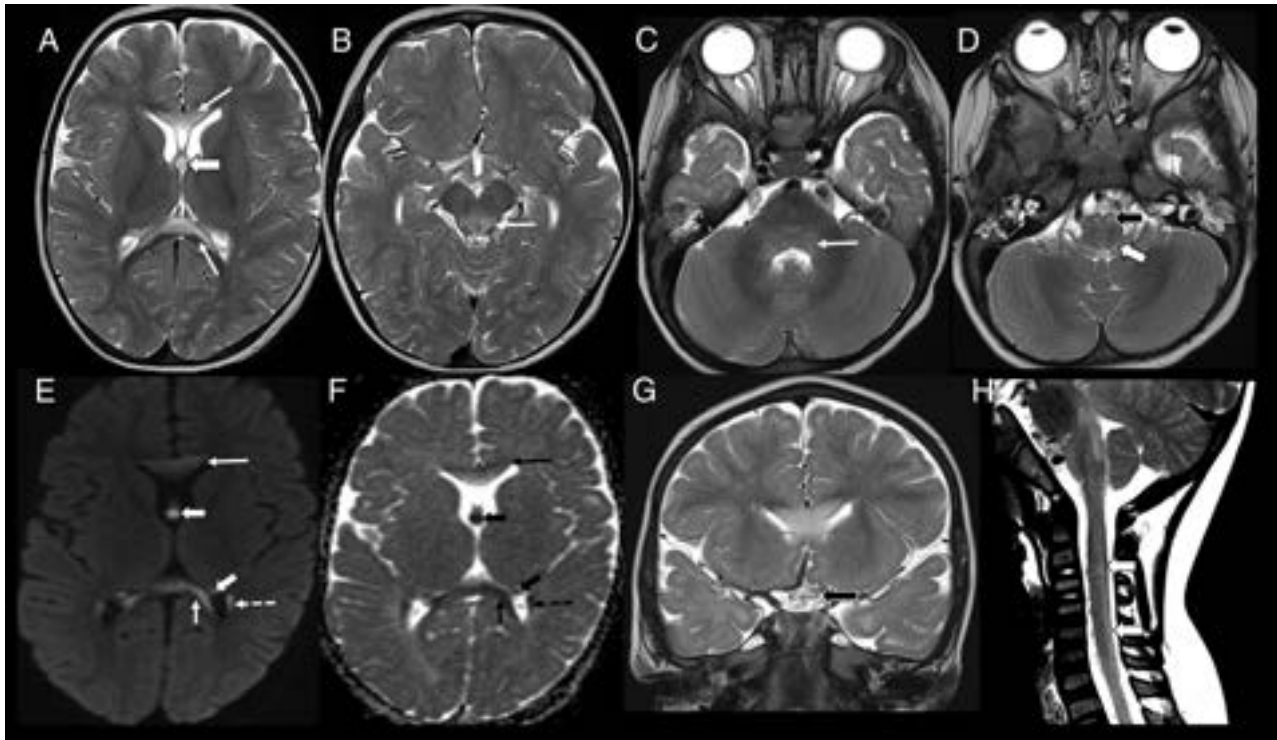


FIG 3. Imaging appearance in the early childhood age group (patient 8, 18 months of age). Axial T2-weighted images show hyperintense lesions involving the genu and splenium of corpus callosum (A, arrows), forniceal columns (A, arrowhead); dorsal midbrain including the periaqueductal gray matter (B, arrow); dorsal pons (C, arrow), medullary pyramids (D, black arrowhead), and dorsal medulla (D, white arrowhead). Axial DWI (E) and ADC (F) images show restricted diffusion involving the corpus callosum (arrows), fornices (arrowheads), and tapetum (dashed arrow). Coronal T2-weighted image (G) shows involvement of the optic chiasm (black arrowhead). Sagittal T2-weighted image of the cervical spine (H) shows faint hyperintensity involving the dorsal cervical cord (white arrowheads).

hypotonia. Two patients each had seizures (patients 2 and 6) and ataxia (patients 2 and 8). One patient (patient 6) had hearing and vision loss.

All 3 patients showed signal abnormalities in the fornices (confined only to the body in patient 2), periaqueductal gray matter, dorsal pons, and medullary pyramids. Two patients (patients 6 and 8) also had signal abnormalities in the superior and inferior colliculi; superior, middle, and inferior cerebellar peduncles; corpus callosum (inner blade of genu in patient 6, middle blade of the entire corpus callosum in patient 8); prechiasmatic optic nerves and optic chiasm; and cervical spinal cord (lateral columns in patient 6, dorsal columns in patient 8). Patient 2 also showed signal abnormalities in the medial thalami, whereas patient 6 also showed involvement of the lateral geniculate bodies, hippocampal formations, parahippocampal gyri, mamillary bodies, and hypothalamus. Imaging findings in patient 8 are depicted in Fig 3.

All patients were treated with biotin (10 mg in patients 2 and 8 and 15 mg in patient 6). Follow-up imaging was not available for any patient. On clinical follow-up, patients 2 and 8 recovered completely with no residual deficits, whereas patient 6 had bilateral optic atrophy and bilateral moderate sensorineural hearing loss.

Late Childhood Group (Presentation between 5 and 14 Years of Age)

Four patients (3 girls, 1 boy) presented between 5 and 14 years of age. All patients had ataxia, and 3 had myelopathy. Developmental

delay was seen in 3 patients (patients 11, 12, and 13) and seizures and encephalopathy, in 2 patients (patients 11 and 12). In addition, patient 13 had regression of motor milestones. Other symptoms seen during the course of illness were vision loss ($n = 3$, patients 11, 12, and 14), skin rash and alopecia ($n = 2$, patients 11 and 14), hyperventilation ($n = 2$, patients 11 and 12), hearing loss ($n = 1$, patient 11), and vomiting ($n = 1$, patient 12).

Although patient 12 presented to us at 14 years of age with vision loss and myelopathy, she had a history of developmental delay, seizures, and encephalopathy at 6 months of age, at which point she was diagnosed as having a suspected metabolic disorder. No imaging was performed at this time, and she was treated with a mitochondrial cocktail of vitamins, including biotin. She developed symptoms once biotin was discontinued and was then referred for tertiary care.

The spinal cord was involved in all patients (entire cross-sectional area of the cervicothoracic cord in patient 11; lateral corticospinal tract and dorsal columns of the cervical cord in patient 12; dorsal columns of cervicothoracic cord in patient 13; and lateral and dorsal columns of the cervical cord in patient 14).

Three patients (patients 11, 13, and 14) had involvement of the fornices. In patients 11 and 13, there was symmetric forniceal involvement at onset, whereas patient 14 initially had asymmetric involvement (left > right) followed by symmetric involvement of both fornices during the next 3 months. Two patients (patients 11 and 13) had signal abnormalities in the periaqueductal gray matter, dorsal pons, and dorsolateral medulla.

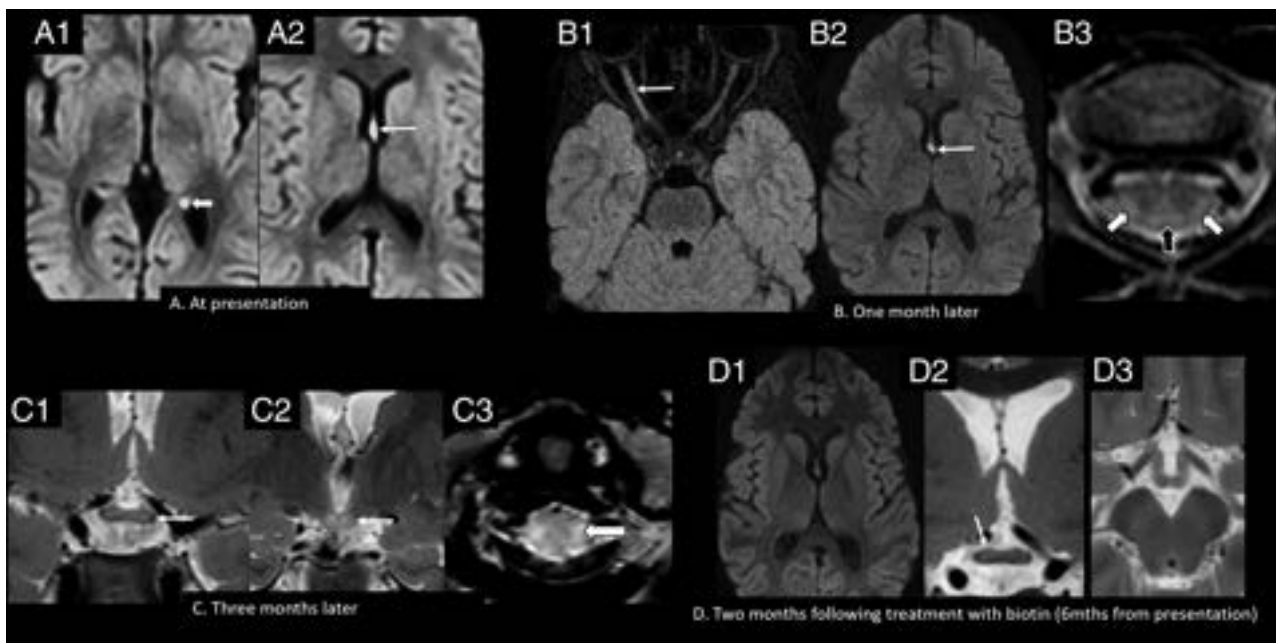


FIG 4. Imaging appearance and follow-up in the late childhood age group (patient 14, six years of age). A, Axial DWI (b-value = 1000) shows hyperintense signal involving the fornical columns (arrow, A2) and the left fornical crus (arrowhead, A1). Axial FLAIR (B1) and axial DWI (b-value = 1000) (B2) show hyperintense signal involving the right optic nerve (arrow, B1), with persistent signal abnormality in the fornices (arrow, B2). Axial T2-weighted image of the cervical spine (B3) shows hyperintense lesions involving the dorsal (black arrowhead) and lateral columns (white arrowheads). Coronal T2-weighted images (C1 and C2) show extension of signal abnormality to involve the optic chiasm (arrow, C1) and mammillary bodies (arrow, C2). Axial T2-weighted image of the cervical spine (C3) shows increased signal abnormality in the lateral columns (arrowhead). Axial DWI (b-value = 1000) (D1), coronal T2 (D2), and axial T2 (D3) weighted images show resolution of the forniceal and mammillary body hyperintensity, with faint residual signal change in the optic chiasm on the right (arrow, D2). Mths indicates months.

The optic pathway was involved in 2 patients. In patient 11, the prechiasmatic optic nerve and optic chiasm showed abnormal signal at onset. Patient 14, on the other hand, initially showed subtle signal change at the optic chiasm, which progressed during 3 months to symmetrically involve both optic nerves and the chiasm. Other findings included involvement of the pulvinar and hippocampal formations in patient 13 and the hypothalamus and mammillary bodies in patient 14. Imaging findings at presentation and follow-up in patient 14 are shown in Fig 4.

All patients were treated initially with 20 mg of biotin. The dose of biotin was gradually increased to 80 mg/day in patient 14, due to worsening of symptoms, and this dose has been continued since. Follow-up details for 1 patient (patient 13) were not available. The other 3 patients had residual symptoms at follow-up, with strabismus in patients 11 and 12 and rash, mild distal hypotonia and muscular weakness, and ataxia in patient 14.

Follow-up imaging following initiation of biotin therapy was available in patients 11 and 14. Both patients showed resolution of the intracranial signal abnormalities (Fig 4) but residual signal changes in the spinal cord.

DISCUSSION

All patients in the early infantile group showed diffuse cerebral and cerebellar white matter swelling and abnormal T2 hyperintense signal on imaging during presentation. These are congruent with the findings of other studies describing a similar pattern in patients presenting between 4 weeks and 5 months of age.¹¹⁻¹⁴ Cases with a predilection for the frontal and frontoparietal lobes

have also been described,¹² similar to 2 cases in our series. We, however, did not find any reports describing predominant involvement of the superior and inferior semilunar lobules of the cerebellum, as was seen in 2 of our cases. Similarly, T2-hyperintense signal at the level of the medullary pyramids has not been previously described.

Various hypotheses that have been proposed for diffuse white matter signal abnormality in infants with biotinidase deficiency include interstitial edema,^{11,12,14} delayed myelination,¹¹ dysmyelination,¹² ischemia,¹¹ and leukodystrophy.¹³ Given the presence of swelling and striking T2 hyperintensity, we believe that the main process driving these changes is interstitial edema rather than leukodystrophy or dysmyelination. The diffuse pattern of involvement (involving both myelinated and unmyelinated white matter) and the reversibility of changes in most patients in our series, and others^{12,15-17} favor this hypothesis. Atrophy on follow-up imaging was seen in only one of our patients, involving the frontal lobes and cerebellar semilunar lobules, suggesting a degree of irreversible injury in this patient by the time treatment was initiated.

Another finding we present in 2 of our patients in the early infantile age group is restricted diffusion in the perirolandic regions. Soares-Fernandes et al¹⁴ described a strikingly similar case and attributed it to accelerated myelination, possibly induced by the repeat neuronal electrical activity of seizures. This may be plausible, given that all patients in our series in this age group presented with seizures. Also, early regions of myelination have increased metabolic activity/requirements and therefore might be more susceptible. Interestingly, a few case reports have described striking,

restricted diffusion in the internal capsules, optic radiations, corticospinal tracts of the brainstem,¹⁸⁻²⁰ splenium of corpus callosum,^{18,20} cerebellar white matter,^{18,20} and the hippocampi and medial temporal regions,¹⁹⁻²¹ none of which were observed in our series. Most of these patients presented at, or were imaged between 3 and 8 months of age, and whether this differential pattern therefore relates to the timing of metabolic decompensation is a matter of debate.

In our series, there was considerable overlap in imaging features in the early and late childhood age groups. The unifying finding in all 3 patients in the early age group was T2 hyperintensity in the fornices, periaqueductal gray matter, dorsal pons, and medullary pyramids, with variable involvement of the corpus callosum, cerebellar peduncles, optic pathway, diencephalic structures, and cervical spinal cord. Restricted diffusion of the fornices was seen in all 3 patients, whereas the other structures showed variable features on DWI. Forniceal, diencephalic, and brainstem involvement has previously been reported in various age groups, ranging from 3 years to adulthood,^{16,17,22-24} whereas only 1 case describing this pattern was found in toddlers younger than 2 years of age (case 1, Mc Sweeney et al²²). Similarly, spinal cord and optic chiasm involvement have been described infrequently in children 3 years of age and older,^{15-17,21,23-25} whereas 2 of our patients younger than 2 years of age showed variable involvement of these structures. Interestingly, in 1 case each, there was involvement of the tapetum and lateral geniculate bodies, respectively, both not previously described.

The imaging finding common to all patients in the late childhood age group was spinal cord involvement, with variable involvement of the other structures that were also involved in the early childhood age group. In those with spinal cord involvement, the cervical cord was involved in all patients across both groups, and this involvement is in keeping with the findings of other series.^{15-17,22-26} Thoracic or holocord involvement contiguous with cervical cord abnormality has also been commonly described^{15,17,21-24,26} but was seen only in 2 of our patients across both groups. In those with spinal cord involvement, only one of our patients showed involvement of the entire cross-sectional area, whereas the others showed selective involvement of certain columns, with the dorsal column being commonly involved. Other authors have shown more common involvement of the entire cross-sectional area,^{15,26} though selective column involvement has also been described.^{15,21,24,25} The reason for this differential involvement is unknown. Optic pathway involvement in our series was confined to the optic nerves and chiasm, similar to findings in other reports.^{17,24} Additional previously described components of the optic pathway include the optic tracts²³ and optic radiations.^{18,19}

Similar to findings in other studies,^{12,15-17} there was clinical and radiologic improvement in all patients following initiation of treatment. The most common residual deficits after treatment in our series included sensorineural hearing loss and visual impairment, the latter attributable to optic atrophy. Irreversibility of established hearing and vision loss is well-known in biotinidase deficiency.²⁷ Other residual deficits in our series and others^{15,23,24,26} included learning difficulties, ataxia, hypotonia, and quadriparesis.

Imaging-based differential diagnoses for biotinidase deficiency vary depending on the pattern of involvement. For instance, diffuse white matter T2 hyperintensity and swelling are nonspecific and may be seen in urea cycle defects, organic acidemias, and amino-acidemias presenting with metabolic decompensation.²⁸ Recently, forniceal restricted diffusion was demonstrated to be present in 53/714 (7.4%) children younger than 2 years of age.²⁹ The authors postulated this to be a transient abnormality possibly related to seizures, though only 4/53 patients had follow-up imaging showing resolution. It is unclear whether any of these children were screened for biotinidase deficiency. Finally, signal alterations in the optic chiasm, brainstem, and spinal cord should prompt the consideration of demyelinating disorders such as myelin oligodendrocyte glycoprotein antibody disease and neuromyelitis optica spectrum disorder in the appropriate clinical setting.³⁰

Given the dramatic impact of neonatal screening and treatment before development of symptoms,³¹ screening for biotinidase deficiency is now offered in >30 countries worldwide.³² Most countries, however, do not routinely screen for this disease; early recognition and treatment are, therefore, crucial to prevent long-term sequelae.

CONCLUSIONS

Recognizable imaging features of biotinidase deficiency at different age groups include a predilection for diffuse white matter edema in young infants and a predilection for the involvement of the fornices, diencephalic structures, optic pathway, brainstem, and spinal cord in toddlers and older children.

Disclosure forms provided by the authors are available with the full text and PDF of this article at www.ajnr.org.

REFERENCES

1. Moss J, Lane MD. **The biotin-dependent enzymes.** *Adv Enzymol Relat Areas Mol Biol* 1971;35:321-442 CrossRef Medline
2. Wolf B, Feldman GL. **The biotin-dependent carboxylase deficiencies.** *Am J Hum Genet* 1982;34:699-716 Medline
3. Wolf B. **Clinical issues and frequent questions about biotinidase deficiency.** *Mol Genet Metab* 2010;100:6-13 CrossRef Medline
4. Thoma RW, Peterson WH. **The enzymatic degradation of soluble bound biotin.** *J Biol Chem* 1954;210:569-79 Medline
5. Craft DV, Goss NH, Chandramouli N, et al. **Purification of biotinidase from human plasma and its activity on biotinyl peptides.** *Biochemistry* 1985;24:2471-76 CrossRef Medline
6. Wolf B. **The neurology of biotinidase deficiency.** *Mol Genet Metab* 2011;104:27-34 CrossRef Medline
7. Heard GS, Wolf B, Reddy JK. **Pancreatic biotinidase activity: the potential for intestinal processing of dietary protein-bound biotin.** *Pediatr Res* 1984;18:198A CrossRef
8. Wolf B, et al. **Biotinidase deficiency.** In: Adam MP, Evereman DB, Mirzaa GM, et al, eds. *GeneReviews [Internet]. University of Washington, Seattle*; 1993 Medline
9. Wolf B, Heard GS, Weissbecker KA, et al. **Biotinidase deficiency: initial clinical features and rapid diagnosis.** *Ann Neurol* 1985;18:614-17 CrossRef Medline
10. Wolf B, Pomponio RJ, Norrgard KJ, et al. **Delayed-onset profound biotinidase deficiency.** *J Pediatr* 1998;132:362-65 CrossRef Medline
11. Grünewald S, Champion MP, Leonard JV, et al. **Biotinidase deficiency: a treatable leukoencephalopathy.** *Neuropediatrics* 2004;35:211-16 CrossRef Medline

12. Desai S, Ganesan K, Hegde A. **Biotinidase deficiency: a reversible metabolic encephalopathy—neuroimaging and MR spectroscopic findings in a series of four patients.** *Pediatr Radiol* 2008;38:848–56 CrossRef Medline
13. Haagerup A, Andersen JB, Blichfeldt S, et al. **Biotinidase deficiency: 2 cases of very early presentation.** *Dev Med Child Neurol* 1997;39:832–35 Medline
14. Soares-Fernandes JP, Magalhães Z, Rocha JF, et al. **Brain diffusion-weighted and diffusion tensor imaging findings in an infant with biotinidase deficiency.** *AJNR Am J Neuroradiol* 2009;30:E128 CrossRef Medline
15. Yang Y, Li C, Qi Z, et al. **Spinal cord demyelination associated with biotinidase deficiency in 3 Chinese patients.** *J Child Neurol* 2007;22:156–60 CrossRef Medline
16. Cabasson S, Rivera S, Mesli S, et al. **Brainstem and spinal cord lesions associated with skin changes and hearing loss: think of biotinidase deficiency.** *J Pediatr* 2015;166:771 CrossRef Medline
17. Chedrawi AK, Ali A, Al Hassnan ZN, et al. **Profound biotinidase deficiency in a child with predominantly spinal cord disease.** *J Child Neurol* 2008;23:1043–48 CrossRef Medline
18. Ranjan RS, Taneja S, Singh A, et al. **Congenital biotinidase deficiency: MRI findings in 2 cases.** *Indian J Radiol Imaging* 2019;29:99–103 CrossRef Medline
19. Singh P, Gurnani R, Rawat A, et al. **Brain MRI findings in an infant with congenital biotinidase deficiency.** *BMJ Case Rep* 2021;14:e246167 CrossRef Medline
20. Viyannan M, Palanisamy S, Balalakshmoji D. **Congenital biotinidase deficiency: clinching the diagnosis with classic imaging features.** *Academia* 2019;18:17–20
21. Bhat MD, Bindu PS, Christopher R, et al. **Novel imaging findings in 2 cases of biotinidase deficiency: a treatable metabolic disorder.** *Metab Brain Dis* 2015;30:1291–94 CrossRef Medline
22. Mc Sweeney N, Grunewald S, Bhate S, et al. **Two unusual clinical and radiological presentations of biotinidase deficiency.** *Eur J Paediatr Neurol* 2010;14:535–38 CrossRef Medline
23. Raha S, Udani V. **Biotinidase deficiency presenting as recurrent myelopathy in a 7-year-old boy and a review of the literature.** *Pediatr Neurol* 2011;45:261–64 CrossRef Medline
24. Bottin L, Prud'hon S, Guey S, et al. **Biotinidase deficiency mimicking neuromyelitis optica: Initially exhibiting symptoms in adulthood.** *Mult Scler* 2015;21:1604–07 CrossRef Medline
25. Komur M, Okuyaz C, Ezgu F, et al. **A girl with spastic tetraparesis associated with biotinidase deficiency.** *Eur J Paediatr Neurol* 2011;15:551–53 CrossRef Medline
26. Wiznitzer M, Bangert BA. **Biotinidase deficiency: clinical and MRI findings consistent with myelopathy.** *Pediatr Neurol* 2003;29:56–58 CrossRef Medline
27. Wolf B. **Biotinidase deficiency: new directions and practical concerns.** *Curr Treat Options Neurol* 2003;5:321–28 CrossRef Medline
28. Poretti A, Blaser SI, Lequin MH, et al. **Neonatal neuroimaging findings in inborn errors of metabolism.** *J Magn Reson Imaging* 2013;37:294–312 CrossRef Medline
29. Rootman MS, Kornreich L, Osherov AN, et al. **DWI hyperintensity in the fornix fimbria on MRI in children.** *AJNR Am J Neuroradiol* 2022;43:480–85 CrossRef Medline
30. Fadda G, Armangue T, Hacoheh Y, et al. **Paediatric multiple sclerosis and antibody-associated demyelination: clinical, imaging, and biological considerations for diagnosis and care.** *Lancet Neurol* 2021;20:136–49 CrossRef Medline
31. Maguolo A, Rodella G, Dianin A, et al. **Newborn screening for biotinidase deficiency. The experience of a regional center in Italy.** *Front Pediatr* 2021;9:661416 CrossRef Medline
32. Hsu RH, Chien YH, Hwu -L, et al. **Genotypic and phenotypic correlations of biotinidase deficiency in the Chinese population.** *Orphanet J Rare Dis* 2019;14:6 CrossRef Medline

Medullary Tegmental Cap Dysplasia: Fetal and Postnatal Presentations of a Unique Brainstem Malformation

M. Gafner,¹ C. Garel,² Z. Leibovitz,³ S. Valence,⁴ K. Krajdjen Haratz,⁵ R. Oegema,⁶ G.M.S. Mancini,⁷ D. Heron,⁸ E. Bueltmann,⁹ L. Burglen,¹⁰ D. Rodriguez,¹¹ T.A.G.M. Huisman,¹² M.H. Lequin,¹³ A. Arad,¹⁴ D. Kidron,¹⁵ M. Muqary,¹⁶ L. Gindes,¹⁷ D. Lev,¹⁸ E. Boltshauser,¹⁹ and T. Lerman-Sagie²⁰



ABSTRACT

BACKGROUND AND PURPOSE: Medullary tegmental cap dysplasia is a rare brainstem malformation, first described and defined by James Barkovich in his book *Pediatric Neuroimaging* from 2005 as an anomalous mass protruding from the posterior medullary surface. We describe the neuroimaging, clinical, postmortem, and genetic findings defining this unique malformation.

MATERIALS AND METHODS: This is a multicenter, international, retrospective study. We assessed the patients' medical records, prenatal ultrasounds, MR images, genetic findings, and postmortem results. We reviewed the medical literature for all studies depicting medullary malformations and evaluated cases in which a dorsal medullary protuberance was described.

RESULTS: We collected 13 patients: 3 fetuses and 10 children. The medullary caps had multiple characteristics. Associated brain findings were a rotated position of the medulla, a small and flat pons, cerebellar anomalies, a molar tooth sign, and agenesis of the corpus callosum. Systemic findings included the following: polydactyly, hallux valgus, large ears, and coarse facies. Postmortem analysis in 3 patients revealed that the cap contained either neurons or white matter tracts. We found 8 publications describing a dorsal medullary protuberance in 27 patients. The syndromic diagnosis was Joubert-Boltshauser syndrome in 11 and fibrodysplasia ossificans progressiva in 14 patients.

CONCLUSIONS: This is the first study to describe a series of 13 patients with medullary tegmental cap dysplasia. The cap has different shapes: distinct in Joubert-Boltshauser syndrome and fibrodysplasia ossificans progressiva. Due to the variations in the clinical, imaging, and postmortem findings, we conclude that there are multiple etiologies and pathophysiology. We suggest that in some patients, the pathophysiology might be abnormal axonal guidance.

ABBREVIATIONS: AMCD = anterior mesencephalic cap dysplasia; BPAN = β propeller protein-associated neurodegeneration; CC = corpus callosum; FOP = fibrodysplasia ossificans progressive; INAD = infantile neuroaxonal dystrophy; JBTS = Joubert-Boltshauser syndrome; MTCD = medullary tegmental cap dysplasia; PTCd = pontine tegmental cap dysplasia; TOP = termination of pregnancy

Medullary tegmental cap dysplasia (MTCD) is a rare brainstem malformation, first described and defined by James Barkovich¹ in his book *Pediatric Neuroimaging* from 2005, as an anomalous mass protruding from the posterior medullary surface. MTCD shares common features with 2 other brainstem malformations, both suspected to result from impaired axonal

guidance or abnormal neuronal migration: pontine tegmental cap dysplasia (PTCD, Online Mendelian Inheritance in Man [OMIM] No. 614688) and anterior mesencephalic cap dysplasia (AMCD).²⁻⁴ In all 3, there is an abnormal "cap" protruding from the brainstem, located anteriorly in AMCD and posteriorly in PTCd and MTCD.^{3,5} A mass protruding from the dorsal medulla

Received October 14, 2022; accepted after revision January 9, 2023.

From the Department of Pediatrics B (M.G.), Schneider Children's Medical Center of Israel, Petach Tikva, Israel; Sackler Faculty of Medicine (M.G., K.K.H., L.G., D.L., T.L.-S.), Tel Aviv University, Tel Aviv, Israel; Department of Radiology (C.G.) and Reference Center for Cerebellar Malformations and Congenital Diseases (C.G., S.V., D.H., L.B., D.R.), Hôpital d'Enfants Armand-Trousseau, Assistance Publique-Hôpitaux de Paris, Paris, France; Obstetrics and Gynecology Ultrasound Unit (Z.L.), Bnai-Zion Medical Center, Rappaport Faculty of Medicine, Technion-Israel Institute of Technology, Haifa, Israel; Service de Neuropédiatrie (S.V., L.B., D.R.), Hôpital Trousseau, Assistance Publique-Hôpitaux de Paris, Paris, France; Division of Ultrasound in ObGyn (K.K.H.), Lis Maternity Hospital, Tel Aviv Sourasky Medical Center, Tel Aviv, Israel; Departments of Genetics (R.O.) and Radiology (M.H.L.), University Medical Center Utrecht, Utrecht University, Utrecht, the Netherlands; Department of Clinical Genetics (G.M.S.M.), Erasmus MC University Medical Center, GD Rotterdam, the Netherlands; Service de Génétique Clinique (D.H.), Hôpital de la Pitié-Salpêtrière, Assistance Publique-Hôpitaux de Paris, Paris, France; Institute of Diagnostic and Interventional Neuroradiology (E. Bueltmann),

Hannover Medical School, Hannover, Germany; Edward B. Singleton Department of Radiology (T.A.G.M.H.), Texas Children's Hospital and Baylor College of Medicine, Houston, Texas; Department of Pathology (A.A.), Bnai-Zion Medical Center, Haifa, Israel; Department of Pathology (D.K.), Meir Medical Center, Kfar Saba, Israel; Department of Obstetrics and Gynecology (M.M.), Poriya Medical Center, Tiberias, Galilee, Israel; Department of Obstetrics and Gynecology (L.G.), The Rina Mor Institute of Medical Genetics (D.L.), Fetal Neurology Clinic (D.L., T.L.-S.), Magen Center for Rare Diseases (T.L.-S.), and Pediatric Neurology Unit (T.L.-S.), Wolfson Medical Center, Holon, Israel; and Pediatric Neurology (Emeritus) (E. Boltshauser), Children's University Hospital, Zürich, Switzerland.

Please address correspondence to Michal Gafner, MD, Department of Pediatrics B, Schneider Children's Medical Center of Israel, Kaplan 14 St, Petach Tikva, Israel; e-mail: michalgurevitch@gmail.com

Indicates article with online supplemental data.
<http://dx.doi.org/10.3174/ajnr.A7805>



FIG 1. Illustration of the medullary cap morphologic characteristics: A, Smooth; B, Stick sign; C, Globular; D, Step sign; E, Caterpillar sign.

has also been described in Joubert-Boltshauser syndrome (JBTS) and in fibrodysplasia ossificans progressiva (FOP) syndromes, but never defined as MTCD.

In a teaching neuroimage paper previously published, the MR images showed an anomalous mass of gray matter signal intensity protruding from 1 side of the medulla, a hypoplastic pons and thickened medulla oblongata, a dysplastic cerebellum, and partial agenesis of the corpus callosum (CC).⁶

Following the presentation of a prenatal diagnosis of MTCD in 2 fetuses at the meetings of the International Research Consortium for the Corpus Callosum and Cerebral Connectivity and NeuroMIG Cost Action project, we collected a total of 13 patients (3 fetuses and 10 children).

We describe the neuroimaging, clinical, postmortem, and genetic findings defining this unique brainstem malformation.

MATERIALS AND METHODS

This is a multicenter international retrospective study (Israel, France, Switzerland, Spain, the Netherlands, Germany, United States). Patients with a dorsally protruding mass from the medulla were extracted from personal teaching files of neuroradiologic colleagues across the globe. We assessed the medical records, prenatal ultrasounds, MR images, genetic findings, and postmortem results of the patients. We reviewed the medical literature for all studies describing medullary malformations and evaluated the cases in which a dorsal medullary protuberance was described.

The study was approved by the Wolfson Medical Center's institutional review board [WOMC-0188-18].

Imaging Techniques

Fetal neurosonograms were obtained according to the International Society of Sonography in Obstetrics and Gynecology guidelines.^{7,8} The examinations were performed on Voluson E8 and E10 ultrasound machines (GE Healthcare, Kretz Sonography) using transabdominal and transvaginal probes or an Aplior i800 U (Canon Medical Systems).

MR imaging brain scans, fetal or postnatal, were obtained in all cases. Fetal MR imaging (Sigma Horizon LX and EchoSpeed MR imaging scanners, 1.5T; GE Healthcare) scans were obtained using an ultrafast, T2-weighted single-shot fast spin-echo MR imaging in the axial, coronal, and transversal planes (acquisition time = 40–45 seconds). During fetal scans, patients received oral

diazepam and zopiclone, 7.5 mg, before the MR imaging to reduce fetal and maternal movements for imaging. In postnatal scans, the same sequences were used in addition to FLAIR and STIR.

MTCD Characterization. The cap was characterized on the midsagittal plane by the authors Prof. Tally Lerman-Sagie and Prof. Eugen Boltshauser. The cap was described according to its shape (Fig 1), size in relation to the medulla (anterior-posterior diameter in the midsagittal plane), craniocaudal extension

(pontomedullary, medullary, low medullary), axial projection (unilateral, bilateral), relation to the cerebellar peduncles (connected, separated, or unknown), and signal intensity (Online Supplemental Data).

We defined 5 distinct shapes (Fig 1):

- A) Smooth: the cap borders blend into the medulla, and the contour is smooth (Fig 2E).
- B) Stick sign: the cap is thin and elongated (Fig 2F).
- C) Globular: the cap is round (Fig 2A).
- D) Straight-angled, “step sign”: there is a straight angle between the cap and the medulla (Fig 2D).
- E) Tubercle, “caterpillar sign”: the cap consists of multiple tubercle-like protruberances (Fig 2K).

Postmortem Examinations

Postmortem examinations were performed according to protocols previously described and included a detailed examination of the fetus and placenta.⁹ For gross examination of the brain, the brainstem was separated from the cerebral hemispheres by a section at the level of the midbrain. The cerebral hemispheres were bisected along the midsagittal plane. The separate hemispheres were placed back together, followed by coronal sectioning of the cerebral hemispheres. The brainstem and cerebellum were sectioned along the axial plane. Histologic sections 4- μ m-thick were prepared and stained with H&E. The histologic sections were examined along with the corresponding gross photographs. Immunohistochemical stains for calretinin and synaptophysin were performed as indicated.⁹

Data Availability

Anonymized imaging data not published within this article will be made available by request from any qualified investigator.

RESULTS

The study included 13 unrelated patients: 3 fetuses (diagnosed at 17, 21, and 32 weeks of gestation), and 10 children and adolescents (9 months to 18 years of age at the latest clinical follow-up). All pregnant couples opted for termination of pregnancy (TOP) according to the national laws, allowing TOP in cases with imaging findings implying a high risk of severely impaired neurodevelopmental outcome. Two children died in infancy following an infection. Eight patients are alive.

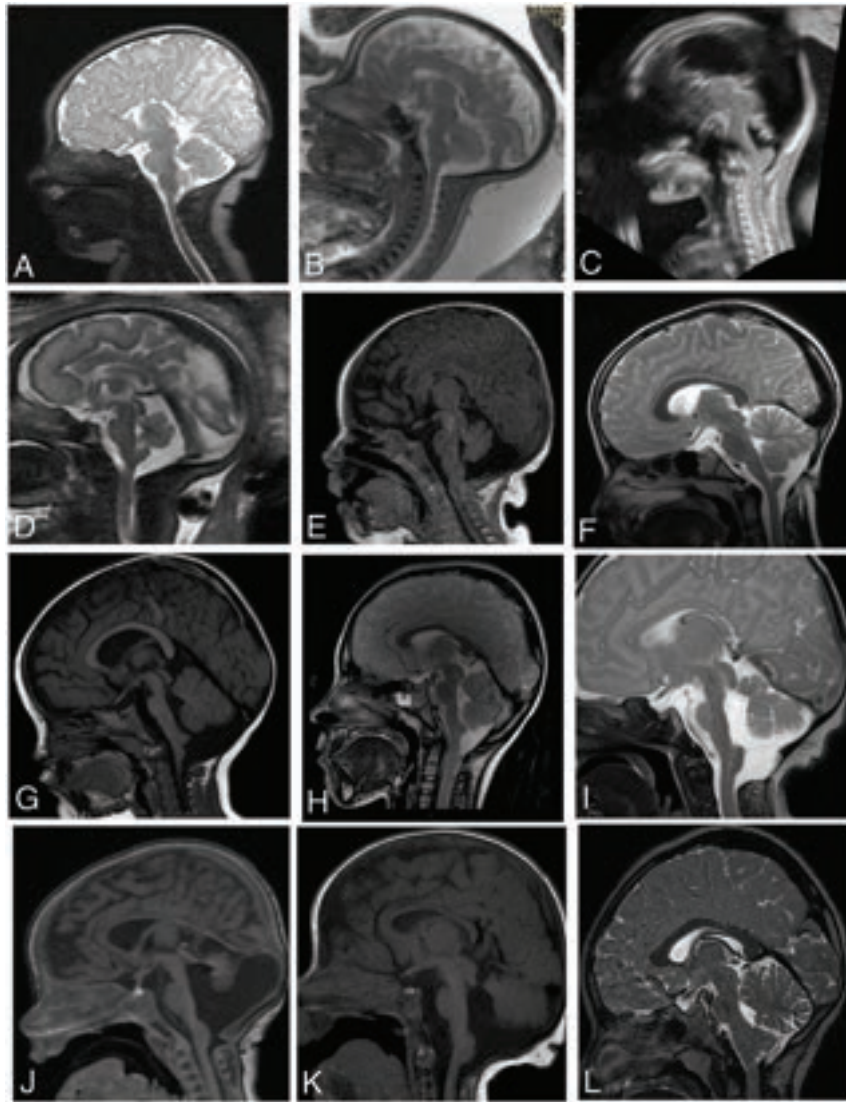


FIG 2. MR imaging and ultrasound showing the medullary cap in 12 patients, midsagittal view. A, Patient 1; B, Patient 2; C, Patient 3; D, Patient 4; E, Patient 5; F, Patient 6; G, Patient 7; H, Patient 8; I, Patient 9; J, Patient 11; K, Patient 12; L, Patient 13. Of note, patient 10's MR imaging is separately shown in the Online Supplemental Data.

We found 8 publications describing a dorsal medullary protuberance in 27 patients. The syndromic diagnosis was JBTS in 11 and FOP in 14 patients.^{1,6,10-15}

Clinical Features

A clinical evaluation extracted from the medical charts was available in only 9 of our 10 patients (all 3 pregnant couples opted for TOP), as detailed in the Online Supplemental Data. Patients' ages ranged between 6 months and 18 years at diagnosis, with 3 females and 5 males (in 5 patients the sex was unknown). Cognitive function was normal in 4 patients, 2 patients had severe global developmental delay, 1 patient was in the low-average range, and 3 patients had no information. Delayed motor milestones were observed 5 patients, of whom 3 had severe and 1 had mild developmental delay, and 1 had left hemiparesis.

Two patients presented with central apneic episodes. Neurologic examination findings were normal in 3 patients and abnormal in 5

patients, including axial hypotonia and normal reflexes in patient 1; hypotonia, dysarthria, strabismus, nystagmus in patient 7; left hemiparesis in patient 8; patient 9, had no eye contact/tracking, abnormal movement, self-mutilation, and exclusive gastrostomy, and in patient 10, with no eye contact, hyperkinetic limb movements, and hypotonia. Neurologic examination was unavailable in 5 patients. Two patients had cutaneous skull lesions. Three patients were diagnosed with JBTS. Bilateral hallux valgus (diagnosed with FOP), vocal cord paresis, and hematologic disorders with hepatic cholestasis were observed in 1 patient each. Two patients died, one from cardiac arrest following a respiratory infection at 9 months and the other from coronavirus disease 2019 (COVID-19) infection, at 11 months.

Neuroimaging Findings

The imaging findings of our 13 patients and all those previously described in the literature (27 patients) are detailed in the Online Supplemental Data.

Main Features According to the Anatomic Structure

Medulla Oblongata. Cap morphology (illustrated in Fig 1) was smooth in 1/13 and 16/27, globular in 5/13 and 0/27, step sign in 6/13 and 9/27, stick sign in 3/13 and 0/27, and caterpillar sign in 3/13 and 5/27 patients.

Cap size in relation to the medulla was smaller 1/13 and 15/27 patients, equal in 7/13 and 9/27, and larger in 5/13 patients (in 1 patient, the cap was extremely enlarged and resembled a tumor, Fig 2L).

Craniocaudal extension was midmedullary in 5/13 and 2/27 patients, lower medullary in 8/13 and 9/25 patients (no information was available in 2 patients), and pontomedullary in 0/13 and 14/27 patients.

Axial projection was unilateral in 4/13 (unknown in 5) and 9/27 and bilateral in 11/27 patients (in the 13 patients described by Severino et al,¹⁴ axial projection varied).

The relation to the cerebellar peduncles was connected to the cerebellar peduncles in 1/13 and 1/27, and separated from the cerebellar peduncles in 10/13 and 22/27.

Signal intensity was equal to the medulla in 11 patients and different in 2. In the literature, signal intensity was equal in 22 patients, 2 had gray matter intensity, and FLAIR signal intensity was increased in 13 patients (Online Supplemental Data).

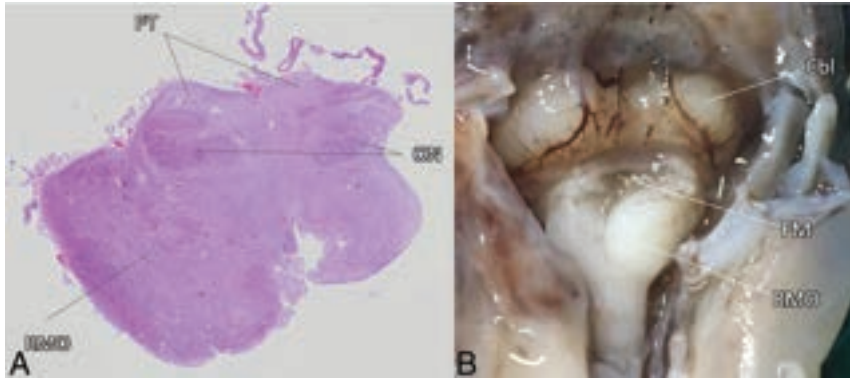


FIG 3. A, Axial microscopy photograph of the medulla oblongata of patient 2 at 35 gestational weeks. The right-posterior bulge of the medulla oblongata (RMO) contains many mature neurons, consistent with a hamartoma, connected to the cerebellum. The inferior olivary nuclei (ON) are well-developed, and the pyramidal tracts (PT) are intact. B, Postmortem photograph of patient 3 depicts the fetal posterior fossa after removal of the occipital bone, performed at 17 gestational weeks. Note the thickening and internal rotation of the RMO, producing the medullary cap shape. Cbl indicates cerebellum; FM, opening of the foramen of Magendi.

The midbrain was abnormal in 1/40; the pons, in 9/40; and the cerebellum, in 20/40 patients. Details of the abnormal CNS findings are found in the Online Supplemental Data.

Regarding posterior fossa anomalies, there was a hypoplastic vermis in 11 patients from the literature¹⁰⁻¹³ and in 6 of our patients (patients 1, 3, 5, 9, 11, and 12) and an oversized vermis in 2 patients from the literature.¹⁶ Cerebellar malformations including hemisphere hypoplasia and dislocated fastigium were observed in our cohort in 1 patient each. A total of 3 patients from our cohort (patients 9, 11, and 12) and 11 patients from the literature had a diagnosis of Joubert syndrome.¹⁰⁻¹³

An anomaly of the CC was found the original description by Barkovich,¹ the neuroimage by Jurkiewicz and Nowak,⁶ and in 4 patients from our cohort (patients 1, 2, 4, and 10).

Sulcation was abnormal in 2 of our 13 patients.

Other anomalies included ventriculomegaly, frontoparietal interhemispheric cyst, and peritrigonal focal white matter abnormalities in 1 patient each from our cohort.

Genetic Findings

The genetic investigation included the following: karyotype (1/13), chromosomal microarray (5/13), exome sequencing (5/13), genome sequencing (3/13), and targeted gene analysis (1/13) (Online Supplemental Data). Chromosomal microarray in patient 5 revealed a paternally inherited 15q21.2 deletion, which included part of the *GLDN* gene. Targeted analysis of the *ACVR1* gene was performed in patient 1 due to hallux valgus and revealed the classic p.Arg206His mutation. Patient 9 had an anomaly of the entire short arm of chromosome 11 in mosaicism, consistent with Beckwith-Wiedemann syndrome. Patient 11 had a *CSPP1* gene mutation and was diagnosed with JBTS.

Postmortem Analysis

A postmortem examination was available in 2 of the 3 fetuses that underwent TOP (Fig 3) and in 1 of the postnatal cases.

In patient 2, the macroscopic evaluation revealed a mass protruding from the dorsolateral right side of the medulla. The

ventral pons was hypoplastic on the right. The right inferior peduncle was thickened relative to the other side. Microscopically, the mass contained many mature neurons that could be consistent with a hamartoma. The inferior olivary nuclei were well-developed, and the pyramidal tracts were intact. Few neurons were seen in the pons; the transverse and pyramidal tracts were observed. The cerebellar cortex was normal (Fig 3A), as well as the rest of the brain and organs.

In patient 3, the macroscopic evaluation showed a wide interhemispheric space; an asymmetrically rotated medulla oblongata with a posterior mass protruding on the right from the dorso-lateral aspect; agenesis of the CC; and ventricular asymmetry. The medial part

of the cortex in the left hemisphere was thicker than on the right, with an irregular structure with multiple sulcations (Fig 3B). Microscopic evaluation disclosed asymmetry of the medulla due to the occupying white matter. In the occipital lobe of the left hemisphere, an area of polymicrogyria with cortical disorganization was noted.

In patient 10, postmortem examination revealed that the hypersignal on the dorsal surface of the brainstem corresponded to spheroids in the posterior tracts of the medulla, in favor of a neuroaxonal dystrophy.

DISCUSSION

James Barkovich¹ was the first to describe this unique brainstem malformation, MTCD, in 2005, and included it in the classification of midbrain-hindbrain malformations in 2009.¹⁶ It was described as a dorsal medullary protuberance identified on MR imaging in infants being imaged for multiple anomalies of the musculoskeletal, genitourinary, or gastrointestinal systems. On sagittal images, a dorsal (tegmental) cap was seen at the level of the medulla, associated with absence or severe hypogenesis of the corpus callosum.

No additional patients with MTCD were described in the literature until 2015, when Jurkiewicz and Nowak⁶ supplied MR images of this brainstem anomaly in *Neurology*. They described a 3-year-old boy who presented with respiratory distress and apnea. MR imaging showed a hypoplastic pons and thickened medulla oblongata with an anomalous mass of gray matter signal intensity around it.

To the best of our knowledge, MTCD has not been defined in any other cases in the literature, however, when searching the literature for medullary anomalies, we found 27 cases fulfilling the definition of an anomalous mass protruding from the posterior medullary surface.

We analyzed our 13 cases and the additional 27 cases from the literature for the characteristics of the cap, additional findings, clinical presentation, postmortem results, and genetic evaluation. We discovered that the dorsal medullary cap is not a single entity but

has different characteristics: shape, size, signal intensity, craniocaudal location, laterality, and relation to the cerebellar peduncles (Online Supplemental Data). Furthermore, the etiology was diverse, there were specific additional CNS or systemic findings, and there was a range of clinical presentations, from no symptoms to profound developmental delay.

The clinical presentation of the patients with MTCD was considerably variable. Some patients did not have neurologic involvement at all. Patients with FOP (*ACVR1* mutations) had only skeletal anomalies. Patient 1 from our cohort with an *ACVR1* mutation had normal development and hallux valgus typical of FOP.¹⁷ In patients 6 and 13, the MTCD was an incidental finding during a cutaneous skull lesion evaluation. It seems that the underlying symptoms are related to the syndromic diagnosis (as in patients with JBTS) or associated findings. Three patients presented with profound developmental delay (patients 5, 9, and 10), and 2 had early death (patients 5 and 10). Brainstem dysfunction is described in 3/13 patients (patient 5, vocal cord paresis; patients 9 and 11, apnea). Eight patients had other brainstem anomalies (Online Supplemental Data).

The child described by Jurkiewicz and Nowak⁶ also had absence of the middle and distal phalanges of the hands and feet, gastroesophageal reflux, hiatal hernia, abnormal findings on auditory brainstem response testing, and dysmorphic features including facial asymmetry, large dysplastic earlobes, and deep-set eyes.⁶ He presented with apnea at 3 years of age. Whether these presentations are related to the medullary tegmental cap dysplasia or the underlying genetic syndrome remains unknown. In the 2 other brainstem malformations that share a cap (protruding from the dorsal pons in PTC and the anterior mesencephalon in AMCD), the cap always has a distinct shape: in PTC an abnormal curved structure covering the middle third of the pontine tegmentum and projecting into the fourth ventricle,^{4,5} and in AMCD, a rounded bulging obliterating the interpeduncular fossa.³ In contrast, in MTCD, the cap has multiple shapes as depicted in Figs 1 and 2.

AMCD has been described in only 3 patients with JBTS.³ Clinically, the patients manifested typical features of this syndrome: hypotonia, developmental delay, ataxia, intellectual disability, and neuro-ophthalmologic signs.³ Two patients were compound heterozygous for *TMEM67* missense variants.¹⁸

PTCD is not considered inherent in JBTS, but rather a distinct category, part of the “molar tooth” family of brainstem anomalies, due to its particular posterior fossa characteristics and associated CNS findings (subtotal absence of the middle cerebellar peduncles, flattened ventral pons, vaulted pontine tegmentum, a molar tooth aspect of the pontomesencephalic junction, an absent inferior olivary prominence, vermal hypoplasia, and corpus callosum hypoplasia or agenesis⁵) that differentiate it from the Joubert spectrum of disorders.¹⁹ Prenatal diagnosis of patients with PTC has been previously described in 4 fetuses. In the 3 living children, global developmental delay and multiple cranial nerve impairment were observed. A genetic etiology of PTC has not been found, and it is considered a sporadic disorder because no familial cases have been described.^{2,4,5,20}

MTCD is also a unique category within the classification of midbrain-hindbrain malformations,¹⁶ but it has multiple etiologies and different forms and clinical presentations. JBTS is one of the possible etiologies.

Poretti et al¹⁰⁻¹² described a posterior medullary protuberance in 7 patients with JBTS; images consistent with MTCD were supplied in 2 studies. In our cohort, there were 3 patients with this diagnosis (patients 9, 11, and 12). In most of these cases, the cap had distinct features: It was straight-angled, tubular, equal in size with the medulla, and located in the low-medullary region. We suggest that the step sign and the caterpillar sign adequately describe the typical appearance of the cap in JBTS because it is straight-angled and in some cases reminiscent of a caterpillar clinging to a stem (Fig 1 and Fig 2I, -K).

The step sign is reminiscent of clava hypertrophy, a relatively consistent imaging finding in infantile neuroaxonal dystrophy (INAD)/*PLA2G6* (OMIM No. 256600).^{21,22}

Recently (2022), clava prominence has also been mentioned in 6/27 scans of patients with β propeller protein-associated neurodegeneration (BPAN).²³ Distinction between JBTS and INAD or BPAN is not problematic from the clinical and the imaging perspective. Imaging in INAD shows almost consistent cerebellar atrophy and inconsistent cerebellar cortex hyperintensity, and BPAN shows intense iron deposition in the substantia nigra, while JBTS presents (in addition to the molar tooth sign) with vermis hypodysplasia and cranial dislocation of the fastigium, while cerebellar atrophy is not a feature.^{21,24,25} Patient 10 from our cohort had a progressive course, both clinically (postnatal progressive microcephaly, development of hyperkinetic movements, and so forth, Online Supplemental Data) and radiologically. Prenatal MR imaging showed partial agenesis of the CC and a small pons, with no MTCD, which was only diagnosed later on MR imaging performed at 11 months (Online Supplemental Data), suggesting that MTCD could sometimes develop progressively, for example, in neurodegenerative disorders. This patient was suspected clinically of having atypical neuroaxonal dystrophy, further supported by the presence of spheroids in the posterior tracts of the medulla. However, findings of whole-genome sequencing including mitochondrial DNA were normal.

Patient 11 from our cohort was diagnosed with JBTS and has a *CSPPI* gene mutation, also reported in a patient with JBTS and an occipital encephalocele published by Tuz et al.¹³ In both cases, the cap shared similar characteristics: It was in the lower medulla and separated from the cerebellar peduncles, and the step and caterpillar signs were noted.

PTCD and AMCD are considered the result of aberrant axonal guidance. AMCD is part of the JBTS spectrum and is associated with the molar tooth sign, which is a hallmark of this syndrome.²⁶⁻²⁸ PTC differs from JBTS, in the imaging, clinical, and genetic aspects. A displaced decussation of the superior cerebellar peduncles is noted anteriorly-posteriorly in both AMCD and PTC.^{2,3,20,29}

Further supporting evidence is supplied by fiber tractography, which showed an abnormal transverse bundle of fibers in the pons forming the cap in PTC^{2,20,29} and an ectopic white matter bundle in AMCD. In the patient described by Jurkiewicz and Nowak,⁶ tractography revealed no decussating pontine fibers nor crossing of the corticospinal tracts, also implying abnormal axonal decussation in this entity. Postmortem analysis of patient 3 confirmed abnormal pathways because there was a continuation of fibers between the medullary mass and the white matter of the cerebellum (Fig 3).

The pathogenesis of JBTS, hypothesized to cause AMCD as well, is a ciliary dysfunction.^{2,3,30,31} Primary cilium has a key role in modulating neurogenesis, cell polarity, and axonal guidance, all essential for wiring the developing brain. Disrupted ciliary signaling contributes to axonal tract malformations in JBTS.³⁰⁻³² In our cohort, the additional findings in some patients such as midline distortion, a rotated position of the medulla on axial planes, and CC agenesis/partial agenesis as well as clinical features like polydactyly might support the hypothesis that MTCD can also be caused by impaired ciliary function in at least some patients. Callosal anomalies have also been mentioned by Barkovich,¹ Jurkiewicz and Nowak,⁶ and Barkovich et al.¹⁶

A de novo mutation in the *ACVRI* gene was found in one of our patients (patient 1, Fig 2A, p.Arg206His). This gene plays an essential role in ciliary formation.³² *ACVRI* deletion in mouse embryonic fibroblasts compromised ciliary development and resulted in defects in leftward fluid flow and, thus, abnormalities in left-right patterning.³² Mutations in *ACVRI* cause FOP, an autosomal dominant disorder causing progressive heterotopic endochondral ossifications.¹⁴ In 2016, Severino et al¹⁴ described a well-defined nonenhancing lesion at the level of the dorsal medulla with variable morphology, ranging from a thin band of tissue to an exophytic mass, in 13 patients with FOP. All also showed thin tissue bands at the ventral pons. We have re-classified this lesion as MTCD.

The cap in FOP seems to display a distinct form; it is “soft,” smooth, and rather flat, and its position is exceptionally higher in most cases, reaching the midpons. The mass has been suspected to represent a hamartoma;^{14,15} however, a postmortem examination of a 75-year-old patient revealed that the cap consisted of glial hyperplasia.³³

In patient 2 from our cohort, the postmortem examination in the fetus revealed that the mass contained mature neurons consistent with a hamartoma. In contrast, in patient 10, the postmortem examination at the age of 11 months revealed that the cap consisted of spheroids, a feature of axonal degeneration.³⁴ In this patient, the medullary cap was present prenatally (retrospectively) but was much less prominent and was noticeable postnatally, possibly due to progressive atrophy of the tegmentum as demonstrated by sequential MR images at 33 weeks’ gestation, 1 month, and 11 months (Online Supplemental Data). Also, the resolution of fetal MR imaging is inferior to that of postnatal MR imaging. The clinical picture and postmortem examination were reminiscent of neuroaxonal dystrophy; however, findings of genetic studies were negative.

Our study has several limitations. The main limitation is its retrospective nature, an evaluation of patients that have been collected by several groups across the globe. Therefore, a true incidence cannot be established. In addition, imaging protocols may have varied, the clinical data were limited in some of the cases, and no high-end functional imaging data were available (ie, DTI, which may allow studying of the internal architecture of the cap).

The inclusion of patients with JBTS might have led to a selection bias because their MTCD characteristics are distinctly different from those in the rest of the cohort. Future studies are warranted and may answer these open questions.

Differential diagnoses of abnormal dorsal medullary masses, causing a distortion of the brainstem, are brainstem tethering or proliferative disorders (tumor and metastasis). Brainstem tethering can be excluded because the mass is longer and, unlike MTCD, connects the dorsal medulla to the inner surface of the occipital skull,^{35,36} and a proliferative disorder can be excluded on the basis of lack of infiltrative features and imaging characteristics.³

CONCLUSIONS

This is the first study to delineate a series of patients with the rare malformation medullary tegmental cap dysplasia. The cap has different shapes, distinct in JBTS and FOP. Due to the variations in the clinical, imaging, and postmortem findings, we conclude that there are multiple etiologies and pathophysiology. We suggest that in some of the patients, the pathophysiology might be abnormal axonal guidance.

Disclosure forms provided by the authors are available with the full text and PDF of this article at www.ajnr.org.

REFERENCES

1. Barkovich AJ. *Pediatric Neuroimaging*. 5th ed. Lippincott Williams & Wilkins; 2005:932
2. Jissendi-Tchofo P, Doherty D, McGilivray G, et al. **Pontine tegmental cap dysplasia: MR imaging and diffusion tensor imaging features of impaired axonal navigation.** *AJNR Am J Neuroradiol* 2009;30:113–19 CrossRef Medline
3. Arrigoni F, Romaniello R, Peruzzo D, et al. **Anterior mesencephalic cap dysplasia: novel brain stem malformative features associated with Joubert syndrome.** *AJNR Am J Neuroradiol* 2017;38:2385–90 CrossRef Medline
4. Blondiaux E, Valence S, Friszer S, et al. **Prenatal imaging findings of pontine tegmental cap dysplasia: report of four cases.** *Fetal Diagn Ther* 2019;45:197–204 CrossRef Medline
5. Barth PG, Majoie CB, Caan MW, et al. **Pontine tegmental cap dysplasia: a novel brain malformation with a defect in axonal guidance.** *Brain* 2007;130:2258–66 CrossRef Medline
6. Jurkiewicz E, Nowak K. **Medullary cap dysplasia.** *Neurology* 2015;84:102–03 CrossRef Medline
7. Yagel S, Valsky DV. **Re: ISUOG Practice Guidelines (updated): sonographic examination of the fetal central nervous system, Part 1: performance of screening examination and indications for targeted neurosonography.** *Ultrasound Obstet Gynecol* 2021;57:173–74 CrossRef Medline
8. Paladini D, Malinger G, Birnbaum R, et al. **ISUOG Practice Guidelines (updated): sonographic examination of the fetal central nervous system, Part 2: performance of targeted neurosonography.** *Ultrasound Obstet Gynecol* 2021;57:661–71 CrossRef Medline
9. Kidron D, Shapira D, Ben Sira L, et al. **Agenesis of the corpus callosum: an autopsy study in fetuses.** *Virchows Arch* 2016;468:219–30 CrossRef Medline
10. Poretti A, Huisman TA, Scheer I, et al. **Joubert syndrome and related disorders: spectrum of neuroimaging findings in 75 patients.** *AJNR Am J Neuroradiol* 2011;32:1459–63 CrossRef Medline
11. Poretti A, Snow J, Summers AC, et al. **Joubert syndrome: neuroimaging findings in 110 patients in correlation with cognitive function and genetic cause.** *J Med Genet* 2017;54:521–29 CrossRef Medline
12. Poretti A, Vitiello G, Hennekam RC, et al. **Delineation and diagnostic criteria of oral-facial-digital syndrome type VI.** *Orphanet J Rare Dis* 2012;7:4 CrossRef Medline
13. Tuz K, Bachmann-Gagescu R, O’Day DR, et al. **Mutations in *CSPP1* cause primary cilia abnormalities and Joubert syndrome with or without Jeune asphyxiating thoracic dystrophy.** *Am J Hum Genet* 2014;94:62–72 CrossRef Medline

14. Severino M, Bertamino M, Tortora D, et al. **Novel asymptomatic CNS findings in patients with ACVR1/ALK2 mutations causing fibrodysplasia ossificans progressiva.** *J Med Genet* 2016;53:859–64 CrossRef Medline
15. Kan L, Kitterman JA, Procissi D, et al. **CNS demyelination in fibrodysplasia ossificans progressiva.** *J Neurol* 2012;259:2644–55 CrossRef Medline
16. Barkovich AJ, Millen KJ, Dobyns WB. **A developmental and genetic classification for midbrain-hindbrain malformations.** *Brain* 2009;132:3199–230 CrossRef Medline
17. Akyuz G, Gencer-Atalay K, Ata P. **Fibrodysplasia ossificans progressiva: lessons learned from a rare disease.** *Curr Opin Pediatr* 2019;31:716–22 CrossRef Medline
18. Abdelhamed ZA, Natarajan S, Wheway G, et al. **The Meckel-Gruber syndrome protein TMEM67 controls basal body positioning and epithelial branching morphogenesis in mice via the non-canonical Wnt pathway.** *Dis Model Mech* 2015;8:527–41 CrossRef Medline
19. Harbert MJ, Gleeson JG. **Classifying a novel brain malformation.** *Brain* 2007;130:2242–44 CrossRef Medline
20. Briguglio M, Pinelli L, Giordano L, et al; CBCD Study Group. **Pontine tegmental cap dysplasia: developmental and cognitive outcome in three adolescent patients.** *Orphanet J Rare Dis* 2011;6:36 CrossRef Medline
21. Illingworth MA, Meyer E, Chong WK, et al. **PLA2G6-associated neurodegeneration (PLAN): further expansion of the clinical, radiological and mutation spectrum associated with infantile and atypical childhood-onset disease.** *Mol Genet Metab* 2014;112:183–89 CrossRef Medline
22. Al-Maawali A, Yoon G, Feigenbaum AS, et al. **Validation of the finding of hypertrophy of the clava in infantile neuroaxonal dystrophy/PLA2G6 by biometric analysis.** *Neuroradiology* 2016;58:1035–42 CrossRef Medline
23. Papandreou A, Soo AKS, Spaul R, et al. **Expanding the spectrum of early neuroradiologic findings in β propeller protein-associated neurodegeneration.** *AJNR Am J Neuroradiol* 2022;43:1810–14 CrossRef Medline
24. Boltshauser E, Isler W. **Joubert syndrome: episodic hyperpnea, abnormal eye movements, retardation and ataxia, associated with dysplasia of the cerebellar vermis.** *Neuropadiatrie* 1977;8:57–66 CrossRef Medline
25. Gregory A, Kurian MA, Haack T, et al. **Beta-propeller protein-associated neurodegeneration.** In: Adam MP, Everman DB, Mirzaa GM, et al. eds. *GeneReviews University of Washington*; Seattle; 1993–2023
26. Ferland RJ, Eyaid W, Collura RV, et al. **Abnormal cerebellar development and axonal decussation due to mutations in AHI1 in Joubert syndrome.** *Nat Genet* 2004;36:1008–13 CrossRef Medline
27. Yachnis AT, Rorke LB. **Neuropathology of Joubert syndrome.** *J Child Neurol* 1999;14:655–59 CrossRef Medline
28. Poretti A, Boltshauser E, Loenneker T, et al. **Diffusion tensor imaging in Joubert syndrome.** *AJNR Am J Neuroradiol* 2007;28:1929–33 CrossRef Medline
29. Cadman CJ, Fraser L, McArthur C. **Case 266: pontine tegmental cap dysplasia.** *Radiology* 2019;291:814–18 CrossRef Medline
30. Guo J, Otis JM, Suci SK, et al. **Primary cilia signaling promotes axonal tract development and is disrupted in Joubert syndrome-related disorders models.** *Dev Cell* 2019;51:759–74.e5 CrossRef Medline
31. Doherty D. **Joubert syndrome: insights into brain development, cilium biology, and complex disease.** *Semin Pediatr Neurol* 2009;16:143–54 CrossRef Medline
32. Komatsu Y, Kaartinen V, Mishina Y. **Cell cycle arrest in node cells governs ciliogenesis at the node to break left-right symmetry.** *Development* 2011;138:3915–20 CrossRef Medline
33. Mori S, Suzuki SO, Honda H, et al. **Symmetrical glial hyperplasia in the brainstem of fibrodysplasia ossificans progressiva.** *Neuropathology* 2021;41:146–51 CrossRef Medline
34. Yong Y, Hunter-Chang S, Stepanova E, et al. **Axonal spheroids in neurodegeneration.** *Mol Cell Neurosci* 2021;117:103679 CrossRef Medline
35. Liu Z, He Y, Li S, et al. **Brainstem tethering with Ondine's curse.** *World Neurosurg* 2011;76:592.e11–14 CrossRef Medline
36. Buyse GG, Caekebeke J, Demaerel P, et al. **Primary brain stem tethering: a rare cause of geniculate neuralgia.** *J Laryngol Otol* 1999;113:945–47 CrossRef Medline

Modified Dynamic CT Myelography for Type 1 and 2 CSF Leaks: A Procedural Approach

M.D. Mamlouk, P.Y. Shen, and B.C. Dahlin



ABSTRACT

BACKGROUND AND PURPOSE: Dynamic CT myelography can identify spinal CSF leaks secondary to dural tears (type 1) and ruptured meningeal diverticula (type 2), but the radiation can be high secondary to multiple successive acquisitions. The purpose of this article is to discuss the procedural approach of a modified dynamic CT myelography technique with single scan acquisitions, reduced contrast volume, and condensed scan coverage and compare its radiation dose with that in traditional dynamic CT myelography.

MATERIALS AND METHODS: Retrospective review was performed for patients with spontaneous CSF leaks showing extradural collections on spine MR imaging who underwent traditional and modified dynamic CT myelography. The radiation doses between the 2 cohorts were compared.

RESULTS: Thirty-seven patients (25 women, 12 men) had a type 1 or 2 CSF leak on dynamic CT myelography. Thirty-one patients had a type 1 CSF leak, and 6 patients had type 2 leaks. The traditional dynamic CT myelography was performed in 25 patients, and the average number of acquisitions per dynamic CT myelography was 3.6. The mean total effective dose per dynamic CT myelography was 31.3 mSv (range, 11.3–68.4 mSv). The modified dynamic CT myelography was performed in 12 patients, and the average number of acquisitions was 2.8. The mean total effective dose per dynamic CT myelography was 15.1 mSv (range, 4.8–24.6 mSv). The effective dose and dose-length product between the cohorts were statistically significant ($P < .0001$ and $.01$, respectively).

CONCLUSIONS: Modified dynamic CT myelography performed with single scan acquisitions, smaller volume of contrast, and reduced scan coverage can reduce the radiation dose for type 1 and 2 CSF leak detection.

ABBREVIATIONS: CTM = CT myelography; DSM = digital subtraction myelography; SIH = spontaneous intracranial hypotension

Spontaneous intracranial hypotension (SIH) has 4 known causes: dural tears (type 1), ruptured meningeal diverticula (type 2), CSF-venous fistulas (type 3), and distal nerve root sleeve leaks (type 4).^{1,2} Type 1 and 2 CSF leaks manifest well on spine MR imaging as an extradural collection;³ however, location of the leak site is not often possible on MR imaging, and myelography is often necessary for accurate localization. Various types of myelography have been reported to identify type 1 CSF leaks, which include dynamic CT myelography (CTM),^{4,5} digital subtraction myelography (DSM),^{2,6,7} and conventional fluoroscopic

myelography.⁸ All 3 examinations can identify the exact transition of iodinated contrast from the subarachnoid-to-extradural space, which corresponds to the leak site. While no publications have compared the sensitivity and specificity among the 3 examination techniques, CSF leak localization is often achievable with all 3 examinations.

The dynamic CTM technique has the major advantage in identifying a calcified disc, which is very commonly seen with type 1 CSF leaks and is often small and located in the upper thoracic spine.⁹ In fact, because of the high spatial resolution of CT, a post-myelography CT is performed after DSM or conventional fluoroscopic myelography for disc detection and treatment planning.^{7,8} One major limitation for dynamic CTM is the radiation dose because multiple scans of the spine, reported up to 10 times,⁵ are performed consecutively to ensure a high temporal resolution and to identify the leak location. Our institution initially used this technique, obtaining 3 acquisitions of the total spine from caudal-cranial, cranial-caudal, caudal-cranial, and then additional scans afterward as needed. We then observed that the CSF leak can often be identified with 3 modifications: single-scan acquisitions, reduced contrast dose, and condensed scan coverage. The purpose

Received December 8, 2022; accepted after revision January 6, 2023.

From the Department of Radiology (M.D.M., P.Y.S.), The Permanente Medical Group, Kaiser Permanente Medical Center, Santa Clara, Santa Clara, California; Department of Radiology and Biomedical Imaging (M.D.M.), University of California, San Francisco, San Francisco, California; and Department of Radiology (B.C.D.), The Permanente Medical Group, Kaiser Permanente Medical Center, Sacramento, Sacramento, California.

Please address correspondence to Mark D. Mamlouk, MD, Department of Radiology, The Permanente Medical Group, Kaiser Permanente Medical Center, Santa Clara, 700 Lawrence Expressway, Santa Clara, CA 95051; e-mail: mark.d.mamlouk@kp.org; @MarkMamloukMD

Indicates open access to non-subscribers at www.ajnr.org

<http://dx.doi.org/10.3174/ajnr.A7784>

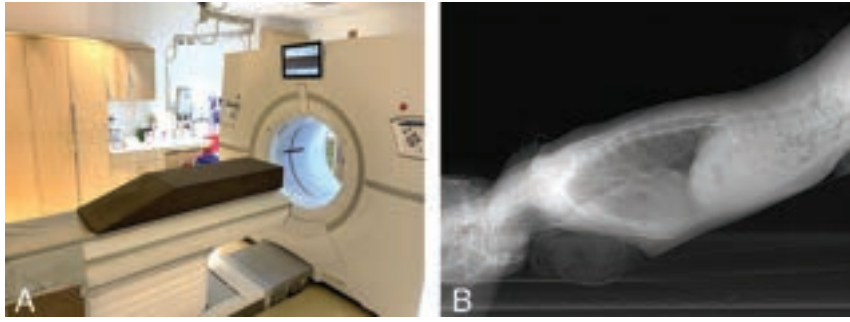


FIG 1. Patient positioning for modified dynamic CTM. *A*, A custom-made firm wedge with a 15° slope is placed on the CT gantry. The hips are placed at the apex of the wedge, with the feet closest to the scanner. The patient is positioned Trendelenburg prone for presumed ventral dural tears (type 1 CSF leaks) and positioned Trendelenburg decubitus for presumed ruptured meningeal diverticula (type 2 CSF leaks). *B*, A lateral scout radiograph shows an adequate angle for contrast to flow from the lumbar puncture site to the cervical spine.

of this article is to discuss the procedural approach of this modified dynamic CTM technique and compare the radiation dose with that in traditional dynamic CTM.

MATERIALS AND METHODS

Patient Selection

Institutional review board approval (Kaiser Permanente IRB# 1620615–2) was obtained, which waived the requirement for informed consent. The study population consisted of all patients with spontaneous CSF leaks showing extradural collections on spine MR imaging, from August 2018 to November 2022, who underwent spinal CSF leak detection using traditional or modified dynamic CTM techniques. The spinal CSF leak levels were subdivided into cervical spine, upper thoracic spine (T1–T6 levels), lower thoracic spine (T7–T12 levels), and lumbar spine. It was noted if a calcified disc was associated with the spinal leak.

Modified Dynamic CTM Technique

In patients with a high clinical suspicion for SIH and/or intracranial imaging findings consistent with SIH, a noncontrast total spine MR imaging is performed with fat-suppressed T2-weighted sequences. In our experience, as well as another study,¹⁰ MR imaging can reliably detect extradural fluid collections similar to conventional CT myelography. Thus, we do not perform conventional CT myelography simply to identify the presence or absence of an extradural collection.

The patient position for the dynamic CTM is predicated on the location of the extradural collection on spine MR imaging. If the collection is ventral or both ventral and dorsal, these collections are often secondary to ventral CSF leaks (type 1). If the extradural collection is predominantly lateral and centered along the meningeal diverticula, a ruptured meningeal diverticulum is often the cause (type 2). On the basis of these findings, we place the patient Trendelenburg prone for type 1 leaks and Trendelenburg decubitus for type 2 leaks using a custom-made wedge with a 15° angle (Fig 1A). Depending on the patient body habitus, if the angle is still not adequate, we will often place blankets or pillows under the hips to ensure an adequate angle of 15°–20°, because this is one of the

key requisites to ensure that the contrast bolus adequately coats the upper thoracic and cervical spine.

Frontal and lateral scout images of the total spine are obtained, and the angle is evaluated again to ensure that the patient is adequately Trendelenburg (Fig 1B) or to determine if adjustments are needed. After satisfactory positioning, a lumbar puncture is typically performed at the L3–L4 level. To ensure that the needle is subarachnoid, we perform a test dose of 0.2 mL of preservative-free iohexol contrast (Omnipaque 300; GE Healthcare). After confirmation of contrast within the subarachnoid space, image planning with the CT technician

is performed to obtain 1 caudal-to-cranial acquisition from the needle entry site to the C2 vertebral body using a standard kernel, 0.625-mm section thickness, and automatic exposure control radiation setting. The proceduralist will then inject 3 mL of the aforementioned contrast, exit the CT suite, and the CT technologist will perform the preset scanning acquisition.

The proceduralist will evaluate the axial images on the CT scanner console for the contrast transition from the subarachnoid-to-extradural space. If additional scrutiny is needed, the proceduralist will evaluate the axial and sagittal images on a dedicated radiology workstation located near the CT suite. The proceduralist is afforded this time to review the scans because a small volume of contrast is administered. If the images are satisfactory and the leak site and cause are identified, the myelogram is complete. If confirmation is needed, only the scan plane of the area of interest is prepared—not the total spine—to minimize radiation, followed by an additional 2–3 mL of contrast injection; then the scan is performed. If the contrast has not migrated cranially, additional contrast is administered up to a maximum of 10 mL. If the more caudal aspect of the spine does not show the CSF leak, a portion can be omitted in the subsequent scanning acquisition to conserve the radiation dose. A small volume of contrast is intentionally used initially. If a large volume (eg, 10 mL) is administered initially, exact leak localization may not be possible because the extradural contrast can diffuse throughout the spine, akin to spine MR imaging or a conventional CTM. If there is a suspicion of a lower thoracic CSF leak on the spine MR imaging, an initial dose of 1–2 mL of iodinated contrast can be used on the first scan acquisition. In case a follow-up dynamic CTM is needed for treatment planning, the scan coverage can be restricted to the spinal leak location to minimize the radiation dose.

Traditional Dynamic CTM Technique

The patient positioning and lumbar puncture technique were the same. Intrathecal contrast was injected with 3–10 mL, depending on the preference of the radiologist, and 3 scans of the total spine were obtained from caudal-cranial, cranial-caudal, and caudal-cranial, followed by additional single-scan acquisitions as necessary until the leak site was identified.

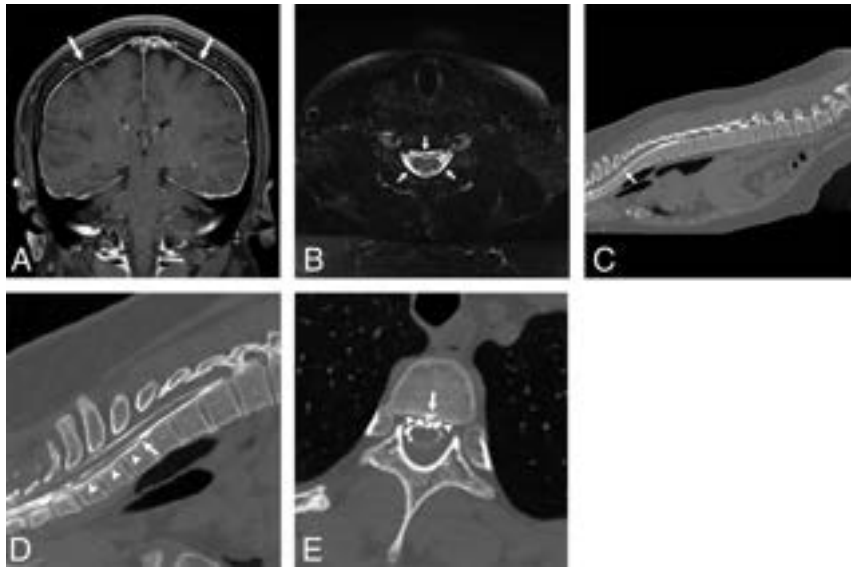


FIG 2. Detection of type 1 CSF leak with modified dynamic CTM in 2 scan acquisitions. *A*, Coronal contrast-enhanced fat-suppressed T1-weighted image shows dural enhancement (arrows) consistent with spontaneous intracranial hypotension. *B*, Axial fat-suppressed T2-weighted image shows ventral and dorsal extradural fluid (arrows) consistent with a CSF leak. *C*, Sagittal image from dynamic CTM after 3 mL of intrathecal iodinated contrast shows coating of the entire ventral spine, with a transition point at the T1–T2 level (arrow). *D*, Sagittal image from dynamic CTM after additional injection of 2 mL of contrast and scanning of the cervicothoracic junction only confirms a leak at the T1–T2 level, where there is a split in the contrast column (arrow) and extradural contrast layering dependently with gravity in the cervical spine (arrowheads). *E*, Axial image from the dynamic CTM shows that the CSF leak (arrowheads) is secondary to a ventral midline calcified disc (arrow).

Table 1: Patient demographics of spinal CSF leaks

Demographics	
No.	37
Mean age (SD) at symptom onset (yr)	44.1 (10.2)
Sex	
Female	25
Male	12
Type 1 leak location (<i>n</i> = 31)	
Cervical	2
Upper thoracic (T1–T6)	22
Lower thoracic (T7–T12)	7
Lumbar	0
Type 2 leak location (<i>n</i> = 6)	
Lower thoracic (T7–T12)	6

Image Review and Reporting

The dynamic CTM is evaluated for the presence of a type 1 or 2 CSF leak. The transition point where the contrast media flows from subarachnoid to extradural in location corresponds to the leak site. If there is an associated calcified disc, the location and size are reported (Fig 2). Type 1 leaks may occasionally be posterior or lateral in location, and we report the leak location and whether there is an associated dorsal osteophyte.¹¹ For type 2 leaks, we evaluate for CSF leakage centered at a meningeal diverticulum.

Radiation Data

The number of dynamic CTM examinations was recorded until the CSF leak level was identified, and the number of scan acquisitions per CTM examination was tallied. The CT dose index and

dose-length product were obtained for each acquisition, and an average per CTM examination was calculated. The effective dose per scan acquisition was obtained using a commercial software DoseWatch (GE Healthcare), and the total effective dose was calculated for each CTM examination.

Statistical Analysis

To identify any differences in CT dose index, dose-length product, and total effective dose between the traditional and modified dynamic CTM techniques, we performed homoscedastic *t*-tests (Excel; Microsoft), and *P* values < .05 were considered statistically significant.

RESULTS

There were 38 patients with a spontaneous extradural collection on spine MR imaging who underwent dynamic CTM. One patient was excluded because the dynamic CTM was negative for an extradural collection. We presumed that this was related to spontaneous patching of the spinal leak because the patient's symptoms resolved. There were 37 patients (25 women, 12 men) with a type

1 or 2 CSF leak on dynamic CTM with a mean age of 44.1 years and a mean Bern SIH score of 5.7 (Table 1). Thirty-one patients had a type 1 CSF leak, and the leak locations were 2 cervical, 22 upper thoracic (T1–T6), 7 lower thoracic (T7–T12), and no lumbar spine. Thirty of 31 patients with type 1 CSF leaks had a ventral tear, with 24 calcified discs identified as the leak cause, while 1/31 patients had a lateral tear. Six patients had type 2 leaks with ruptured meningeal diverticula, and they were all in the lower thoracic (T7–T12) spine. The specific leak location was identified on the first dynamic CTM in 35 patients and on the second dynamic CTM in 2 patients: One patient had a traditional CTM, and the other patient had a modified CTM.

The traditional dynamic CTM was performed in 25 patients, and the average number of acquisitions per dynamic CTM was 3.6 (range, 1–7). The mean CT dose index, dose-length product, and total effective dose per dynamic CTM were 13.4 mGy (range, 6.6–31.6 mGy), 647.2 mGy cm (range, 259.1–727.2 mGy cm), and 31.3 mSv (range, 11.3–68.4 mSv), respectively (Table 2). The radiation dose was not available in 2 patients.

Modified dynamic CTM was performed in 12 patients, and the average number of acquisitions per dynamic CTM was 2.8 (range, 2–4). The mean CT dose index, dose-length product, and total effective dose per dynamic CTM were 10.6 mGy (range, 4.0–28.3 mGy), 406.7 mGy cm (range, 165.7–747.5 mGy cm), and 15.1 mSv (range, 4.8–24.6 mSv), respectively.

The modified dynamic CTM mean effective dose and dose-length product were statistically significant compared with the

Table 2: Radiation doses of traditional and modified dynamic CTM

	Traditional Dynamic CTM Technique	Modified Dynamic CTM Technique	P Value
No of patients	25	12	
Mean radiation dose			
CTDI	13.4 (range, 6.6–31.6) mGy	10.6 (range, 4.0–28.3) mGy	.24
DLP	647.2 (range, 259.1–727.2) mGy cm	406.7 (range, 165.7–747.5) mGy cm	.01
Total effective dose	31.3 (range, 11.3–68.4) mSv	15.1 (range, 4.8–24.6) mSv	<.0001

Note:—CTDI indicates CT dose index; DLP, dose-length product.

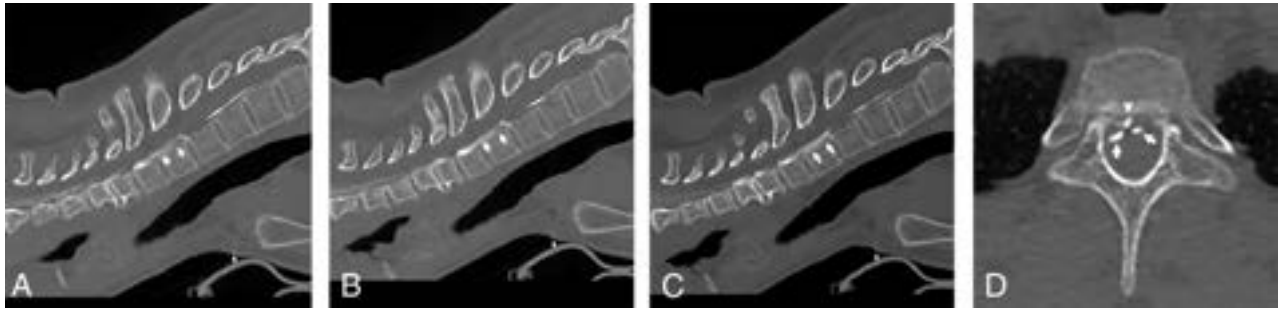


FIG 3. Detection of type 1 CSF leak with traditional dynamic CTM in 3 scan acquisitions. A–C, Sagittal images from 3 successive acquisitions of the total spine dynamic CTM show a split of contrast at the T1–T2 level with contrast accumulating in the ventral extradural space (arrows). This was first evident on the first acquisition, and the leak site can be determined with this acquisition alone. The second and third acquisitions show slightly more contrast accumulation in the extradural space. D, Axial image of the first acquisition of the dynamic CTM shows a calcified disc (arrowhead) splitting the contrast within the subarachnoid space (arrows).

traditional technique ($P < .0001$ and $.01$, respectively). The CT dose index was not statistically significant ($P = .24$).

In all patients with ≥ 4 scan acquisitions per dynamic CTM (traditional and modified), there was an average of 2.6 acquisitions in which the injected intrathecal contrast did not extend to the cervical spine. In patients with < 4 scan acquisitions per dynamic CTM examination, there was an average of 0.21 acquisitions in which the injected intrathecal contrast did not extend to the cervical spine.

DISCUSSION

Dynamic CTM is a valuable tool to identify the precise leak site in patients with type 1 (dural tear) and type 2 (ruptured meningeal diverticula) CSF leaks. The technique was originally devised by performing multiple consecutive scan acquisitions of the total spine to identify the leak site. In 1 report by Thielen et al⁴ with 14 patients, a noncontrast CT of the spine was performed, followed by the operator injecting contrast, while up to 6 acquisitions of the total spine were performed with alternating caudal-cranial and cranial-caudal scans. The mean effective dose per study was 70.64 mSv (range, 21.5–182.9 mSv). Another study by Dobrocky et al⁵ with 14 patients used a similar technique of obtaining multiple acquisitions (mean, 7; range, 3–10 acquisitions) but had a smaller volume of coverage (mean, 8 vertebral body levels; range, 4–12 levels). The mean effective dose per study was 24.4 mSv (range, 9.8–67.5 mSv). Early in our practice, we performed a similar technique of obtaining multiple successive scans, and the mean effective dose per study was 31.3 mSv (range, 11.3–68.4 mSv). After we switched to our modified dynamic CTM technique, the mean effective dose per study was 15.1 mSv (range, 4.8–24.6 mSv). This is a radiation savings of approximately 50% effective dose compared with our older technique, 40% compared with the dose of

Dobrocky et al, and 80% compared with Thielen et al. Thus, radiation savings is possible with a modified dynamic CTM technique, and this modified technique may be beneficial in all patients but particularly young adults and children with spinal CSF leaks. In addition to our lower radiation dose, we had an average of 2.8 acquisitions with our new technique, which is also less than those in both aforementioned studies.

For type 1 CSF leaks, most leaks were ventral in location (30/31 patients) and were often secondary to calcified discs (24/31 patients) in the upper thoracic spine (22/31 patients). One tip that we found helpful either during the myelogram or afterward is to scrutinize the sagittal reformatted images of the CTM rotated in a horizontal plane (Fig 2) and observe this transition point, because the extradural collection can be easier to identify in its entirety as opposed to 1 section on the axial imaging. For type 2 leaks, all of these were in the lower thoracic spine. We scrutinize the ruptured meningeal diverticulum predominantly on axial imaging but have also found the coronal plane helpful in characterization.

Both the traditional and modified dynamic CTMs were successful in finding the exact leak site, which was identified in 35 patients on the first dynamic CTM and 2 patients on the second dynamic CTM. While dynamic CTM, in general, is helpful in characterizing the leak site, the traditional technique that uses multiple successive scans may be unnecessary. In our experience using the traditional method, we often found the leak site on the first scan. The additional acquisitions increased the radiation dose and did not necessarily provide much additional information (Fig 3). Insufficient contrast coating of the upper spine is one of the challenges that can be encountered with dynamic CTM. This is usually secondary to a shallow Trendelenburg angle, and if present, the patient can be elevated higher to ensure an approximately 15°–20° angle. This pitfall is something we encountered early in our practice

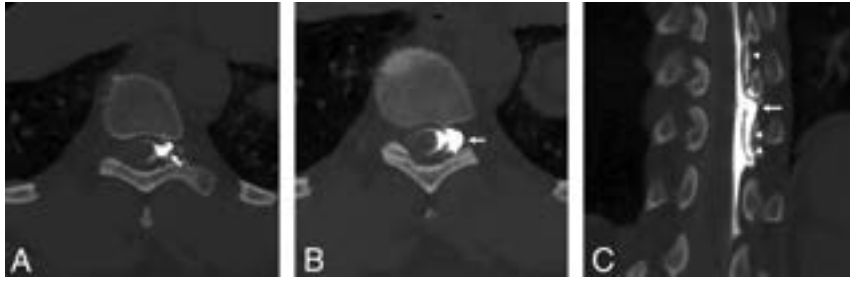


FIG 4. Detection of a type 2 CSF leak with a modified dynamic CTM in 2 scan acquisitions. *A*, Axial image from left decubitus dynamic CTM after 1 mL of intrathecal iodinated contrast shows extradural contrast leaking from a ruptured left T9–T10 meningeal diverticulum (*arrow*). *B*, Axial image after an additional 2 mL of contrast was administered shows further leakage at this site (*arrow*), providing additional confirmation in the leak location. *C*, Coronal image from the same second CTM acquisition shows the leak extent better—ruptured diverticulum (*arrow*) and extradural contrast cranially and caudally (*arrowheads*).

and was magnified when we used to perform successive scan acquisitions in dynamic CTM, and additional scans were required to ensure that the contrast media went acceptably cranial. This pitfall was a promulgating factor to switch to the modified dynamic CTM technique with single scan acquisitions. In addition, our data show that patients with ≥ 4 scan acquisitions per dynamic CTM had more acquisitions in which the contrast did not extend to the cervical spine as opposed to patients with < 4 scan acquisitions.

Dynamic fluoroscopic myelography and DSM are additional techniques that can identify type 1 and 2 CSF leaks. The former provides high temporal resolution, and the detector can be moved to follow the contrast media flowing cranially. DSM also has high temporal resolution but has a limited area of scan coverage and is sensitive to breathing and motion artifacts, resulting in general anesthesia in certain scenarios. DSM also has higher radiation compared with fluoroscopic myelography. Dynamic CTM has relatively less temporal resolution but has excellent spatial resolution, particularly when evaluating calcified discs in the upper thoracic, which is an area that can be obscured on planar imaging due to superimposed shoulders and ribs.⁸ Last, dynamic CTM can image the whole spine, and, in our experience, is a fairly easy technique to learn.

There are relatively fewer reports discussing the imaging evaluation of type 2 leaks (ruptured meningeal diverticula) compared with other types of CSF leaks, probably related to the rarity of these leaks. While type 2 leaks are less common, the same modified dynamic CTM can precisely identify the specific ruptured meningeal diverticulum with reduced radiation. One report describes decubitus dynamic CTM for lateral leaks with 6 acquisitions of the spine.¹² Our modified technique was able to reduce the number of scan acquisitions and area of contrast (Fig 4). Last, owing to the rarity of these leaks, one may misinterpret the extradural collection on the spine MR imaging and position the patient in a Trendelenburg prone position and fail to identify the ruptured meningeal diverticulum. In these cases, the patient may be rotated to a decubitus position to identify the leak, or the patient may have to return on a separate day and undergo the dynamic CTM in the decubitus position.

Precise localization of all CSF leaks is important for treatment planning. At our institution, we perform targeted blood

and fibrin glue patches for types 1 and 2 CSF leaks via a foraminal and/or interlaminar approach, trying to place the needle as close to the leak site as possible. We have witnessed symptomatic improvement in all patients. We refer patients with incomplete resolution of symptoms for neurosurgical treatment. Thus, identifying the precise leak site is paramount for surgical referrals.

Our study has limitations, including its retrospective nature and is subject to bias. Second, our study sample size with the modified dynamic CTM technique is small. Nonetheless, this sample size is comparable with that in

2 other previously mentioned studies on traditional dynamic CTM.^{4,5}

CONCLUSIONS

Dynamic CTM is a useful technique to help identify the exact spinal leak location and cause in patients with type 1 (dural tears) and 2 (ruptured meningeal diverticula) CSF leaks. A modified version of this technique by performing single scan acquisitions with a smaller volume of contrast and reduced scan coverage can help reduce the radiation dose.

Disclosure forms provided by the authors are available with the full text and PDF of this article at www.ajnr.org.

REFERENCES

- Schievink WI, Maya MM, Jean-Pierre S, et al. **A classification system of spontaneous spinal CSF leaks.** *Neurology* 2016;87:673–79 CrossRef Medline
- Farb RI, Nicholson PJ, Peng PW, et al. **Spontaneous intracranial hypotension: a systematic imaging approach for CSF leak localization and management based on MRI and digital subtraction myelography.** *AJNR Am J Neuroradiol* 2019;40:745–53 CrossRef Medline
- Dobrocky T, Winklehner A, Breiding PS, et al. **Spine MRI in spontaneous intracranial hypotension for CSF leak detection: non-superiority of intrathecal gadolinium to heavily T2-weighted fat-saturated sequences.** *AJNR Am J Neuroradiol* 2020;41:1309–15 CrossRef Medline
- Thielen KR, Sillery JC, Morris JM, et al. **Ultrafast dynamic computed tomography myelography for the precise identification of high-flow cerebrospinal fluid leaks caused by spiculated spinal osteophytes.** *J Neurosurg Spine* 2015;22:324–31 CrossRef Medline
- Dobrocky T, Mosimann PJ, Zibold F, et al. **Cryptogenic cerebrospinal fluid leaks in spontaneous intracranial hypotension: role of dynamic CT myelography.** *Radiology* 2018;289:766–72 CrossRef Medline
- Hoxworth JM, Patel AC, Bosch EP, et al. **Localization of a rapid CSF leak with digital subtraction myelography.** *AJNR Am J Neuroradiol* 2009;30:516–19 CrossRef Medline
- Hoxworth JM, Trentman TL, Kotsenas AL, et al. **The role of digital subtraction myelography in the diagnosis and localization of spontaneous spinal CSF leaks.** *AJR Am J Roentgenol* 2012;199:649–53 CrossRef Medline
- Piechowiak EL, Pospieszny K, Haeni L, et al. **Role of conventional dynamic myelography for detection of high-flow cerebrospinal fluid leaks: optimizing the technique.** *Clin Neuroradiol* 2021;31:633–41 CrossRef Medline

9. Mamlouk MD, Shen PY, Jun P, et al. **Spontaneous spinal CSF leaks stratified by age, body mass index, and spinal level.** *AJNR Am J Neuroradiol* 2022;43:1068–72 CrossRef Medline
10. Tay ASS, Maya M, Moser FG, et al. **Computed tomography vs heavily T2-weighted magnetic resonance myelography for the initial evaluation of patients with spontaneous intracranial hypotension.** *JAMA Neurol* 2021;78:1275–76 CrossRef Medline
11. Madhavan AA, Shlapak DP, Benson JC, et al. **Osseous spicules of the posterior elements causing fast cerebrospinal fluid leaks.** *Neuroradiology* 2022;64:1689–93 CrossRef Medline
12. Madhavan AA, Verdoorn JT, Shlapak DP, et al. **Lateral decubitus dynamic CT myelography for fast cerebrospinal fluid leak localization.** *Neuroradiology* 2022;64:1897–903 CrossRef Medline

Conebeam CT as an Adjunct to Digital Subtraction Myelography for Detection of CSF-Venous Fistulas

A.A. Madhavan, J.K. Cutsforth-Gregory, J.C. Benson, W. Brinjikji, I.T. Mark, and J.T. Verdoorn



ABSTRACT

SUMMARY: Lateral decubitus digital subtraction myelography is an effective technique for precisely localizing CSF-venous fistulas, a common cause of spontaneous intracranial hypotension. However, despite an optimal imaging technique, digital subtraction myelography fails to identify some CSF-venous fistulas for a variety of reasons. Here, we describe a technique involving conebeam CT performed during intrathecal contrast injection as an adjunct to digital subtraction myelography, allowing identification of some otherwise-missed CSF-venous fistulas.

ABBREVIATIONS: CBCT = conebeam CT; CTM = CT myelography; CVF = CSF-venous fistula; DSM = digital subtraction myelography; LDDSM = lateral decubitus digital subtraction myelography

Spontaneous intracranial hypotension is caused by spinal CSF leaks, which, in turn, have multiple etiologies. These include dural tears (type 1), leaking meningeal diverticula (type 2), and CSF-venous fistulas (CVFs, type 3).¹ Myelographic techniques with high spatial and temporal resolution are needed to localize CSF leaks, including CVFs, which may be seen for only a short time after intrathecal contrast injection.^{2,3} Currently, digital subtraction myelography (DSM) and dynamic CT myelography (CTM) are among the most widely used techniques for CSF leak localization.^{4,5} Both examinations are performed with the patient in the lateral decubitus position when a CVF is suspected, to maximize their yield.^{6,7}

Conebeam CT (CBCT) has been used in neuroangiography for many years as an adjunct to DSA, and it has multiple applications in this field.⁸ CBCT uses a rotating x-ray source and detector to acquire multiple fluoroscopic images, which are subsequently reconstructed into a 3D, cross-sectional data set. Unlike with traditional CT, the cone-shaped x-ray source covers the entire imaging FOV in each image, allowing the entire CT to be rendered with a single rotation. Modern equipment allows the user to select variable frame rates, degrees of rotation, and other imaging parameters to balance image quality with radiation dose. CBCT has multiple emerging applications. One prior report described 2

patients in whom CBCT was used to help localize a dural tear.⁹ To our knowledge, however, CBCT has not been previously reported in the assessment of CVFs. Here, we describe a technique for lateral decubitus DSM (LDDSM) with subsequent CBCT that can be used to identify CVFs that may not be apparent on DSM alone.

TECHNICAL REPORT

Our institution's technique for LDDSM has been previously described in detail but has been recently modified to incorporate CBCT.⁴ For patients with clinically suspected spontaneous intracranial hypotension based on the International Classification of Headache Disorders Criteria and no extradural fluid on spine MR imaging that would suggest a type 1 leak, we routinely pursue 2-day LDDSM, starting with the patient in the right lateral decubitus position on the first day.

Patients are placed in the lateral decubitus position with a custom cushion under the pelvis to promote caudocranial flow of contrast. After lumbar puncture with a 20- or 22-gauge spinal needle, a straight anterior-posterior projection is obtained, imaging from C7–T1 through the lowest level that can be seen without electronic magnification. DSM is performed at 1 frame per second for about 90 seconds while injecting 5 mL of Omnipaque 300 (GE Healthcare) and flushing with 5 mL of normal saline. A second straight anterior-posterior projection is obtained from the lumbar puncture site to the highest spinal level that can be seen, and dynamic imaging is repeated during injection of 3 mL of Omnipaque 300.

The images are immediately reviewed while the patient is on the table. If a definite CVF is seen, no further imaging is done. If no definite CVF is seen, the images are further scrutinized for indeterminate findings that may warrant CBCT. These include

Received December 5, 2022; accepted after revision January 13, 2023.

From the Division of Neuroradiology (A.A.M., J.C.B., W.B., I.T.M., J.T.V.), Department of Radiology and Department of Neurology (J.K.C.-G.), Mayo Clinic, Rochester, Minnesota.

Please address correspondence to Ajay Madhavan, MD, Division of Neuroradiology, Department of Radiology, Mayo Clinic, 200 First St SW, Rochester, MN 55905; e-mail: madhavan.ajay@mayo.edu



Indicates article with supplemental online video.

<http://dx.doi.org/10.3174/ajnr.A7794>



FIG 1. A 52-year-old woman with years of orthostatic headaches and brain MR imaging demonstrating brain sag and pachymeningeal enhancement. Right lateral decubitus DSM (A) shows a large, right T10 meningeal diverticulum (A, *dashed arrow*), but no venous opacification was seen on dynamic imaging. Axial (B) and sagittal (C) images from CBCT obtained during contrast injection demonstrate subtle opacification of intramuscular venous branches (B and C, *arrows*) adjacent to the diverticulum (B and C, *dashed arrows*), compatible with CSF-venous fistula. Sagittal 50-keV monoenergetic reconstruction from right lateral decubitus CT obtained 15 minutes later (D) no longer shows opacification of these veins in the same location (D, *arrow*). The patient was treated with transvenous Onyx embolization of the right T10 fistula, with complete resolution of symptoms in 3 months.

but are not limited to the following: 1) “flickering” densities that could represent subtle venous opacification, 2) dense foci superimposed on a meningeal diverticulum that could represent a vein overlapping a diverticulum, and 3) large or irregular diverticula that may conceal an occult CVF (Figs 1–3 and Online Video). If such findings are seen, the flat panel detector is centered over the spinal level of greatest concern based on imaging review, and the machine is prepared for CBCT. Depending on the degree of geometric magnification and patient size, about 6 vertebral levels can be captured within the FOV, and we typically place the level of interest in the center of the imaging field. Another 3 mL of Omnipaque 300 is injected during continuous fluoroscopy, which allows immediate visualization of ascending contrast. Once the contrast bolus reaches the spinal level of interest, CBCT is immediately performed. To minimize motion, we obtain the CBCT at end inspiration with the patient holding his or her breath. Finally, the spinal needle is removed, and the patient is taken for immediate lateral decubitus CT myelography using a dual-energy scanner (Somatom Force; Siemens).

We use an Allura Xper FD 20/20 x-ray system (Philips Healthcare). Specific parameters for CBCT include 117 kV, 132 mA, 60 frames per second, and rotation time of 8 seconds with a single rotation (thus, the total acquisition time is 8 seconds as well). This

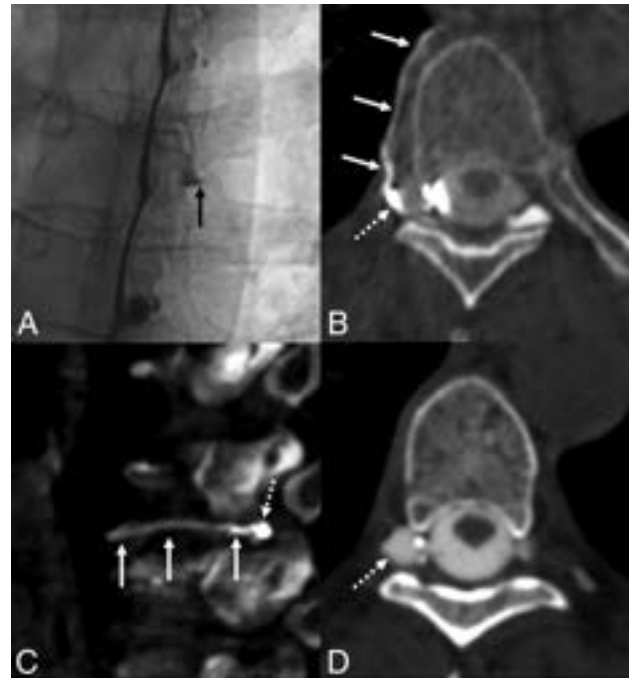


FIG 2. A 56-year-old woman with several months of orthostatic headaches. Brain MR imaging (not shown) demonstrated brain sag and pachymeningeal enhancement. Unsubtracted image from right lateral decubitus DSM (A) shows a prominent right T6 meningeal diverticulum (A, *arrow*), with subtle flickering density along the lateral edge of the diverticulum during dynamic imaging. Axial (B) and sagittal (C) images from CBCT obtained during contrast injection demonstrate opacification of the right T6 paraspinal vein (B and C, *solid arrows*), distinct from the diverticulum (B and C, *dashed arrows*), overall compatible with CSF-venous fistula. Axial 50-keV reconstruction from delayed right lateral decubitus CT obtained 15 minutes later (D) shows a prominent right T6 meningeal diverticulum (D, *dashed arrow*) without convincing venous contrast. Transvenous Onyx embolization of the right T6 fistula is pending.

procedure provides images with a section thickness of 0.6 mm. The effective radiation dose varies depending on patient factors and the portion of the body in the FOV, but the median dose in 15 consecutive patients at our institution was estimated to be 8.7 mSv. By comparison, the median effective radiation doses for DSM and CTM alone were 13 mSv and 19.7 mSv, respectively, in 1 recent study.¹⁰

DISCUSSION

We have described a technique involving the use of CBCT as an adjunct to LDDSM for localization of CVFs in patients with spontaneous intracranial hypotension. Although LDDSM is an excellent technique for CVF localization, it has limitations that result in missed CVFs in some cases. Some of these can be found using CBCT.

The limitations of LDDSM are varied. First, although LDDSM can be performed using biplane fluoroscopy, the lateral view provides limited information in patients with a large body habitus. Therefore, we routinely use only a single anterior-posterior projection.⁴ As a result, venous opacification that overlaps meningeal diverticula or other opacified structures can be missed on the

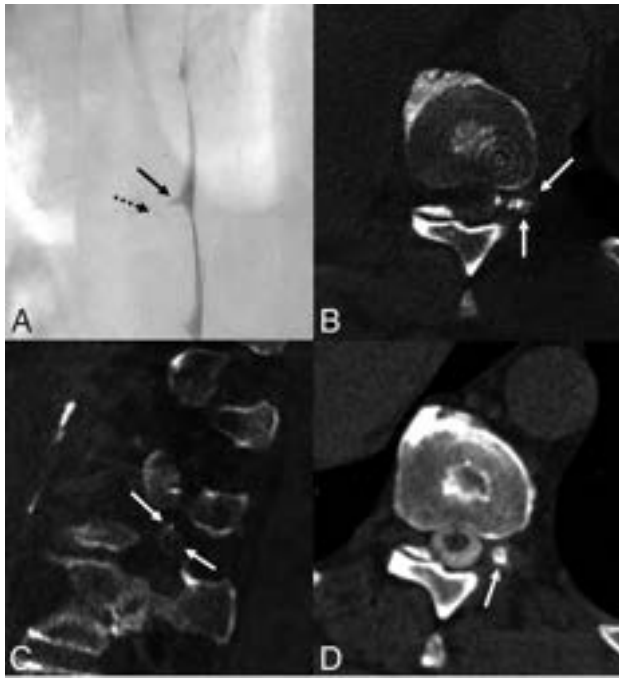


FIG 3. A 66-year-old man with many years of orthostatic headaches that improved after surgical treatment of a left T10 CSF-venous fistula and then recurred. Left lateral decubitus DSM (A) shows a mildly prominent left T10 meningeal diverticulum (A, arrow), with no definite venous contrast on dynamic imaging. Minimal hyperdensity seen adjacent to the diverticulum (A, dashed arrow) was initially thought to be artifactual, secondary to motion or a multilobed diverticulum. CBCT was performed to further investigate the finding. Axial (B) and sagittal (C) images from CBCT obtained during contrast injection demonstrate opacification of numerous left T10 foramina (B and C, arrows), compatible with CSF-venous fistula. Axial 50-keV reconstruction from a delayed left lateral decubitus CT obtained 20 minutes later (D) shows a prominent left T10 meningeal diverticulum (D, arrow) without convincing venous contrast. The patient was treated with transvenous Onyx embolization of the left T10 fistula, with complete resolution of symptoms in 3 months.

single anterior-posterior view. CBCT allows identification of these veins (Fig 1). Second, tiny flickering densities seen on DSM can be caused by pulmonary markings, motion, or subtle opacifying veins, leading to uncertainty in image interpretation. This dilemma can be obviated by performing DSM with the patient under general anesthesia, but that is challenging at some institutions and increases the procedural risk to patients. CBCT can help clarify such DSM findings and determine whether they represent true venous opacification (Fig 2). Finally, since DSM does not provide cross-sectional anatomic information, it is sometimes difficult to differentiate complex, multilobed meningeal diverticula from CVFs. CBCT provides 3D anatomic information that allows a more accurate determination (Fig 3). Additionally, characterization of the anatomic drainage of CVFs can be helpful for subsequent neurointerventional procedures, such as transvenous Onyx (Medtronic) embolization of CVFs.¹¹

Many institutions, including ours, also use lateral decubitus dynamic CTM to localize CVFs. While this technique overcomes many of the limitations of DSM, it has substantially less temporal resolution than DSM. While DSM provides continuous imaging

at a high frame rate, lateral decubitus dynamic CTM allows imaging at only a few separate points in time and, as a result, may miss CVFs that opacify only intermittently after contrast injection. However, further study is needed to determine how frequently CVFs have such transient or intermittent opacification, particularly accounting for factors such as the respiratory phase during imaging and layering contrast density. Nonetheless, 1 theoretic advantage of LDDSM with CBCT is that the former provides the temporal resolution of dynamic myelography needed to identify CVFs that may only opacify intermittently, while the latter provides an option to visualize potential CVFs in 3D to clarify indeterminate DSM findings. Additionally, CBCT may have advantages over delayed decubitus CTM. We have found that CVFs seen using CBCT may not be apparent on a delayed CTM obtained as early as 15 minutes later (Figs 1–3). We speculate that delayed decubitus CTM no longer has layering contrast that is sufficiently dense to visualize CVFs, even with 50-keV monoenergetic reconstructions (Figs 2–3).

Our technical report has limitations. We have only performed LDDSM with CBCT in a small number of patients and are not yet able to determine how frequently it provides additional value. To date, we have used CBCT in 15 patients who had indeterminate findings on initial review of their LDDSM. In 7 cases, a CVF was found using CBCT. Five of these patients have undergone transvenous Onyx embolization for treatment, and 4 have had clinical follow-up documenting resolution of symptoms (1 patient has not yet been seen for follow-up). As more data are accrued, further study will be needed to better elucidate the yield of CBCT. Additionally, other modifications to our typical LDDSM technique, such as the use of biplane fluoroscopy, may sometimes be a better alternative to CBCT. Comparison between CBCT and lateral decubitus dynamic CTM will also be helpful. Nonetheless, we have encountered cases in which CBCT is an invaluable adjunctive tool to identify CVFs and currently consider it a worthwhile technique.

Disclosure forms provided by the authors are available with the full text and PDF of this article at www.ajnr.org.

REFERENCES

- Schievink WI, Maya MM, Jean-Pierre S, et al. **A classification system of spontaneous spinal CSF leaks.** *Neurology* 2016;87:673–79 CrossRef Medline
- Hoxworth JM, Patel AC, Bosch EP, et al. **Localization of a rapid CSF leak with digital subtraction myelography.** *AJNR Am J Neuroradiol* 2009;30:516–19 CrossRef Medline
- Hoxworth JM, Trentman TL, Kotsenas AL, et al. **The role of digital subtraction myelography in the diagnosis and localization of spontaneous spinal CSF leaks.** *AJR Am J Roentgenol* 2012;199:649–53 CrossRef Medline
- Kim DK, Brinjikji W, Morris PP, et al. **Lateral decubitus digital subtraction myelography: tips, tricks, and pitfalls.** *AJNR Am J Neuroradiol* 2020;41:21–28 CrossRef Medline
- Kim DK, Carr CM, Benson JC, et al. **Diagnostic yield of lateral decubitus digital subtraction myelogram stratified by brain MRI findings.** *Neurology* 2021;96:e1312–18 CrossRef Medline
- Kranz PG, Gray L, Amrhein TJ. **Decubitus CT myelography for detecting subtle CSF leaks in spontaneous intracranial hypotension.** *AJNR Am J Neuroradiol* 2019;40:754–56 CrossRef Medline
- Mamlouk MD, Ochi RP, Jun P, et al. **Decubitus CT myelography for CSF-venous fistulas: a procedural approach.** *AJNR Am J Neuroradiol* 2021;42:32–36 CrossRef Medline

8. Angle JF. **Cone-beam CT: vascular applications.** *Tech Vasc Interv Radiol* 2013;16:144–49 CrossRef Medline
9. Chu E, McAuliffe W. **Use of flat panel DynaCT myelography to locate the site of CSF leak.** *J Med Imaging Radiat Oncol* 2013;57:455–59 CrossRef Medline
10. Nicholson PJ, Guest WC, van Prooijen M, et al. **Digital subtraction myelography is associated with less radiation dose than CT-based techniques.** *Clin Neuroradiol* 2021;31:627–31 CrossRef Medline
11. Borg N, Cutsforth-Gregory J, Oushy S, et al. **Anatomy of spinal venous drainage for the neurointerventionalist: from puncture site to intervertebral foramen.** *AJNR Am J Neuroradiol* 2022;43:517–25 CrossRef Medline

Postoperative Lumbar Fusion Bone Morphogenetic Protein–Related Epidural Cyst Formation

F. Abel, E.T. Tan, D.B. Sneag, D.R. Lebl, and J.L. Chazen



ABSTRACT

SUMMARY: Bone morphogenetic protein is broadly used in spinal surgery to enhance fusion rates. Several complications have been associated with the use of bone morphogenetic protein, including postoperative radiculitis and pronounced bone resorption/osteolysis. Bone morphogenetic protein–related epidural cyst formation may represent another complication that has not been described aside from limited case reports. In this case series, we retrospectively reviewed imaging and clinical findings of 16 patients with epidural cysts on postoperative MR imaging following lumbar fusion. In 8 patients, mass effect on the thecal sac or lumbar nerve roots was noted. Of these, 6 patients developed new postoperative lumbosacral radiculopathy. During the study period, most patients were managed conservatively, and 1 patient required revision surgery with cyst resection. Concurrent imaging findings included reactive endplate edema and vertebral bone resorption/osteolysis. Epidural cysts had characteristic findings on MR imaging in this case series and may represent an important postoperative complication in patients following bone morphogenetic protein–augmented lumbar fusion.

ABBREVIATIONS: ALIF = anterior lumbar interbody fusion; BMP = bone morphogenetic protein; LLIF/XLIF = lateral/extreme lateral lumbar interbody fusion; L-spine = lumbar spine; PLIF = posterior lumbar interbody fusion; PLL = posterior longitudinal ligament; rhBMP-2 = recombinant bone morphogenetic protein-2; TLIF = transforaminal lumbar interbody fusion

Bone morphogenetic proteins (BMPs) are multifunctional growth factors with osteoinductive properties that were first described in 1965.¹ Since recombinant bone morphogenetic protein-2 (rhBMP-2) was FDA-approved for anterior lumbar interbody fusion (ALIF) in 2002, rhBMP-2 has been widely used in spine surgery and extended to off-label indications.² The increasing popularity is attributed to enhancement of fusion rates that are not associated with disadvantages of iliac crest bone grafting, including donor site pain, increased operative time, and limited availability.^{3,4} However, several concerns related to adverse effects and complications have been addressed that raised questions regarding its safety profile.⁵ Thus, complications of rhBMP-2 bone grafting in spinal fusion procedures include but are not limited to radiculitis, marked bone resorption, heterotopic ossification, seroma/hematoma formation, and prevertebral swelling.⁶

The osteogenic effects are induced by supraphysiologic rhBMP-2 doses administered locally during surgery, which can trigger a severe local inflammatory response and may result in a subset of these complications, such as cystlike bone osteolysis and soft-tissue swelling.^{7,8}

In this case series, we reviewed patients with epidural cyst formation and concurrent imaging findings after rhBMP-2-augmented lumbar spinal fusion who underwent postoperative MR imaging between 2016 and 2022.

Case Series

Ethics approval to retrospectively review clinical, pathologic, and imaging findings was obtained from the local institutional review board. Patients with postoperative MR imaging who underwent lumbar spinal fusion and decompression surgery with rhBMP-2 bone grafting (Infuse Bone Graft; Medtronic) were retrospectively identified. A consensus interpretation was established regarding the presence of epidural cysts/fluid collections and concurrent imaging findings on the postoperative lumbar spine (L-spine) MR imaging between a board-certified radiologist with a Certificate of Added Qualification in neuroradiology (J.L.C. with 15 years of experience) and a radiology resident (F.A. with 3 years of experience). We collected 16 patients (mean age, 60.1 [SD, 7.7] years; mean body mass index, 25.8 [SD, 3.7] kg/m²; 7 women) between 2016 and 2022. Preoperative indications for surgery consisted of

Received October 25, 2022; accepted after revision January 27, 2023.

From the Departments of Radiology and Imaging (F.A., E.T.T., D.B.S., J.L.C.) and Spine Surgery (F.A., D.R.L.), Hospital for Special Surgery, New York, New York.

Drs Lebl and Abel received research support from the Rama and Shashi Marda Foundation.

Please address correspondence to J. Levi Chazen, MD, Department of Radiology and Imaging, Hospital for Special Surgery, 535 E 70th St, NY, NY 10021; e-mail: chazenjl@hss.edu



Indicates article with supplemental online video.

<http://dx.doi.org/10.3174/ajnr.A7799>

Table 1: Patients with epidural cysts after use of rhBMP-2

Patient	Age (yr)	Diagnosis	Interval MR Imaging (days)	Procedure	Levels
1	49	Congenital spinal stenosis	253	TLIF + laminotomy	L4–L5
2	56	Degenerative spinal stenosis	161	XLIF + TLIF	L3–L5
3	52	Degenerative spondylolisthesis	204	ALIF	L4–L5
4	71	Lumbosacral radiculopathy	70	XLIF	L2–L3
5	62	Lumbosacral radiculopathy	119	ALIF	L5–S1
6	57	Isthmic spondylolisthesis	101	PLIF + laminectomy	L4–S1
7	60	Lumbosacral radiculopathy	35	TLIF + laminectomy	L4–L5
8	60	Pseudoarthrosis	480	TLIF	L4–L5
9	64	Lumbosacral radiculopathy	465	XLIF	L3–L5
10	51	Degenerative spinal stenosis	202	LLIF	L3–L5
11	73	Degenerative spinal stenosis	61	XLIF + laminectomy	L3–L4
12	49	Degenerative spinal stenosis	19	PLIF + laminectomy	L5–S1
13	61	Scoliosis	37	XLIF + PLIF	L4–S1
14	58	Degenerative spinal stenosis	60	XLIF + PLIF + laminectomy	L4–S1
15	71	Lumbosacral radiculopathy	38	PLIF + laminectomy	L3–L5
16	68	Degenerative spinal stenosis	134	TLIF	L4–L5



FIG 1. Images in a 56-year-old woman approximately 5 months following BMP-augmented extreme lateral and transforaminal lumbar interbody fusion of L3–L5 with persistent left-sided L5 radiculopathy. A, Sagittal T1-weighted MR image of the lumbar spine demonstrates a hypointense epidural collection at L5 (arrow). B, Corresponding sagittal STIR MR image shows the epidural cyst at L5 (black arrow), cystic osteolysis of the L4 and L5 vertebral bodies (white arrows), with endplate edema signal (arrowheads) and postoperative changes. C, Axial T2-weighted image at L5 (blue dashed line, A) illustrates the cyst (dashed black arrow) with the fluid-fluid level that narrows the left subarticular recess. Note the connection of the cyst to the bone resorptions within the vertebral body (arrowheads) and the discontinuity of the posterior longitudinal ligament (white arrow).

manifestations of lumbosacral spondylosis including lumbosacral radiculopathy and spinal stenosis (Table 1). The most common fusion procedure performed was a lateral/extreme lateral interbody fusion (LLIF/XLIF, $n = 7/16$), and the mean number of instrumented levels was 1.4 (SD, 0.6). Approximately 60% (10/16) of patients had a history of fusion or decompression surgery. In all cases, rhBMP-2 was packed centrally into the intervertebral implant in the form of absorbable collagen sponges with doses ranging from 1.05 to 4.2 mg (range, 1.4–2.8 mL) per patient. In 2 patients, rhBMP-2 was additionally distributed between the transverse processes to enhance posterolateral fusion. MR imaging was performed for ongoing or new lumbosacral pain or radiculopathy. Follow-up MR imaging (median days postsurgery: 152 [IQR, 148]) was acquired for each case using a standard-of-care protocol with conventional sequences, including axial, coronal, and sagittal T2-weighted pulse sequences and a sagittal T1-weighted and sagittal STIR sequence.

All patients demonstrated expansile cystic lesions within the lumbar epidural region located between the thecal sac and the intervertebral rhBMP-2-augmented graft. The epidural lesions had a characteristic MR imaging appearance with well-defined,

occasionally lobulated T2-weighted hyperintense cysts. In 9 patients (56%), the cysts demonstrated internal T2-weighted hypointense fluid-fluid levels that gravitated and settled dependently, while MR imaging was acquired with the patient in a supine position. For all patients, a communication of the epidural collections with vertebral body resorptions adjacent to the graft was identified (Fig 1). The cysts were solitary in 1-level spinal instrumentations and limited to the level of the rhBMP-2 graft; however, in 3 patients (19%) with multi-level instrumentation, the epidural cystic lesions were distributed across >1 spinal level. Mass effect on the thecal sac and neural elements was observed in 8 patients (50%). Depending on the size and location of the epidural cysts, mass

effect was exerted on exiting roots within the neuroforamen, traversing roots within the subarticular recess, or the thecal sac within the spinal canal.

Patient 1 presented with worsening back pain after undergoing rhBMP-2-enhanced transforaminal lumbar interbody fusion (TLIF), with left-sided decompression at L4–L5 approximately 8 months ago. The L-spine MR imaging revealed an epidural fluid collection with a fluid-fluid level that filled the laminotomy defect and abutted the L4 nerve, causing moderate-to-severe foraminal stenosis (Fig 2). Ongoing symptoms of L4–L5 lumbosacral radiculopathy required revision surgery with resection of the cyst. Intraoperatively, the cyst presented with a thick pseudocapsule and serosanguineous fluid (Online Video). The pathologic report of the specimen showed reactive woven bone formation with a cystic lining. Notably, there were no significant features of inflammation, and the microbiologic culture showed no growth.

Most commonly, the formation of epidural cysts resulted in mass effect on the lateral recess of the descending nerve roots at the level of the intervertebral rhBMP-2 graft, which was identified in 5 patients (patients 2, 6, 7, 14, and 16). Among these, patient

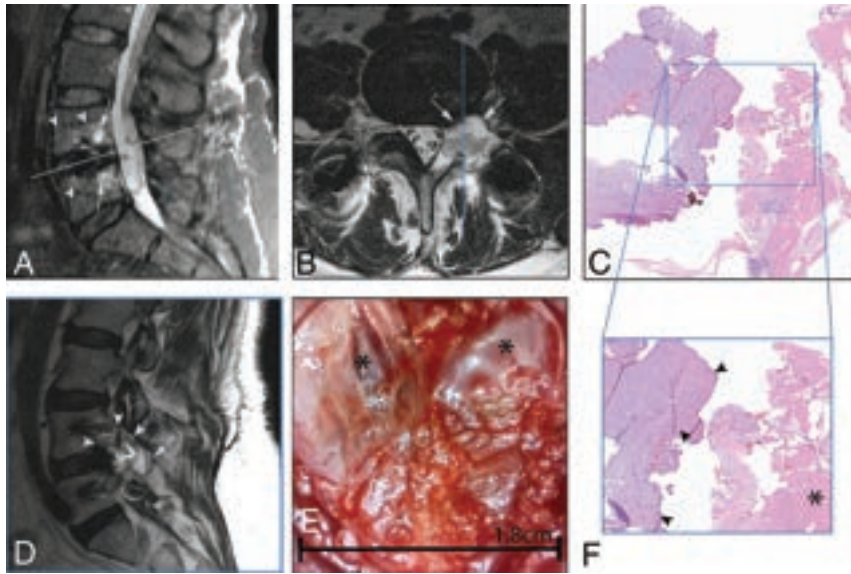


FIG 2. Images in a 49-year-old woman following transforaminal lumbar interbody fusion and left-sided laminotomy of L4–L5 with BMP grafting approximately 8 months ago and new-onset left-sided L4–L5 radiculopathy. *A*, Sagittal STIR MR image demonstrates a BMP graft with adjacent osteolysis (*arrows*) and endplate edema signal (*arrowheads*). *B*, Axial T2-weighted MR image at L4–L5 (*dashed line*, *A*) shows a left-sided epidural cyst (*arrows*) with a fluid-fluid level. *D*, Parasagittal T2-weighted MR image at the level of the left laminotomy (*dashed blue line*, *B*) illustrates the epidural cyst (*arrow*) that fills the decompression defect and causes moderate-to-severe foraminal stenosis at L4–L5 (*arrowheads*). *E*, Intraoperative photo of the serous cystic structure shows a thick pseudocapsule (*asterisks*). *C* and *F*, Histopathologic specimen (magnification factor, 1.6×/4×, respectively) demonstrates fragments of the thin fibrous cystic lining (*arrowheads*, *F*) and a segment of woven bone formation with chondrocytic metaplasia (*asterisk*, *F*).

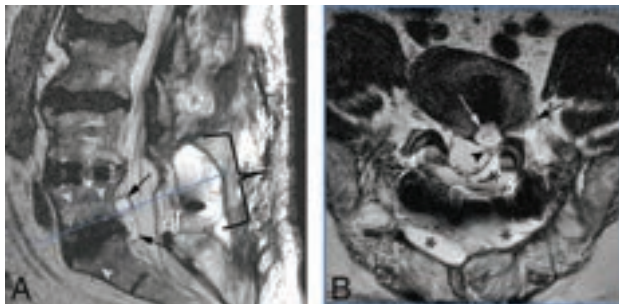


FIG 3. MR images in a 58-year-old man 2 months following BMP-augmented combined extreme lateral and posterior lumbar interbody fusion with laminectomy of L4–S1 and new-onset left foot drop. *A*, Sagittal T2-weighted MR image shows a lobulated epidural cyst at L5–S1 dorsal to the BMP graft (*black arrows*), endplate edema signal of the adjacent endplates (*arrowheads*), and the laminectomy defect with seroma formation (*bracket*). *B*, Axial T2-weighted MR image at L5–S1 (*dashed blue line*, *A*) demonstrates the left subarticular, epidural cyst (*white arrow*) adjacent to the BMP graft, abutting the left descending S1 nerve root (*arrowhead*) and the left exiting L5 nerve root (*black arrow*). Concomitant seroma is present and fills the laminectomy defect (*asterisks*).

14 demonstrated epidural cystic collections, extending from L5–S1 along the surgical corridor 60 days after combined extreme and posterior lumbar interbody fusion (XLIF + PLIF) of L4–S1 with laminectomy (Fig 3). The patient developed a new left foot drop and was diagnosed with an L5 radiculopathy with active denervation by electrophysiology. However, conservative management

was successful, and the symptoms subsided. The cysts nearly resolved on the follow-up study 79 days later.

Patients 2, 6, 7, and 14 presented with varying degrees of lumbosacral radiculopathy that was treated with epidural injections but did not require revision surgery. For these patients, a correlating single-level cyst located within the ventrolateral epidural space was observed on L-spine MR imaging postoperatively, exerting mild mass effect on the traversing L5 or S1 nerve roots.

For 2 patients (patients 13 and 15), mild compressions of the thecal sac caused by single-level, ventral epidural collections were reported on L-spine MR imaging. In these cases, the epidural cysts did not affect the clinical course, and both patients had a good recovery.

The remaining 8 patients (50%) with epidural cystic formations but without signs of mass effect had an uneventful clinical course without cyst-related complications such as new onset of radiculopathy or the need for revision surgery. Patient 9, however, developed a new left-sided foot drop that was likely caused by a focal, heterotopic calcifica-

tion adjacent to the rhBMP-2 graft that extended into the outer portion of the L3–L4 foramen and caused compression of the L3 nerve. The patient underwent a revision decompression with relief of the foot drop.

Concurrent imaging findings are depicted in Table 2 and comprised postoperative changes, including soft-tissue/muscle edema and seromas. Edema-like marrow signal of the vertebral endplates adjacent to the BMP grafts, indicated by T2-weighted hyperintense endplate signal, was present in all patients except patients 8 and 9 who underwent a comparatively late follow-up MR imaging at 480 and 465 days, respectively. Bone resorptions/osteolysis, not exceeding the cortical margins of the vertebral bodies, were observed in 11 patients (69%), of whom 5 patients had T2-weighted hypointense fluid-fluid levels, similar to the epidural cysts.

DISCUSSION

This case series described formation of epidural cysts as a complication following rhBMP-2-augmented lumbar spinal fusion and decompression surgery. The popularity of rhBMP-2 in spinal fusion has grown since clinical approval in 2002, and its application reached a peak in 2010, accounting for approximately 30% of all spinal fusions performed in the United States.² Since then, mounting reports about adverse events and a warning issued by the FDA in 2008 related to BMP use in off-label anterior cervical spine surgery eventually initiated a trend reversal.⁶ Nevertheless, widespread use has resumed since, and the volume of BMP procedures may increase in the future.⁹ In our institution, rhBMP-2

Table 2: Concurrent imaging findings on the postoperative MRIs

Finding	No. of Cases	%
Epidural cysts with mass effect	8/16	50
Epidural cysts without mass effect	8/16	50
Bone resorptions/osteolysis	11/16	69
Endplate marrow, edema	14/16	88
Seroma	11/16	69

is readily applied in most lumbar fusion procedures at the discretion of the spinal surgeon and in the context of informed decision-making (because most indications remain off-label), often in patients with prior spinal surgery or risk factors for pseudoarthrosis. Previously described complications include radiculitis, graft subsidence, and pronounced vertebral bone resorption/osteolysis, which may be linked to the inherent inflammatory potential of rhBMP-2 with release of several inflammatory metabolites such as interleukins or tumor necrosis factor.^{10,11}

Epidural cysts, as identified in our 16 patients, are a rarely reported complication in the literature, and their incidence remains elusive. In a prospective study, Mannion et al¹² observed epidural cyst formation in 2/30 (6.7%) patients following TLIF or PLIF with rhBMP-2, one of whom required re-intervention. Additionally, epidural cysts have been described in case reports after rhBMP-2 use in lumbar fusion.^{13,14} In both reports, the cysts had an appearance similar that of most cysts in our series, exhibiting T2-hypointense fluid-fluid levels. The cyst described in the case report by Choudhry et al¹⁴ required decompression due to the patient's radiculopathy, and the pathologic specimen revealed parts of the rhBMP-2 absorbable collagen sponge with infiltration of inflammatory cells. The authors, therefore, concluded that the cystic formation may have resulted from an inflammatory response to bone resorption caused by an extruded and overpacked rhBMP-2 sponge. Varying degrees of bone resorptions are frequently observed following rhBMP-2 grafting in vivo, particularly within the first 3 months after the operation.¹⁵ This paradoxical effect of bone catabolism rather than anabolism is attributed to stimulation of both osteoblasts and osteoclasts by supraphysiologic concentrations of rhBMP-2 and may lead to unwanted bone resorptions.¹⁶

The histopathologic specimen of the resected epidural cyst in our patient revealed a cystic lining with neovascularization and reactive woven bone that was compatible with heterotopic ossification with cystic change and likely associated with rhBMP-2 use. Heterotopic ossification is a more frequently reported complication of rhBMP-2, and varying degrees of ectopic bone formation may be observed in up to 75% of patients following lumbar fusion.¹⁷ Heterotopic ossifications result from BMP leaking out of the disc space, and occasionally, focal ectopic ossifications cause severe clinical symptoms such as radiculitis and require surgical excision.¹⁸ In one of our patients, we noted focal ectopic ossification within the L3–L4 foramen, causing radiculopathy and needed revision surgery to relieve symptoms.

Mass effect of the epidural cysts on the thecal sac or nerve roots was observed in 50% of the postoperative MRIs in our cohort. Of these, 6 patients developed radiculopathy that was managed conservatively, and 1 patient required re-exploration to

relieve radiculopathy. Notably, all of the patients with symptomatic mass effect of epidural cysts underwent either a TLIF or PLIF. Both methods may require partial dissection of the posterior longitudinal ligament (PLL) to approach the intervertebral disc space.¹⁹ Communication of the epidural cysts with bone osteolysis adjacent to the grafts was visualized in all cases, and partial discontinuity of the PLL could be identified in all TLIF and PLIF cases. Therefore, epidural cysts may result from vertebral bone osteolysis with secondary extrusion through defects in the PLL or from BMP extending from the interbody space to induce epidural cyst formation, ultimately causing compression of the traversing or exiting nerve roots.

Conversely, as part of ALIF procedures, the PLL is semi-circumferentially maintained and the epidural space is not exposed, possibly preventing cyst formation. Strategies to avoid occurrence of epidural cysts may be accomplished by central positioning of the rhBMP-2-packed interbody graft, effort to preserve parts of the PLL during PLIF/TLIF, or removal of redundant rhBMP-2 around the graft. However, future studies are warranted that systematically investigate a potential association of epidural cysts with the surgical techniques and strategies to avoid them in lumbar fusions, with particular attention paid to the anatomic direction of the surgical approach.

The management of epidural cysts after rhBMP-2-augmented lumbar fusion is not clearly defined in the literature due to the rare occurrence. Options include conservative treatment with medical therapy and injections, CT-guided aspiration, or surgical decompression. Observation may be the preferred approach because only 1 patient in our cohort required a revision surgery, and in most cases, the radiculopathy resolved during the clinical course. In 3 patients, the cysts maintained their size, and in 2 patients, the epidural cysts decreased on the follow-up MR imaging. However, for most of the patients, no second study was available to evaluate the evolution of the cysts, but adequate recovery suggests there was no symptomatic enlargement.

CONCLUSIONS

Epidural cyst formation after rhBMP-2 use in lumbar spinal fusion is a potential complication with characteristic imaging findings for radiologists to be aware of for appropriate diagnosis and treatment of affected patients.

Disclosure forms provided by the authors are available with the full text and PDF of this article at www.ajnr.org.

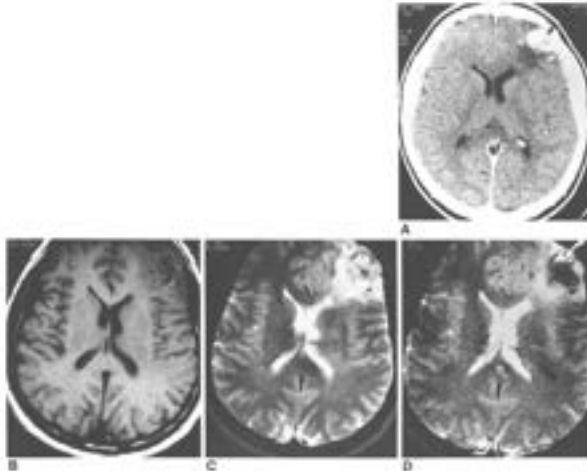
REFERENCES

1. Urist MR. **Bone: formation by autoinduction.** *Science* 1965;150:893–99 CrossRef Medline
2. Kerezoudis P, Alvi MA, Freedman BA, et al. **Utilization trends of recombinant human bone morphogenetic protein in the United States.** *Spine (Phila Pa 1976)* 2021;46:874–81 CrossRef Medline
3. Liu Z, Zhou B, Chen L, et al. **Bone morphogenetic protein-2 against iliac crest bone graft for the posterolateral fusion of the lumbar spine: a meta-analysis.** *Int J Clin Pract* 2021;75:e13911 CrossRef Medline
4. Liu S, Wang Y, Liang Z, et al. **Comparative clinical effectiveness and safety of bone morphogenetic protein versus autologous iliac crest bone graft in lumbar fusion: a meta-analysis and systematic review.** *Spine (Phila Pa 1976)* 2020;45:E729–41 CrossRef Medline

5. Guzman JZ, Merrill RK, Kim JS, et al. **Bone morphogenetic protein use in spine surgery in the United States: how have we responded to the warnings?** *Spine J* 2017;17:1247–54 CrossRef Medline
6. Carragee EJ, Hurwitz EL, Weiner BK. **A critical review of recombinant human bone morphogenetic protein-2 trials in spinal surgery: emerging safety concerns and lessons learned.** *Spine J* 2011;11:471–91 CrossRef Medline
7. Zara JN, Siu RK, Zhang X, et al. **High doses of bone morphogenetic protein 2 induce structurally abnormal bone and inflammation in vivo.** *Tissue Eng Part A* 2011;17:1389–99 CrossRef Medline
8. Shields LB, Raque GH, Glassman SD, et al. **Adverse effects associated with high-dose recombinant human bone morphogenetic protein-2 use in anterior cervical spine fusion.** *Spine (Phila Pa 1976)* 2006;31:542–47 CrossRef Medline
9. Dietz N, Sharma M, Kelly M, et al. **Recombinant human bone morphogenetic protein-2 use in adult spinal deformity surgery: comparative analysis and healthcare utilization at 24 months' follow-up.** *Global Spine J* 2022;12:92–101 CrossRef Medline
10. Nguyen V, Meyers CA, Yan N, et al. **BMP-2-induced bone formation and neural inflammation.** *J Orthop* 2017;14:252–56 CrossRef Medline
11. Lee KB, Taghavi CE, Murray SS, et al. **BMP induced inflammation: a comparison of rhBMP-7 and rhBMP-2.** *J Orthop Res* 2012;30:1985–94 CrossRef Medline
12. Mannion RJ, Nowitzke AM, Wood MJ. **Promoting fusion in minimally invasive lumbar interbody stabilization with low-dose bone morphogenetic protein-2: but what is the cost?** *Spine J* 2011;11:527–33 CrossRef Medline
13. Baron EM, Mejia DM, Drazin D, et al. **Postoperative cyst associated with bone morphogenetic protein use in posterior and transforaminal lumbar interbody fusion managed conservatively: report of two cases.** *Cureus* 2016;8:e485 CrossRef Medline
14. Choudhry OJ, Christiano LD, Singh R, et al. **Bone morphogenetic protein-induced inflammatory cyst formation after lumbar fusion causing nerve root compression.** *J Neurosurg Spine* 2012;16:296–301 CrossRef Medline
15. Sethi A, Craig J, Bartol S, et al. **Radiographic and CT evaluation of recombinant human bone morphogenetic protein-2-assisted spinal interbody fusion.** *AJR Am J Roentgenol* 2011;197:W128–33 CrossRef Medline
16. Bordukalo-Nikšić T, Kufner V, Vukicōević S. **The role of BMPs in the regulation of osteoclasts resorption and bone remodeling: from experimental models to clinical applications.** *Front Immunol* 2022;13:869422 CrossRef Medline
17. Haid RW, Branch CL, Alexander JT, et al. **Posterior lumbar interbody fusion using recombinant human bone morphogenetic protein type 2 with cylindrical interbody cages.** *Spine J* 2004;4:527–38 CrossRef Medline
18. Chrastil J, Low JB, Whang PG, et al. **Complications associated with the use of the recombinant human bone morphogenetic proteins for posterior interbody fusions of the lumbar spine.** *Spine (Phila Pa 1976)* 2013;38:E1020–27 CrossRef Medline
19. Mobbs RJ, Phan K, Malham G, et al. **Lumbar interbody fusion: techniques, indications and comparison of interbody fusion options including PLIF, TLIF, MI-TLIF, OLIF/ATP.** *J Spine Surg* 2015;1:2–18 Medline

Celebrating 35 Years of the AJNR

March 1988 edition



Calcified Intracranial Lesions: Detection with Gradient-Echo-Acquisition Rapid MR Imaging

Scott W. Atlas,¹ Robert L. Grossman,¹ David B. Reardon,¹ John M. Garcia,¹ Nicholas Capaniga,¹ Herbert I. Goldberg,¹ Larissa T. Sklar,¹ Robert A. Zimmerman¹

Brainstem patients with primary intracranial lesions, as demonstrated by CT, were evaluated with MR imaging at 1.5 T. All patients were imaged with both conventional spin-echo techniques and reduced flip-angle gradient-echo acquisition (GEA) sequences during which a signal is acquired in the absence of a 90° radiofrequency pulse. GEAs parameters were implemented so that T2* effects were minimized in these scans. In all 17 patients GEA images showed superior sensitivity throughout the entire area of calcification, including the calcified regions as seen on CT. In contrast, spin-echo findings in the calcified portions of the scans were extremely variable, precluding accurate identification of calcification in these images. The detection of regions of calcification as marked hyperintensity on GEA images correlates well with T2* shortening from acute focal magnetic field gradients at interfaces of regions differing in magnetic susceptibility, a phenomenon that is well documented in steel, when ferromagnetic objects are placed in magnetic suspensions. However, we cannot exclude the possible additional role of accompanying paramagnetic ions, which sometimes are present with demagnetically calcified cells in certain intracranial calcifications. Since the hyperintensity due to calcification on GEA images is not specific, shortened T2* would be used to confirm its presence.

Although the lack of specificity and the artifacts that obscure true demagnetically calcified areas in spin-echo techniques somewhat limit the application of GEA techniques, we suggest that rapid MR imaging using GEA sequences can routinely identify demagnetically intracranial calcification, and that this technique may serve as a useful adjunct to conventional spin-echo imaging.

Although spin-echo (SE) MR imaging has rapidly evolved into the most sensitive imaging technique for detection of intracranial disease (1, 2), one of its deficiencies lies in its well-recognized inability to detect calcification consistently (3-6). Since the detection of calcification within certain intracranial lesions can provide important differential information, and because CT is highly sensitive for calcification, this has been regarded as a limitation of MR, both as a screening test for certain diseases and as an aid to specific diagnosis.

Recently, investigators have used gradient-echo signal acquisition (GEA) rather than conventional SE techniques to maximize the detection of lesions having magnetic susceptibility differences from T2* effects. Due to static field gradients created by these susceptibility differences and by imperfect 180° refocusing pulses used in SE sequences (3-6), this technique has been especially useful in demonstrating previously undetectable signal intensity information from SE MR imaging in the case of metal shrapnel (3, 4). Furthermore, it is well documented in steel that the introduction of various particulate solids into suspension creates static magnetic susceptibility gradients that change with local magnetic field inhomogeneity, and consequently shorten T2* (3, 4). Early in our experimental work with reduced flip-angle GEA rapid MR imaging, we noted that calcified intracranial lesions were consistently and markedly hyperintense on GEA images, whereas these same areas were usually not detected by SE images (Fig. 1). This observation prompted

This article appears in the December 1988 issue of AJNR and the June 1989 issue of JAMA.
Received June 15, 1988; accepted after revision December 10, 1988.
Reprinted by permission of the American Society of Neuroradiology, New York, NY, 1988.
Reprints: Department of Radiology, University of Pittsburgh Medical Center, 3535 La Fayette Ave., Pittsburgh, PA 15261.
Address reprint requests to Dr. Atlas.
© 1988 American Society of Neuroradiology.
AJNR 9:100-104, December 1988.
0195-9581/88/090100-05\$03.00/0

MR Imaging of Cerebellopontine Angle and Internal Auditory Canal Lesions at 1.5 T

Gary A. Press,¹ John H. Peckner¹

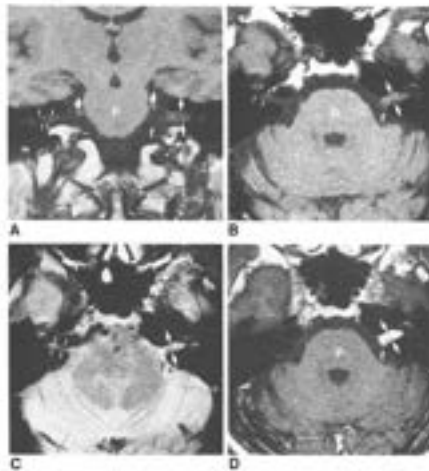
The high-field, low-noise (2-5 tesla) MR imaging characteristics of the cerebellopontine angle and internal auditory canal lesions were assessed. The dynamic characteristics of acoustic neuromas, eighth nerve schwannomas, and other cranial lesions including the fifth cranial nerve and the vestibular nerve (V-VII), spinal meningiomas, the vestibular fold collections, four trigeminal neurons with complete trigeminal, most geniculate ganglion, and spinal trigeminal, and six facial artery aneurysms, V-VII, and posteriorly weighted images were obtained in all cases. T1-weighted images most accurately showed the margins of the cerebellum and eighth nerve in the internal auditory canal and were most sensitive in detecting small lesions in the cerebellopontine angle. Differentiation of meningiomas from acoustic neuromas by MR was provided most reliably by acquisition of the meningioma from the same direction and seventh and eighth nerves and not by digital-selective techniques. A hyperintense capsule was seen as MR in seven of 10 demagnetically calcified lesions and in three of seven meningiomas.

Recent reports of MR imaging of the normal anatomy and of lesions of the cerebellopontine angle (CPA) and internal auditory canal (IAC) at low (1-4) and moderate (5, 6-8) magnetic field strengths have been most encouraging. Absence of spin-holding artifacts, multiphase imaging capabilities, and greater tissue soft-tissue contrast are emphasized as significant advantages of MR imaging relative to high-resolution CT in the assessment of lesions of the CPA and IAC. MR at 1.5 T has an advantage over CT in the diagnosis of all sizes of acoustic tumors (7). The ability to demonstrate the normal contents of the IAC, to facilitate differentiation of acoustic tumors from meningiomas and other lesions originating in the CPA (8, 9), and to also conduct the diagnostic study of lesions for the evaluation of patients with suspected acoustic neuromas (3, 4, 6).

These reports of high-field strength (2-5 T) MR of the CPA and IAC included only a few abnormal patients (10), described very small or infraclinically lesions (7), or combined results of numerous (2, 5) and high-field strength imaging with 1.5-tesla data (10). In this report, the results of a large series of patients with diverse abnormalities of the CPA and IAC imaged exclusively at a high field strength with this technique (2-5 tesla).

Materials and Methods

We evaluated retrospectively 1000 consecutive brain MR examinations and identified 22 patients with CPA and IAC lesions. Multiple lesions were found in five patients with known demagnetically calcified lesions. One additional patient without demagnetically calcified lesions, the patients were 5-70 years old. 18 were females and 4 were males. The demagnetically calcified lesions included, eight additional eighth nerve tumors (the remaining seven were 4 and had findings similar to 10), seven meningiomas, five trigeminal ganglion lesions, four vestibular fold collections, four trigeminal ganglion lesions, three geniculate ganglion lesions, and spinal trigeminal and six facial artery aneurysms. Four patients with intracanalicular



This article appears in the December 1988 issue of AJNR and the June 1989 issue of JAMA.
Received July 15, 1988; accepted after revision October 1, 1988.
Reprints: Department of Radiology, University of Pittsburgh Medical Center, 3535 La Fayette Ave., Pittsburgh, PA 15261.
Address reprint requests to Dr. Press.
© 1988 American Society of Neuroradiology.
AJNR 9:100-104, December 1988.
0195-9581/88/090100-05\$03.00/0

This erratum corrects the article “Multivariate Analysis of MRI Biomarkers for Predicting Neurologic Impairment in Cervical Spinal Cord Injury” (J. Haefeli, Mabray MC, Whetstone WD, et al. *AJNR Am J Neuroradiol* 2017;38:648–55 10.3174/ajnr.A5021).

In the original publication, there was an error in the Materials and Methods section on page 649 under the Image Analysis heading related to a description of the Brain and Spinal Injury Center (BASIC) score grading, which erroneously included a description of 6 distinct grades. The corrected version of text for this section is below and describes the correct 5 grades (grade 0 through grade 4) composing the BASIC score.

A neuroradiology fellow (M.C.M.) and attending physician (J.F.T.) performed consensus MR imaging ratings for all metrics while blinded to clinical outcome. The interrater reliability and BASIC axial MR imaging grading have been previously described as follows:^{4,30} grade 0, no cord signal abnormality; grade I, T2 hyperintensity confined to GM; grade II, intramedullary T2 hyperintensity extending beyond the expected gray matter margins to involve spinal white matter but not involving the entire transverse extent of the spinal cord; grade III, T2 hyperintensity involving the entire axial plane of the spinal cord; grade IV, grade III injury with the addition of foci of T2 hypointensity consistent with hemorrhage. Sagittal grading was assigned as previously described as follows: grade I, no spinal cord signal abnormality; grade II, single-level T2 hyperintensity; grade III, >1 vertebral-level T2 signal hyperintensity; grade IV, T2 signal hyperintensity with areas of hypointensity representing hemorrhage.^{1,19} The greatest length (millimeters) of injury on sagittal T2 was measured as described in the National Institutes of Health/National Institute of Neurological Disorders and Stroke SCI Common Data Elements, Version 1.0.³ Maximum canal compromise (MCC) and maximum spinal cord compression (MSCC) assessed midsagittal images by dividing the anterior-posterior diameter of the canal (on sagittal T1 for MCC) and the anterior-posterior diameter of spinal cord (on sagittal T2 for MSCC) by the average of the canal or spinal cord above and below as previously described.^{8,15,16,22}

The authors regret this error.

<http://dx.doi.org/10.3174/ajnr.A7797>

Myelographic Timing Matters

We read with great interest the article by Huls et al¹ titled, “Utility of Dual-Energy CT to Improve Diagnosis of CSF Leaks on CT Myelography following Lateral Decubitus Digital Subtraction Myelography with Negative Findings.” The authors report that dual-energy CT myelography (CTM) aided in the detection of subtle CSF leaks after normal findings on decubitus digital subtraction myelography (DSM) and suggested that dual-energy CTM may serve as another diagnostic tool in certain patients with CSF leaks that are difficult to detect.

While further use of dual-energy CT may indeed show some additional benefit in the diagnosis of a spinal CSF leak, the timing of the myelographic examination with respect to the injection of contrast is important in CSF leak detection and was not well-addressed in the article. For CSF-venous fistulas, prompt imaging after the contrast injection is paramount; delayed imaging is not helpful.² In our experience using decubitus CTM, delayed scanning even a few minutes after the contrast injection can fail to show the CSF-venous fistula.³ The authors describe how dual-energy CTM was performed after the DSM examination; there is undoubtedly more than a few minutes between examinations, and we suspect that this lapsed time is an important limitation of the examination. None of the CSF-venous fistulas shown in the examples demonstrate a full venous course, just small foci of enhancement. In addition, it is difficult to confidently distinguish which type of spinal CSF leak (dural tear, ruptured meningeal diverticulum, or CSF-venous fistula) is shown in these images. If this dual-energy CTM were performed in a dedicated fashion immediately after the contrast injection instead of the DSM, perhaps the findings would have been more conspicuous and would have more definitively guided treatment. We recognize that the authors primarily relied on DSM for CSF-venous fistula evaluation and that this post-DSM CTM serves as an adjunctive tool.

The authors’ study also raises a larger question of the sensitivity and specificity of CSF leak detection between decubitus CTM and decubitus DSM, particularly for CSF-venous fistula evaluation. We recognize that this issue was not the intent of the study, but it does generate discussion. To date, there are no direct comparisons between the 2 techniques, and most centers perform one or the other, depending on operator preference and equipment

availability.² While performing a study comparing the 2 techniques would be cumbersome and result in excess radiation to patients undergoing up to 4 myelographic examinations (2 CTMs and 2 DSMs to image both sides of spine well), the results could potentially lead to a paradigm shift in the spinal CSF leak evaluation. In the absence of a study and in a patient with a high suspicion for CSF-venous fistula and negative findings on decubitus DSM or CTM, it may be beneficial to try the other technique to improve detection. This complementary role of dedicated decubitus DSM and CTM examinations may help in patients with elusive spinal CSF leaks.

In summary, the timing of the myelographic examination with respect to the contrast injection plays a key role in the detection of spinal CSF leaks. Further studies are needed to compare CTM, DSM, and the adjunctive role of dual energy.

Disclosure forms provided by the authors are available with the full text and PDF of this article at www.ajnr.org.

REFERENCES

1. Huls SJ, Shlapak DP, Kim DK, et al. **Utility of dual-energy CT to improve diagnosis of CSF leaks on CT myelography following lateral decubitus digital subtraction myelography with negative findings.** *AJNR Am J Neuroradiol* 2022;43:1539–43 CrossRef
2. Kranz PG, Gray L, Malinzak MD, et al. **CSF-venous fistulas: anatomy and diagnostic imaging.** *AJR Am J Roentgenol* 2021;217:1418–29 CrossRef Medline
3. Mamlouk MD, Ochi RP, Jun P, et al. **Decubitus CT myelography for CSF-venous fistulas: a procedural approach.** *AJNR Am J Neuroradiol* 2021;42:32–36 CrossRef Medline

● M.D. Mamlouk

Department of Radiology, The Permanente Medical Group
Kaiser Permanente Medical Center, Santa Clara
Santa Clara, California

Department of Radiology and Biomedical Imaging
University of California, San Francisco
San Francisco, California

● P.Y. Shen

Department of Radiology, The Permanente Medical Group
Kaiser Permanente Medical Center, Santa Clara
Santa Clara, California

REPLY:

Thank you for such a thoughtful and timely letter. It certainly brings up important and actively researched points of myelographic contrast timing and the preferred study for CSF leak detection (particularly, CSF-venous fistulas).

We do agree with Drs Mamlouk and Shen on the importance of prompt imaging after contrast injection for CSF-venous fistula localization and further evaluation of sensitivity and specificity for this type of CSF leak detection with lateral decubitus CT myelography (CTM) versus lateral decubitus digital subtraction myelography (DSM). We would like to clarify, though, that our article was not investigating these issues, but rather addressing contrast conspicuity at different energy levels and the utility of dual-energy CT for CSF leak visualization.

We concur that preferred studies and even techniques for CSF-venous fistula localization vary among institutions and are usually based on institutional and proceduralist preference, comfort level, and study familiarity. We also agree with the authors of the letter that in patients with a high suspicion of a CSF-venous fistula and negative findings on lateral decubitus DSM or lateral decubitus CTM, it may be beneficial to pursue the other technique to improve leak detection. At our institution, for example, while we do perform dynamic lateral decubitus CTMs in select

patients (usually with previous negative findings on lateral decubitus DSM), our initial study for CSF leak investigation in patients without extradural spinal fluid remains lateral decubitus DSM. DSM is then followed by the dual-energy CTM with the patient in the same lateral decubitus position, usually approximately 15–20 minutes after the DSM.

Given the potential intermittent nature of the CSF-venous fistulas, in our experience, this as well as other types of CSF leaks are sometimes only or better visualized on the post-DSM dual-energy CTM (particularly on 50-keV virtual monoenergetic images), which was the focus of our article. Therefore, while efforts evaluating the sensitivity and specificity of lateral decubitus DSM versus lateral decubitus CTM for CSF-venous fistula detection continue, if CT myelography (immediate dynamic or delayed as described in our article) is pursued, proceduralists should consider dual-energy CT for optimal extradural contrast visualization.

Thank you again for your letter and the effort to improve patient care in this rapidly evolving field.

● **S.J. Huls**
● **D.P. Shlapak**
● **D.K. Kim**
● **S. Leng**
● **C.M. Carr**

Department of Radiology
Mayo Clinic, Ringgold Standard Institution
Rochester, Minnesota

<http://dx.doi.org/10.3174/ajnr.A7803>

Correlation between Sagittal Angle of the Trigeminal Nerve and the Grade of Neurovascular Conflict

We read with interest the recent article by Branstetter et al¹ describing the sagittal angle of the trigeminal nerve at the porus trigeminus in the setting of trigeminal neuralgia (TN). The study found that a small subset of patients (17%) with TN had angles that were more acute at the entry of the ipsilateral trigeminal nerve into the Meckel cave compared with controls and the unaffected contralateral side. The authors suggested that such aberrant anatomy may be associated with symptoms and that these patients could potentially benefit from an operation other than microvascular decompression (MVD). We find this concept novel, but we also believe that the readers should take home the message presented in this article with a few important caveats.

During the past 2 decades, several studies have been published discussing the MR imaging characteristics of the trigeminal nerve and its relevance to prognostication. We now understand that neurovascular conflict is present in an overwhelming majority (95%) of patients with TN.² Such neurovascular conflict is routinely graded² in an increasing order of severity from minimal contact in grade I, to distortion in grade II, and marked indentation of the nerve in grade III. In their series of 579 patients, Sindou et al² found that 33.2% of patients had marked indentation (grade III) with displacement of the trigeminal nerve; in other words, the affected nerves showed an altered course in one-

third of patients. Furthermore, Leal et al³ studied the impact of nerve atrophy and grades of conflict on clinical outcomes after MVD. They found that patients with higher grades of neurovascular conflict had a statistically significant response to MVD.³ All patients with grade III conflict in their study benefited from an operation; more important, none of the patients with persistent or recurrent symptoms had a grade III conflict. The authors thus concluded that MVD is the best treatment for patients with grade II and III neurovascular conflict; in other words, MVD is the best treatment for patients with an altered course of the affected trigeminal nerve.³

The present study by Branstetter et al¹ does not provide the grade of neurovascular conflict in the 17% of patients showing smaller angles at the Meckel cave. It is entirely plausible that all patients with smaller angles had grade II or III neurovascular conflict. Also, it is highly improbable that nerves with a smaller angle of entry showed a completely normal course and absent neurovascular conflict. Thus, we believe that this missing information about the grade of neurovascular conflict has a potential bearing on the measured angle and is therefore vital to any inference that one may draw from the study (Figure).

Last, the authors suggest that patients with an aberrant course of the nerve may potentially benefit from a different surgical procedure than MVD. This suggestion, if true, would be in contradiction

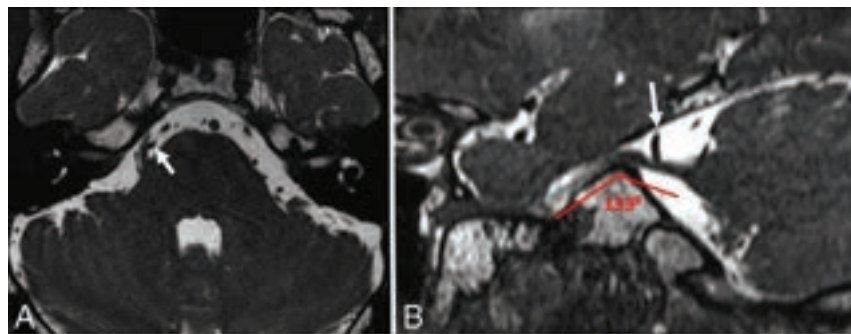


FIGURE. Sample measurement of the sagittal angle of the trigeminal nerve at the porus trigeminus (SATNaPT) in a 53-year-old man with right TN. A, Axial steady-state free precession (SSFP) MR image shows indentation and displacement of right trigeminal nerve (grade III) by the right superior cerebellar artery (white arrow). B, Sagittal SSFP image shows a SATNaPT of 133° with indentation on the right trigeminal nerve by the right superior cerebellar artery (white arrow).

to other larger and prospective studies such as by Leal et al,³ showing a statistically significant response to the exact same procedure in a similar cohort of patients.

Disclosure forms provided by the authors are available with the full text and PDF of this article at www.ajnr.org.

REFERENCES

1. Branstetter BF, Reddy N, Patel K, et al. **Sagittal angle of the trigeminal nerve at the porus trigeminus: a novel measurement to distinguish different causes of classic trigeminal neuralgia.** *AJNR Am J Neuroradiol* 2022;43:1460–63 CrossRef Medline
2. Sindou M, Howeidy T, Acevedo G. **Anatomical observations during microvascular decompression for idiopathic trigeminal neuralgia (with correlations between topography of pain and site of the neurovascular conflict): prospective study in a series of 579 patients.** *Acta Neurochir (Wien)* 2002;144:1–13 CrossRef Medline
3. Leal PR, Barbier C, Hermier M, et al. **Atrophic changes in the trigeminal nerves of patients with trigeminal neuralgia due to neurovascular compression and their association with the severity of compression and clinical outcomes.** *J Neurosurg* 2014;120:1484–95 CrossRef Medline

● P.P. Suthar
● K. Hughes
● M. Mafraji
● S.G. Dua

Department of Diagnostic Radiology and Nuclear Medicine
Rush University Medical Center
Chicago, Illinois

REPLY:

We wish to thank Dr Suthar and colleagues for their interest in our work¹ on the sagittal angle of the trigeminal nerve at the porus trigeminus (SATNaPT) in patients with classic trigeminal neuralgia (cTN). Suthar and colleagues correctly point out that the degree of neurovascular compression (NVC) is an important predictor of surgical outcome in patients with cTN. We agree; in fact, our own work on this topic² confirms the importance of the degree of NVC as an imaging biomarker. The article by Sindou et al³ as well as other intraoperative anatomic studies in patients with trigeminal neuralgia (TN) undergoing microvascular decompression⁴ likely overestimate the incidence and degree of NVC because CSF drainage during the operative approach draws the vasculature into further contact with the trigeminal nerve. Preoperative high-resolution MR imaging is probably better at determining the degree of NVC of the trigeminal nerve.^{2,5}

We did not intend to suggest that SATNaPT would replace the degree of NVC in the preoperative assessment of cTN. Rather, we believe that SATNaPT can be an additional biomarker that identifies a distinct subset of patients with cTN. Similarly, we are not suggesting that microvascular decompression be supplanted as the preferred surgical technique for patients with cTN. Perhaps, in patients without NVC but with decreased SATNaPT, other surgical techniques may be considered, either in combination with microvascular decompression or as an alternative.

In the discussion section of our article,¹ we acknowledge that severe displacement of the cisternal segment of the trigeminal nerve by a compressing artery could result in a decreased SATNaPT, but we note that subjective evaluation of the patients in our series did not support this theory. In our series, 83% of patients with cTN had a SATNaPT that was similar to that in healthy individuals, so we are trying to measure the effect of an anatomic difference in a small subset of patients. In this circumstance, the effect of the smaller group is often overwhelmed statistically by the larger cohort, so one should expect that the effect of SATNaPT would not be evident in a large series that did not take SATNaPT into account. Patients with a rare anomaly need to be studied separately, lest the effect of the novel finding be overwhelmed by the larger population without the predictive biomarker.

We are grateful that Suthar and colleagues included a figure with their letter in which they demonstrate a diminished SATNaPT in conjunction with NVC. This gives us the opportunity to point out that the SATNaPT must be measured between the cisternal segment of the trigeminal nerve and the uppermost branch of the trigeminal nerve within the Meckel cave. Measurements made on the largest or most convenient branch will underestimate the SATNaPT and lead to false-positive results.

The underlying question of whether SATNaPT is truly an independent biomarker of surgical outcome, distinct from the degree of NVC, will require further research. These studies are ongoing, and we look forward to sharing the results of our research on the predictive value of the SATNaPT as an independent preoperative imaging biomarker.

REFERENCES

1. Branstetter BF, Reddy N, Patel K, et al. **Sagittal angle of the trigeminal nerve at the porus trigeminus: a novel measurement to distinguish different causes of classic trigeminal neuralgia.** *AJNR Am J Neuroradiol* 2022;43:1460–63 CrossRef Medline
2. Hughes MA, Jani RH, Fakhran S, et al. **Significance of degree of neurovascular compression in surgery for trigeminal neuralgia.** *J Neurosurg* 2020;133:411–16 CrossRef Medline
3. Sindou M, Howeydy T, Acevedo G. **Anatomical observations during microvascular decompression for idiopathic trigeminal neuralgia (with correlations between topography of pain and site of the neurovascular conflict): prospective study in a series of 579 patients.** *Acta Neurochir (Wien)* 2002;144:1–13 CrossRef Medline
4. Jani RH, Hughes MA, Gold MS, et al. **Trigeminal nerve compression without trigeminal neuralgia: intraoperative vs imaging evidence.** *Neurosurgery* 2019;84:60–65 CrossRef Medline
5. Maarbjerg S, Wolfram F, Gozalov A, et al. **Significance of neurovascular contact in classical trigeminal neuralgia.** *Brain* 2015;138:311–19 CrossRef Medline

B.F. Branstetter

Departments of Radiology, Otolaryngology, and Biomedical Informatics
University of Pittsburgh
Pittsburgh, Pennsylvania

R.F. Sekula

Department of Neurosurgery
Columbia University
New York, New York

<http://dx.doi.org/10.3174/ajnr.A7802>